Influence of the epitaxial strain on magnetic anisotropy in LSMO thin films for spintronics applications

Sandeep Kumar Chaluvadi

Normandie Université

THESE

Pour obtenir le diplôme de doctorat

Spécialité ELECTRONIQUE, MICROELECTRONIQUE, OPTIQUE ET LASERS, OPTOELECTRONIQUE MICROONDES

Préparée au sein de l'ENSICAEN et de l'UNICAEN

Influence of the epitaxial strain on magnetic anisotropy in LSMO thin films for spintronics applications

Présentée et soutenue par
Sandeep Kumar CHALUVADI

Thèse soutenue publiquement le 13 décembre 2017 devant le jury composé de		
M. VIRET Michel	Chercheur (HDR), CEA Saclay	Rapporteur
M. BELMEGUENAI Mohamed	Maître de conférences (HDR), Université Paris 13	Rapporteur
Mme MOUGIN Alexandra	Directrice de recherches CNRS, Université Paris 11	Examinateur
M. MAZALEYRAT Frédéric	Professeur des universités, ENS Cachan	Examinateur
M. PERNA Paolo	Chercheur, IMDEA Madrid	Examinateur
Mme MECHIN Laurence	Directrice de recherches CNRS, Université Caen Normandie	Directeur de thèse

Thèse dirigée par Laurence MECHIN, laboratoire GREYC (UMR 6072)

UNIVERSITÉ CAEN NORMANDIE

ENSICAEN
ÉCOLE PUBLIQUE D'INGÉNIEURS
CENTRE DE RECHERCHE

MISΣ

GREYC

Contents

List of Abbreviations

AFM	Atomic Force Microscopy
AI	Artificial Intelligence
AMR	Anisotropic Magnetoresistance
Ar	Argon
Au	Gold
BOX	Buried Oxide
CHF_3	Trifluoromethane
CMP	Chemical Mechanical Polishing or Planarization
CMR	Colossal Magnetoresistance
DE	Double Exchange
DSO	Dysprosium Scandate ($DyScO_3$)
EUV	Extreme Ultraviolet
FM	Ferromagnetic Metal
FWHM	Full Width Half Maximum
GMR	Giant Magnetoresistance
H_C	Coercive field
HF	Hydrofluoric
H_S	Switching field
IBE	Ion Beam Etching
IoT	Internet of Things
JT	Jahn-Teller
KrF	Krypton Fluoride
$LaMnO_3$	Lanthanum Manganite
LAO	Lanthanum Aluminate ($LaAlO_3$)
LASER	Light Amplification Stimulated Emission of Radiation
LSAT	LanthanumAluminate-StrontiumAluminumTantalate $(LaAlO_3)_{0.3}(Sr_2AlTaO_6)_{0.7}$
LSGO	Lanthanum Strontium Gallium ($LaSrGaO_4$)
LSMO	Lanthanum Strontium Manganite ($La_{1-x}Sr_xMnO_3$) (X = 0.3, 0.33 and 0.38)
LT-MOKE	Low-Temperature Magneto-Optical Kerr Magnetometry
MA	Magnetic Anisotropy
MBE	Molecular Beam Epitaxy
MEMS	Micro-Electro-Mechanical Systems
MgO	Magnesium Oxide
MIT	Metal Insulation transition
MOKE	Magneto-Optical Kerr Magnetometry
MR	Magnetoresistance
MRAM	Magnetic Random Access Memory
MTJ	Magnetic Tunnel Junctions
N_2	Nitrogen
NGO	Neodymium Gallium Oxide ($NdGaO_3$)

Nm	nanometer
o	Orthorhombic
O_2	Oxygen
pc	Pseudocubic
PLD	Pulsed Laser Deposition
PMN-PT	Lead Magnesium Niobate-Lead Titanate $[Pb(Mg_{1/3}Nb_{2/3})O_3]_{(1-x)}$ $[PbTiO_3]_x$
PR	Photoresist
PVD	Physical Vapor Deposition
RHEED	Reflection High Energy Electron Diffraction
RIE	Reactive Ion Etching
RMS	Root Mean Square
RSM	Reciprocal Space Mapping
RT	Room Temperature
SEM	Scanning Electron Microscope
SF_6	Sulphur Hexafluoride
Si	Silicon
SMO	Strontium Manganite ($SrMnO_3$)
SOI	Silicon-on-Insulator
SQUID	Superconducting Quantum Interference Device
STO	Strontium Titanate ($SrTiO_3$)
T_c	Curie temperature
TCR	Temperature Coefficient of Resistance
T_p	Maximum Resistance
uc	unitcell
UHV	ultrahigh vacuum
UV	Ultraviolet
V-MOKE	Vectorial Magneto-Optical Kerr Magnetometry
XLD	X-ray Linear Dichroism
XRD	X-ray Diffraction
YSZ	Yttrium Stabilized Zirconia
μm	micrometer

List of Symbols

θ	Angle between applied magnetic field and [100] crystallographic axis
θ_H	Angle between magnetization and [100] crystallographic axis
α	Angle between two consecutive easy axes in symmetry broken systems
β	Angle between Biaxial and Uniaxial anisotropy and
γ	Shear strain
δ	Lattice mismatch
K_u	Uniaxial anisotropy
K_b	Biaxial anisotropy
ϵ^*	Biaxial strain
ϵ_B	Bulk strain
μ_o	Vacuum permeability
M_s	Saturation Magnetization
I_Δ	Differences in intensity (Polarization changes)
I_Σ^{AC}	Sum of AC component (Reflectivity changes)
I_Σ^{DC}	Total reflectivity

1 Introduction

The 21st century is known as *"information age"* or *"digital age"*, thanks to the silicon technology. Due to ever-increasing consumers demand and competition between industries, the silicon technology is shrinking or doubling the transistor density for every 18 months that termed as "Moore's law" [1]. Rapid advancements in the technology towards Artificial Intelligence (AI), augmented reality, Internet of Things (IoT), cloud storage etc. are putting more pressure on information storage even beyond the requirements of today's smartphones and tablets. It is a never-ending challenge for any data storage technology to increase the storage density. In addition, lithography industries are making tremendous advancements in Extreme Ultraviolet (EUV) [2] lithography to take silicon technology beyond 7 nm technology node and to extend Moore's law for another decade. On the other hand, the power consumption and the production cost are expected to increase exponentially.

Therefore, parallel research is essential and it is being conducted in different fields that may possibly replace the magic of Moore's law. Some of them are quantum-well transistors, optoelectronics, molecular electronics, neuromorphic computing, carbon nanotube transistors, 2D materials (graphene, MoS_2 etc.), spintronics [3] etc. "Spintronics" is the name used to describe technologies that exploit both the spin and the charge of the electron. Spintronics promises great advantages over conventional electronics, including lower power consumption and higher speed [4]. Magnetic storage density is increasing steadily in almost the same way as electronic device size. Thus, magnetism, in general, appears to be a new contender for many novel computing applications that were considered traditionally beyond its range [5]. The applications of the spintronics technology will be used in magnetic sensors, spintronics couplers, and magnetic random access memory (MRAM), magnetic tunnel junctions (MTJs), domain wall race-track memories [6] etc. Hence, the interests in magnetic materials among researchers, industries have experienced a tremendous boost due to their versatile applications in sensors, actuators, and magnetic data storage.

Irrespective of the application, one of the key properties that need to be considered for a ferromagnetic sample is its magnetic anisotropy that dictates the magnetization reversals pathways. Depending on the specific desired application, easy plane (isotropic, uniaxial, biaxial etc.), easy cone, and perpendicular magnetic anisotropy (PMA) systems can be used.

For example, an *isotropic* magnetic material can be magnetized easily in any direction. In other words, the energy needed to orient the magnetization is the same in all the directions. Hence, by taking advantage of shape effects, one can design on purpose the device geometry (by resorting to lithography) of the magnetically isotropic medium to turn the net magnetization direction favorable to his applications.

Instead, in *anisotropic* magnetic materials, the magnetization aligns in two (uniaxial), four (biaxial) or more preferential directions (which are called magnetization easy axes). Therefore, the energy employed to orient the magnetization in a specific direction varies. In particular, a defined *uniaxial anisotropy* is required for good definition and retention of

digital information in magnetic recording or magnetic memories. It is also necessary for magnetic field sensors based on anisotropic magneto-resistance (AMR) [7] to obtain a linear hysteresis-free response. In the latter case, the anisotropy defines both the sensing direction and the sensitivity.

A defined *biaxial anisotropy* has four stable magnetization states compared to two stable magnetization states in the uniaxial system. Therefore, a magnetic material with biaxial anisotropy has a capability to encode more information (four binary bits: “00”, “01”, “10”, “11”) and can be used in memory and logic devices [8], [9]. Apart from the logic gate devices, biaxial magnetic anisotropy is been used in voltage controlled resistive switching by approximately 90° for giant magnetoresistance (GMR) and MTJ.

Magnetic materials with very strong *perpendicular magnetic anisotropy* (PMA) or out-of-plane magnetization offers superior qualities in magnetic recording and memory applications [10]–[12]. In in-plane magnetic anisotropy materials, the data is stored in the plane of the film. Whereas in PMA materials, the data bits are stored perpendicular to the plane of the film. This PMA helped to increase the density of storage bits by an order of magnitude. It has been successfully commercialized as MRAM.

Similarly, *easy cone* magnetic anisotropy is introduced into a ferromagnet (FM) electrode that enhances the performance of spin transfer torque (STT) – MRAM [13], [14]. Recent advancements in spin-torque oscillators [13] use a combination of *in-plane, out-of-plane* and *easy cone (canted)* magnetic anisotropy by fabricating thin film heterostructures of different materials.

Having discussed the advantages and applications of magnetic anisotropies, understanding and controlling the interfacial magnetic properties and the magnetization direction of ferromagnetic thin films are crucial for spintronic device applications. In this thesis, I point out the attention to the half-metallic manganite $La_{1-x}Sr_xMnO_3$ (LSMO) with an optimum doping concentration of strontium (Sr), $x \cong 0.3$ that is considered as a potential candidate for spintronic devices. In fact, it is half-metal, room temperature ferromagnetic metal (FM) with Curie temperature T_C ~ 370 K and nearly 100% spin polarized.

A variety of vacuum deposition and non-equilibrium plasma techniques are used to produce artificial heterostructures, nano-composites etc. In particular, *epitaxial strain* imposed in complex oxide thin films by heteroepitaxy is recognized as a powerful tool for identifying new properties and exploring the vast potential of materials performance [15].

This experimental study aimed therefore to address the following questions:

i. How does the magnetic anisotropy symmetry in LSMO thin films changes by tuning the epitaxial strain?
ii. How does the slight change in ‘Sr’ composition could tremendously affect the magnetic anisotropy properties?

The overall structure of the thesis takes the form of eight chapters, including this introductory chapter. Chapter 2 deals with the importance of functional oxides with focus on

LSMO structure and its strain dependent properties. The latter part briefly deals with the thin film growth techniques (Pulsed Laser Deposition (PLD), Molecular Beam Epitaxy (MBE)), as thin films are essential for realizing any practical applications. Difference between two techniques is also presented.

Chapter 3 concerns with the factors influencing magnetic anisotropy (magneto-crystalline, magneto-elastic, shape etc.) in LSMO thin films grown on different substrates. The latter part deals with the Magneto-Optical Kerr Magnetometry (MOKE) technique that was used for studying the magnetic anisotropy.

Chapter 4 presents the results of the research focusing on structural, surface morphology, electrical and magnetic transport properties of $La_{1-x}Sr_xMnO_3$ (LSMO) $(x = 0.33)$ thin films under tensile and compressive strain states.

As most part of my thesis is aimed to address the *magnetic anisotropy* properties of epitaxially strained LSMO thin films, chapters 5 – 7 are fully dedicated to deal with magnetic anisotropy. Chapter 5 analyses the thickness and temperature dependent *in-plane* magnetic anisotropy properties of epitaxial LSMO $(x = 0.33)$ thin films that were grown under *tensile* strain (STO (001) and STO *buffered* MgO (001) substrates) by PLD technique.

Chapter 6 analyses the thickness and temperature dependent *in-plane* magnetic anisotropy properties of epitaxial LSMO $(x = 0.33)$ thin films that were grown under *compressive* strain (NGO (110), LSAT (001) substrates) by PLD technique.

Chapter 7 especially focuses on the fabrication of epitaxial LSMO $(x = 0.3 \text{ and } 0.38)$ thin films of various thicknesses by MBE technique on a peculiar substrate (LSAT (001)). It also deals with the thickness, temperature, and composition dependent magnetic anisotropy uncertainties.

In order to explore the potential applications of these oxide materials in microelectronic devices, the integration of their functionality on the silicon technology, i.e. using Si (100) substrates, is highly required. Therefore, chapter 8 presents a few available ideas from the literature and few challenges that we faced during the fabrication of devices. It also presents another idea to tune strain in epitaxial thin films by thinning the substrate which could en route them towards flexible electronics using functional oxides.

Finally, the conclusion gives the highlights of this study

Keywords: Epitaxial strain, magnetic anisotropy, thin films, manganites

2 Manganite ($La_{1-x}Sr_xMnO_3$) properties

2.1 Functional oxide perovskites

Since the discovery of high-temperature superconductors (HTS), functional oxides perovskites have gained a lot of interest in the research community. In the last 50 years, immense research has been done, which empowered us to understand their deep underlying physics, their wide range of functional properties such as colossal magnetoresistance, superconductivity, magnetism, piezo- and ferroelectricity, multiferroics etc. These unusual properties arise from the metal-oxygen bonds and very strong electron correlations, which results in various interactions such as Coulomb repulsions, strain, orbital bandwidth, structural changes, and Hund's exchange coupling. All these interactions in functional oxides are quite different from the conventional semiconductors where one property is dominant over other and tend to be of similar magnitude as shown in Figure 2.1. Therefore, the interplay between these competing energies results in the ordering of spins (which is an essential property for spintronic devices), charge and orbital degrees of freedom. Also, these interactions are very sensitive to various parameters such as strain, temperature, pressure etc., which explains why these materials can be of high interest for sensors.

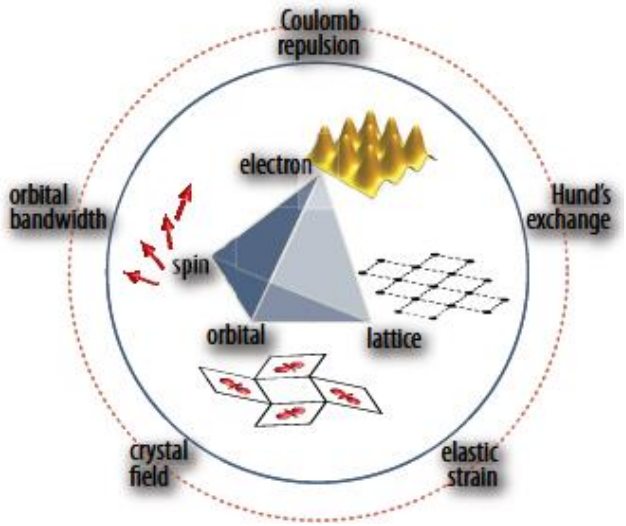

Figure 2.1: The various competing energies of functional oxides listed around the circle lead to strong coupling between electron, spin, orbit, and lattice degree of freedom [16].

Among the various complex functional oxides, here in this thesis, we will mostly focus on mixed-valence manganese oxide namely, $La_{1-x}Sr_xMnO_3$ that exhibits metal-insulator transition temperature (MIT) accompanied by colossal magnetoresistance [17] (CMR).

2.1.1 Perovskite crystal structure

The general formula of perovskite, which originally designed $CaTiO_3$, is ABO_3. Its ideal structure is cubic and its space group belongs to P_{m3m}. The cations 'A' and 'B'

occupies simple cube (SC) and body centered cube (BCC) whereas, anion 'O' occupies face-centered cube (FCC). By joining the 6 oxygen atoms present around the cation 'B' resembles the shape of octahedra often termed as 'BO_6' octahedral network. Therefore, in an ideal perovskite, all the bond lengths $B-O$ are equal and bond angle $B-O-B$ is equal to 180° as shown in Figure 2.2. Although most of the perovskites deviate from its 'ideal cubic' structure to either orthorhombic ($GdFeO_3$ type), rhombohedral and triclinic etc. depending upon the radii of dopant cation. The structure of the perovskite according to cation radii can be identified by using Goldschmidt tolerance factor 't' as given in (2.1)

$$\boldsymbol{t = \frac{r_A + r_O}{\sqrt{2} r_B + r_O}} \tag{2.1}$$

For $t \leq 0.96$: Orthorhombic, $0.96 \leq t \leq 1$: Rhombohedral, and $t \cong 1$: Cubic.

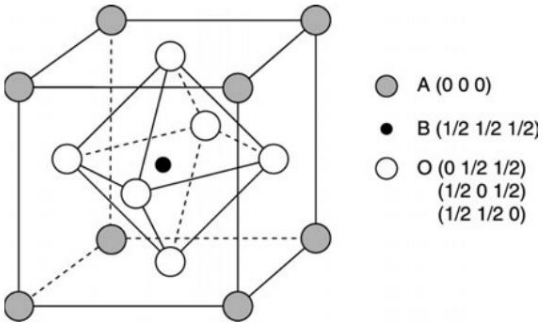

Figure 2.2: Ideal cubic perovskite structure ABO_3 with atoms A, B and O occupying simple cube (SC), body-centered (BC) and face-centered (FC) positions, respectively [18].

2.1.2 Phase diagram of $La_{1-x}Sr_xMnO_3$

Doping concentrations and atomic radii of cations could determine the physical and structural properties of manganites perovskites. Figure 2.3 shows the rich phase diagram of the $La_{1-x}Sr_xMnO_3$ manganites as a function of 'Sr' dopant concentration that enables different properties. In brief, both the extreme dopant concentrations i.e., for $x = 0$ ($LaMnO_3$) and $x = 1$ ($SrMnO_3$) exhibit antiferromagnetic (A-type and G-type) and insulating behavior. For $x < 0.17$, a long-range cooperative Jahn-Teller (JT) effect establishes the orbital ordering and has A-type antiferromagnetic property. For $x > 0.17$, the long-range JT distortions are suppressed and display ferromagnetic metal (FM) phase. This FM phase is quite stable up to the 'Sr' dopant concentration of $x = 0.5$. At $x = 0.33$, the compound is half metal and exhibit FM with highest Curie temperature ~350 K. Therefore, this particular doping concentration (around $x = 0.33$) is of our interest as it can enable us to explore the possibilities for developing room temperature spintronic devices.

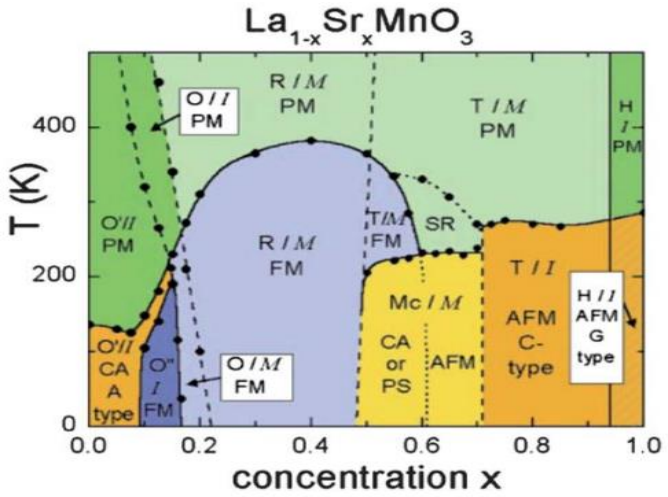

Figure 2.3: $La_{1-x}Sr_xMnO_3$ phase diagram with 'Sr' doping concentration 'X' [19]**. The crystal structures (Jahn-Teller distorted orthorhombic: O′ orthorhombic O; orbital-ordered orthorhombic: O,″ rhombohedral: R, tetragonal: T, monoclinic: Mc, and hexagonal: H) are indicated as well as the magnetic structures [paramagnetic: PM (green), short-range order (SR), canted (CA), A-type antiferromagnetic structure: AFM (yellow), ferromagnetic: FM (blue), phase separated (PS), and AFM C-type structure] and the electronic state [insulating: I (dark), metallic: M (light)].**

2.1.3 Crystal structure and properties

Bulk $La_{0.67}Sr_{0.33}MnO_3$ (LSMO) possesses rhombohedral crystal structure [20] with lattice constants $a_r=b_r=c_r$=0.5471 nm, angles $\alpha_r=\beta_r=\gamma_r$=60.43° and space group belongs to $R\bar{3}c$. The rhombohedral unit cell is often considered as pseudocubic structure as shown in Figure 2.4.

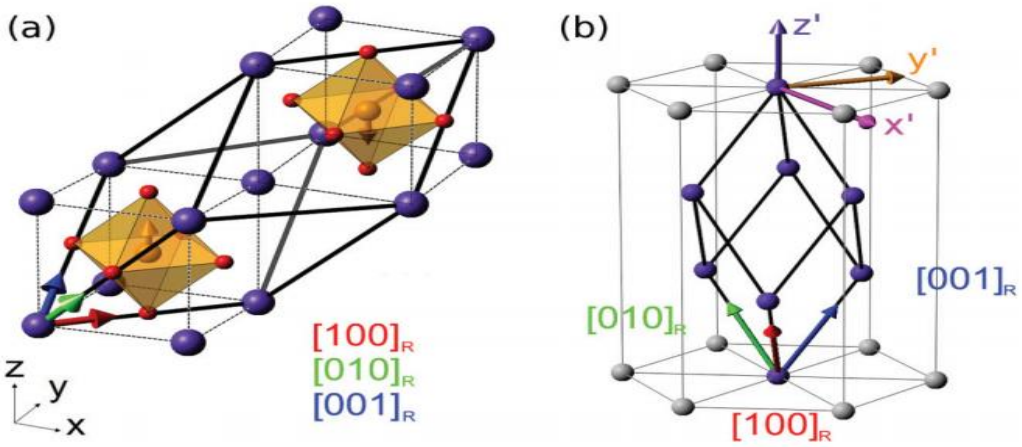

Figure 2.4: Crystal structure of LSMO and coordinate systems. (a) The transformation between rhombohedral unit cell (solid lines) and pseudocubic (dotted lines) perovskite structures. The atoms lanthanum & strontium, manganese, and oxygen are represented by blue, orange and red colors, respectively. The Cartesian axes x, y, z points to the pseudocubic structure and the unit vectors belong to the rhombohedral structure. (b) The Cartesian axes x', y', z' used to describe the properties of the rhombohedral structure (blue circles, thick lines) are shown along with the alternative trigonal cell (gray circles, thin lines) [21]**.**

The pseudocubic lattice parameters of LSMO that are derived from equation (2.2) [22] are $a_{pc} = 0.3876$ nm.

$$\boldsymbol{a_{pc} = \frac{\sqrt{2}a_r}{1+\cos\alpha_{pc}}}, \boldsymbol{\alpha_{pc} = \text{acos}\left[\frac{1-2\cos\alpha_r}{2\cos\alpha_r - 3}\right]} \quad (2.2)$$

Where, a_{pc}, a_r and α_{pc}, α_r are lattice constants and angles of pseudocubic and rhombohedral structures, respectively. In an isolated 'Mn' ion, all the five '3d' orbitals are bound together and there is no splitting of orbitals because there is no interaction with other orbitals. However, due to doping of divalent cation 'Sr', there exists mixed valence of manganese ions such as 'Mn^{3+}'and 'Mn^{4+}' in MnO_6 octahedral network, that lifts the degeneracy of five '3d' orbitals into three lower lying t_{2g} and two higher e_g states as shown in Figure 2.5. Further, due to the JT distortion, the degeneracy of orbitals split into different energy states causing distortion in oxygen octahedral network.

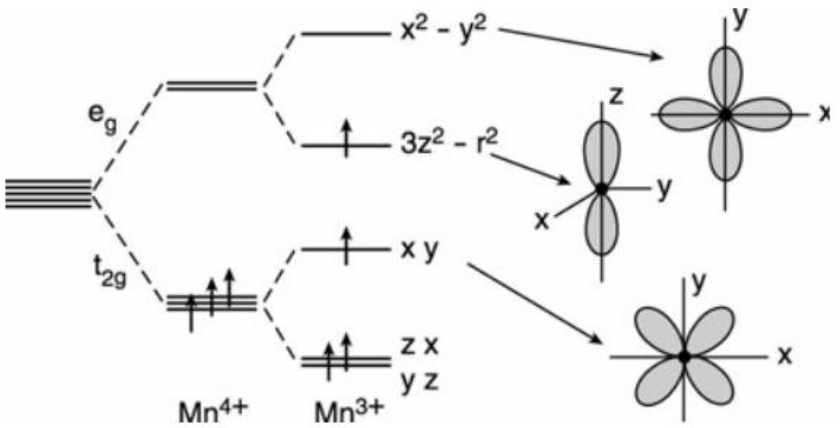

Figure 2.5: Crystal field splitting of five 3d orbitals into lower and higher energy states and the electronic configuration for Mn^{3+} and Mn^{4+} ions respectively [18]**.**

For Mn^{3+} compounds, the electronic configuration is $t_{2g}^3 e_g^1$ with total spin $S = 2$ whereas, in the case of Mn^{4+} compounds, the electronic configuration is $t_{2g}^3 e_g^0$ with $S = 3/2$, thus creating holes. Therefore, due to 0.33% dopant of Sr, it creates 0.33% of holes i.e., Mn^{4+} and 0.67% of electrons i.e., Mn^{3+}. Therefore, the electrons from Mn^{3+} ion can hop onto Mn^{4+} ion via oxygen 2p orbital by a process called double exchange (DE) mechanism, that leads to conduction in manganites as shown in Figure 2.6. These hopping of 'e_g' electrons depends upon the relative angle between the spins present in neighboring 'i' and 'j' sites. The inter-site hopping interaction 't_{ij}' can be expressed as $t_{ij}\cos(\theta_{ij}/2)$. So, the probability of hopping an electron from 'i' to 'j' site is higher for the situation in which spins are aligned in parallel ($\theta_{ij} = 0°$) and thus enhancing the conductivity [23], [24]. If the electron spins are aligned in anti-parallel direction i.e. $\theta = 180°$, then the hopping probability of an electron from 'i' to 'j' site is $t_{ij} = 0$. Due to the strong Hund's coupling ~2.5 eV, which is larger than the crystal field splitting ~1.5 eV ensures the parallel alignment of electron spins in the neighboring sites.

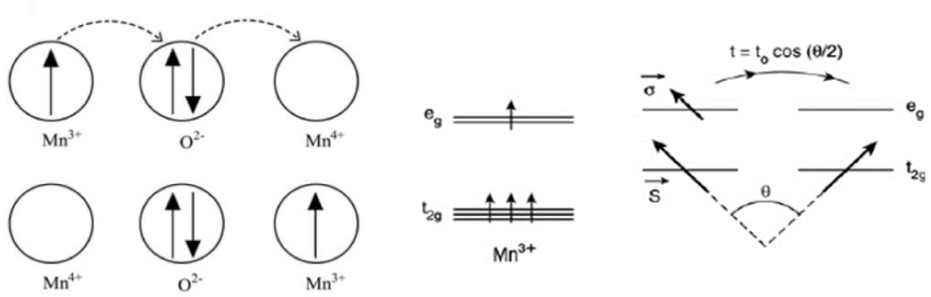

Figure 2.6: Transfer of electron from Mn^{3+} to Mn^{4+} via O – 2p orbital, and angle dependent transfer of e_g electron between 'i' and 'j' sites, respectively [25]**.**

As the temperature increases, the thermal energy overcomes the polarized spin alignment from ordered to a disordered state near around Curie temperature (T_c). This leads to the reduction in inter-site hopping of electrons and thus increases in resistance. Figure 2.7 shows the temperature-dependent magnetization and resistivity curves of bulk LSMO with the doping concentration of Sr = 0.3. The metal-insulator transition temperature (MIT) and ferromagnetic to paramagnetic Curie temperature (T_c) are occurring at same temperature ~370 K.

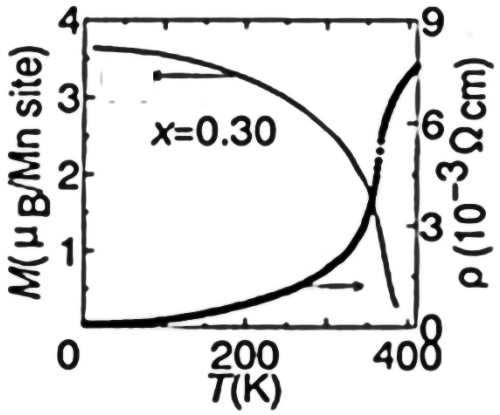

Figure 2.7: Temperature-dependent magnetization and resistivity of bulk $La_{0.7}Sr_{0.3}MnO_3$ [20]**.**

2.2 Thin films

In order to apply these fascinating physical properties of complex functional oxides for any practical applications, it is necessary to grow high-quality epitaxial thin films. A wide range of physical properties can emerge by growing thin films because their properties are very sensitive to small perturbations as structure, bond lengths, and bond angles in MnO_6 octahedra etc. Therefore, it is quite challenging to grow functional oxide thin films. However, thanks to the advanced techniques such as Molecular Beam Epitaxy (MBE) or Pulsed Laser Deposition (PLD), it is now possible to grow high-quality multifunctional oxides thin films. However, depending on the growth process, underlying substrate, the thickness of the film and technique used, the film can belong to one of the three different growth modes as discussed in the following sections.

2.2.1 Epitaxy

The term 'epitaxy' derived from the Greek word '*epi'* means '*top'* and '*taxis'* meaning '*ordered'*. It refers to the deposition of crystalline layers on the top of the crystalline substrate. Depending upon the underlying substrate and the material of the film, it is further classified into two types of epitaxy i.e., homoepitaxy and heteroepitaxy. If the thin film and substrate are of the same material, then it is "*homoepitaxy"*. Therefore, in *homoepitaxy*, the lattice mismatch between substrate and film is negligible, which reduces the defects in the film growth process (Figure 2.8(a)). If the thin film is of a different material than the substrate, then it is called *heteroepitaxy* growth; which is a widely used technique for device applications in semiconductor industries. Therefore, in *heteroepitaxy*, film grown onto different substrates experiences residual strain due to lattice mismatch between substrate and film as shown in Figure 2.8(b). The lattice mismatch (δ) is calculated as from equation (2.3)

$$\boldsymbol{\delta = {(a_s - a_f)}/{a_s}} \tag{2.3}$$

Where 'a_s' and 'a_f' are lattice constants of substrate and film respectively. For $\delta > 0$, i.e. when the lattice constant of the substrate (a_s) is greater than the lattice constant of the film (a_f), then the film undergoes an *in-plane* tensile strain. Similarly, for $\delta < 0$, i.e. when the lattice constant of the substrate (a_s) is less than the film (a_f), then the film undergoes an *in-plane* compressive strain. In both the cases, the total volume of the unit-cell almost and always remains constant. When the film grows on matched or nearly lattice matched substrates, the film grows defect free. Whereas, when the film is grown on large lattice mismatched substrate as shown in Figure 2.8(c), defects develop at the interface between film and substrate in form of dislocations, oxygen vacancies and intermixing of cations etc.

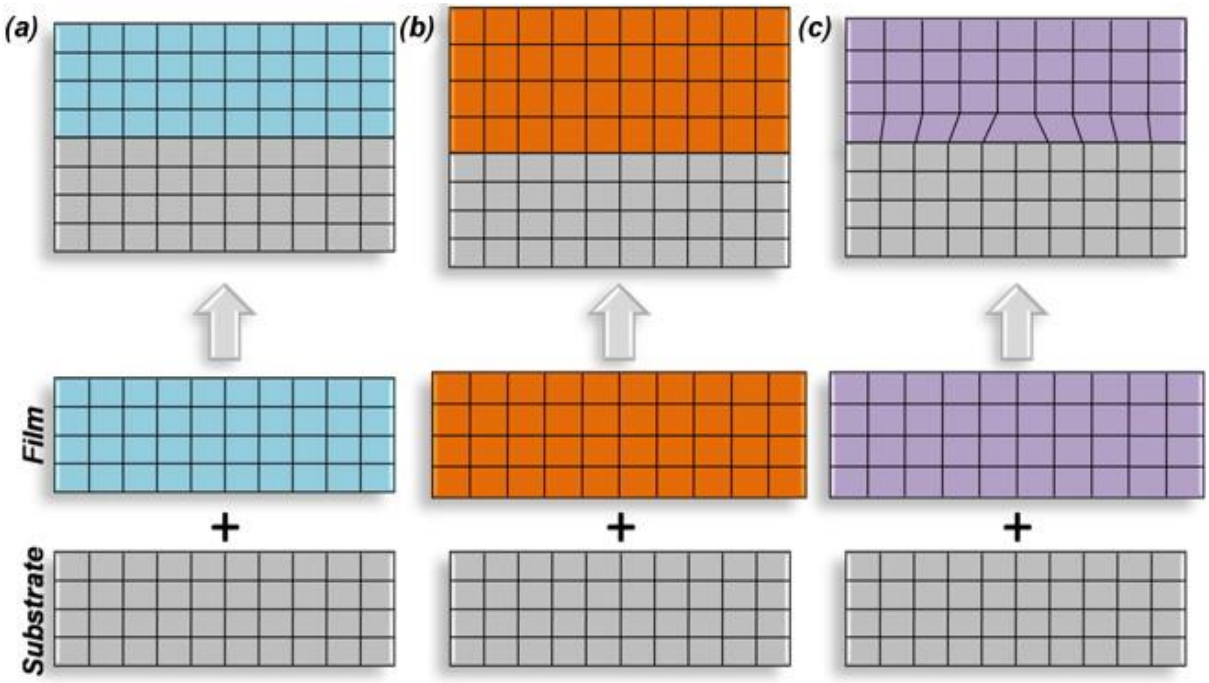

Figure 2.8: Schematic illustration of (a) lattice matched, (b) strained and (c) relaxed or unstrained epitaxial thin films [26]**.**

2.2.2 Growth modes

The growth of the epitaxial thin film on single crystal substrates depends on the interaction between incoming clusters of molecules, adatoms, and the substrate surface. Depending on these interactions, the growth mode of the film can be changed from layer-by-layer to island growth. Since the thin film deposition is a non-equilibrium kinetic process; a minimization of surface energy is attained, which includes free energy of film surface (γ_f), substrate surface (γ_s) and the interface (γ_i) between film and substrate.

2.2.2.1 2D or Frank-Van der Merwe or Layer growth

When the interactions between adatoms-substrate surfaces overcome the adatoms-adatoms interactions i.e. $\gamma_s + \gamma_i > \gamma_f$, adatoms strongly attach to the substrate surface and preferentially forming very smooth 2D or layer-by-layer growth as shown in Figure 2.9(a).

2.2.2.2 3D or Volmer-Weber or Island growth

When the interactions between adatoms-adatoms overcome the adatoms-substrate surface interactions, then the most energetically favorable condition leads to the formation of 3D islands on the surface of the substrate Figure 2.9(b). In this mode, the free energy of the adatoms overcomes the total free energy of the substrate surface and interface i.e. $\gamma_f > \gamma_s + \gamma_i$. As the thickness increases, the growth of these 3D islands coalesces together resulting in rough film surfaces [27].

2.2.2.3 2D + 3D or Stranski - Krastanov or layer + island growth

This mode is an intermediate process that includes both 2D layer growth and 3D island growth (Figure 2.9(c)). Here, strain and critical thickness of the film plays an important role. As the strain gets relaxed or critical thickness is reached, then the 2D layer-by-layer growth mode changes to 3D Island-based growth mode.

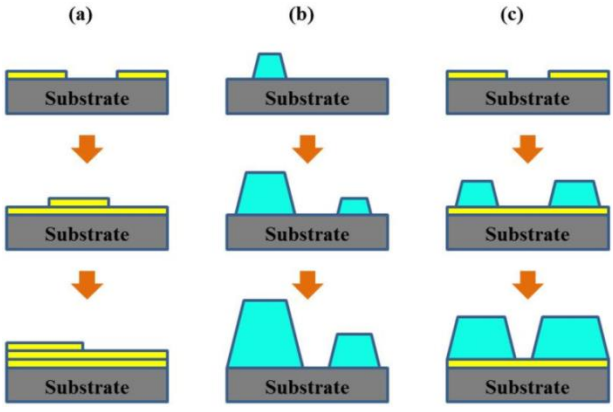

Figure 2.9: Schematic of different growth modes of thin films (a) Frank-Van der Merwe (2D) (b) Volmer-Weber (3D) (c) Stranski – Krastanov (2D + 3D) [28]**.**

2.2.3 Thin film growth techniques

2.2.3.1 Pulsed Laser Deposition (PLD)

Since the discovery of high Tc superconductivity [29], the research community has renewed its interest in PLD. PLD belongs to the family of PVD techniques and is well-known for its stoichiometric transfer of complex oxide materials [30]–[34] from target to the substrate in the oxygen environment. The basic principle involved in this technique is as follows. A high energetic pulsed laser beam (few hundreds of eV) [35] is focused onto the target with the help of various lenses as shown in Figure 2.10. The laser hits the target at an angle of 45° or 60° and particles with high kinetic energy are ejected from the target in form of atoms, molecules, and ions and form the plasma with a characteristic shape known as "Plume" (inset of Figure 2.10). The plume is directed towards the heated substrate facing the target and then condenses on the substrate. Depending on the oxygen partial pressure in the deposition chamber, the shape of the plume differs. If the oxygen partial pressure is higher, the mean free path of the ejected particles from the target decreases and scattering increases thus forming a bright, wide shaped plasma plume.

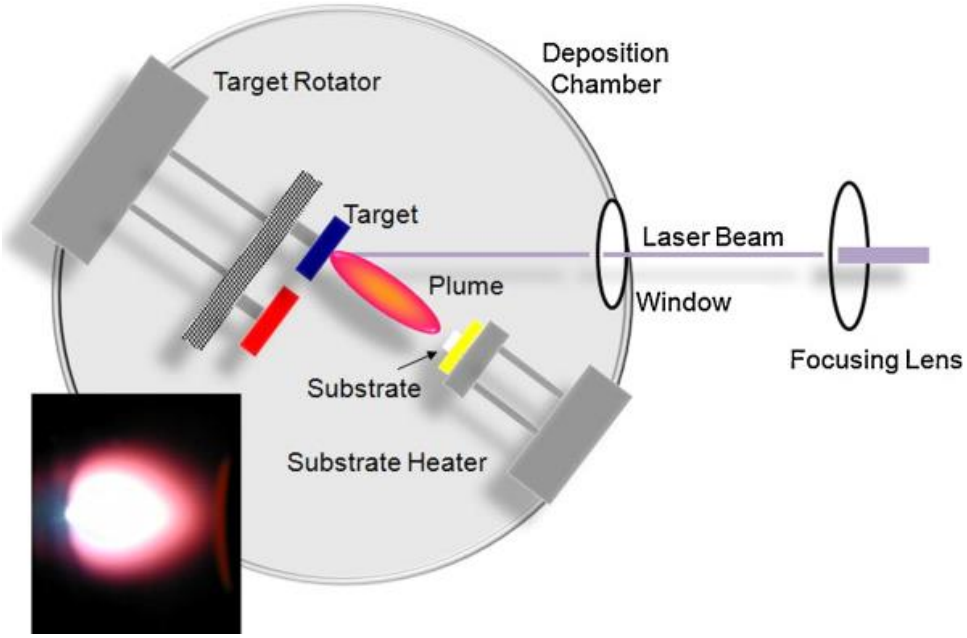

Figure 2.10: Schematic representation of pulsed laser deposition system and the inset shows the plume during the laser/target interaction [26]**.**

PLD technique was confined so far to laboratory scale because the uniformity of the film is achieved for less than $10\ \text{mm} \times 10\ \text{mm}$ substrates. However, Twente group [31] recently managed to grow thin films on large wafers, up to 200mm, that could provide the path for industrial applications.

2.2.3.2 Molecular Beam Epitaxy (MBE)

MBE also belongs to the PVD family but the growth mechanism is entirely different from PLD [36]. In this technique, the material elements of interest are individually

evaporated in an oxidizing environment (generally oxygen and ozone for oxides). In contrast to PLD, the typical thermal energies are less than 1 eV in MBE. Therefore, the deposition rate is very slow as it takes several hours to deposit > 100 nm thick film. Two types of deposition methods are being used namely *co-deposition* and *shutter* method. In *co-deposition* method, all the atoms are evaporated simultaneously whereas, in *shutter* method, the atoms are deposited one after another through computer controlled sequence [37], [38]. The latter method with *in-situ* reflection high-energy electron diffraction (RHEED) is widely used as the RHEED oscillations and intensity allow us to precisely control the termination and thickness of the film. So, with MBE, virtually any device structure can be made such as artificial superlattices, quantum devices etc.

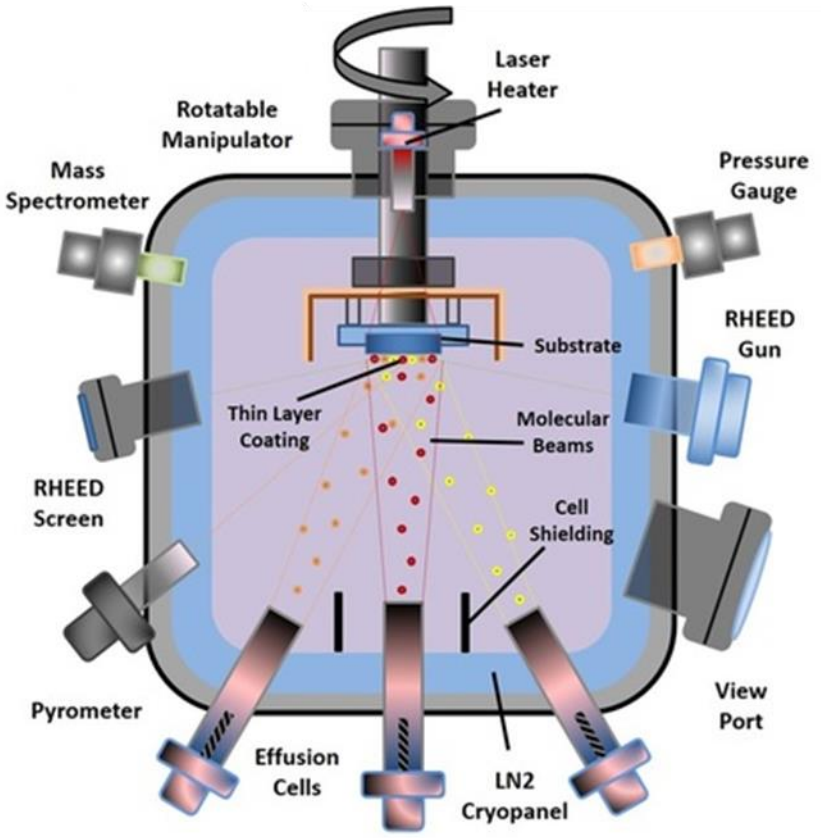

Figure 2.11: Schematic representation of molecular beam epitaxy with *in-situ* RHEED [39]**.**

J. Shen *et al.* [30], B. Shin *et al.* [35] observed the differences in the evolution of film growth, morphology and roughness by using PLD and MBE growth techniques. Under identical conditions, they reported that the film morphology is similar by using both MBE and low energy PLD[i], whereas, with the high-energy PLD (which is commonly used for oxides), the surface morphology is quite different and is due to high kinetic energy. Therefore, depending on application, structure etc. of the film, the growth technique should be wisely chosen.

[i] Laser fluence of ~ 4 and ~ 7 J/cm^2 is considered as low and high energy for Ge (001) thin films by PLD [35]

2.2.3.3 Reflection High-Energy Electron Diffraction (RHEED)

Reflection High-Energy Electron Diffraction (RHEED) is a versatile *in-situ* technique in MBE and PLD, which is used for real-time monitoring of film growth process in ultra-high vacuum (UHV). RHEED has been a powerful technique for the study of the surface structure and surface ordering phenomena due to the limited penetration and escape depths of electrons [40]. In this technique, a high-energy electron beam with 35 keV and 1.5 Amp is directed towards the sample surface at grazing incidence angle ($< 5°$) and the RHEED pattern is formed on the phosphor screen. As the beam penetrates through only a few atomic layers thick, this makes the technique extremely surface sensitive. The crystalline surface, which acts as 2D gratings diffracts the electron beam after interacting with the sample, impinge on the phosphor screen, mounted opposite to the electron gun.

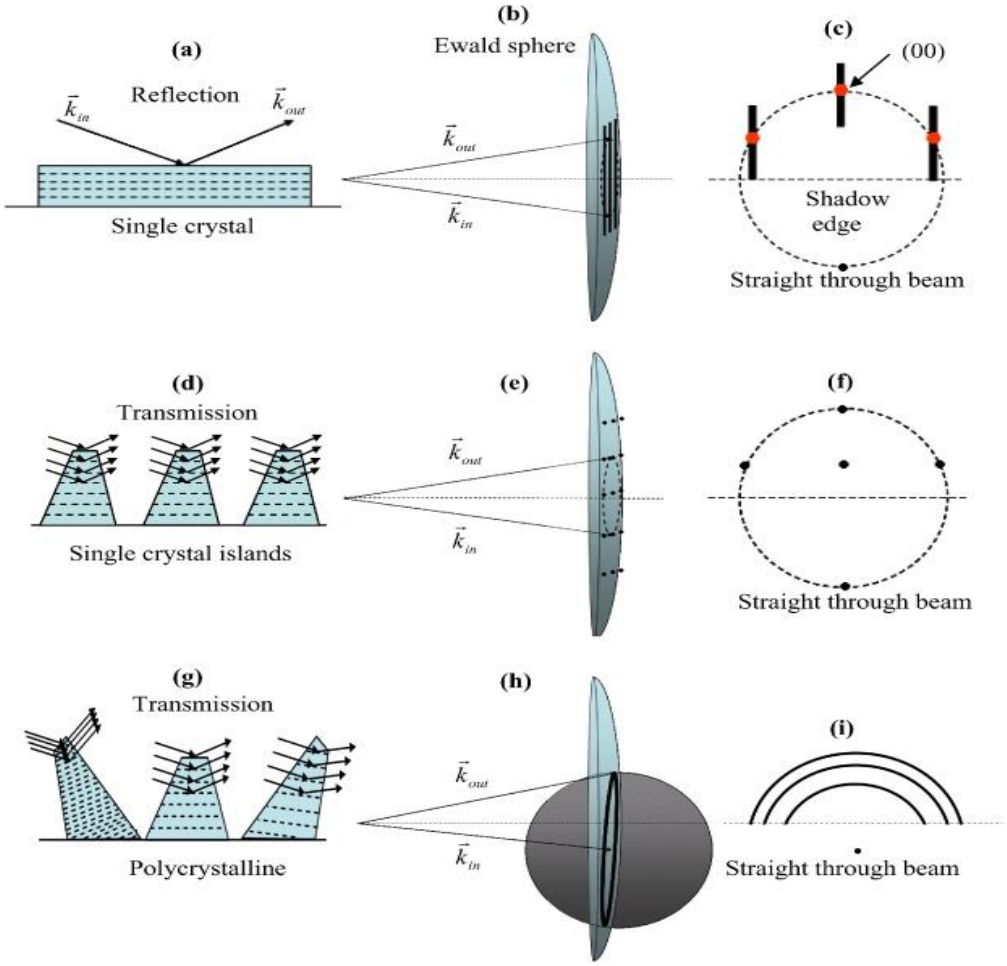

Figure 2.12: The schematics of various electron scattering geometries, film morphologies, and crystalline structures. (a) Single crystal film with a smooth surface. (d) Single crystal film with islands. (g) Polycrystalline film. In (a) the electron beam is reflected from the top surface layer. In (d) and (g) the electron beam is transmitted through tips of islands or crystallites. $\vec{K}_{in}$ and $\vec{K}_{out}$ are the wave vectors of the incident and scattered electron beams, respectively. The Ewald sphere constructions of electron scattering in these three cases are shown in (b), (e) and (h). Their corresponding diffraction patterns are shown in (c), (f) and (i), respectively. The horizontal dashed line in each of (c), (f) and (i) represents the shadowing edge. The straight through beam is the incident electron beam without hitting the substrate. The (0 0) in (c) represents the specular spot. The dark shaded sphere in (h) is the reciprocal structure from a polycrystalline that contains randomly orientated crystals [40]**.**

The Ewald sphere construction in the reciprocal lattice is shown in Figure 2.12. RHEED patterns can be classified into reflection and transmission pattern. Depending on the growth type, both reflection and transmission patterns are observed in the single crystal films (Figure 2.12 (a-f)) while only transmission pattern is observed in the polycrystalline films as shown in Figure 2.12 (g-i). The purpose of the RHEED is to monitor and control the real-time growth of the films. By monitoring the temporal evolution of the RHEED signal one can study the growth dynamics of the film. During film growth, the RHEED signal shows oscillatory behavior directly related to the growth rate. A flat and smooth surface prior to growth gives the maximum signal. As growth progresses, scattering from the small 2-dimensional nucleating islands decreases the beam intensity and it shows a minimum at half monolayer coverage, which is the roughest phase of the film growth. The intensity of the beam is restored after the growth of one monolayer as the surface again flattens by the coalescence of the islands shown in Figure 2.13. Thus, the oscillations are a result of the periodic changes in the roughness of the growing surface and the growth rate can be deduced from the time taken for one complete oscillation of the RHEED signal. Each maximum indicates growth of one complete monolayer.

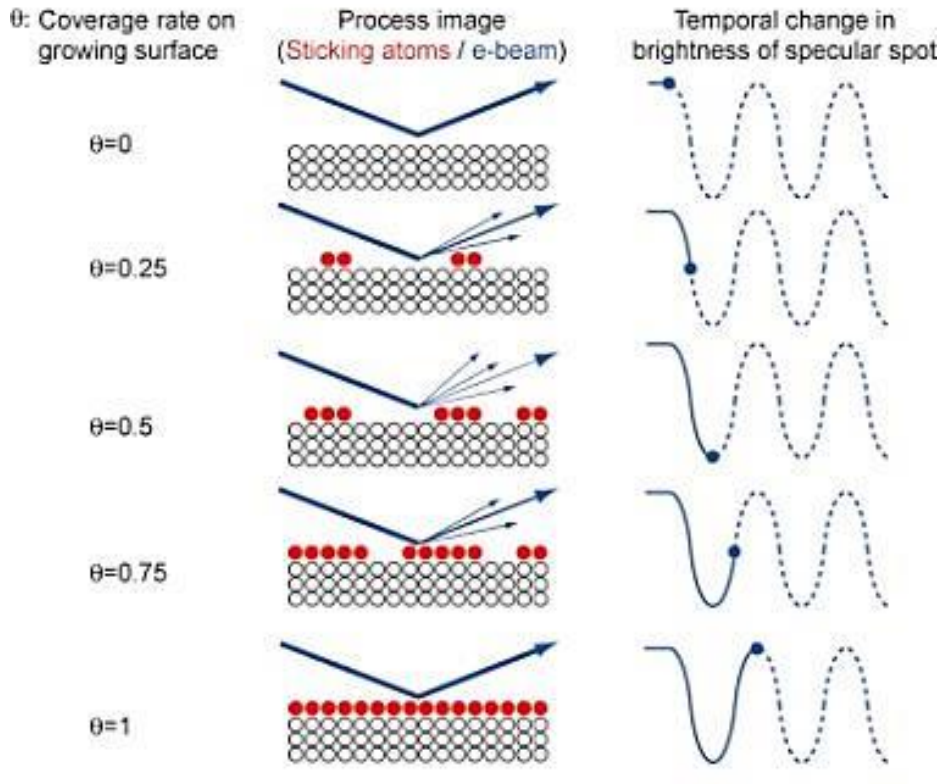

Figure 2.13: Systematic analysis of RHEED oscillations that corresponds to monolayer growth [41]**.**

2.3 Strain engineering

2.3.1 How to induce and/or tune strain

Functional oxide materials with technologically useful properties can be sensitively controlled by external perturbations. Because of the strong interplay between spin, charge,

orbital and lattice degree of freedom, functional oxides are very sensitive to subtle changes. The strain is one of the external factors along with oxygen vacancies, defects, thickness, and deposition conditions and many others. It can be noted that strain is also one of the key parameters to enhance the conductivity and device performance in CMOS technology. Similarly, strain engineering is also an attractive route to control the physical properties of multifunctional oxides [42]–[44]. Therefore, strain engineering has become an important tool to alter the structural properties that can open us to new challenges and possibilities. There are different techniques to induce strain into thin films. Some of them are:

i. Strain engineering due to lattice mismatch
ii. Strain engineering by substrate bending (semi-flexible type of substrates) [45], [46]
iii. Strain engineering by Micro-Electro-Mechanical Systems (MEMS) etc. [47]–[49]

Some other ways to tune the strain are by growing epitaxial films on vicinal substrates [50], [51], on piezoelectric substrates [52], [53] and by controlling strain through the formation of epitaxial nanoscaffolds in nanocomposite films [54]. In the next section, I will briefly introduce the strain-dependent properties by lattice mismatch. The other techniques (ii and iii) are beyond this chapter and will be presented later in Chapter 8.

2.3.2 Strain engineering due to lattice mismatch

From the last decade, the choice of the substrate has been critical for growing epitaxial perovskites films [55]–[60], in which strain is governed primarily by lattice mismatch. It is an approach taken from the design and growth of compound semiconductors, where strain has increased the efficiency of devices in terms of enhancement in conductivity, switching speed etc. Therefore, the elastic strain due to mismatch is imposed on the film by the underlying substrate.

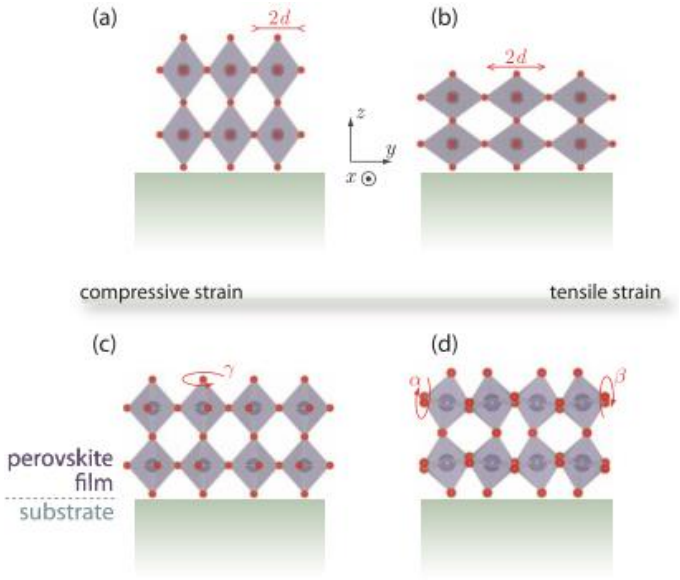

Figure 2.14: Schematic of lattice distortions in strained epitaxial perovskite thin film under (a) in-plane compressive strain, (b) in-plane tensile strain, respectively. Simultaneously or alternatively, BO_6 octahedra can accommodate the substrate-induced changes by rotation either perpendicular to substrate (c), and/or parallel to the substrate plane [16]**.**

This accommodates the changes in the film lattice parameters to get matched with the substrates either by compressive / contraction in $B-O$ bond length or by elongation in $B-O$ bond length as shown in Figure 2.14(a, b). In addition, strain also influences the changes in corner connected flexible oxygen octahedral network by rotations either in perpendicular or parallel or both to the substrate as shown in Figure 2.14(c, d). These octahedral rotations do not only depend on strain but also depend on the substrate octahedral rotation patterns as described by Glazer [61]. Due to the difficulties in determining experimentally the oxygen positions, the strain-octahedral coupling is not fully exploited so far. The most commonly used commercial perovskite substrates for the growth of perovskite films are shown in the Figure 2.15. The most commonly used perovskite substrates for the epitaxial growth of LSMO thin films are $LaAlO_3$ (LAO), $(LaAlO_3)_{0.3}(Sr_2TaAlO_6)_{0.7}$ (LSAT), $NdGaO_3$ (NGO), $SrTiO_3$ (STO), $DyScO_3$ (DSO) etc. LSMO films that are grown onto STO, DSO will experience in-plane biaxial tensile strain whereas, on LAO, LSAT and NGO experience in-plane biaxial compressive strain.

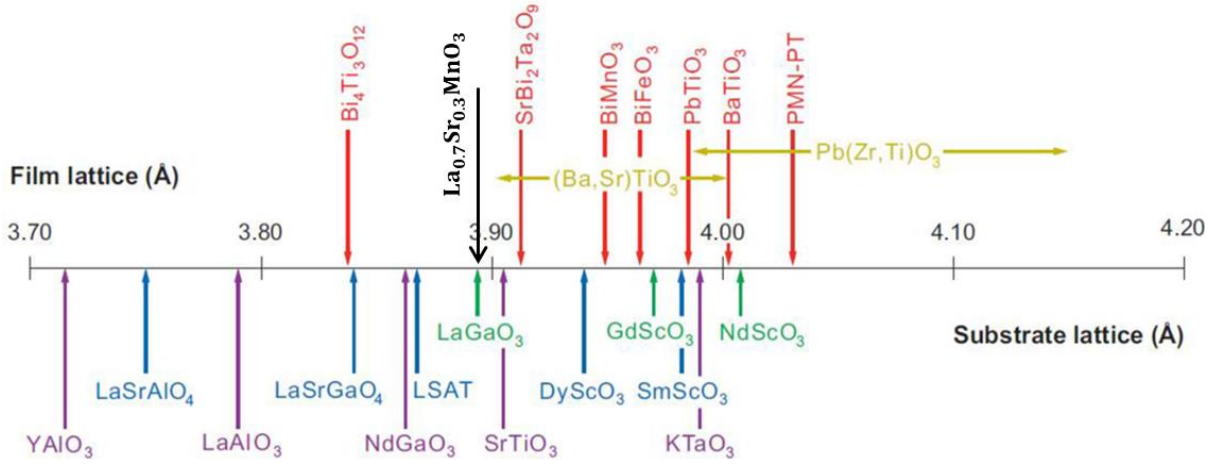

Figure 2.15: A number line showing the pseudotetragonal or pseudocubic a-axis lattice constants (in angstroms) of some perovskites (above the number line) and some of the perovskite and perovskite-related substrates that are available commercially (below the number line) (after [62]**).**

2.3.2.1 Orbital occupancy

Misfit strains have important consequences on the electronic structure of the LSMO films. In bulk LSMO, the partially filled orbitals $(x^2-y^2/3z^2-r^2)$ are responsible for the conduction through DE mechanism. However, strain in epitaxial thin films lifts the degeneracy of $(x^2-y^2/3z^2-r^2)$ orbitals and could change the electrical and magnetic properties [63]. As the LSMO film experiences strain (compressive or tensile), the BO_6 octahedra either compress or elongates, inducing Jahn-teller distortions, which in-turn lifts the degeneracy of the higher energy 'e_g' orbitals [64]. Many authors [65]–[67] investigated how the strain modifies the electron occupancy in the half-filled site in 'e_g' orbital by X-ray linear dichroism (XLD) measurements. They observed that the tensile strain favors the electron occupancy of in-plane x^2-y^2 orbital, while the compressive strain promotes the electron occupancy to out-of-plane $3z^2-r^2$ orbital as shown in the Figure 2.16.

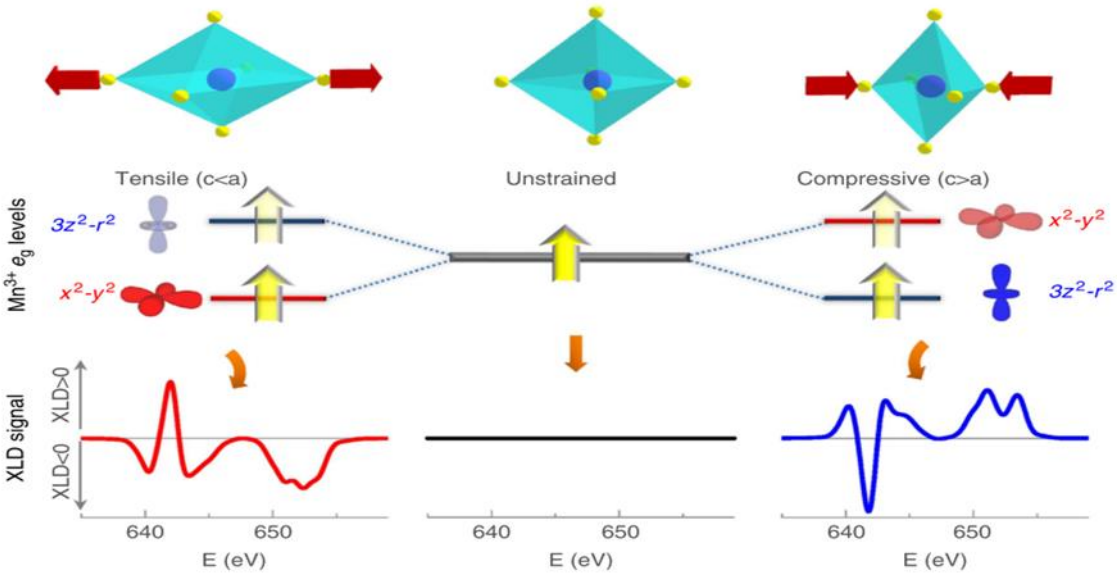

Figure 2.16: Preferential orbital occupancy and XLD signal of LSMO under tensile, unstrained and compressive strain [67].

However, theoretical [68] and XLD studies [67] on ultrathin (4 unit cell (uc)) LSMO films grown on STO has the tendency to occupy $3z^2 - r^2$ orbitals, decrease of double exchange[ii] and the strong reduction in Curie temperature that is termed as "dead layer". At the free surface, again LSMO displays a preferred occupancy of $3z^2 - r^2$ orbitals due to the absence of apical oxygen coordination and the reduction in electron-electron interaction.

2.3.2.2 Octahedral rotations

Along with the JT distortions and Mn^{3+} ion 'e_g' orbital occupancy, the strain in ABO_3 perovskite thin film accommodates by the combination of 'tilts' and 'rotations' of corner connected 'BO_6' octahedral network as shown in Figure 2.17(a). In an ideal cubic perovskite, the bond lengths and bond angles in BO_6 octahedra are equal. However, due to doping, the ionic radii differ and could lead to non-cubic structure, results in unequal $B-O$ bond length or/and $B-O-B$ bond angle [69]. The magnitude of octahedral rotation increases with increases in strain. These structural changes and octahedral tilting [70],[71] in perovskites can alter the physical properties of overall material and allows us to control the properties such as conductivity [72],[73], magneto-resistance [74], MIT [44], magnetization [75], magnetic anisotropy etc. [76],[22]. These tilts and rotations are written by using Glazer notations[61] as $a^{\#}b^{\#}c^{\#}$ where the letters a, b, c indicates the magnitude of rotations about their pseudocubic axis and the superscripts indicates in-phase (+), out-of-phase (-) and no tilt (0) to its adjacent octahedral network.

[ii] The delocalization process is less effective in $d^{Mn}_{z^2} - p^{O}_{x/y} - d^{Mn}_{z^2}$ compared to $d^{Mn}_{x^2-y^2} - p^{O}_{x/y} - d^{Mn}_{x^2-y^2}$, reducing conductivity and Curie temperature.

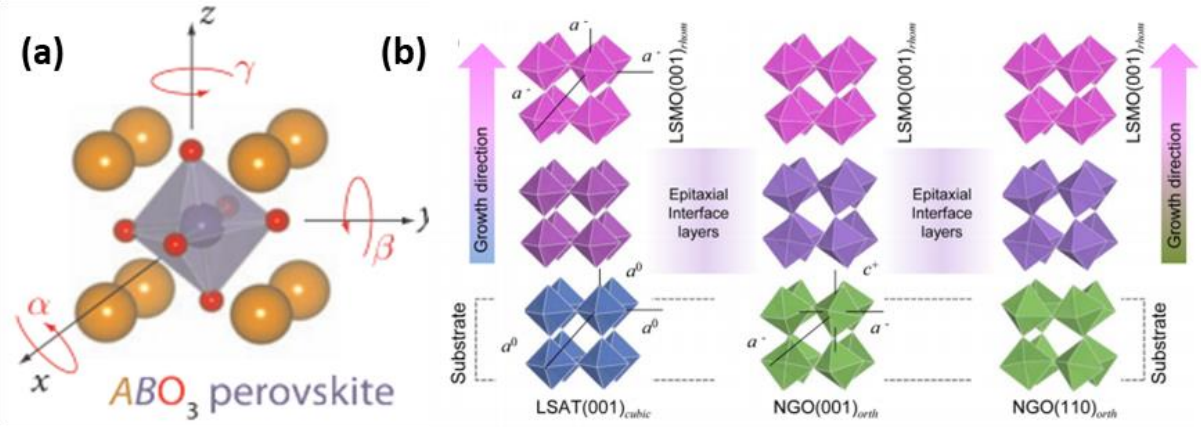

Figure 2.17: (a) Octahedral rotation phase space in perovskites [16] **and (b) schematic of LSMO on LSAT and NGO substrates highlighting the octahedral distortions at the interface towards the film growth direction** [77]**.**

As bulk LSMO has the rhombohedral structure with tilt pattern $a^-a^-a^-$, LSMO film will undergoes structural changes depending on the substrate [16] tilt pattern as shown in Figure 2.17(b). Vailionis *et al.*[22] suggested that when LSMO epitaxially grew under tensile strain ($a = b > c$), then the BO_6 octahedra distorts to #18 $a^+b^-c^0$ tilt pattern with tetragonal structure and space group belongs to C_{mcm} (No. 63). Under compressive strain ($a = b < c$), BO_6 octahedra distorts to #9 $a^+a^-c^-$ tilt pattern with monoclinic structure and space group belongs to $P2_{1/m}$ (No.11). In the case of orthorhombic NGO (110) substrate, the in-plane lattice constants are not equal in two different crystal directions. So, the film grown on NGO undergoes unequal magnitude of rotation along two crystallographic axes with tilt system #8 $a^+b^-c^-$. A summary of the film and substrate tilt system is given in Table 2.1.

Table 2.1: Structure and lattice constants of substrates that are used in this study and their corresponding space groups. By using pseudocubic lattice parameter of LSMO, the lattice mismatch between LSMO film and substrates are calculated. '-' and '+' values in the column lattice mismatch represents compressive and tensile with respect to LSMO.

Substrate	Structure	Orthorhombic unit cell (nm)	Pseudocubic unit cell (nm)	Lattice mismatch (%)	Space group	Glazer [61] Tilt system	LSMO [22] film tilt system[iii]
LAO	Rhombohedral		0.3821	−1.36	R$\bar{3}$c	#14 $a^-a^-a^-$	
NGO (110)	Orthogonal	a = 0.543, b = 0.550, c = 0.771	a = 0.3856, b = c = 0.3864	−0.51 −0.31	Pnmb	#10 $a^+b^-b^-$	#8 $a^+b^-c^-$
LSAT	Cubic		0.3868	−0.2	Pm$\bar{3}$m	#23 $a^0a^0a^0$	#9 $a^+a^-c^-$
LSMO	Rhombohedral	0.541	0.3876	---	R$\bar{3}$c	#14 $a^-a^-a^-$	
STO	Cubic		0.3905	+0.74	Pm$\bar{3}$m	#23 $a^0a^0a^0$	#18 $a^+a^-c^0$
MgO	Cubic		0..4212	+7.9	Pm$\bar{3}$m	#23 $a^0a^0a^0$	

[iii] LSMO octahedral tilting system can be different in the first few unit cells at the interface between film/substrate.

2.3.2.3 Electrical and magnetic properties

By now, it is evident that the electron occupancy, octahedral rotations, and structure of the film are strongly influenced by epitaxial strain. Similarly, here we will discuss the electrical and magnetic properties that are dependent on strain by growing epitaxial thin films. The biaxial strain dependent Curie temperature (T_c) in LSMO thin films as proposed by Millis *et al.* [78] is dependent on bulk strain (ϵ_B) and biaxial strain (ϵ^*) as given in equation 2.4.

$$T_C(\epsilon_B, \epsilon^*) = T_C^0[1 - a\epsilon_B - b\epsilon^{*2}]$$
$$\text{Where } \epsilon_B = \frac{1}{3}(\epsilon_{xx} + \epsilon_{yy} + \epsilon_{zz}),\ \epsilon^* = \frac{1}{2}(\epsilon_{zz} - \epsilon_{xx}), \tag{2.4}$$
$$\epsilon_{xx} = (a_{xx} - a_{bulk}/a_{bulk}),\ \epsilon_{zz} = (a_{zz} - a_{bulk}/a_{bulk})$$

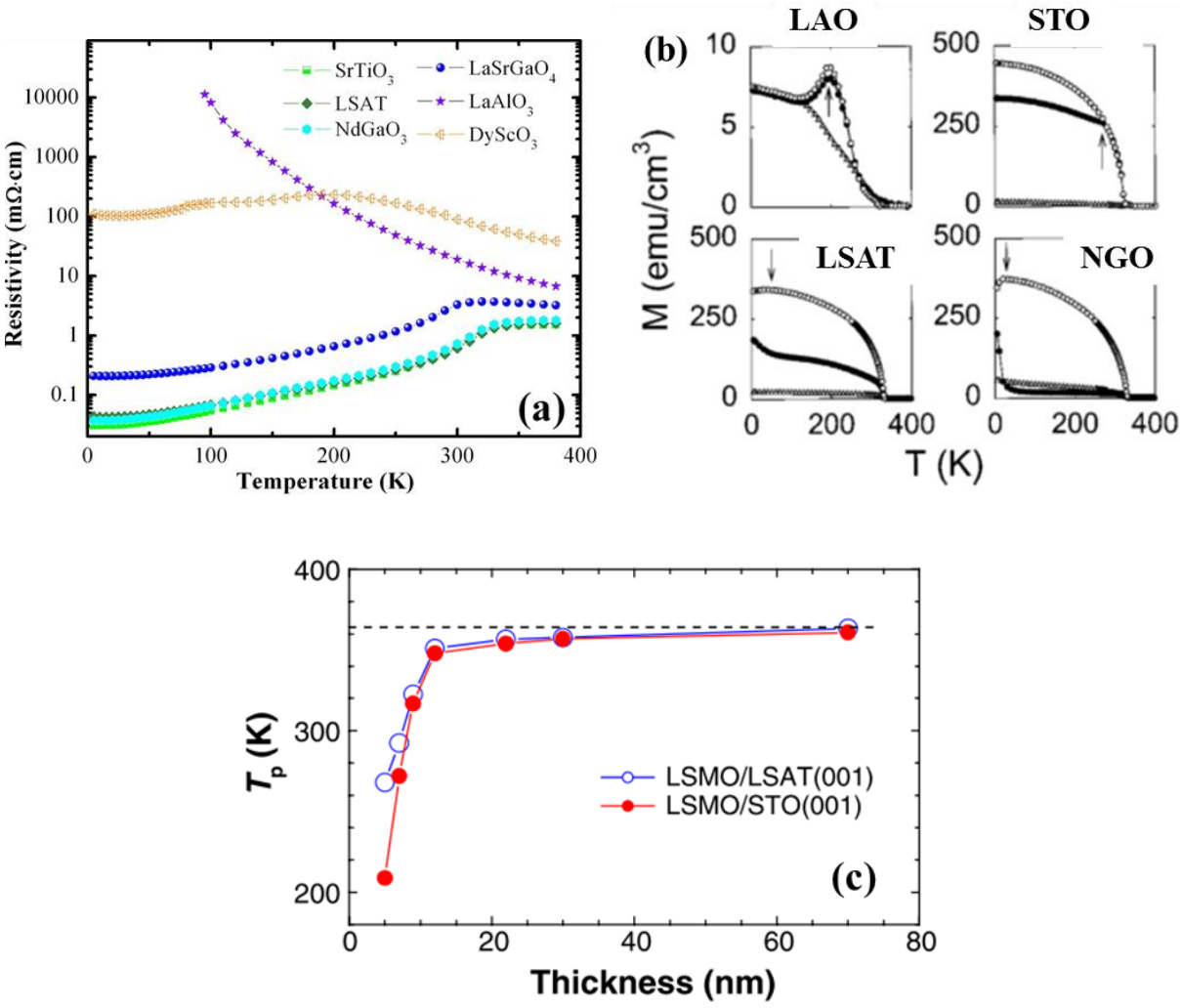

Figure 2.18: (a) Resistivity vs. temperature R(T) of LSMO thin films deposited on different substrates [44]**, (b) temperature dependent magnetization of LSMO films on LAO, STO, LSAT and NGO substrates along 3 different crystallographic directions** [79]**, (c) thickness dependence of T_p of LSMO films on LSAT (001) and STO (001) substrate** [80]**.**

Adamo *et al.* [44] and Wang *et al.* [42] have grown high-quality epitaxial thin films on various substrates and observed strain dependent T_c and T_p and concluded that as the strain increases, the T_p and T_c fall rapidly in accordance with Millis equation. As the strain due to lattice mismatch increases, the resistivity of the films increased monotonically. Temperature dependent resistivity of LSMO thin films grown on nearly matched substrates such as STO, LSAT, NGO and LSGO shows metallic behavior with very high T_p whereas, on large mismatched substrates such as LAO, DSO shows insulating behavior as shown in Figure 2.18(a). Similarly, temperature dependent magnetization T_c reduces from ~360 K on nearly matched substrates to below room temperature on large mismatched substrates such as LAO. Figure 2.18(b) shows the magnetization vs. temperature of LSMO thin films deposited on different substrates as LAO (001), STO (001), LSAT (001) and NGO (110) measured along different crystallographic axes, which shows different magnetization behavior owing to magnetic anisotropy and spin reorientation transitions as represented by arrow marks [79]. Figure 2.18 (c) shows thickness dependent T_p of LSMO films on STO (tensile strain) and LSAT (compressive strain) substrates. At low thickness, strain has a dominant effect in the T_p. As the thickness increases, the LSMO film tends to relax and the properties of the film would return to its bulk value. Therefore, strain is an easy and predominant factor to alter the physical properties of the material.

3 Magnetic anisotropy and Magneto-Optical Kerr Magnetometry

3.1 Magnetic Anisotropy

In an isotropic system, the magnetic properties of a material exhibit same responses to external stimuli in all directions (direction independent). For an anisotropic system (which is the case for most of the ferromagnets), the magnetic responses of the material are different in different crystallographic directions owing to anisotropy (direction dependent). This anisotropy arises due to several factors such as crystal structure, stoichiometry, strain, temperature, growth conditions etc. For any system in thermodynamic equilibrium, falls to its possible lowest energy state. Therefore, in a magnetic anisotropy system, all spins tend to align in a preferential direction (easy axis), which is most energetically favorable for spontaneous magnetization [81]. In general, the magnetic anisotropy (MA) in manganite thin films can be described by multiple factors such as shape anisotropy (depends mainly on grain growth), magneto-crystalline anisotropy (due to crystal structure), magnetostriction (change in shape by applying magnetic field) and magneto-elastic (stress) anisotropy (due to lattice mismatch between thin film and substrate), octahedral tilting [82], [83] etc.

3.1.1 Why does it matter…?

From the traditional magnetic compass to sophisticated novel spintronics devices, all work on the basic principle of magnetic anisotropy. Depending on the type of application, magnetic materials have to be chosen. For example, materials with low magnetic anisotropy usually have low coercivity (soft magnets) are often used to make magnetic cores for inductors and transformers to minimize the energy dissipation with the alternating fields associated with AC electrical applications. On the other hand, materials with high anisotropy energy have higher coercivity (hard magnets) and are often used make permanent magnets, magnetic recordings and memory devices.

In particular, in thin films, the magnetic anisotropy can be tailored by varying the thickness of the film, creating artificial multilayers etc. The ability to control the local orientation of spin precisely will open up the new possibilities of creating computer memory [84]. Magnetic anisotropy is very interesting for spintronics devices that do not work rather with conventional electrons to store bits; instead, it uses the spin of the electron. This can tremendously improve memory density, improve device performance and could possibly scale to extremely small dimensions.

3.1.2 Factors influencing magnetic anisotropy

3.1.2.1 Shape anisotropy

The shape anisotropy or magnetic dipolar anisotropy is mediated through the dipolar interactions. These dipole interactions are long range and its contribution purely depends on the shape of the sample [85]. Therefore, shape anisotropy becomes very important in particular, in thin films, and is largely responsible for the in-plane magnetization that is

usually observed. The magnetostatic energy (E_A) per unit volume of the film can be expressed as in equation (3.1)

$$E_A = -\frac{\mu_o}{2} M_S^2 \cos^2\theta \tag{3.1}$$

Here, the magnetization is assumed to be uniform with the magnitude equal to the saturation magnetization M_S which subtends an angle θ with the film normal, μ_o is the permeability of vacuum. Thus, the dipolar energy is minimized for an angle $\theta = 90°$ i.e. magnetization lying in the plane of the film.

3.1.2.2 Magnetocrystalline anisotropy

The magnetocrystalline anisotropy is most common in ferromagnetic materials and it arises mainly from the spin-orbit coupling [85], [86]. The exchange interaction and magnetic dipole interactions could also contribute to magnetocrystalline anisotropy in the lesser extent. The exchange interaction or exchange energy (E_{ex}) [87] in a ferromagnetic material between the spins S_i and S_j which is proportional to $S_i.S_j$ is given as in equation (3.2)

$$E_{ex} = -\sum_{i \neq j} J_{ij} S_i . S_j \tag{3.2}$$

Here, the coefficient J_{ij} is the exchange integral. If the spins are parallel as in the case of ferromagnetic materials, the coefficient J_{ij} is positive which in turn reduces the total exchange energy. Whereas in the case of antiferromagnetic materials, the spins are anti-parallel, this results in an increase of total exchange energy. The exchange interaction cannot give rise to anisotropy since it is proportional to the scalar product of spin vectors and is independent of the angle between the spins and crystal axes. On the other hand, the dipolar interaction depends on the orientation of the magnetization relative to the crystal axes. However, in symmetry systems (cubic), the dipole interactions cancel each other, whereas, for the lower symmetry systems (hexagonal), this contribution is non-negligible. Therefore, the primary cause for the magnetocrystalline anisotropy is because of spin-orbit interaction. In an atom, when the electron circulates (solid line) around the nucleus of charge +Ze, alternatively the motion of the nucleus can also be seen orbiting around the electron (dashed lines) as shown in Figure 3.1 resulting the spin-orbit Hamiltonian term H_{SO} as given in equation (3.3)

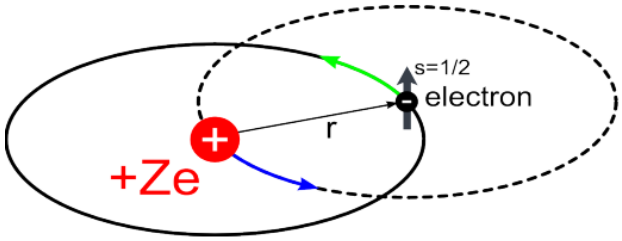

Figure 3.1: Schematic representation of electron and nucleus orbiting around each other resulting in the spin-orbit coupling.

$$H_{SO} \cong \vec{L}.\vec{S} \tag{3.3}$$

Where $\vec{L}$ and $\vec{S}$ are the orbital and spin angular momentum.

The orbital moment of the electron is influenced by the crystal symmetry. Therefore, different orientations of electron spins correspond to different orientations of atomic orbitals that are relative to the crystal structure. Consequently, some orientations of the resultant magnetic moment are more energetically favorable – "easy directions". Therefore, the exchange energy tries to align spins parallel to each other to minimize the energy and the anisotropy tries to align them along a certain crystallographic direction.

The magnetocrystalline anisotropy also has a strong influence on the temperature. In general, the magnetocrystalline anisotropy energy decreases rapidly as approaches to the Curie temperature. Therefore, in most of the cases, as the temperature decreases to below Curie temperature, the magnetic anisotropy in LSMO thin films exhibit four-fold or cubic symmetry owing to magnetocrystalline anisotropy with easy axes aligned towards the <110> crystallographic axes.

3.1.2.3 Magneto-elastic anisotropy

Magneto-elastic or strain anisotropy in the ferromagnets also arises from the spin-orbit interaction. As the material experiences strain (which is the case in heteroepitaxial thin films), the distance between the atoms changes and induces changes in spin-orbit interaction. This produces magneto-elastic energy. This is opposite of magnetostriction effect, where the material changes its shape when subjected to a magnetic field. For an elastically isotropic medium, with isotropic magnetostriction constant λ, the magneto-elastic energy per unit volume is given by [88] equation (3.4)

$$E_{me} = -\frac{3}{2}\lambda\sigma cos^2\theta \tag{3.4}$$

Where $'\sigma'$ is the stress that is related to the strain ϵ, via the elastic modulus E by $\sigma = \epsilon E$. The angle 'θ' is the angle between the magnetization and stress directions. For positive values of λ, the easy axis magnetic direction will be along a direction of tensile strain or perpendicular to the compressive strain. Strain in thin films and multilayers can be produced by the growth conditions, such as lattice mismatch between layers, the thermal strain caused by differences in thermal expansion coefficients of adjacent layers. For the elastically anisotropic medium (such as the films that are grown on orthorhombic substrate i.e., NGO (110) etc.), the easy axis magnetization usually lies along the direction with higher strain.

3.1.2.4 Surface anisotropy

Surface anisotropy, as pointed out by Neel in 1954 [89] becomes very important in the reduced symmetry at the surface of the ferromagnets. By considering the surface, the spin that has the nearest neighbor on one side does not have on another side. Therefore, the exchange interactions are different at the surface than in the bulk. Also, if a ferromagnetic material is deposited on a non-magnetic material, the interactions at the interfaces between two materials are quite different. Therefore in the case of thin films, the total

magnetocrystalline anisotropy energy has the contribution from the bulk or volume anisotropy 'K_V' per unit volume and the contribution from the surface anisotropy 'K_S' per unit area. A general expression for the total anisotropy energy in terms of the volume and the interface contributions describing the angular orientation of the magnetization of the polycrystalline films can be written as (3.5)

$$E = -K_{eff} cos^2\theta \tag{3.5}$$

$$K_{eff} = K_V + \frac{K_S}{t} \tag{3.6}$$

Here, 'θ' is the angle between magnetization 'M' and the anisotropy axis 'K', 't' is the thickness of the ferromagnetic thin film. From equation (3.6) thickness term is inversely proportional to the surface anisotropy. Therefore, surface anisotropy would be negligible in very thick films and the whole contribution would come from the volume anisotropy. The interfacial/surface anisotropy would make a significant contribution only in the case of ultrathin ferromagnetic layers.

3.1.3 Magnetic anisotropy in bulk $La_{0.7}Sr_{0.3}MnO_3$

A single crystal $La_{0.7}Sr_{0.3}MnO_3$ (LSMO) was prepared by M. Konoto *et al.* [90] using float zone method in order to define its easy axis magnetization direction. The pseudocubic perovskite structure of LSMO is shown in Figure 3.2(a). For LSMO single crystal, the magnetic anisotropy with easy axis is expected to lie along its diagonal plane i.e., (111) because of the rhombohedral distortion and it is associated to magnetocrystalline anisotropy. In the case of [111] easy axis anisotropy, the LSMO (001) sample has an out-of-plane component of magnetization in the bulk. However, magnetization at the surface inclines from [111] to [110] surface plane, as shown in Figure 3.2(b). This inclination of spins at the surface would reduce the density of surface magnetic charge while keeping the bulk magnetic domain pattern. In view of anisotropic energy, this inclination is probably preferable, since the [110] direction makes the minimum angle against the [111] direction as long as the surface magnetization lies in the surface plane.

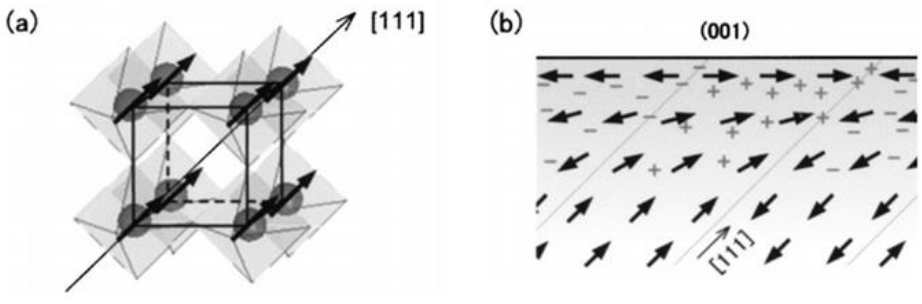

Figure 3.2: (a) $La_{0.7}Sr_{0.3}MnO_3$ pseudocubic perovskite crystal structure with corner connected MnO_6 octahedra (b) schematic diagram of magnetization rearrangements and magnetic charge (+) and (-) distribution in the (001) surface region with the easy axis in LSMO bulk along [111] crystal direction [90] [91]**.**

3.1.4 Magnetic anisotropy in LSMO thin films

The bulk properties are always different from the thin films due to a lot of constraints that are involved in the fabrication process. In the following sections, let us see how the magnetic anisotropy is modified in epitaxial LSMO thin films and the role of thickness, substrate, strain etc. in determining the magnetization reversal pathways. Here, I am focusing on selected substrates that were used later in this thesis.

3.1.4.1 LSMO on STO substrates

The rhombohedral unit cell of LSMO undergoes an in-plane biaxial tensile strain on 001-oriented STO substrate and imposes a tetragonal distortion into the film. As STO is cubic, an *in-plane* biaxial tensile strain is induced in the LSMO film (0.74%) along both (100) and (010) crystallographic axes directions as shown in Figure 3.3. As the in-plane strain is isotropic in the plane of the film, one can also predict that the magnetic anisotropy would have a bi-axial or four-fold symmetry. The origin of magnetic anisotropy can be explained in terms of magnetocrystalline and magneto-elastic anisotropy. However, as STO is cubic, the strength of the magneto-elastic anisotropy is negligible [92] and dominant effect comes from magnetocrystalline anisotropy. Lecoeur *et al.*[93] observed buckled remanent spin states along $<110>_{pc}$ and its equivalent directions in epitaxial LSMO thin films on STO substrate and shows a biaxial (four-fold) anisotropy as shown in Figure 3.4 (a).

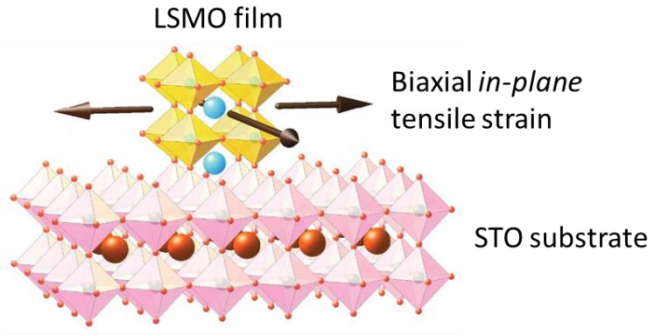

Figure 3.3: Schematic of the STO substrate onto which LSMO film grew under isotropic biaxial in-plane tensile strain. The MnO_6 octahedral present in LSMO film would elongate (compress) in-plane (out-of-plane) in order to match with the underlying substrate lattice parameters.

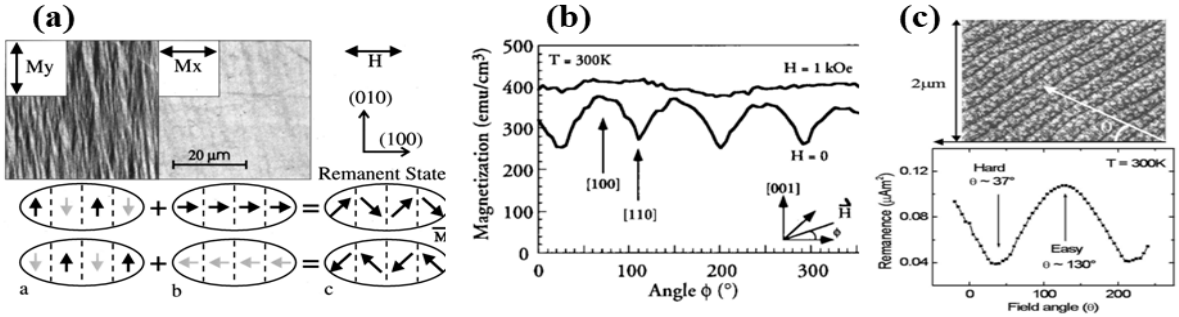

Figure 3.4: (a) Room temperature Magneto-Optical Kerr Microscopy (MOKE) images of epitaxial LSMO film grown on STO (001). The magnetic field (H) is applied in two different directions shows the different contrast in the image with the schematics shows the buckled remanent spin states [93]**. Angular dependent remanence measured on LSMO/STO films shows (b) biaxial** [94] **and (c) uniaxial** [50] **magnetic anisotropy.**

Several studies also reported that LSMO films on STO (001) show a bi-axial anisotropy [93],[95],[79],[96] at room temperature with the easy axis along $<110>_{pc}$ and its equivalent pseudocubic axes while the hard axis is present along $<100>_{pc}$ direction. In contrast, Suzuki *et al.*[94] observed biaxial anisotropy but the easy axes are aligned towards $<100>_{pc}$ as shown in Figure 3.4 (b). In all the above cases, the observed four-fold symmetry is due to the cubic magneto-crystalline anisotropy of LSMO film strained bi-axially in the plane.

However, studies [50], [51] also reported that LSMO/STO film exhibits uniaxial (two-fold) anisotropy due to step edges and miscut angle originating from STO substrate, induced into the film as shown in Figure 3.4 (c). The origin of uniaxial magnetic anisotropy is due to broken bonds and missing atoms along the step edge with easy axis present along parallel steps [97]. On the other hand, Lee *et al.* [98] reported uniaxial anisotropy for 30 nm LSMO film and the easy axis direction is not parallel to the step direction. Therefore, microstructure does not have any effect in determining magnetic anisotropy but rather it affects only coercivity. R.M. Reeve *et al.* [99] investigated magnetic anisotropy in 50 nm thick LSMO film and observed the combination of biaxial and weak uniaxial anisotropy. Here, the biaxial anisotropy is arising from magnetocrystalline and weak uniaxial from the surface steps. Although, at low temperatures, LSMO films exhibit biaxial anisotropy clearly originated from magnetocrystalline anisotropy. Therefore, there is a clear anomaly in determining the MA of LSMO on STO substrate. It was not the case for LSMO (110) films grown on STO (110) [94], [96],[51],[92],[100] because due to different in-plane lattice strain, the easy axis is always along the higher strain i.e. <001> whereas, hard axis present along $<1\bar{1}0>$ as shown in Figure 3.5 (b).

In addition to above studies, several authors artificially tuned uniaxial anisotropy of LSMO (001) films with the easy axis along the step edge direction by growing on vicinal STO (001) substrates [101],[51],[50]. Figure 3.5 (a) shows the normalized hysteresis loops of the parallel and transverse component of LSMO thin films grown on 10° vicinal STO (001) substrate. Due to artificially created steps and miscut angle, it shows profound uniaxial anisotropy along the step direction with the easy axis along [110] and the hard axis along $[1\bar{1}0]$ crystallographic axis. Table 3.1 gives the details of different magnetic anisotropies observed by different groups on different substrates respectively.

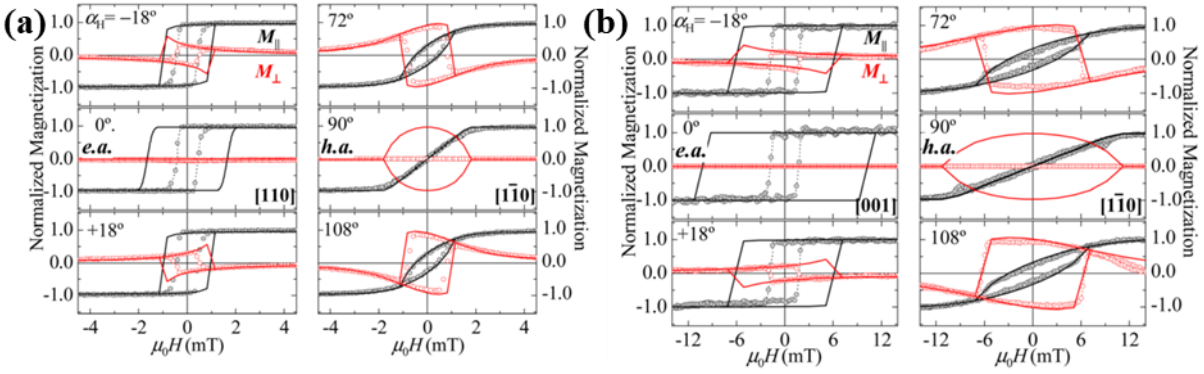

Figure 3.5: Magnetization reversal study of LSMO thin films. grown on (a) vicinal 10° STO (001) substrate, (b) STO (110) substrates [51]**.**

Table 3.1: Magnetic anisotropy studies of LSMO thin films grown on STO, STO (110), vicinal STO, LAO, NGO (110) and LSAT substrates

Substrate[iv]	Film	t (nm)	T (K)	Magnetic Anisotropy	e.a Direction	h.a Direction	Ref
STO	LSMO	50-300	300 K	Biaxial	<100>	<110>	[94]
STO	LSMO	50	300 K	Biaxial	<110>	<100>	[93]
LSMO (100) single crystal circular disk[v]				uniaxial	<001>	<010>	[96]
STO	LSMO	26	60 K	Biaxial	<110>	<100>	[102]
STO	LSMO	25	160 K	Biaxial	<110>	<100>	[50]
STO	LSMO	50-70	300 K	Weak uniaxial	[010]	[100]	[103]
STO	LSMO	25, 7	300 K	Uniaxial	∥ to step	⊥ to step	[50]
STO	LSMO	30	300 K	Uniaxial	[010], not ∥ to step	[100]	[98]
STO	LSMO	70	300 K	Weak uniaxial	[100] ∥ to step	[010]	[51]
STO	LSMO	50	300 K	Biaxial + weak Uniaxial	<110> + ∥ to step		[99]
STO (110)	LSMO (110)	50-300	300 K	Uniaxial	<001>	$<1\bar{1}0>$	[94], [96] [92][100]
10° vic STO	LSMO	16-70	300 K	Uniaxial	∥ to step	⊥ to step	[101]
LAO	LSMO	35	100 & 260 K	Biaxial	<110>	<100>	[102]
NGO	LSMO	6 uc	100 K	Uniaxial	$[1\bar{1}0]$	[001]	[82]
	6uc LSMO / 9uc STO		100 K	Uniaxial	[001]	$[1\bar{1}0]$	
NGO (110)	LSMO (001)	18, 50		Uniaxial	$[1\bar{1}0]$	[001]	[103]–[106]
LSMO nanowires on STO (001) fabricated in any direction				Uniaxial	∥ to nanowire	⊥ to nanowire	[106]
LSMO nanowires on NGO (110) fabricated in any direction				Uniaxial	$[1\bar{1}0]$	[001]	[106]
LSAT	LSMO		300 K	Biaxial	<110>	<100>	[75] [103]
LSAT	LSMO	25	5 K	Biaxial	30° from <100>		[79]
LSAT	LSMO	12 40	300 K	Bi+ Uni Uniaxial	<110> [100]	<100> [010]	[107]
LSAT	LSMO	200	300-360	OOP	[001]		[108]

[iv] Note that the substrate orientation is always (001) if not precised and otherwise the orientation is mentioned next to the substrate.

[v] LSMO (100) single crystal grown by float-zone method exhibits uniaxial due to rhombohedral magnetocrystalline anisotropy

3.1.4.2 LSMO on NGO (110) substrates

The crystal structure of NGO (110) is orthorhombic with lattice constants $a_o = 0.543\ nm, b_o = 0.550\ nm\ and\ c_o = 0.771\ nm$. Orthorhombic NGO (110) can be viewed into its pseudocubic form as given by equation (3.7)

$$a_{pc} = c_o/2, \qquad b_{pc} = c_{pc} = \sqrt{{a_o}^2 + {b_o}^2}/2 \tag{3.7}$$

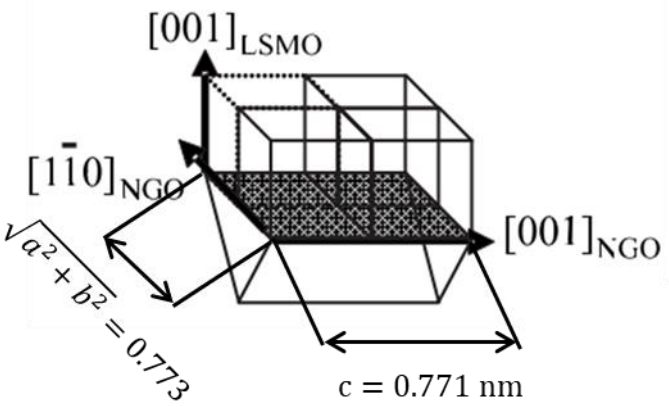

Figure 3.6: Schematic of the orthorhombic NGO (110) substrate and LSMO (001) oriented film. The crystallographic axis of both substrate and the film are also presented in the figure [105]**.**

The pseudocubic in-plane lattice parameters of NGO are 0.3856 nm and 0.3864 nm respectively. Epitaxial LSMO (001) films grown on NGO $(110)_o$ will experience a bi-axial anisotropic *in-plane* compressive strain and imposes either monoclinic [22] or distorted orthorhombic [109] crystal structure into the film; the out-of-plane tiling of oxygen octahedra [22] deviates by an angle $\gamma \neq 90°$. Due to the unequal lattice constants of NGO $(110)_o$, the strain developed in the thin film is different along two different directions. The two in-plane bonds angles (α, β) are perpendicular to each other but their bond lengths are strained differently [110]. Therefore, the magnetic easy axis always tends to align towards longest bond length or maximum strain in order to minimize the total anisotropy energy. V. V Demidov *et al.* [103], M. Mathews *et al.* [106], H. Boschker *et al.* [105], Z. Liao *et al.* [104] reported that LSMO grown on NGO (110) always shows uniaxial anisotropy in the film plane with the easy axis and hard axis lie along $[1\bar{1}0]$ and [001] i.e. towards high strain and low strain directions respectively. The magnetic anisotropy observed in LSMO films grown on STO (001) is due to magneto-crystalline anisotropy whereas, in the case of NGO $(110)_o$, the anisotropy is due to strain [105]. The magnetic anisotropy in thin films can then be expressed as $E_{ms} = \frac{3}{2}\lambda(\sigma_b - \sigma_a)sin^2\theta$; where, '$\lambda$' is magnetostrictive constant at saturation, 'σ_b' and 'σ_a' are the strain along their axis and 'θ' is the angle between magnetization and stress directions. On the other hand, Mathews *et al.* [106] reported that LSMO nanowires fabricated in any direction on NGO (110) substrate always shows uniaxial anisotropy with easy axis present along $[1\bar{1}0]$ and it is rather due to stress anisotropy dominating the shape anisotropy imposed from the nanowires. Therefore, it was demonstrated that LSMO films always shows a very strong uniaxial anisotropy with easy and hard axis directions aligned along $<1\bar{1}0>$ and

<001> crystal directions on NGO (110) substrate [79],[105],[111],[106].

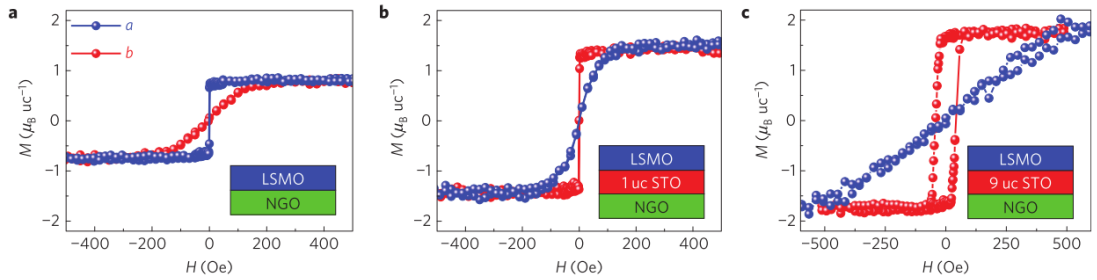

Figure 3.7: M (H) loops of LSMO thin film measured along different axes grown on a) NGO (110), (b) 1 uc STO buffered NGO (110) and (c) 9 uc STO buffered NGO (110) [82].

However, recent work from Z. Liao *et al.* [82] show that the magnetic anisotropy of ultrathin LSMO film on NGO (110) measured at 100 K changes its direction as increase in thickness from 7 uc to 9 uc i.e., from the short axis to long axis and relates it to octahedral rotations imposed into the film at the interface. In addition, by controlling oxygen octahedral network, they have artificially tuned in-plane magnetic anisotropy by 90° just by inserting 1 uc of STO (Figure 3.7). It opens up new challenges that these octahedral rotations at the interface are strong enough and can control the direction of magnetic anisotropy.

3.1.4.3 LSMO on LSAT (001) substrates

LSAT has a cubic structure that is similar to STO substrate except that the strain imposed on the LSMO film is opposite i.e. compressive (-0.2%). Therefore, LSMO film when grown on LSAT, the rhombohedral uc of LSMO experiences compressive strain and undergoes structural changes from rhombohedral to either tetragonal or monoclinic [22] structure as shown in Figure 3.8. Similar to LSMO films grown onto STO, one would also expect biaxial or four-fold magnetic anisotropy on LSAT substrate. G. A. Ovsyannikov *et al.* [75] V. V. Demidov *et al.* [103] reported that the films exhibit pure biaxial anisotropy with the easy axis along <110> axis as shown in Figure 3.9(c). Along with pure biaxial anisotropy, few authors [79], [107] reported that an additional uniaxial anisotropy component is present along [100] axis as shown in Figure 3.9 (a, b). This additional uniaxial anisotropy is attributed to orthorhombicity of LSMO crystal.

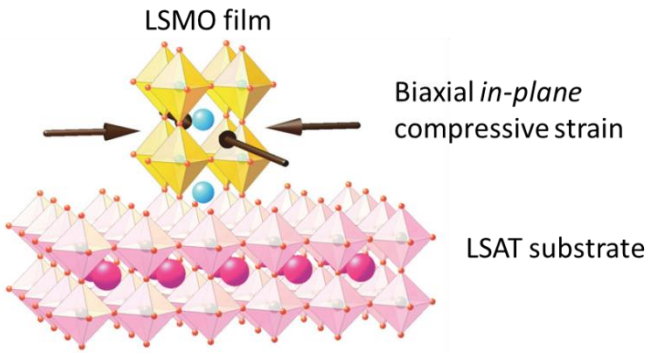

Figure 3.8: Schematic of the LSAT substrate onto which LSMO film grew under isotropic biaxial in-plane compressive strain. The MnO_6 octahedral present in LSMO film would compress (elongate) in-plane (out-of-plane) in order to match with the underlying substrate lattice parameters.

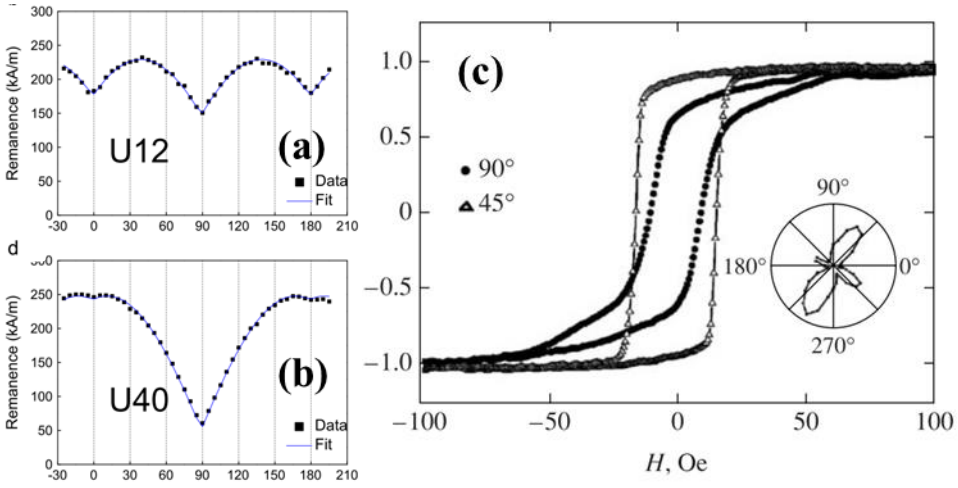

Figure 3.9: Angular dependent remanence 2D plots of (a) 12, (b) 40 nm thick LSMO films on LSAT substrate shows biaxial ad uniaxial anisotropy [107]**. (c) M (H) loops of LSMO film at different angles and the inset shows the angular dependent polar plot shows clear biaxial anisotropy** [75]**.**

Tsui *et al.* [79] observed temperature-dependent anisotropy and observed that the easy axis deviates away from 20° to 30° of [100] axis and related it to spin reorientation transition. This is due to the superposition of biaxial and uniaxial anisotropy and depending on their relative strength, the easy axis direction changes. Boschker *et al.* [107] observed that as the thickness increases from 12 nm to 40 nm, the biaxial anisotropy changed to uniaxial anisotropy owing to the orthorhombic crystal structure. As the films are under compressive strain, there is also a possibility that spins can align towards out-of-plane (OOP). L. Méchin *et al.* [108] observed maze-like structure on 200 nm thick LSMO film by MFM microscopy that shows an existence of OOP component.

3.1.5 Summary

Here, I will briefly recall about the magnetic anisotropies of LSMO on different substrates. For instance, films that are grown on STO substrates are under tensile strain and showed different behaviors such as uniaxial, biaxial, mixed and isotropic behaviors owing from substrate miscut, magnetocrystalline, strain and thickness. As a result, different authors showed different anisotropic behaviors and so there is no well-defined magnetic anisotropy observed on STO substrate. Coming to orthorhombic NGO (110) substrates, the LSMO films under compressive strain always shows uniaxial anisotropy and is due to magneto-elastic nature. On cubic LSAT (001) substrate, LSMO films under compressive strain again show different anomalies in magnetic anisotropy i.e., biaxial, uniaxial, mixed anisotropy and also OOP.

In order to use LSMO in spintronic devices and memory applications, the control of magnetization direction i.e., of the magnetic anisotropy, is very crucial. Further research is needed to examine more closely the links between magnetic anisotropy and its control as a function of strain, thickness, and temperature. Therefore, in this thesis, we focused to do a systematic study of magnetic anisotropy of LSMO on different substrates as STO (001), STO buffered MgO (001), NGO (110), LSAT (001) and to understand their origins and to control

them as a function of thickness. We deposited LSMO thin films by PLD and MBE techniques. The magnetic anisotropy measurements were performed by MOKE magnetometry technique which will be discussed in the next section.

3.2 Magneto-Optical Kerr Magnetometry

Magnetic anisotropy as described in the previous section can be realized by various techniques that are grouped into the static and dynamic response of the magnetic system. The techniques used in the static measurements are namely magneto-optical Kerr effect (MOKE), torque Magnetometry, SQUID etc. Whereas, the techniques used in the dynamic measurements include ferromagnetic resonance (FMR) and Brillouin light scattering (BLS) [85].

However, in this thesis, we measured magnetic anisotropy of our LSMO thin films by using MOKE technique. We have got access to two different MOKE set-ups i.e., vectorial MOKE @ IMDEA Nanociencia, Madrid, Spain and a simple MOKE @ CNR-IOM, Trieste, Italy. Therefore, in the following sections, we will focus only on MOKE technique, different configurations, measurement analysis etc.

3.2.1 MOKE Theory

As the name suggests, magneto-optical effects are the interactions between light and magnetic fields. It was discovered by Rev. John Kerr, while he was examining the change in polarized light reflected from a polished electromagnetic pole. In 1877 [112] he stated in his first article "*on rotation of the plane of polarization by reflection from the pole of magnet*", which is known as polar Kerr effect. Later, in the next year (1878) [113], he comes up with the second article by stating "*the reflection of polarized light from the equatorial surface of the magnet*", which is known as longitudinal Kerr effect. In both of the experiments, the principle of operation is same.

Kerr Effect: When a beam of linearly polarized light is reflected from a magnetized surface changes its plane of polarization (Kerr effect) and its detection reveals the different orientations of the magnetization on the surface of various domains [114]–[116].

Faraday Effect: When a beam of linearly polarized light is passed through a thin magnetized sample, the rotation of its polarization gives the information of the direction of magnetization inside these domains.

MOKE is non-destructive i.e., purely photon based technique (photon-in / photon-out). It is a surface sensitive technique since the light penetration depth varies from few tens [117] to hundreds of nm and it also depends on the material. The technique allows studying magnetic properties such as magnetic ordering, magnetic anisotropy, exchange coupling, among others in systems as thin films [118]–[122], bilayer exchange-bias systems, multilayers such as tunnel junctions or spin valves [123] etc. Although MOKE is known for more than 100 years, the magneto-optical Kerr effects were fully exploited for the first time in surface magnetism studies (SMOKE) on ultrathin Fe films grown on Au (100) substrate [124] in 1985. Because

of its simplicity, MOKE is one of the most widely used techniques to study magnetic thin films [121], [122], [125], [126].

3.2.2 MOKE configurations

There are three configurations of MOKE experiments namely Longitudinal, Transverse and Polar configurations are shown in Figure 3.10. These arise from the direction of the magnetic field with respect to the plane of incidence and the sample surface.

Longitudinal mode: The magnetization vector ($\vec{B}$) is parallel to both the reflection surface (P_r) and the plane of incidence (P_i) of polarized light.

$$\vec{B}||P_i \; and \; \vec{B}||P_r \tag{3.8}$$

Transverse mode: The magnetization vector ($\vec{B}$) is parallel to the reflection surface (P_r) but perpendicular to the plane of incidence (P_i) of polarized light.

$$\vec{B}||P_r \; and \; \vec{B}\perp P_i \tag{3.9}$$

Polar mode: The magnetization vector ($\vec{B}$) is perpendicular to the sample or reflection surface (Pr) and parallel to the plane of incidence (P_i) of polarized light.

$$\vec{B}||P_i \; and \; \vec{B}\perp P_r \tag{3.10}$$

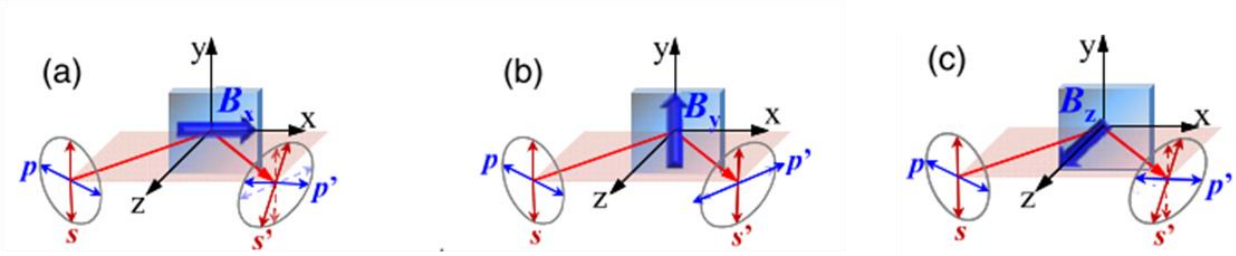

Figure 3.10: Schematic of the three basic MOKE configurations: (a) longitudinal, (b) transverse and (c) polar. The blue arrows illustrate the orientation of the magnetization. The red arrows show the direction of the propagation of the light [127]**.**

Usually, the different MOKE geometries exploit different magneto-optics effects and provide different magnetization components. Within a first-order approximation, Longitudinal and Polar geometries provide information on the magnetization components within the reflection plane (yz) (i.e., M_y and M_z respectively) by measuring their corresponding polarization rotations. In turn, M_x can be determined in transversal geometry by measuring the reflectivity changes. Therefore, vectorial information on the magnetization can be obtained by performing three measurements in the three different MOKE geometries. In practice, however, there are difficulties to overcome, such as second order terms and angular accuracy when both sample and field angles must be rotated simultaneously to get the different geometries.

In order to overcome the above difficulties, a vectorial-Kerr Magnetometry setup in which the two in-plane components of the magnetization vector are acquired simultaneously during the reversal process has been used in this thesis.

3.2.3 Vectorial MOKE set-up @IMDEA Nanociencia, Madrid

The vectorial-MOKE setup[vi] that I used for magnetic anisotropy measurements is installed at IMDEA Nanociencia, Madrid. The experimental set-up can be divided into three stages such as the optical path, the mechanical sample stage, and the control unit as shown in Figure 3.11.

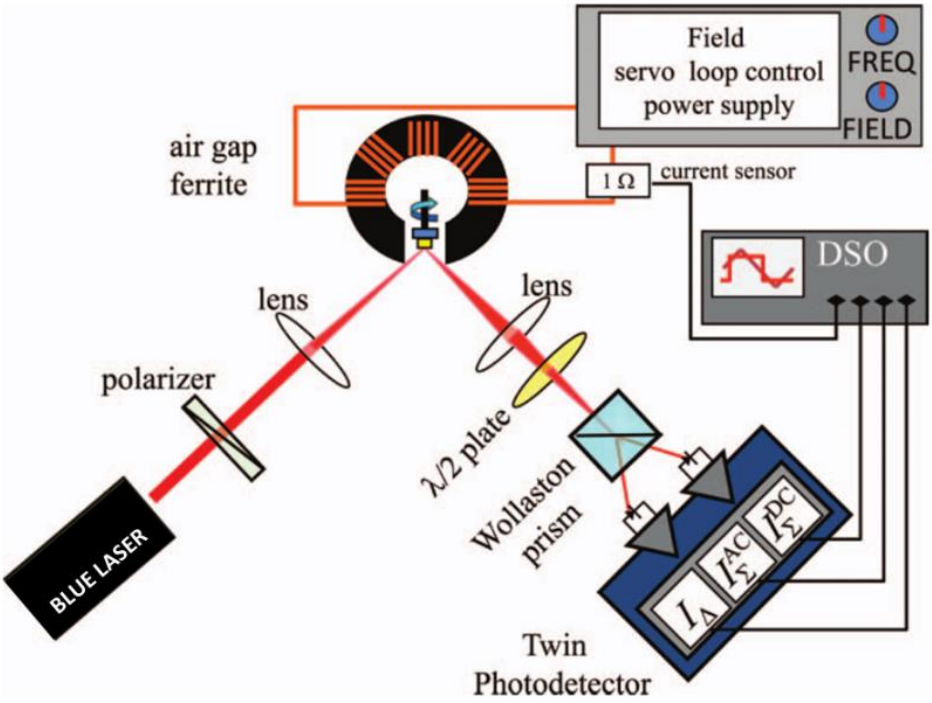

Figure 3.11: Schematic of the v-MOKE setup @ IMDEA-nanoscience, Madrid. The sample is placed in the air gap of an electromagnet. The incident laser light is polarized and focused onto the sample by a focused lens. The light reflected from the sample is passed through the second lens and then to λ/2-retarder to intermix s- and p- waves. The two components are then split by Wollaston prism and their intensities are collected by the photodiode [127], [128]**.**

The first stage i.e., optical path consists of the following:

i. Laser (Red or Blue)
ii. Polarizer
iii. Focusing lens
iv. Sample stage
v. Lens
vi. λ/2 Retarder
vii. Wollaston Prism
viii. Photodiodes

[vi] Room temperature MOKE measurements were done at IMDEA Nanociencia, Madrid

The HeNe red laser of wavelength λ = 632 nm or blue laser (depending on the type of material that you are going to measure) which is randomly polarized is used as a light source. A Glen-Thompson polarizer with extinction coefficient $1x10^{-5}$ is introduced into the optical path so as to select the one particular polarization. In the typical configuration, it is set to p-polarization, although it also allows us to perform measurements with incident s-polarization. Focusing lenses are used before and after the light reflection from the sample surface to focus the divergent beam onto the sample surface and onto photodiodes, respectively. The λ/2 retarder, set to 22.5º of its optical axis, rotates the polarization of the reflected beam and it is set to be close to 45º polarization, i.e., outgoing with similar s- and p-light projections. Finally, the s- and p-waves are split into two separate beams using a Wollaston prism with extinction coefficient $1x10^{-5}$. The intensities of the two waves are measured by two fast photodiodes. These are incorporated into a proper amplification electronics developed at Universidad Autónoma service, SEGAINVEX and ending up with three outputs channels such as sum AC (I_{Σ}^{AC}), sum DC (I_{Σ}^{DC}), and difference DC (I_{Δ}) retrieved from two orthogonal components reflected from the sample surface.

The second stage is the sample stage. In order to quantitatively acquire the angular dependent magnetic measurements, the alignment of the sample reflection plane should be fixed, so that the reflection of the light lies always in the same plane. This is possible only by placing the sample on eucentric goniometer along with the xyz-sample stage for positioning of the sample. The goniometer gives us an additional degree of freedom to eliminate any tilts after placing the sample and xyz stage will allow us to keep the sample in the center of electromagnets so that the applied magnetic field is homogeneous in the whole sample. The sample head can be rotated about 360° with the step size close to 0.9°. In addition, it is very convenient to change from longitudinal to transverse mode just by rotating the electromagnet 90°.

The final stage is the control unit and it includes a computer, an arbitrary function generator, current source, and a digital oscilloscope. The set-up is pc-controlled via home-made software that drives the stepper motor and the applied magnetic field, as well as reads out the signals from the oscilloscope. Commercial arbitrary function generators connected to a bipolar power supply, developed at SEGAINVEX, are used to generate the sinusoidal shape magnetic field. All the measurements presented here were performed at 3.21 Hz (quasi-static conditions). A 4-channel fast digitizing oscilloscope (200 MHz BW, 1GS/s), triggered to the applied field frequency, reads:

i. Sum DC (I_{Σ}^{DC}): The sum of the intensities of the two orthogonal polarization components of the reflected beam (i.e. ∝ total reflectivity)
ii. Diff DC (I_{Δ}): The difference of the intensities (i.e. ∝ polarization changes)
iii. Sum AC (I_{Σ}^{AC}): The sum of intensities of the AC component (i.e. ∝ reflectivity changes)
iv. The voltage applied to the electromagnet, which, after calibration, can be directly transformed into applied field.

Where I_{Δ} and I_{Σ}^{AC} are usually 10^{-4} times I_{Σ}^{DC}. The total reflectivity, i.e., I_{Σ}^{DC} is used to normalize the data. Statistical noise is greatly reduced by averaging the measurements

acquired at same conditions. The difference of the intensities I_Δ is proportional to polarization rotations (i.e. longitudinal or polar component), while the sum of the intensities of the alternating component I_Σ^{AC} is proportional to reflectivity changes (i.e., transversal component). Both Kerr effects are measured at the same time, providing the simultaneous determination of the two in-plane magnetization components. Therefore, in a single automated measurement, it is possible to acquire the hysteresis data of both transverse and longitudinal components of the sample for the whole in-plane angular range.

S- Vs. P- polarized light:

The capability of the v-MOKE setup to acquire simultaneously the two in-plane magnetization components requires only incoming p-polarized light, independently from the Kerr geometry used. For the detailed mathematical analysis, please refer to the thesis by Jiménez, E *et al.* [127][81]. Here, I just provided the final intensities that are read by the two photodiodes for incoming *p*- and *s*- polarized light.

For the incoming pure *p*- polarized light, the electric field vector after passing the λ/2 retarder is given in equation (3.11)

$$\begin{pmatrix} E_s'' \\ E_p'' \end{pmatrix} = E_p \begin{pmatrix} b_1 m_y + c + d m_x \\ b_1 m_y - c - d m_x \end{pmatrix} \tag{3.11}$$

and the intensities read by two photodiodes after dividing with the total reflectivity term $'I_\Sigma^{DC}{}'$ are [127]

$$\frac{I_\Delta}{I_\Sigma^{DC}} = 2Re\left[\frac{r_{sp}}{r_{pp}^{DC}}\right] \approx 2\theta_K^p \propto m_x, \tag{3.12}$$

$$\frac{I_\Sigma^{AC}}{I_\Sigma^{DC}} = 2Re\left[\frac{r_{pp}^{AC}}{r_{pp}^{DC}}\right] \propto m_y \tag{3.13}$$

which are the Kerr rotations and reflectivity changes that are proportional to the two in-plane components of the magnetization m_x and m_y.

Similarly, for the incoming *s*- polarized light, the electric field vector after passing the λ/2 retarder is given in eq (3.14)

$$\begin{pmatrix} E_s'' \\ E_p'' \end{pmatrix} = E_s \begin{pmatrix} a + b_1 m_y \\ a - b_1 m_y \end{pmatrix} \tag{3.14}$$

the intensities read by two photodiodes after dividing with the total reflectivity term $'I_\Sigma^{DC}{}'$ are [127]

$$\frac{I_\Delta}{I_\Sigma^{DC}} = 2Re\left[\frac{r_{ps}}{r_{pp}^{DC}}\right] \approx 2\theta_K^s \propto m_x, \tag{3.15}$$

$$\frac{I_\Sigma}{I_o} = \frac{I_\Sigma^{DC}}{I_o} = R_{ss} \tag{3.16}$$

Which is Kerr rotation and a constant term and in this case, the sum does not contain any useful information such as I_Σ^{AC}. Hence, *P*- polarized light is essential to detect two orthogonal components simultaneously. Now, we can define the in-plane magnetization components parallel $M_{||}$ and perpendicular $M_{\perp}$. Let us now recall the 3 basic Kerr modes as shown in Figure 3.10.

For Longitudinal mode, where the magnetic field is applied in x-direction, the parallel $M_{||}$ and perpendicular $M_{\perp}$ components are defined as

$$M_{||} = m_x \propto 2\theta_K^p \approx \frac{I_\Delta}{I_\Sigma^{DC}} \tag{3.17}$$

$$M_{\perp} = m_y \propto \frac{I_\Sigma^{AC}}{I_\Sigma^{DC}} \tag{3.18}$$

Similarly, for the Transversal mode, where the magnetic field is applied in y-direction, the parallel $M_{||}$ and perpendicular $M_{\perp}$ components are defined as

$$M_{||} = m_y \propto \frac{I_\Sigma^{AC}}{I_\Sigma^{DC}} \tag{3.19}$$

$$M_{\perp} = m_x \propto 2\theta_K^p \approx \frac{I_\Delta}{I_\Sigma^{DC}} \tag{3.20}$$

Therefore, by using pure *p*-polarized light and with either longitudinal or transversal geometry, we can deduce two orthogonal in-plane components. Low-temperature v-MOKE[vii] (LT-MOKE) [128] set up is also used in this thesis to study temperature dependent magnetic properties.

3.2.4 MOKE set-up @CNR-IOM, Trieste, Italy

Here, I will briefly explain about another MOKE set-up that we have got access to measure the magnetic anisotropy of our films. In this set-up, the MOKE is operated in the longitudinal mode. The principle of operation is quite simple.

Incident plane: The blue diode laser is passed through the chopper, p-polarizer and then through the focused lens onto the sample. The chopper is rotated at the frequency other than the natural light frequency in order to avoid the noise from external sources.

Sample stage: The samples are mounted onto the rotatable cryostat head, which is in ultra-high vacuum (UHV) environment. So, we can cool down the samples with liquid Helium from 300 K to down to 40 K and also rotate the sample for measuring magnetic anisotropy. We can even change the samples at low temperature and it will just take 10-15 minutes to fully thermalize the sample before commencing the measurement. Also, this MOKE system

[vii] LT-MOKE measurements were done at Universidad Autónoma de Madrid (UAM), Madrid, Spain.

is connected *in-situ* with MBE, which allows us to measure magnetic properties of the film directly after the film growth.

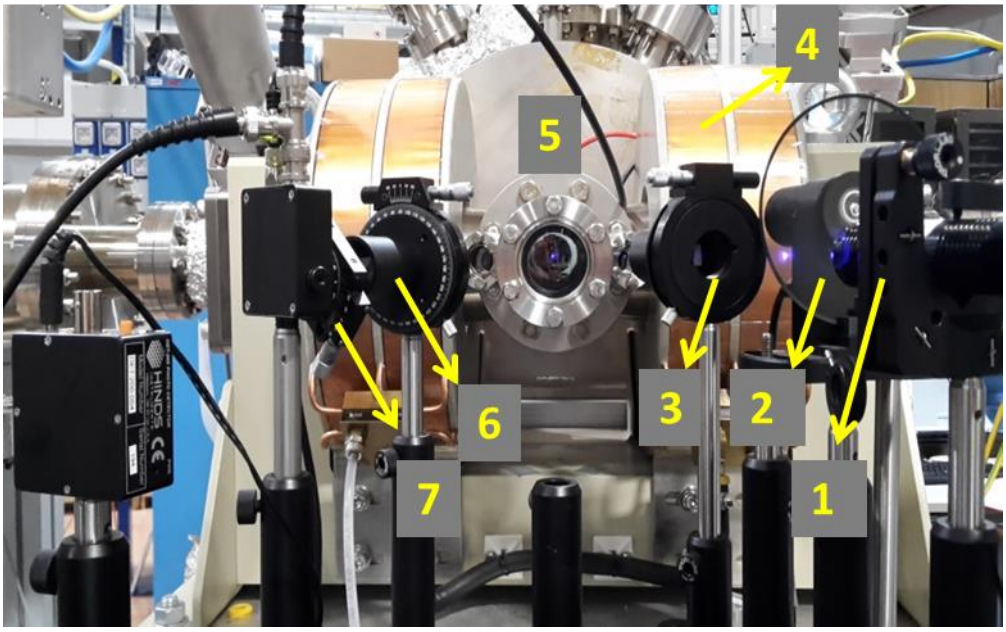

Figure 3.12: Photograph of longitudinal MOKE set-up connected *in-situ* with MBE @ CNR-IOM, Trieste, Italy. The numbers (1, 2, 3) corresponds to the incident plane are a diode laser, chopper and polarizer (4, 5) correspond to magnetic coil and sample stage, (6, 7) corresponds to the reflection plane are analyzer and the photodetector.

Reflection plane: The polarized light reflected from the sample is passed through the analyzer and then onto photodiode to measure the light intensity (Kerr rotation signal). Here, the angle between polarizer and analyzer are kept almost orthogonal to each other in order to pass the minimum reflected signal from the sample onto photodetector in which the valuable information is preserved i.e., Kerr rotation.

3.2.5 Stoner-Wohlfarth Model

The Stoner–Wohlfarth model is a widely used model for the magnetization of single-domain ferromagnets. Stoner Wohlfarth model is based on the coherent rotation of spins. In general, the magnetization at easy axis is followed by nucleation and propagation of domain walls and at hard axis is followed by a rotation. Therefore, this model which is purely based on rotation model will work perfectly at the hard axis and often estimates higher coercive fields at the easy axis. The total anisotropy energy E_{tot} is given [120] as

$$E_{tot} = K_u \sin(\theta - \theta_H)^2 + 0.25\, K_b \cos 2(\theta - \theta_H + \beta - 45^{\circ})^2 - \mu_o M_s h \cos(\theta) \qquad (3.21)$$

Where K_u and K_b are the uniaxial and biaxial terms, θ is the angle between applied magnetic field direction and [100] crystal axis, θ_H is the angle between magnetization and [100] crystal axis, 'β' is the angle between uniaxial and biaxial anisotropy, 'M_S' is the saturation magnetization, and 'μ_o' is the vacuum permeability. The first two terms are the magnetic anisotropy and the last term is the energy of coupling with the applied field (often called the Zeeman energy).

I'm not going into the details of the model. But, I just want to provide you the general view or rather consider as templates for the ideal uniaxial ($K_b = 0$) and biaxial ($K_u = 0$) anisotropy systems as shown in Figure 3.13 and Figure 3.14 that are calculated by using the equation 3.21. The uniaxial anisotropy system behaviors depicted in the Figure 3.13 shows the repeated features for every 180°. Similarly, for the ideal biaxial anisotropy system as shown in Figure 3.14 displays the repeating features for every 90°. Some special cases also needed to be considered in which the anisotropy constants $K_u \neq K_b \neq 0$.

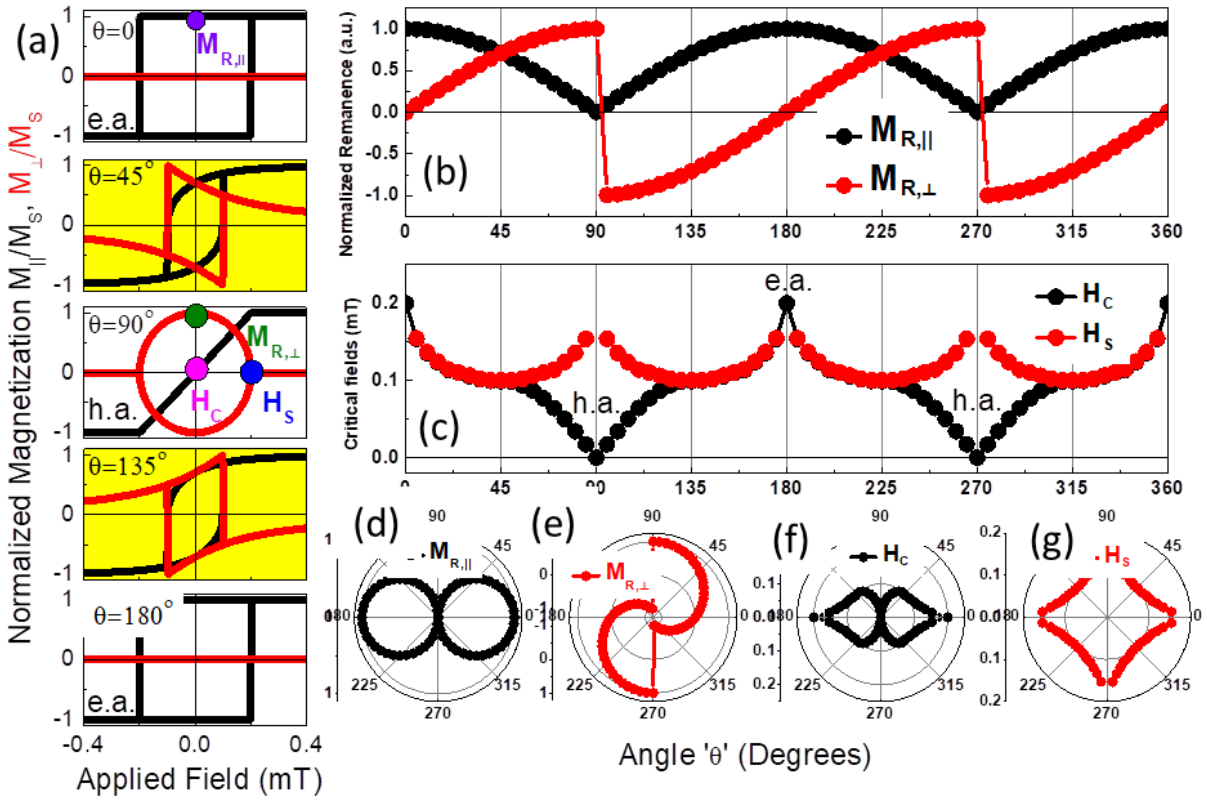

Figure 3.13: Modified Stoner-Wohlfarth model for a pure uniaxial anisotropy system. (a) M (H) loops calculated at different applied field angles (b) The locus of the remanence parallel ($M_{R,||}$) and transverse ($M_{R,\perp}$) component (c) The locus of the critical fields such as coercive field (H_C) and switching field (H_S) as the function of applied field angle (d-g) their corresponding polar plots.

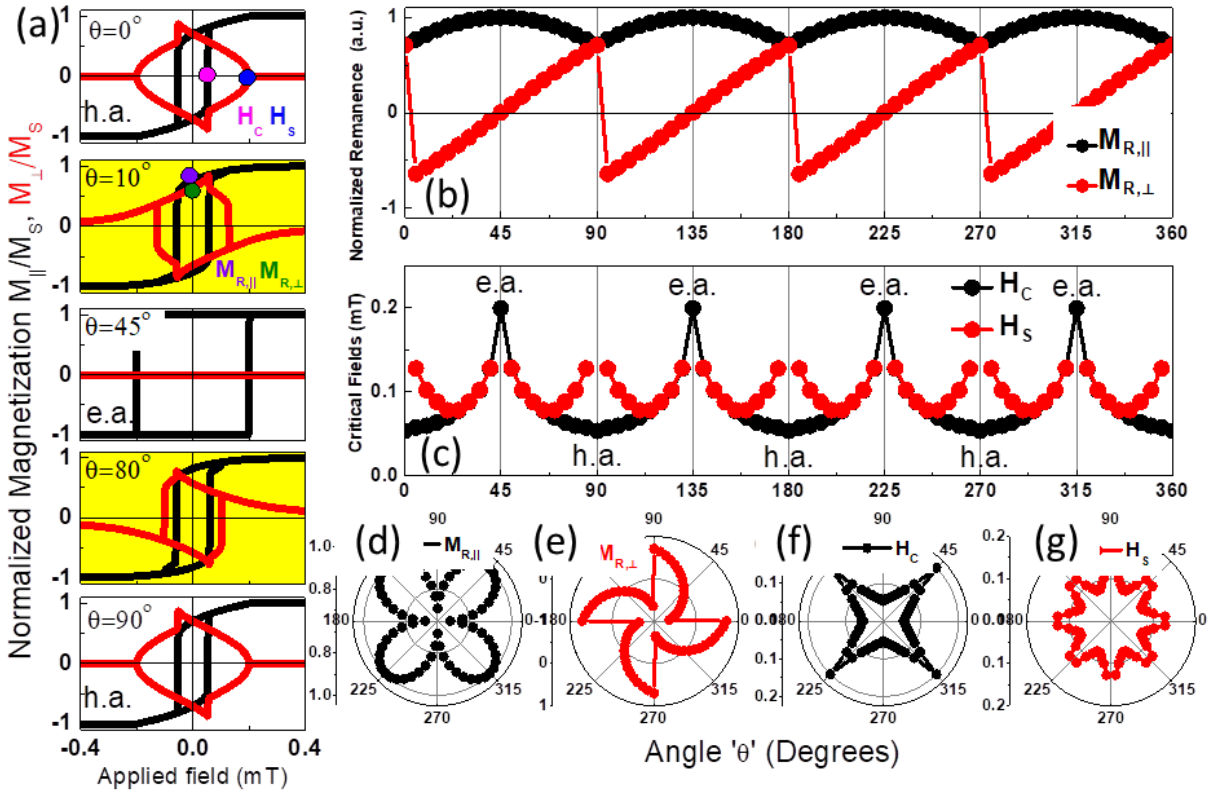

Figure 3.14: Modified Stoner-Wohlfarth model for a pure biaxial anisotropy system. (a) M (H) loops calculated at different applied field angles (b) The locus of the remanence parallel ($M_{R,||}$) and transverse ($M_{R,\perp}$) component (c) The locus of the critical fields such as coercive field (H_C) and switching field (H_S) as the function of applied field angle (d-g) their corresponding polar plots.

3.2.6 Summary

To conclude, we have used two different MOKE set-ups for characterizing our thin films. One set-up is vectorial MOKE magnetometry @ IMDEA, Madrid that has the possibility to acquire two in-plane magnetization components simultaneously by using p-polarized light and has advantages over conventional MOKE technique. Whereas the second MOKE set-up is @ CNR-IOM, Trieste is connected *in-situ* with MBE; therefore, we have the flexibility to measure magnetic anisotropy in the films immediately after the film growth. With this set-up, we can only acquire parallel component and it is very convenient to do measurements at low temperatures.

4 Strain-induced by lattice mismatch in LSMO thin films

4.1 Introduction

In the last two decades, there is a tremendous advancement in the fabrication of very high-quality epitaxial oxide thin films by using different techniques such as Molecular Beam Epitaxy (MBE) [37], [38], Pulsed Laser Deposition (PLD) [31], [34], RF sputtering etc. Thanks to these techniques, it is now possible to grow stoichiometric complex oxide thin films with precise composition, epitaxial growth and termination control. These high-end techniques give us an additional degree of freedom to play with the thickness until few unit cells, to grow artificial heterostructures with different termination control etc.

In the previous chapter, we discussed different possibilities to tune the exotic properties of functional oxides that are otherwise not possible in conventional semiconductors. One of the primary routes is to tune strain in epitaxial thin films by coherently growing onto different lattice mismatched substrates. When pseudocubic perovskite films are epitaxially grown onto pseudocubic perovskite substrates, the in-plane lattice parameters of the film will get constrained with the underlying substrate. Strain due to epitaxy [55], [56] developed in the film have a profound impact in $B-O-B$ bond angle, $B-O$ bond length and ultimately influencing changes in the BO_6 octahedral network. By choosing the appropriate lattice-mismatched substrates, one can engineer the properties by altering the strain in epitaxial films varying between large compressive strains to large tensile strain. LSMO films epitaxially grown onto near lattice matched substrates are usually subjected not only to the lattice-mismatch-induced biaxial strain but also a further type of distortion due to the angle mismatch, namely, shear strain, which can be relaxed by forming structural domains [129]. Secondly, strain in epitaxial thin films can also be tuned by varying thickness of the film while growing on the same substrate. As a result, epitaxial strain due to various substrates and thicknesses can affect structural, morphological, electrical and magnetic properties of thin films, which are explained in the following sections.

4.2 Experimental details

Epitaxial LSMO thin films were grown by PLD technique at GREYC, Caen on different single crystal substrates such as $(001)_{pc}$ –oriented $LaAlO_3$ (LAO), $(110)_o$ -oriented $NdGaO_3$ (NGO), $(001)_{pc}$ -oriented $(LaAlO_3)_{0.3}$-$(Sr_2AlTaO_6)_{0.7}$ (LSAT), $(001)_c$ –oriented $SrTiO_3$ (STO), STO buffered MgO (001), and $(001)_c$ –oriented MgO (001). The subscripts ‘pc’, ‘o’, and ‘c’ represents pseudocubic, orthorhombic and cubic, respectively. All the substrates were bought from CrysTec GmbH.

Before deposition, the substrates were heated to 720°C with a temperature ramp of 15°C per minute in a vacuum. Once the desired temperature achieved, oxygen was introduced into the

chamber until the desired pressure was reached for deposition i.e., 0.35 mbar. During deposition, KrF (Krypton Fluoride) excimer laser of wavelength 248 nm, the energy of 220 mJ with a repetition rate of 3 Hz was used. The substrate to target distance was kept constant to 5 cm. After deposition, substrates were cooled down to room temperature at cooling rate of 10°C per minute in $7x10^2$ mbar oxygen environment. All the films on different substrates were grown at same deposition conditions as shown in Table 4.1. In addition to substrates, LSMO thin films of '3' different thicknesses (50, 25 and 12 nm) are coherently grown on all the substrates. It helps us to study epitaxial strain and thickness dependent properties of films. Our LSMO thin films experience *in-plane* biaxial strain ranging from -1.36% to +8.04 %. The films that were grown onto LAO (-1.36%), NGO (-0.31%) and LSAT (-0.12%) are compressively strained, whereas, the films that were grown onto STO (0.82%), STO buffered MgO (1-8%) and MgO (+8%) are tensile strained as shown in Figure 4.1.

Table 4.1: LSMO thin film deposition conditions by pulsed laser deposition technique

Target	Laser Energy (mJ)	Repetition rate (Hz)	Substrate to target distance (cm)	Substrate temperature (°C)	O_2 Partial pressure (mbar)
$La_{0.67}Sr_{0.33}MnO_3$	220	03	5	720	0.35
$SrTiO_3$	220	03	5	720	0.35

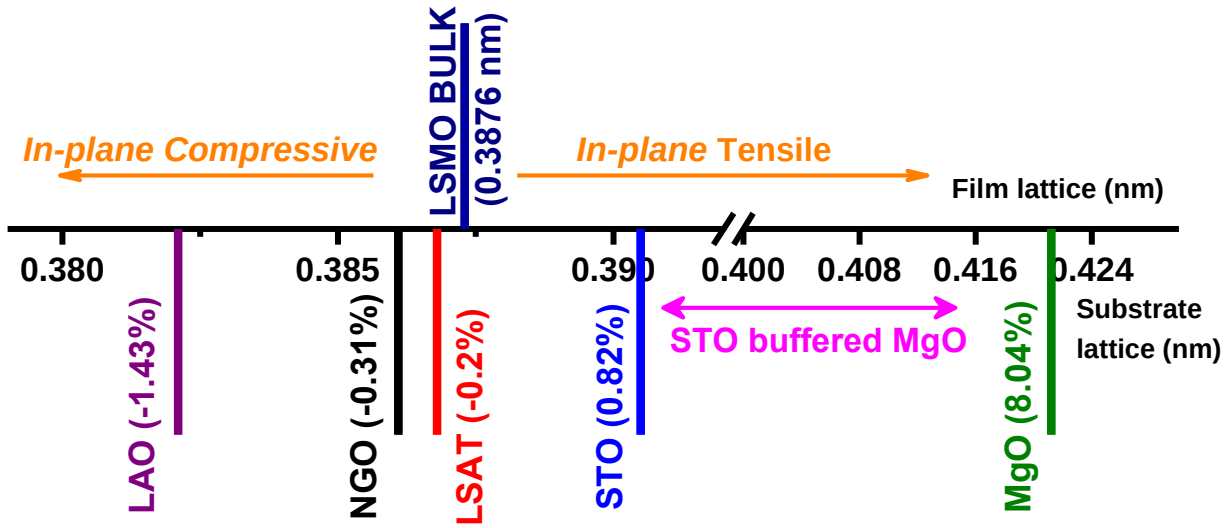

Figure 4.1: Lattice mismatch between LSMO and the substrates that are used in this study; -1.36% for LAO, -0.31% for NGO, -0.12% for LSAT, +0.82% for STO, +8.04% for MgO. '-' indicates compressive strain whereas '+' indicates tensile strain.

The crystal structure and orientation of as-prepared thin films were characterized by PANalytical X'Pert PRO X-Ray Diffraction (XRD) technique at LCS, Caen. θ - 2θ XRD scans were performed on all the films in order to calculate the average strain developed in the film and out-of-plane lattice constant 'c'. Omega scans or rocking curve was also performed on (002) peak of LSMO film to study the orientation of thin film with respect to the substrate. Atomic

Force Microscopy (AFM) was used to study the topography or surface morphology of the as-deposited films. AFM operated in tapping mode using Nanoscope Veeco III at GREYC, Caen. Temperature-dependent electrical transport properties were characterized for all the films by a standard four-probe technique in the temperature range between $77 - 420$ K at GREYC, Caen. Magnetotransport properties were measured by superconducting quantum interference device (SQUID) magnetometer at CRISMAT, Caen in the temperature range of $4 - 400$ K and the direction of the magnetic field was always applied parallel to the film plane. The experimental techniques are detailed in Annex I and II.

In the following sections, I will briefly discuss on the structural, topography, temperature dependent electrical and magnetic transport properties of epitaxially grown LSMO thin films of different thicknesses (50, 25 and 12 nm) on various single crystal lattice mismatched substrates. At first, I will be discussing the properties of tensile strained films (section 4.3), then will go on to compressively strained films (section 4.4) and section 4.5 will give you a broader view by comparing the properties altogether.

4.3 LSMO films under tensile strain by PLD

Epitaxial LSMO film when coherently grown onto the substrates with *in-plane* lattice parameters greater than that of film i.e., $a_s > a_f$, where 'a_f' and 'a_s' are the lattice parameters of the film and substrate respectively, then the film experiences *in-plane* biaxial tensile strain. As a result, the *in-plane* lattice parameters 'a' and 'b' of the film increases and locked with the underlying substrate and the *out-of-plane* lattice parameter 'c' of the film get reduced. In addition, as the thickness reduces, the tensile strain in the film increases that lead to increase in $Mn - O - Mn$ bond angle. As the bond angle increases, the electron hopping probability between Mn^{3+} to Mn^{4+} ions reduce which in turn reduces the T_{MI} and T_c.

4.3.1 LSMO on STO (001)

The STO (001) posses cubic structure with a lattice constant 'a' = 0.3905 nm. The lattice mismatch between STO substrate and LSMO film is about +0.8%. Therefore, LSMO films grown on STO would experience *in-plane* biaxial tensile strain. θ-2θ XRD studies reveal that LSMO film exhibits cube-on-cube epitaxy on STO substrates as shown in Figure 4.2(a). From the XRD measurements, it is quite evident that all the LSMO films coherently tensile strained with STO substrate and *002* peaks of LSMO lie on the right side of the bulk LSMO (dashed line). As the thickness of the film decreases, the in-plane (out-of-plane) lattice parameter of the film increases (decreases), which means the strain in the film also increases. The full width half maximum (FWHM) calculated from the rocking curve of LSMO (002) peaks were about 0.119°, 0.117° and 0.159° for 50 nm, 25 nm and 12 nm, respectively as shown in Figure 4.2(b). These values suggest that the films are of very high quality. Figure 4.2(c) shows the temperature dependent resistance behavior of LSMO/STO films of various thicknesses. As the thickness of the film decreases, there is a gradual reduction in MIT 'T_p' temperature. LSMO film with a

thickness of 50 nm displays T_p greater than 420 K, whereas, for the film of ~12 nm, the T_p is reduced to 349 K. As the thickness reduces, the tensile strain in the film increases, which lead to increase in $Mn-O-Mn$ bond angle. As the bond angle increases, the electron hopping probability from Mn^{3+} to Mn^{4+} ion reduces which in turn reduces the T_p. The topography of LSMO film surfaces are shown in Figure 4.2(d) reveals step flow growth with terraces, which is the replication of terraces on STO (001) substrate. The RMS roughness lies below 0.17 nm for all the thicknesses. In addition, the terrace directions and widths are different and are due to different miscut angles on STO substrates. Also, as the thickness of the film increases, the particles in the film get coalesce and consequently form wider steps. Figure 4.2(e) shows the cross-section profile on 50 nm film surface, which shows the measured terrace height is equivalent to 1 uc. Figure 4.2(f) shows the temperature dependence of magnetization behavior of LSMO films measured by SQUID. All the measurements were performed by applying magnetic field parallel to the film surface. The inset of Figure 4.2(f) shows the enlarged scale of temperature dependence magnetization at the highlighted position. The T_c obtained for 50 nm film was around 348 K whereas for the 12 nm was 340 K which is still well above the room temperature. Pradhan *et al.* [130] reported that the T_c of LSMO films with similar thickness (12 and 25 nm) was around 250 K, which lies far below the room temperature. Therefore, the enhancement in T_p and T_c in the current study is due to the fabrication of very high quality, atomically flat epitaxial thin films of LSMO. Figure 4.2(g) shows the thickness dependent 'T_p' and 'T_c' of LSMO thin films on STO substrates.

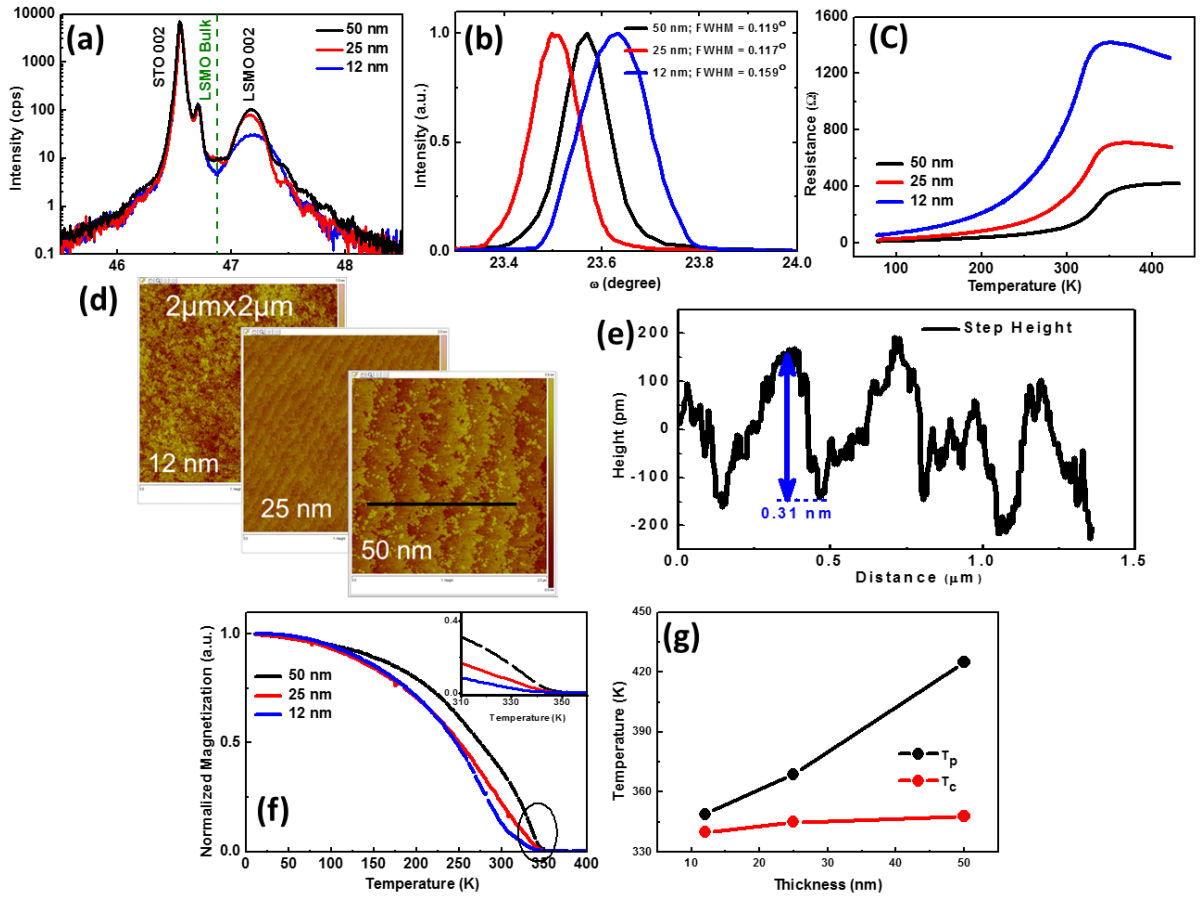

Figure 4.2: LSMO thin films of thicknesses (50, 25 and 12 nm) epitaxially grown on tensile-strained STO (001) substrate. (a) θ-2θ XRD scans of LSMO film and the dashed line indicates bulk LSMO, (b) omega scans around the 002 peak of LSMO; (d) AFM topography images of the LSMO film with scan area of 2μm x 2μm, (e) cross-section profile scanned along the line on 50 nm film surface showing the steps height; Temperature dependent (c) R (T) and (f) M (T) of the LSMO films, and (g) T_p and T_c as a function of LSMO film thickness.

4.3.2 LSMO on MgO (001)

The MgO (001) has rock-salt cubic structure with lattice parameter a = 0.421 nm. Therefore, the lattice mismatch between MgO substrate and LSMO film is about +8% [131], which is very high. For tensile strained films, the lattice parameter 'c' reduces, which results in shifting the LSMO (002) peak to higher angles (right side) compared to the bulk LSMO (002) peak. However, θ - 2θ XRD scans of LSMO films grown on MgO (001) in Figure 4.3(a) shows contradictory. LSMO (002) film peak lies on the left side of the bulk LSMO, indicates that the films are relaxed and is due to large lattice mismatch (8%) between substrate and film. As the thickness decreases from 50 to 12 nm, a slight right shift in LSMO 002 peak is observed, signifying an increase in strain at low thickness. FWHM calculated from rocking curve for 002 peaks of LSMO is about 1.3° to 2.11° on MgO substrate, which is very high compared to the film grown on STO (001) substrate. The higher FWHM values are also observed by Sirena *et al.* [132], Borges *et al.* [133]. Due to the large lattice mismatch, a large number of defects

(dislocations) incorporated in the initial layers of LSMO [134] film. Hence, films that are grown on MgO are not very high quality. AFM topography images on LSMO film reveals island type of growth mode as seen in Figure 4.3(c). Also, as the thickness increases, particles get agglomerated and the size of island increases. Figure 4.3(d) shows the temperature dependent resistance measurement, where for the 50 nm exhibits very high T_p. But, as the thickness decreases, the T_p falls rapidly to far below room temperature.

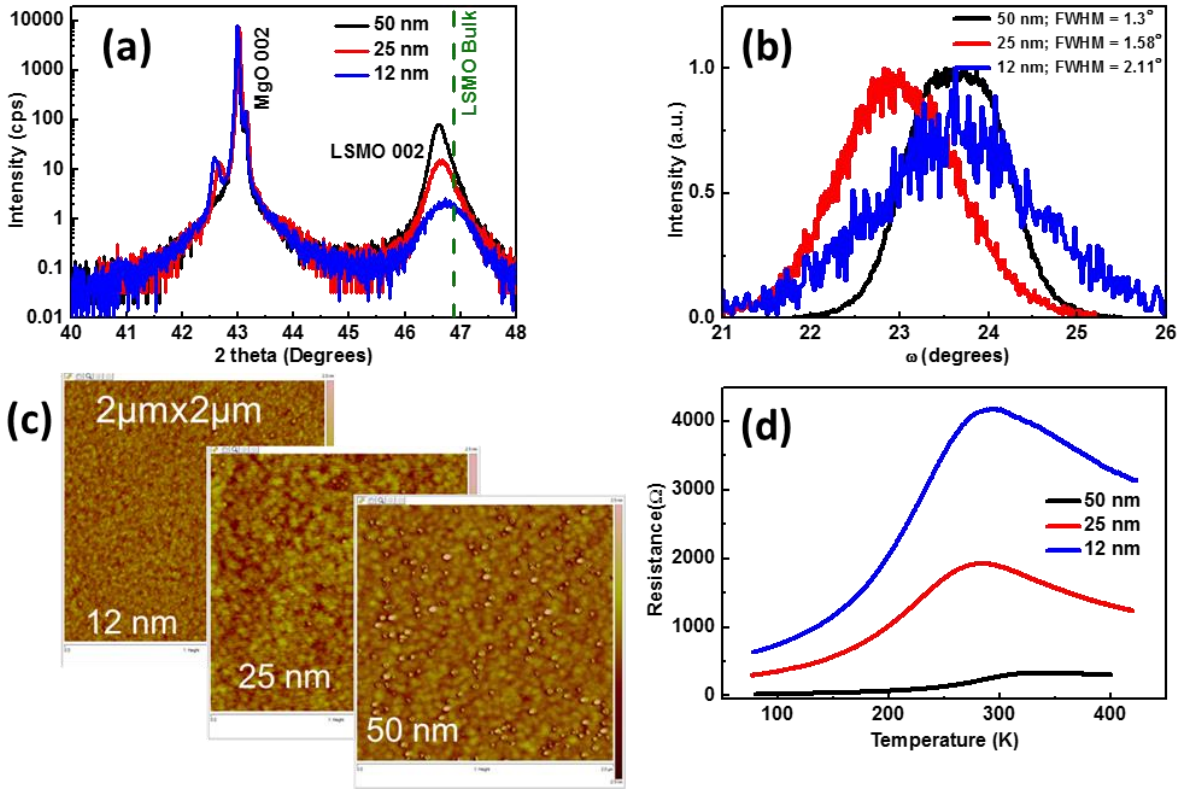

Figure 4.3: LSMO thin films of thicknesses (50, 25 and 12 nm) epitaxially grown on tensile-strained MgO (001) substrate. (a) θ - 2θ XRD scans of LSMO film and the dashed line indicating the pseudocubic lattice parameter of bulk LSMO. As the thickness increases, the film gets relaxes rapidly due to large lattice mismatch between substrate and film. (c) AFM topography images of the LSMO film surface with a scan area of 2μm x 2μm shows island kind of growth mode, and (d) temperature dependent R (T) measured by four-probe technique.

4.3.3 LSMO on STO buffered MgO (001)

In order to reduce the large interfacial strain states and defects developed in the LSMO thin film when directly grown on MgO (001), a buffer layer i.e., STO is introduced, that could improve the properties of LSMO films. The thickness of the buffer layer is kept constant at 12 nm, whereas, the different thicknesses of LSMO are grown as 50, 25 and 12 nm respectively. The θ - 2θ XRD scans of epitaxial LSMO thin films deposited on STO buffered MgO (001) are depicted in Figure 4.4(a). LSMO thin films, that were directly grown on bare MgO (001) substrates possess 8% lattice mismatch are relaxed [135] and also have large interfacial strain

states [133] as shown in Figure 4.3. While the LSMO thin films grown on MgO (001) substrate with STO as a buffer layer will have low interfacial strain states and the lattice mismatch is modulated through the STO buffer layer. It is also evident from the XRD measurements that the 002 peak of LSMO grown on STO buffered layers lie right side of the dashed line (Bulk LSMO pseudocubic) as shown in Figure 4.4(a). It indicates that the STO buffered LSMO films were tensile strained, whereas the film on non-buffered MgO substrates is relaxed. The intensity of STO peak is not dominant and it is pointed out by arrow marks. The FWHM calculated from rocking curve analysis around LSMO (002) film peak for ~50 nm is 1°, that shows signs of improvement in the film quality as compared to the film grown on non-buffered MgO. As the thickness of the LSMO film decreases, the tensile strain developed in the film increases, which also reflected in the increase of FWHM values as shown in Table 4.2.

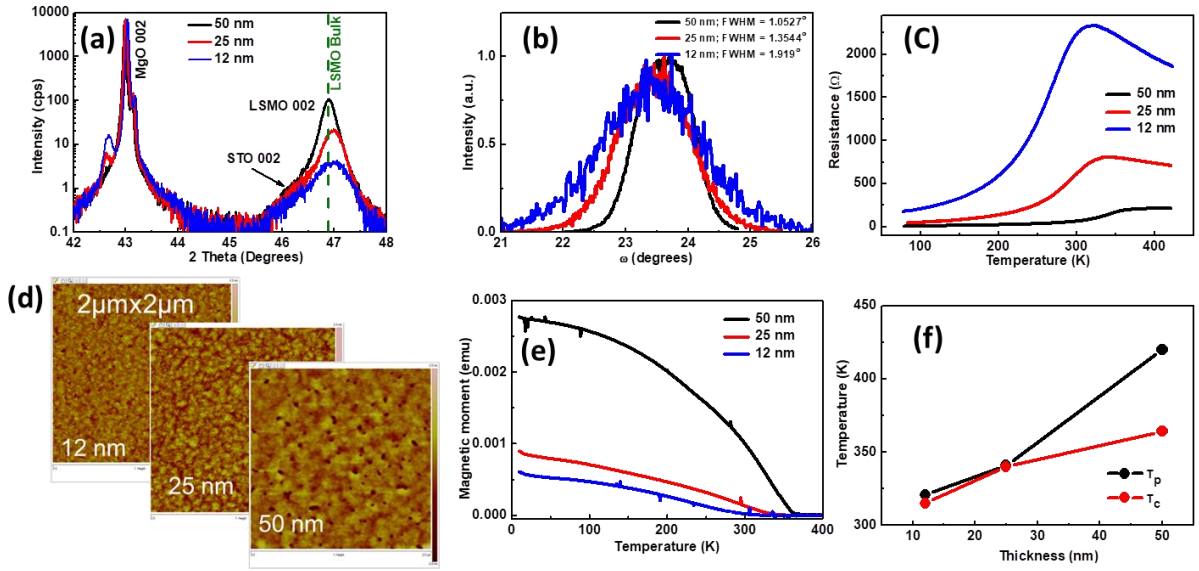

Figure 4.4: Epitaxial LSMO thin films of thicknesses (50, 25 and 12 nm) grown tensile on to STO buffered MgO (001) substrate. (a) θ - 2θ XRD scans of LSMO film and the dashed line indicating the bulk LSMO, an arrow pointing towards STO buffer layer. (b) omega scans around the 002 peak of LSMO; (d) AFM topography images of the LSMO film surface with scan area of 2μm x 2μm, (c) temperature dependent R (T) and (e) M (T) of the LSMO films, and (f) T_p and T_c as a function of LSMO film thickness.

Figure 4.4(c) shows the temperature dependent electrical transport properties of LSMO thin films grown STO buffered MgO (001) substrate. For all the film thicknesses range, STO buffered LSMO shows clear enhancement in T_p compared to the films grown on bare MgO (001) substrate (Figure 4.3(d)). In particular, for the 50 nm film exhibits MIT 'T_p' greater than 420K that is similar to film grown on STO (001) substrate (Figure 4.2(c)). Moreover, as the thickness is halved, the resistance is almost doubled which is expected in the case of uniform film quality. As the thickness decreases, T_{MI} falls rapidly to room temperature on STO buffered MgO films. Figure 4.4(d) shows the surface morphology of STO buffered LSMO films in the scan area of 2x2μm. Pinholes observed on the surface of the 50 nm thick film and could be due to the

formation of dislocations mediated through STO buffer layer. The average RMS roughness for 50 nm films is about 0.35 nm; infer that the films were quite smooth. Figure 4.4(e) shows the temperature dependent magnetic moment behavior of LSMO films measured by SQUID while applying the field in the plane of the film. The ferromagnetic to paramagnetic transition Curie temperature 'T_c' for STO buffered LSMO films of 50, 25 and 12 nm is 360, 320, and 290K respectively. In particular, for 50 nm thick films, it is worth to mention that the film shows very high magnetization at 300 K as compared to 25 or 12 nm. Figure 4.4(f) shows the thickness dependent 'Tp' and 'Tc'. The detailed values such as *out-of-plane* lattice parameter 'c', roughness and 2θ position of the film, electrical and magnetic properties as a function of thickness are reported in Table 4.2

4.4 LSMO films under compressive strain by PLD

Epitaxial LSMO thin films when coherently grown onto the substrates that have *in-plane* lattice parameters less than the film $'a_s < a_f'$, where 'a_f' and 'a_s' are the lattice parameters of the film and substrate respectively, then the film experiences compressive strain. As a result, the *in-plane* lattice parameters 'a' and 'b' of the film decreases and get locked with the underlying substrate and *out-of-plane* lattice parameter 'c' of the film increases. In general, in compressively strained films, the $Mn-O-Mn$ bond angle in MnO_6 octahedral decreases, which enhances the electron hopping probability between Mn^{3+} to Mn^{4+} ions, that in turn, enhance the T_{MI} and T_c.

4.4.1 LSMO on LSAT (001)

The LSAT (001) posses pseudocubic crystal structure with lattice constant a = 0.3868 nm. Therefore, the lattice mismatch between LSAT (001) and LSMO film is about - 0.2%. Due to the difference in lattice mismatch between substrate $a_s = 0.3868$ nm and film $a_f = 0.3875$ nm, LSMO film undergoes an *in-plane* compressive strain when grown on LSAT (001) substrate. *θ-2θ* XRD scans reveals that all the films are fully strained with c-axis perpendicular to the substrate as shown in Figure 4.5(a). The FWHM of LSMO (002) peak calculated from ω-scan rocking curve analysis is ~0.123° as shown in Figure 4.5(b). For 25 nm film, some satellite peaks appear symmetrically on the both sides of the (002) Bragg reflections. It is considered that the observed satellite peaks are the indication of the in-plane superlattices in the LSMO film [129], [136], [22]. The rocking curve for 12 nm film was not measurable; as we couldn't exactly locate its corresponding 002 peak of LSMO in *θ-2θ* XRD scans. Temperature-dependent electrical transport properties of LSMO films of all thicknesses are shown in Figure 4.5(c). All the films exhibit very high T_p i.e., > 420 K, which confirms that the films are of very high quality. In order to verify the roughness of the films, AFM is used in tapping mode on the scan area of 2 µm x 2 µm as shown in Figure 4.5(d). The calculated root mean square (RMS) roughness of the films are ~ 0.2 – 0.6 nm, signifying that the films were flat. Moreover, for 50 nm thick film, steps are observed on the surface and the cross-section profile along the black solid line indicates that the terrace height is about ~0.3 nm i.e., equivalent to 1 uc as shown in Figure 4.5(e). Figure 4.5(f) shows the temperature dependent magnetic moment curves with

ferromagnetic to paramagnetic transition Curie temperature 'T_c' are 352, 357 and 362 K for 12, 25 and 50 nm films respectively. As the films are compressively strained, the $Mn-O-Mn$ bond angle reduces that enhances the probability of double exchange, in turn, increases T_P and T_c. Figure 4.5(g) shows the thickness dependent T_c and T_p. As the thickness decreases from 50 to 12 nm, the T_p value remained constant, whereas, there is a significant reduction in T_c.

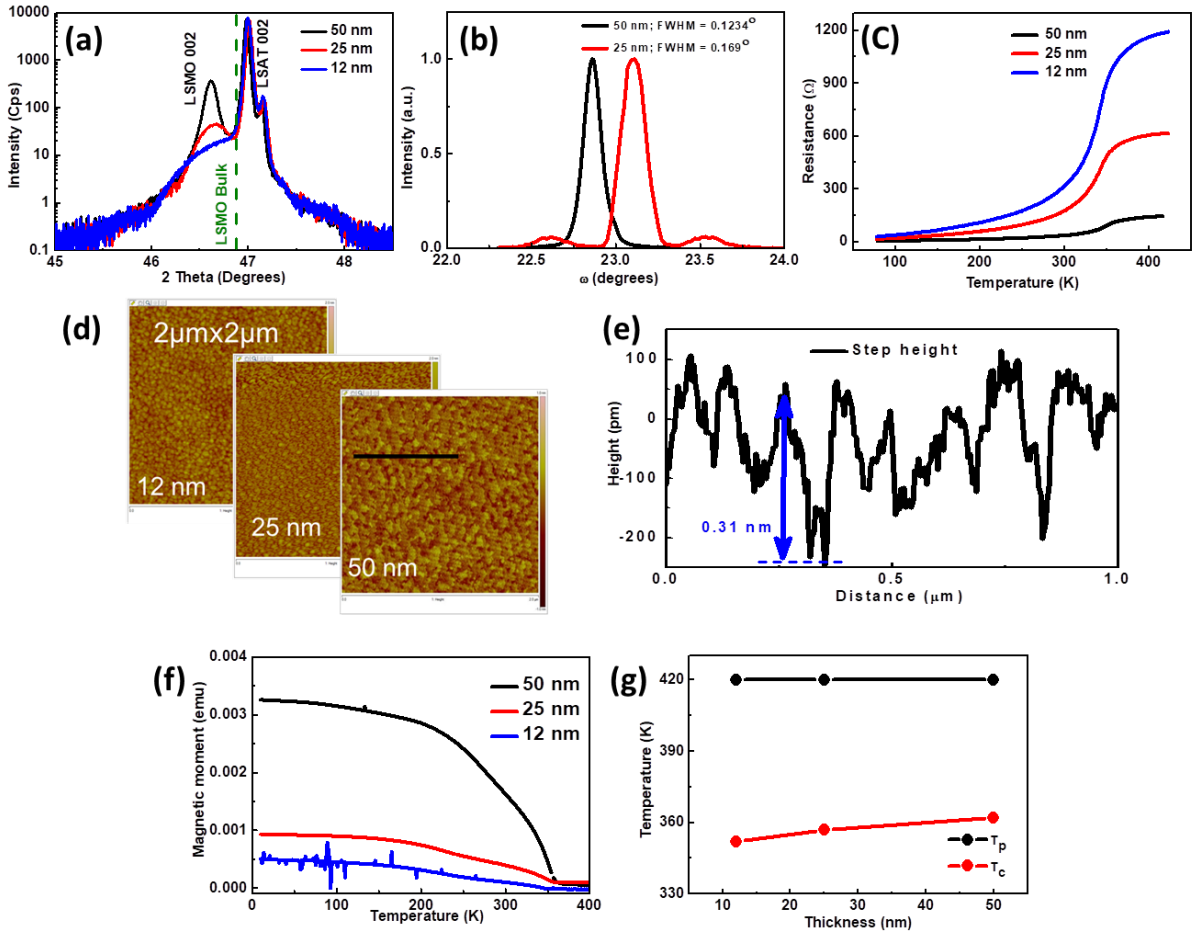

Figure 4.5: LSMO thin films of thicknesses (50, 25 and 12 nm) under compressive strain epitaxially grown onto LSAT (001) substrate. (a) θ - 2θ XRD scans of LSMO film and the dashed line indicating the bulk LSMO, (b) omega scans around the 002 peak of LSMO; (d) AFM topography images of the LSMO film surface with a scan area of 2μm x 2μm. (e) cross-section profile scanned along the line on 50 nm film surface showing the height of the step; temperature dependent (c) R (T) and (f) M (T) of the LSMO films, and (g) Tp and Tc as a function of LSMO film thickness.

4.4.2 LSMO on NGO (110)

The NGO (110) possesses orthorhombic crystal structure with a lattice constants a = 0.543 nm, b = 0.550 nm, and c = 0.771 nm. Orthorhombic NGO (110) can be viewed into its pseudocubic form as:

$$a_{pc} = c_o/2, \tag{4.1}$$

$$b_{pc} = c_{pc} = \sqrt{{a_o}^2 + {b_o}^2}/2 \quad (4.2)$$

Therefore, the calculated pseudocubic lattice parameter of NGO are a_{pc} = 0.3856 nm, $b_{pc} = c_{pc}$ 0.3864 nm. As NGO (110) has two different *in-plane* lattice parameters, the epitaxial strain imposed onto the film from the substrate is anisotropic (different in different in-plane *'a'* and *'b'* directions). Therefore, the lattice mismatch between NGO substrate and LSMO film is -0.5% and -0.3% respectively. NGO $(110)_o$ substrate orientation results in (001)-oriented epitaxial LSMO film cube-on-cube stacking [105], [106]. The in-plane sides of LSMO pseudocube $[010]_{pc}$, $[100]_{pc}$ are aligned along $[\bar{1}10]_o$ and $[001]_o$, and out-of-plane side $[001]_{pc}$ is aligned along $[110]_o$ of NGO substrate. θ-2θ XRD scans (Figure 4.6 (a)) reveals that the films are fully strained and epitaxially grown onto NGO substrate. The FWHM values calculated from rocking curve are ~0.08° for 50 nm film, which is only limited to the instrument resolution, confirming that the films are of very high quality as shown in Figure 4.6 (b). Similar to the LSMO film grown on LSAT substrate, some satellite peaks are also observed on NGO (110) for the 50 and 25 nm films. These satellite peaks are symmetrical on the both sides of the (002) Bragg reflections [22]. Temperature-dependent electrical transport properties of LSMO films of all thicknesses as shown in Figure 4.6(c) exhibits very high T_p i.e., greater than 420 K, which is similar to the films that are grown on LSAT (001) substrate. Figure 4.6(d) shows AFM topography of LSMO films in the scan area of 2µm x 2µm, which reveals step flow growth with meander like terraces formation. The step height measured along the black solid line on 12 nm film surface is equivalent to 1 uc as shown in Figure 4.6(e).

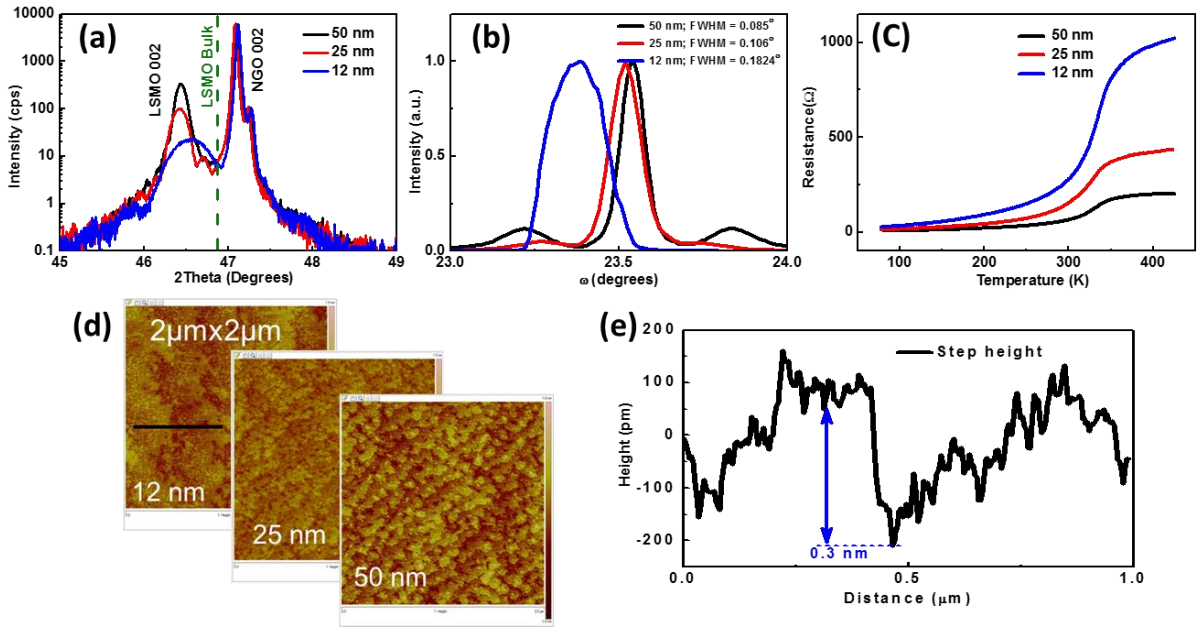

Figure 4.6: LSMO thin films of thicknesses (50, 25 and 12 nm) epitaxially grown on compressively strained NGO (110) substrate. (a) θ - 2θ XRD scans of LSMO film and the dashed line indicating the bulk LSMO, (b) omega scans around the 002 peak of LSMO; (c) temperature dependent R (T) measured by four-probe technique, (d) AFM topography of the LSMO film surface with scan area of 2µm x 2µm, indicates very

smooth surface with terraces formation, (e) cross-section profile scanned along the line on 12 nm film surface showing the terrace steps height.

4.4.3 LSMO on LAO (001)

The LAO (001) posses rhombohedral crystal structure and space group belongs to $R\bar{3}c$ with lattice parameter is given as 'a' = 0.3821 nm. The lattice mis-match between LAO substrate and LSMO film is about -1.36%. Therefore, LSMO film grown on LAO would experience very high compressive strain, which may lead to changes in growth mode, properties of film etc. θ-2θ XRD scans indicate that the films are fully epitaxial with c-axis perpendicular to the substrate as shown in Figure 4.7(a). Surprisingly, a double peak for LSMO 002 (2θ = 45.24° and 45.99°) has been observed for 50 nm film and it is due to the micro-twins present on the LAO substrate along (100) direction. Because of these micro-twins, LSMO film grown on one domain would be partially relaxed compared to the film grown on another domain, splitting the curve. The FWHM calculated from the rocking curve for 50 nm shows that film grown on one domain has much lower value i.e., 0.227° compared to the film on other domain i.e., 0.513°. AFM topography images in Figure 4.7(c) reveals an island type of growth mode. Also due to higher strain, as the thickness increases, the film relaxes quickly and particles start to agglomerate. As a result, the size of the island increases with increase in thickness, as seen in the AFM topography images.

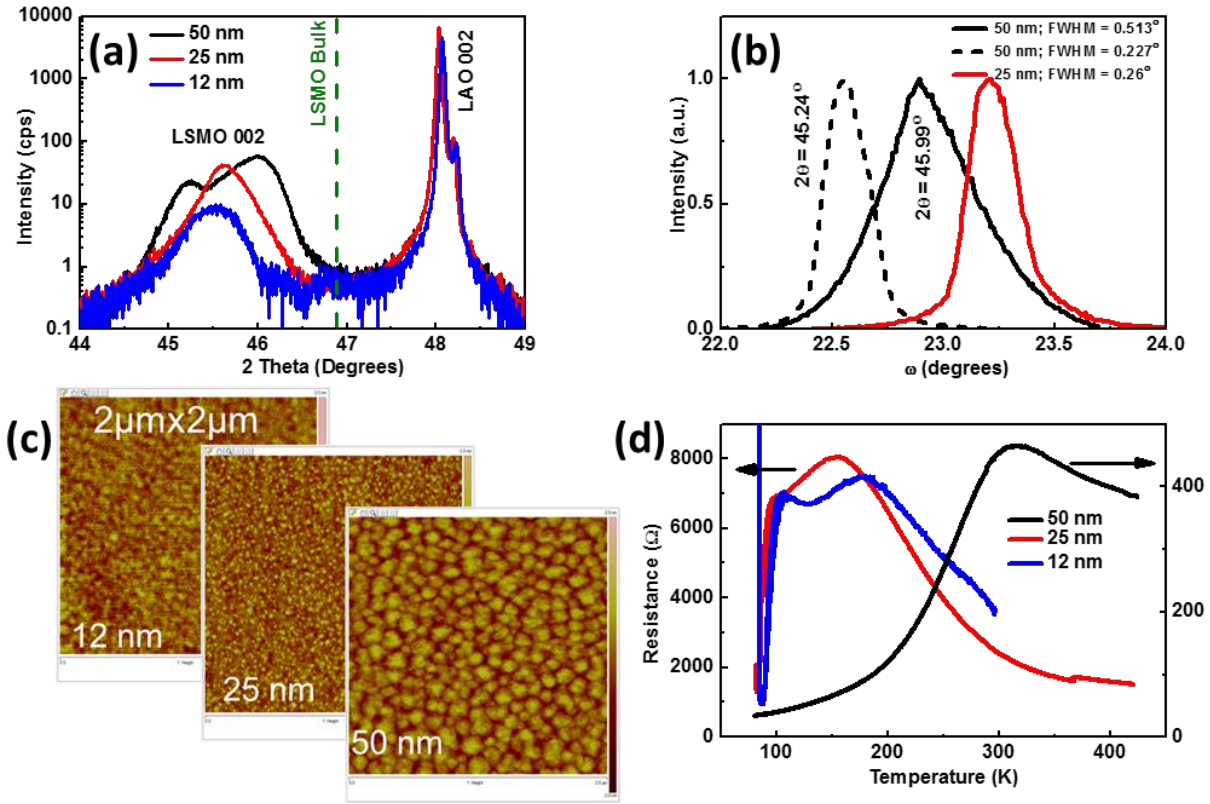

Figure 4.7: LSMO thin films of thicknesses (50, 25 and 12 nm) under compressive strain epitaxially grown onto LAO (001) substrate. (a) θ - 2θ XRD scans of LSMO film and the dashed line indicating the pseudocubic

lattice parameter of bulk LSMO. (b) omega scans around the 002 peak of LSMO; (c) AFM topography images of the LSMO film surface with a scan area of 2µm x 2µm shows an island type growth mode, (d) temperature dependent R (T) measured by four-probe technique.

The average RMS roughness values are ~0.4 nm. Figure 4.7(d) shows the temperature dependent resistance for all the thickness of the film. As the thickness reduces from 50 nm to 12 nm, the film loses its metallic behavior and the MIT falls drastically from 300 K to below 150 K. For LSMO films deposited on LAO substrates, the mechanism causing the degradation [137] of the ferromagnetic double exchange (DE) electrical and magneto-transport properties is the strain-driven elongation of the MnO_6 octahedra along the 'c' axis. Above the critical thickness ~25 nm, film starts to relax and recovers its bulk properties.

4.5 Summary: Compressive strain vs. tensile strain

In the previous sections, we have discussed in detail the properties of LSMO films deposited on different substrates inducing different strained states into the film. Here, we will discuss at glance the comparison between the properties of compressive and tensile strained films as shown in Figure 4.8. The shaded region is under compressive strain whereas unshaded part is under tensile strain.

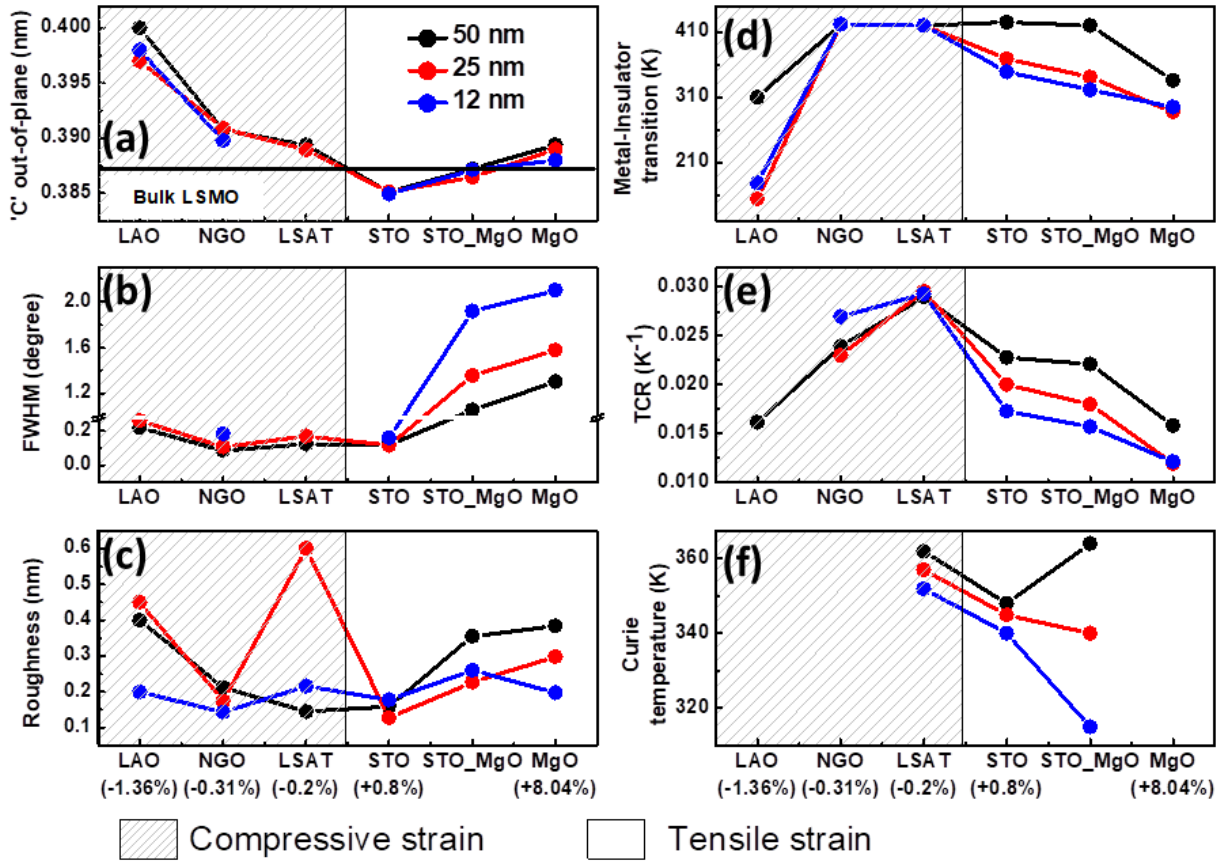

Figure 4.8: Epitaxial strain and thickness dependent properties of LSMO thin films as a function of strain. (a) 'c-axis' out-of-plane lattice parameter measured from XRD scans, (b) FWHM calculated from rocking curves from their corresponding LSMO (002) peak, (c) average RMS roughness values of the thin films measured by AFM on the scan area of 2µm x 2µm, (d, f) metal-insulator transition temperature and Curie temperature of the films, and (e) maximum temperature coefficient of resistance calculated from $\frac{1}{R}\frac{dR}{dT}$.

The measured *out-of-plane* lattice parameter 'c' of the film as a function of thickness and substrate is shown in Figure 4.8(a). Bulk LSMO value is also shown as a black solid line for reference. As we go from the compressive to tensile strain, the lattice parameter of the film 'c' decreases. However, for the film grown on STO buffered MgO shows higher values than that grown on bare STO because the film is partially relaxed, enhancing the 'c'. The films that were grown on MgO too show higher 'c' values because the film is completely relaxed due to large misfit strain (+8.04 %). The similar effect is observed in omega scans as showed in Figure 4.8(b). Films that grown on the low mismatched substrate are of higher quality with FWHM values under ~ 0.15°; whereas on large mismatched substrates (STO buffered MgO and MgO); the values are as high as 2°. Figure 4.8(c) indicates the average RMS roughness of the films. As the strain in the film increases, the roughness of the film also increases, which is consistent with the literature. The influence of biaxial strain on MIT 'T_p' of the thin films grown on various substrates are shown in Figure 4.8(d) clearly indicates that the film under compressive strain exhibits higher 'T_p' compared to the films under tensile strain which is quite consistent with the Millis [78] prediction. However, as the strain increases, the T_p falls rapidly. Also, it should be noted that the 'T_p' values for the 50 nm film on all the substrates are the highest values reported so far. The maximum temperature coefficient of resistance is presented in Figure 4.8(e) has the maximum value on LSAT substrate (nearly matched substrate) compared to all other substrates. Figure 4.8(f) gives the information about the Curie temperature T_C. The T_C of LSMO film increases under compressive strain and it is due to the reduction in $Mn-O-Mn$ bond angle which enhances the electron hopping probability. On the other hand, LSMO films under tensile strain will experience the increase in $Mn-O-Mn$ bond angle which could diminish the electron hopping probability that reduces the T_p and T_C.

Table 4.2: Structural, Morphological, Electrical and Magnetic transport properties of thickness dependent (50, 25 and 12 nm) epitaxial LSMO thin films deposited on different lattice mismatched substrates by Pulsed Laser Deposition (PLD) technique.

Film / Substrate	Sample number	Thickness (nm)	2theta (°)	$C_{out\text{-}of\text{-}plane}$ (nm)	FWHM (°)	Roughness (2x2 μm^2) nm	T_p (K)	R (300K) (Ohms)	Max. TCR (ppm)	Tc (K)
LSMO/LAO (001)	G713	50	45.24 & 45.99	0.4 & 0.39436	0.227 & 0.513	0.4 (G714)	310	453	0.01617	
	G733A	25	45.6175	0.3974	0.2594	0.45(G733B)	154.5	2400	------	
	G749A	12	45.53	0.39813		0.199(G749B)	178	3500	------	
LSMO/NGO (110)	G711	50	46.44	0.39074	0.085	0.212 (G712)	>420	67	0.0239	
	G731A	25	46.42	0.3909	0.106	0.174(G731)	>420	155	0.023	
	G762B	12	46.5636	0.38976	0.1824	0.143(G762A)	>420	280	0.027	
LSMO/LSAT (001)	G717	50	46.615	0.38936	0.1234	0.144(G718)	>420	34.5	0.029	362
	G760B	25	46.6643	0.38897	0.169	0.6 (G760A)	>420	176	0.0296	357
	G761B	12	------	-----	----	0.216(G761A)	>420	316	0.0293	352
Bridge between *in-plane* compressive strain to *in-plane* tensile strain imposed onto the LSMO film										
LSMO/STO (001)	G708	50	47.16	0.38511	0.119	0.159 (G710)	>425	116	0.0228	348
	G729A	25	47.1587	0.38512	0.117	0.127(G729B)	369	324	0.02	345
	G738B	12	47.1844	0.38492	0.159	0.178(G738A)	349	870	0.0173	340
LSMO/STO/MGO (001)	G721	50	46.892	0.38719	1.0527	0.355 (G722)	>420	63	0.0221	364
	G737B	25	46.985	0.38646	1.3544	0.227(G737A)	341	608	0.018	340
	G751B	12	46.8970	0.38715	1.919	0.260(G751A)	321	2238	0.0157	315
LSMO/MGO (001)	G715	50	46.6094	0.3894	1.3	0.384 (G716)	336	282	0.0158	
	G734A	25	46.6612	0.38899	1.578	0.298 (G734)	287	1884	0.0119	
	G750A	12	46.7306	0.38845	2.11	0.197(G750B)	295	4166	0.0121	

5 Magnetic anisotropy of LSMO films under tensile strain grown by PLD

As previously discussed in the section 3.1.4.1, the magnetization in epitaxial LSMO thin films grown under tensile strain would tend to lie in the plane of the film. However, depending on the underlying substrate, structure, strain, thickness, temperature etc., the preferential magnetization aligns to its lowest possible energy i.e., easy axis (e.a.). In the following sections, you will get a glimpse of the magnetic anisotropies of LSMO thin films of different thicknesses grown on STO (001) and STO buffered MgO (001) substrates measured at room temperature and for some thicknesses at low temperature. The tensile strain in LSMO thin films increases with increase in the lattice mismatch. Therefore, LSMO films that are directly grown on MgO (001) substrates with 8% lattice mismatch are not of very high quality. Hence, we didn't study magnetic anisotropy of LSMO films grown on MgO (001) substrate.

5.1 LSMO on STO (001)

LSMO thin films of thicknesses (50, 25 and 12 nm) epitaxially grown onto cubic STO (001) substrate by PLD at GREYC, Caen. Due to lattice mismatch, LSMO film undergoes an *in-plane* biaxial tensile strain. The detailed structural, electrical, morphological properties of LSMO thin films grown onto STO (001) substrates has been discussed in the section 4.3.1

5.1.1 Magnetic characterization

Thickness-dependent in-plane magnetic anisotropy studies of LSMO (001) thin films grown on STO (001) substrates were performed at room temperature by v-MOKE magnetometry at IMDEA, Madrid for all the films. Low-temperature measurements were also done for one selected sample (50 nm thick film). All the measurements are done in a longitudinal mode with using a *P*-polarized blue laser. For all the measurements, the samples are mounted on eucentric goniometer that allows us to keep the reflection plane constant during the angular measurements as shown in Figure 5.1. Here, 'θ' is defined as the angle between applied magnetic field direction and [100] crystallographic direction of STO (001) substrate. For each film thickness, the sample is rotated and the hysteresis loops are acquired at different directions within the film plane with an interval of 4.5° each in the whole angular range. We always measure two *in-plane* components that are parallel ($M_{||}$) and transversal ($M_{\perp}$). The parallel (transverse) component is measured always parallel (perpendicular) to the field direction. The remanence, coercive fields are calculated from each hysteresis loops in order to track the angular evolution of about 360°.

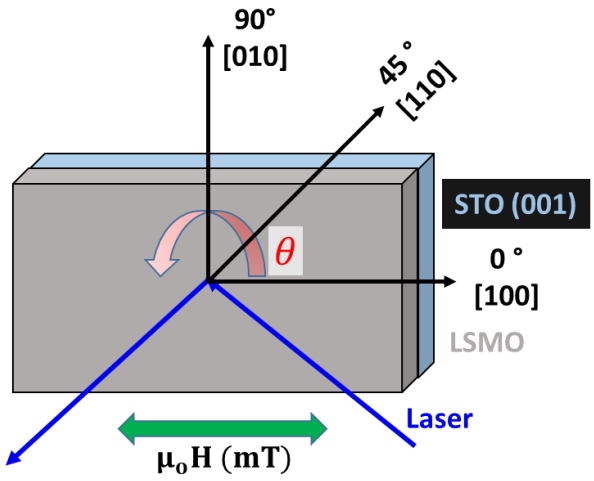

Figure 5.1: Schematic of the sample mounted on the goniometer in the v-MOKE set-up in the longitudinal mode. Here, the angle 'θ' indicates the direction of the rotation of the sample. The applied field direction is also presented. At θ=0°, the applied field is aligned parallel to [100] crystallographic axis.

5.1.1.1 Angular dependent M (H) loops around characteristic axes @ 300 K

In order to give a general view of the magnetic properties of the LSMO films of different thicknesses (50, 25 and 12 nm), we first present their representative Kerr hysteresis loops acquired at θ = 0°, 45° and 90° with only $M_{||}(H)$ component as shown in Figure 5.2. From the hysteresis loops in Figure 5.2 (b and c), it is clear that the LSMO films of thickness 12 and 25 nm exhibit uniaxial anisotropy, whereas, 50 nm thick film (Figure 5.2 (a)) exhibits very weak anisotropy. The easy and hard axes for the 12 nm (25 nm) film present along 90° and 0° (0° and 90°), respectively. The coercive field at the easy axis for the 12 and 25 nm are 0.3 and 0.68 mT and at the hard axes, it almost equals to zero. Similarly, the remanence measured at easy and hard axes for 12 and 25 nm are $M_{R,||} \cong M_S$ and $M_{R,||} = 0$. In the case of 50 nm thick film, very small (negligible) differences are found by comparing the $M_{||}$ (H) loops around θ = 0° and 90° as seen in Figure 5.2(a). In addition, a more detailed angular dependence study of the magnetization reversal and coercivity are presented in the next section.

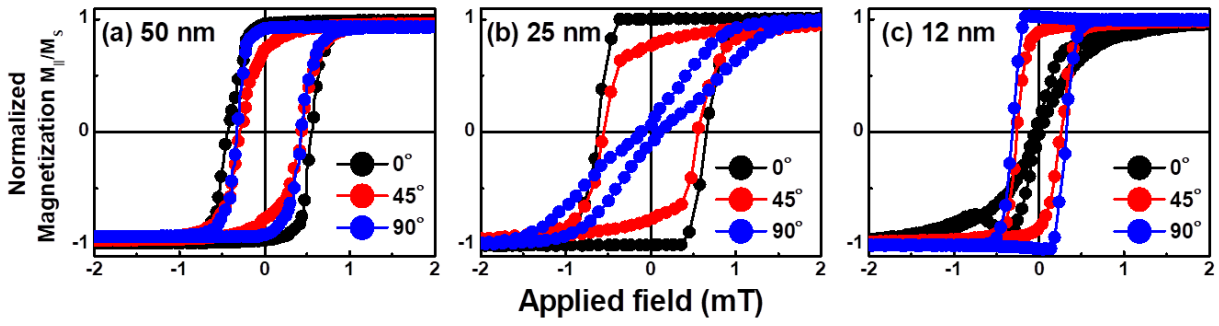

Figure 5.2: Normalized magnetization hysteresis loops of LSMO thin films grown on STO (001) substrate of thicknesses (a) 50 nm, (b) 25 nm, and (c) 12 nm, respectively measured at 300 K at different in-plane angles.

5.1.1.2 Angular dependence of remanence @ 300 K

The remanence is calculated from individual hysteresis loops in order to track their angular evolution of about 360°. Figure 5.3 shows the angular dependence of normalized remanence magnetization of LSMO films of various thicknesses with the easy axis (e.a) and hard axis (h.a) indicated by arrows, respectively. Figure 5.3(a) shows the angular dependent remanence fields of LSMO film of thickness 50 nm. By careful inspection, we can notice that there are two maxima and minima values present in the angular range of 180° that are marked with arrows as e.a.I, e.a.II, h.a.I and h.a.II, respectively. The e.a.I and e.a.II are aligned at $\theta \cong$ 35° and 90° and h.a.I and h.a.II are aligned along $\theta \cong$ 60° and 150° respectively. The percentage of change in remanence between maxima and minima is less than 10% (very weak). Furthermore, the angle between the easy axis and the immediate hard axis is not exactly 45° (in contrast to ideal biaxial anisotropy system, where the angle between an easy and hard axis should be exactly 45°) which suggests that there should be an additional anisotropy present in the film. This additional anisotropy is very weak and maybe due to the terraces at the film surface. Therefore, for the 50 nm thick film, there exists a combination of biaxial (weak) due to magnetocrystalline or cubic anisotropy and uniaxial (very weak) due to the terrace steps.

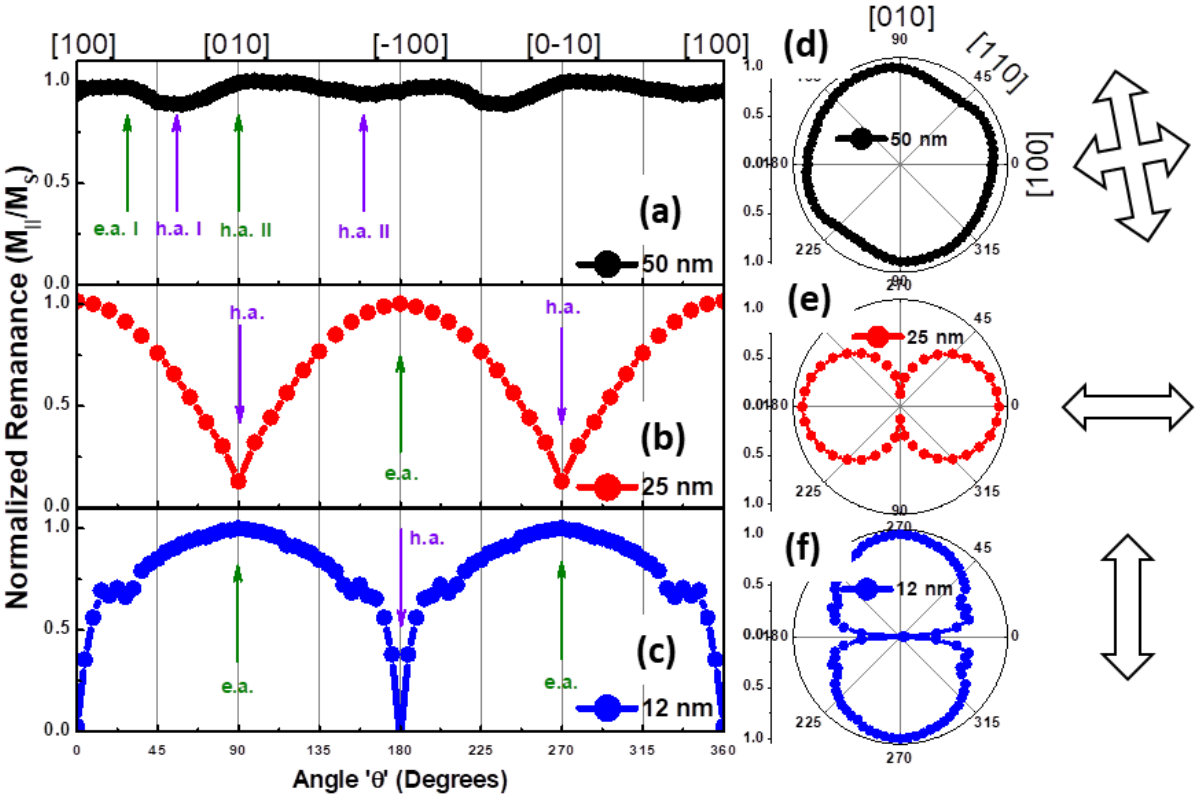

Figure 5.3: Angular dependence of the normalized remanence magnetization ($M_{||}/M_S$) of LSMO films of thickness (50, 25 and 12 nm) grown on STO (001) substrates and their corresponding polar plots (right). The arrows are pointing the direction of the easy axis.

As the thickness of the film decreases from 50 to 25 and 12 nm, there is a change in anisotropy from weak biaxial to pure uniaxial. The results are clearly visualized in the angular dependent remanence polar plots (Figure 5.3 (e)) of the 25 nm film. There are

periodic oscillations with 180° periodicity and easy axes are aligned along [100], whereas, the hard axes are aligned along [010] crystallographic axes. Angular dependent remanence for the 12 nm is shown in Figure 5.3 (c, f) also exhibits periodic oscillations with 180° periodicity. The highest and lowest values of remanence fields were found at [010] and [100] that correspond to the easy and hard axis of the film respectively. Also, there is a change in easy axis direction by 90° compared to 25 nm film[viii]. Both remanence polar plots of 25 and 12 nm in Figure 5.3 (e, f) show the characteristic "two-lobe" behavior originated from uniaxial magnetic anisotropy.

5.1.1.3 Angular dependence of coercive fields @ 300 K

The coercive fields are calculated from individual hysteresis loops in order to track their angular evolution of about 360°. Figure 5.4 shows the angular dependence coercivity ($\mu_o H_C$) of LSMO film all the thicknesses. The four-fold behavior is observed in the angular dependence coercivity for 50 nm film (Figure 5.4(a)). As observed in the remanence plots, the coercive field is higher at e.a. I and e.a. II, that again confirms that the film exhibit mixed anisotropies. In the case of 12 and 25 nm, the two-fold symmetry is also found in angular dependence of coercivity ($\mu_o H_C$) as shown in Figure 5.4 (b, c), revealing 180° periodicity.

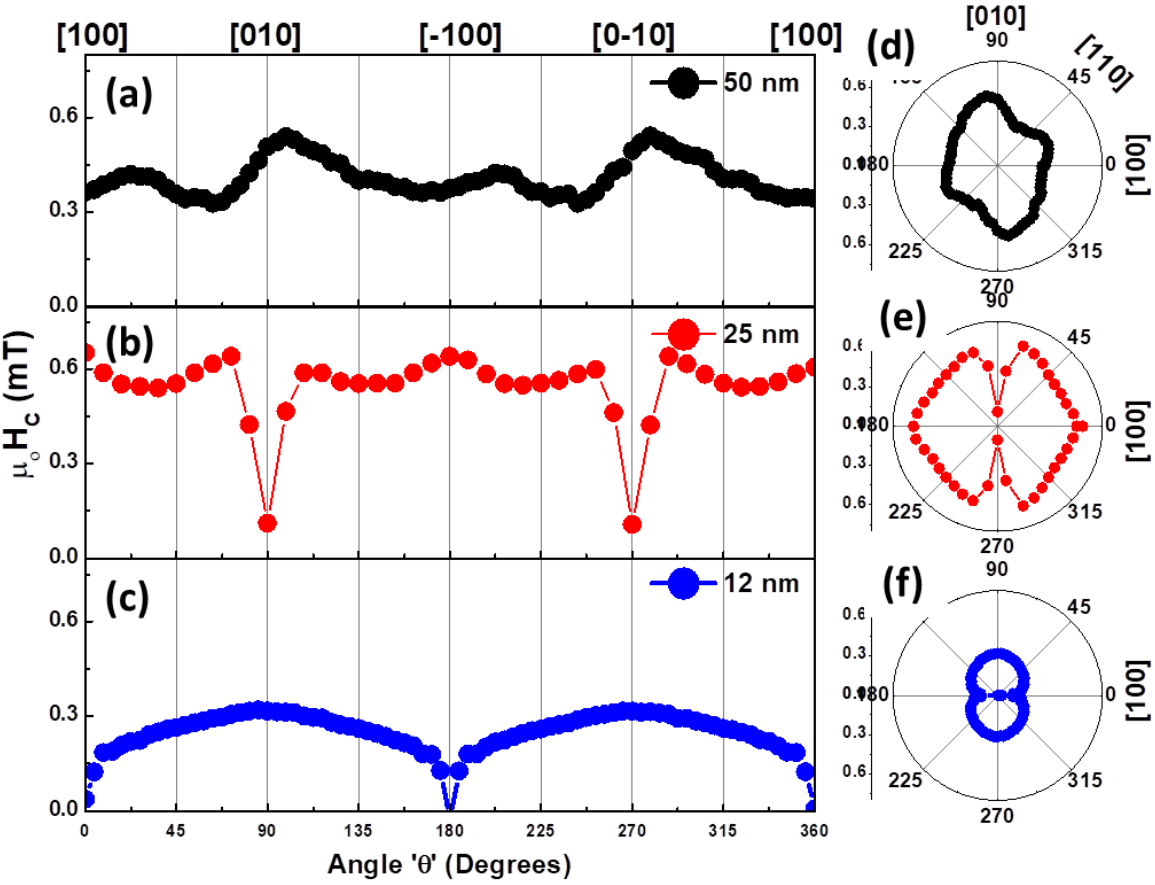

Figure 5.4: (a, b, c) Angular dependence of coercive field of LSMO thin films of thicknesses (50, 25 and 12 nm) grown on STO (001) substrate and their corresponding polar plots (d, e, f).

[viii] At present, *in-plane* XRD measurements are underway to confirm the exact structure and crystallographic axes in order to determine the change in magnetic anisotropy direction.

Discussion:

Here, I would like to recall the AFM images and the remanence polar plots for the comparison of magnetic anisotropy with the topography of the films.

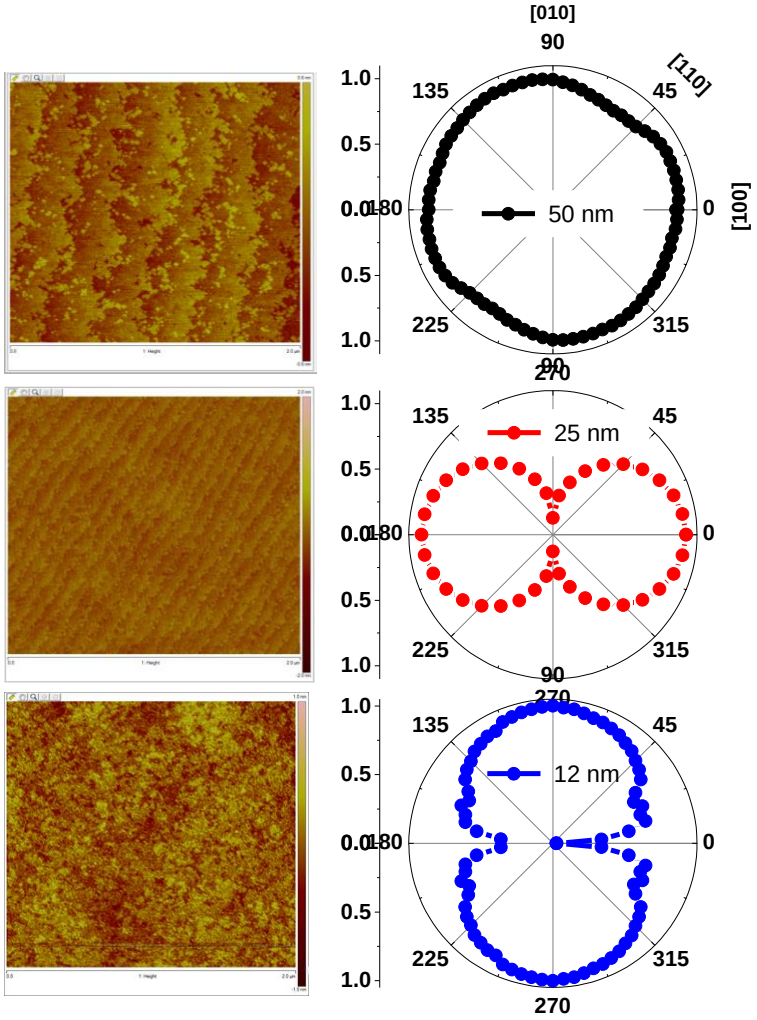

Figure 5.5: (left panel) AFM topography images and (right panel) remanence polar plots of 50, 25 and 12 nm LSMO films on STO substrate, respectively.

As STO (001) is cubic, the LSMO film when grown on STO (001) substrate undergoes an *in-plane* biaxial tensile strain with a strain that is equal in the 'a' and 'b' axes. The magneto-elastic energy, which is due to strain accompanying in the material, is constant in the film plane. Therefore, the cause for anisotropy is not due to magneto-elastic energy but it can be owing to defects in the crystal structure. Due to terrace steps in the LSMO film, broken bonds are present along the step edges as observed in AFM topography, shown in the Figure 5.5 (left panel). Because of these broken bonds, defects are developed along step edges, as a result, films exhibit uniaxial anisotropy with easy axis present parallel, perpendicular, or random to the step direction as observed by many authors [50], [51]. As the thickness of LSMO film decreases, magnetic anisotropy exhibits a strong uniaxial anisotropy. This suggests that the film at the lower thickness, the magnetic anisotropy is due to steps and miscut angle of STO (001) substrate. Compared to the literature data as mentioned in the

Table 3.1, we have also observed discrepancies in magnetic anisotropy. However, reciprocal space mapping (RSM) measurements are underway, which could provide us more information and to relate it with magnetic anisotropy.

In order to have a clear envision about the anisotropy of LSMO films, low-temperature V-MOKE will be discussed in next section.

5.1.1.4 Temperature-dependent magnetic properties

As discussed in the previous sections, the temperature is one of the important parameters that affect the magnetic anisotropy in the films. Here, we will briefly discuss the temperature dependency of the 50 nm LSMO film grown on STO (001) substrate. As shown in Figure 5.3, at room temperature, the 50 nm film exhibits almost isotropic behavior (due to very weak anisotropies competition). As the temperature decreases to 20 K, a change in magnetic anisotropy is observed. Figure 5.6 (a, b) shows the temperature dependent hysteresis loops measured at $\theta = 45°$ and 90° respectively.

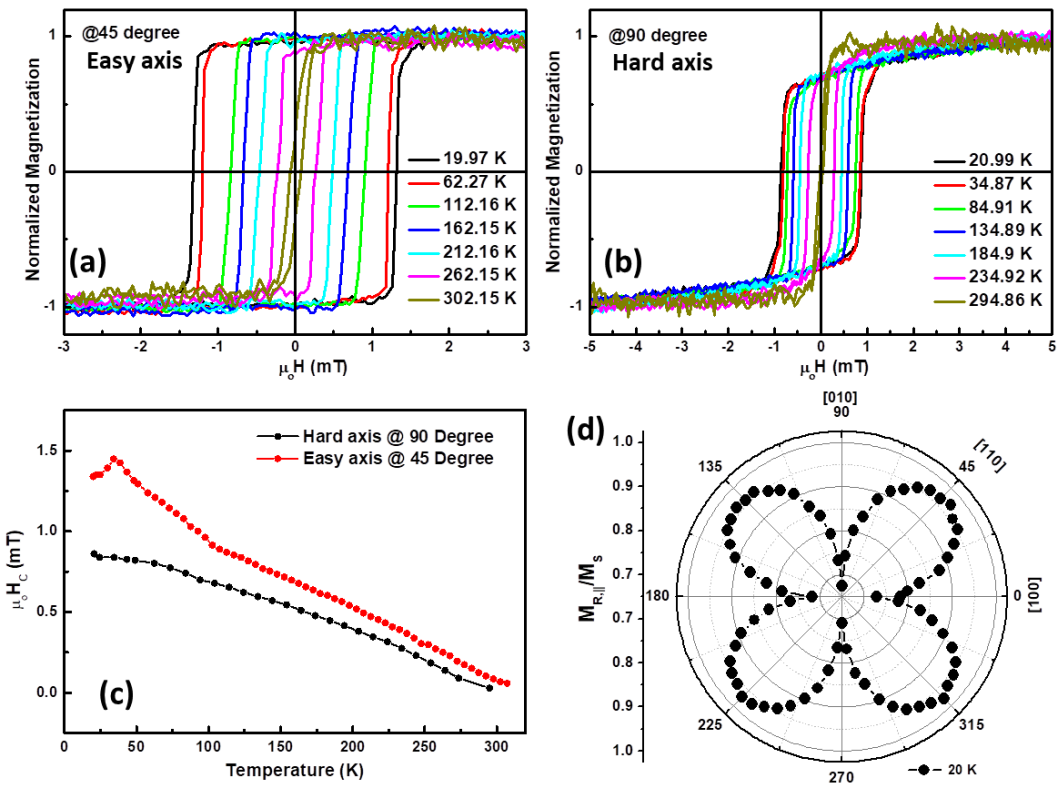

Figure 5.6: Temperature dependence of normalized hysteresis loops in the 50 nm thick LSMO/STO (001) film at easy axis (a), hard axes (b) respectively. (c) Temperature dependence of coercive field measured at easy and hard axes, (d) Angular dependent normalized remanence polar plot measured at 20 K.

As temperature decreases, the coercive field at easy axis increased from 0.058 mT to 1.45 mT and at the hard axis from 0.028 mT to 0.86 mT as shown in Figure 5.6(c). The angular dependent polar plot measured at 20 K (Figure 5.6(d)) exhibits four symmetrical lobes with 90° periodicity that corresponds to a pure biaxial system. The easy and hard axes are therefore located along $< 110 >$ and $< 100 >$ crystallographic axes. The origin of this biaxial anisotropy is magnetocrystalline anisotropy of LSMO, which is usually dominant at

low temperatures. Several authors as reported in section 3.1.4.1 have observed the similar behavior. Hence, by comparing the remanence polar plots in the 50 nm thick film at 300 K and at 20 K, it is clearly evident that the magnetic anisotropy symmetry has been changed from almost isotropic behavior to strong biaxial anisotropy, owing to magnetocrystalline nature of LSMO.

5.1.2 Summary

In summary, we have successfully grown epitaxial LSMO thin films of different thicknesses onto STO (001) substrate by PLD technique. In-plane magnetic anisotropy measurements are performed at room temperature on all the films and at low temperature on 50 nm thick film. At room temperature, the magnetic anisotropy landscape of LSMO thin films depends on the film thickness. At lower thicknesses (12 - 25 nm), uniaxial (two-fold) anisotropy is dominant due to substrate-induced step edges and miscut angles. At the intermediate thickness range (50 nm), depending upon anisotropy strengths, there exists a competition between a uniaxial (step-induced) and biaxial (four-fold) anisotropy (magneto-crystalline or cubic anisotropy). This particular case can be inferred as coexistence between bi-axial and uniaxial anisotropy. However, magnetic anisotropy at low temperature exhibit biaxial anisotropy and is purely due to magnetocrystalline nature of LSMO.

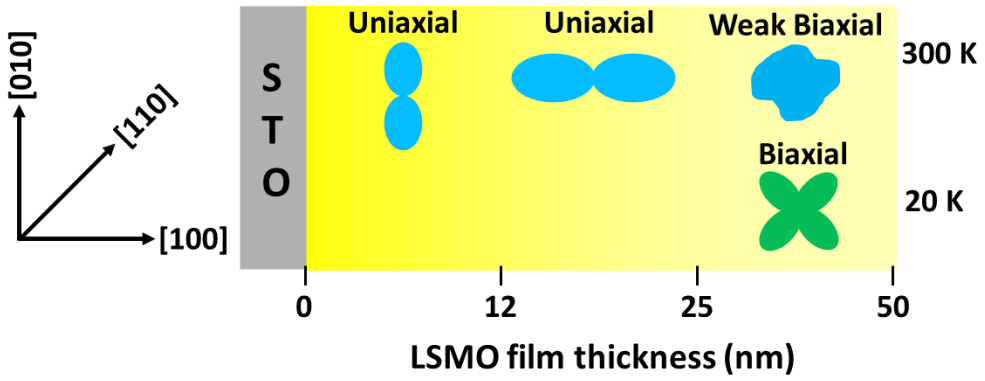

5.2 LSMO on STO buffered MgO (001)

In the section 4.3.3, I have briefly discussed the structural, morphology, electrical and magneto-transport properties of the LSMO film grown onto STO buffered MgO (001) substrate. In the following section, I will discuss in detail the study of magnetization reversal process and in-plane magnetic anisotropy of the STO buffered LSMO film of thickness[ix] 50 nm. Here, the STO buffer layer thickness is 12 nm. Both MgO and STO have cubic structures. Therefore, LSMO film when grown onto STO buffered MgO also exhibits cubic structure, experiencing *in-plane* tensile strain along 'a' and 'b' axes. Therefore, one would expect the magnetic anisotropy of this particular system could exhibit bi-axial anisotropy or four-fold symmetry, which can be related to the magnetocrystalline anisotropy of LSMO. Let's see in detail how the magnetic anisotropy symmetry landscape changes as a function of temperature and also compared to the films that were directly grown onto STO (001) substrates.

5.2.1 Magnetic characterization

In order to understand the inherent magnetic properties of LSMO thin film grown onto STO buffered MgO (001) substrate, angular dependent hysteretic behavior at 300 K was probed by using v-MOKE @ IMDEA, Madrid and at 40 K by using simple MOKE magnetometry @ CNR-IOM, Trieste, Italy. The measurements were performed in the longitudinal mode. The sample is mounted on eucentric goniometer that allows us to keep the reflection plane constant during the angular measurements as shown in Figure 5.7(a). At $\theta = 0°$, the applied external magnetic field is aligned parallel to the [100] crystallographic axis of MgO (001) substrate. *In-plane* Kerr hysteresis loops are acquired between 0° and 360° with the step of every 9° by rotating the sample in the plane of the film and keeping fixed the external magnetic field direction. The remanence, coercive fields are calculated from each hysteresis loops in order to track the angular evolution of about 360°. Figure 5.7(b) shows the schematic of the heterostructures along with the misfit strains at different interfaces in the film.

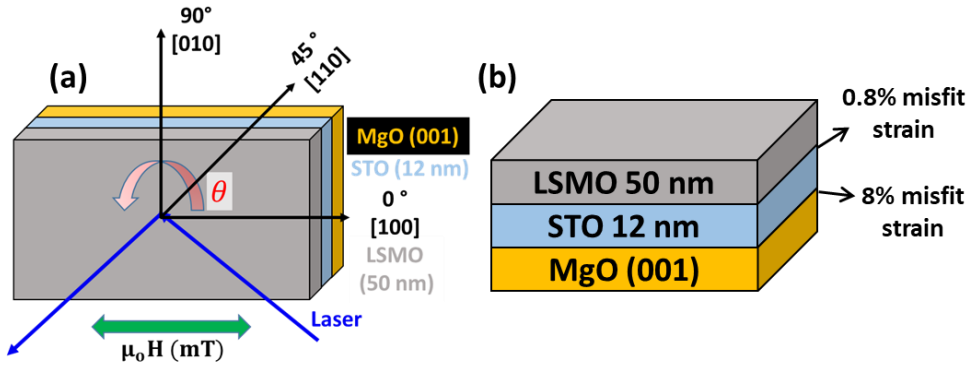

Figure 5.7: (a) Schematic of the sample mounted on the goniometer in the v-MOKE set-up in the longitudinal mode. Here, the angle 'θ' indicates the direction of the rotation of the sample. The applied field direction is also presented. At θ = 0°, the applied field is aligned parallel to [100] crystallographic axis. (b) Schematic of the heterostructures with misfit strain between different layers is also presented.

[ix] For 25 and 12 nm LSMO/STO/MgO films, the magnetic signal measured at 300 K is very low compared to the 50 nm film and the Curie temperature decreases as decrease in thickness as seen in Figure 4.4(e).

5.2.1.1 Angular dependent M (H) loops around characteristic axes @ 300 K

Figure 5.8 shows the normalized Kerr hysteresis loops of the LSMO (001) film grown on STO buffered MgO substrate acquired at θ = 45°, 90° and ±9° i.e., at and around characteristic axes respectively. As discussed in the previous sections, with the simultaneous acquisition of two in-plane components ($M_{||}(H)$ and $M_{\perp}(H)$), we can qualitatively deduce the type of magnetic anisotropy of the film. By carefully inspecting the change of sign in the transversal component ' $M_{\perp}(H)$', one can accurately locate the easy and hard axes directions, respectively. When the magnetic field is applied near around easy i.e., at $\theta = 36°$ and $\theta = 54°$ as shown in Figure 5.8(left), the magnetization switches with only one irreversible transition. Also, there is a sign change in $M_{\perp}(H)$ component. From this, we can deduce that the easy axis of the LSMO film is present at $\theta = 45°$. The remanence of parallel component at the easy axis is $M_{R,||} \cong M_S$ and the coercive field is about 1.8 mT, which is higher than on STO (001). Whereas, the transverse component is almost zero, i.e., the spins at easy axes are always aligned parallel or anti-parallel to the applied field directions.

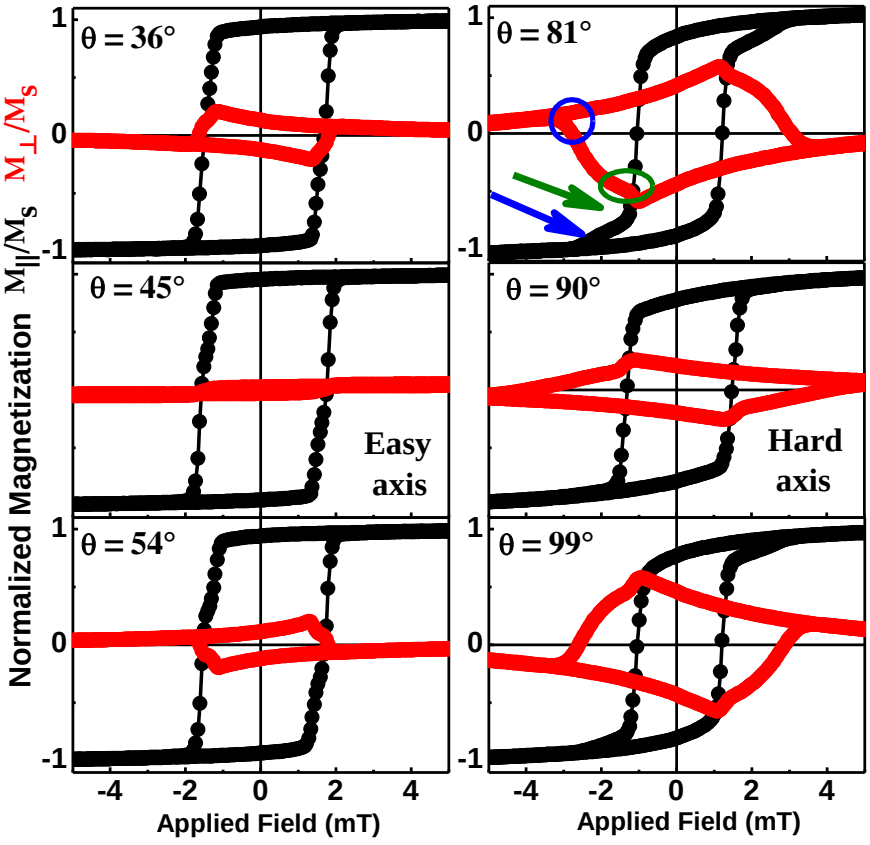

Figure 5.8: Magnetization reversal studies of 50 nm thick LSMO (001) film grown on STO buffered MgO (001) at and around easy (left) and hard (right) axes of magnetization measured by v-MOKE at 300 K. The corresponding applied external magnetic field angles (θ) with respect to crystallographic axis are also specified in the figure. The $M_{||}(H)$ (black) and $M_{\perp}(H)$ (red) loops acquired simultaneously are shown. The arrow (circles) in the top right panel indicates the double transition, which is the signature of biaxial anisotropy.

Similarly, when the field is applied near around hard axes as shown in Figure 5.8(right), the reversal takes place in two steps which are pointed out with arrows and circles in $M_{||}(H)$ and $M_{\perp}(H)$, respectively. These two irreversible transitions take place by nucleation and propagation of two consecutive 90° domain walls as explained by Costa-Krämer et al.[126]. When the field is applied at hard axis i.e., $\theta = 90°$ as shown in Figure 5.8(right), the $M_{||}(H)$ hysteresis loop show rotation of the magnetization followed by sharp irreversible transition and final rotation towards the applied field direction. For every transition in $M_{||}(H)$ component, there is simultaneous transition observed in $M_{\perp}(H)$ component too. In a cubic thin film, the reversal proceeds with one (two) irreversible transition, related to nucleation and propagation of 180° (90°) domain walls, when the field is applied close to one of the two easy (hard) axis orientations of magnetization.

However, just by looking at the hysteresis loops at and around 45° and 90°, the analysis may go wrong in concluding effective anisotropy. Therefore, the complete angular dependent study is necessary in order to effectively deduce the magnetic anisotropy, which is presented in the next section.

5.2.1.2 Angular dependence of remanence @ 300 K

In addition to the hysteresis loops, the magnetic anisotropy becomes more evident when the angular dependence of remanence is plotted with respect to the applied field angle in the range of $0° - 360°$. The normalized remanence plots calculated from two in-plane magnetization components ($M_{R,||}$ and $M_{R,\perp}$) at the applied field $H = 0$ as a function of angle 'θ' is shown in Figure 5.9 (a). Both the magnetization components are repeating their features with the periodicity of 90° owing to biaxial anisotropy. Also, $M_{R,\perp}$ changes its sign for every 45° when it crosses the characteristic easy and hard axes respectively. The polar plots of $M_{R,||}/M_S$ and $M_{R,\perp}/M_S$ are also shown in Figure 5.9 (b, c). The remanence polar plot ($M_{R,||}/M_S$) shows a butterfly structure with the highest and lowest values pointing to easy and hard axes of film i.e., [110] and [100] and their equivalent crystallographic directions respectively. The transversal component shows windmill shape. This windmill shape is related to the inversion of the sign after crossing characteristic easy and hard axes. In addition, the angles between two adjacent easy and hard axes are orthogonal to each other. Therefore, it confirms a pure biaxial (four-fold) symmetry, which is due to strong effects originating from magneto-crystalline nature of LSMO.

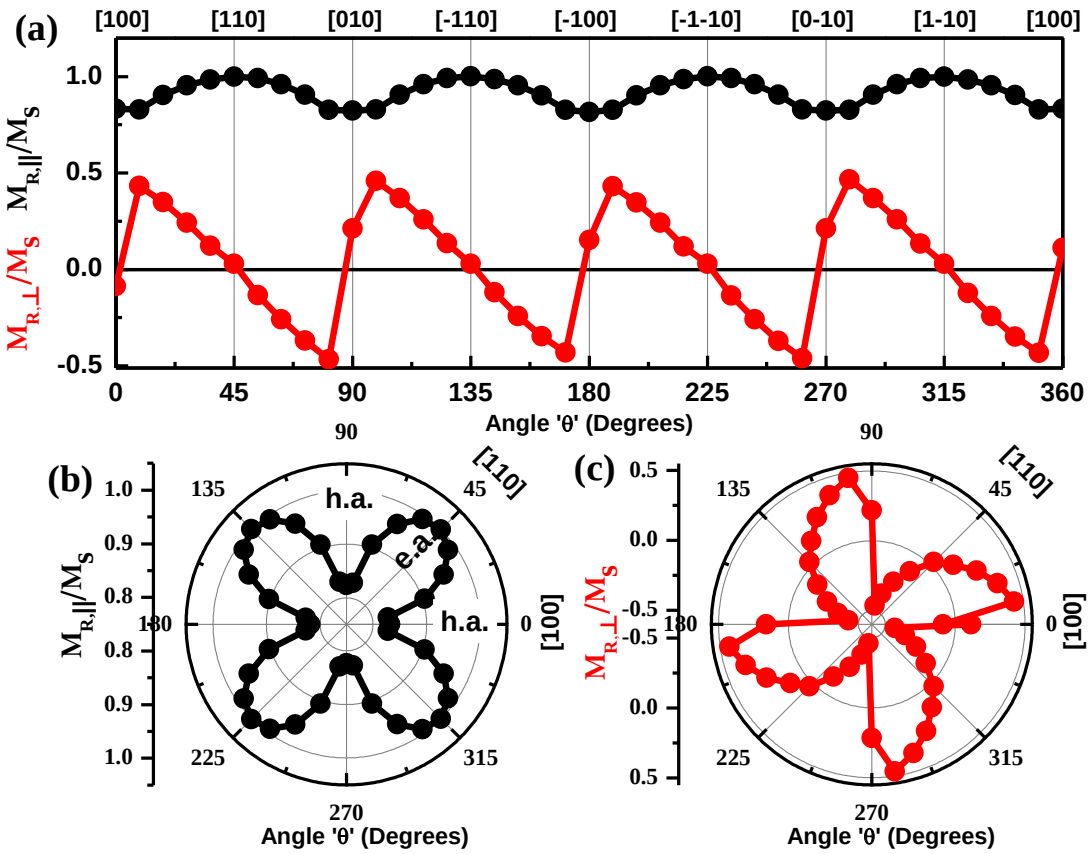

Figure 5.9: (a) RT angular evolution of the normalized remanence magnetization $M_{R,||}/M_s$ (black) and $M_{R,\perp}/M_s$ (red) plots of LSMO (001) thin film of 50 nm thick grown on STO buffered MgO (001) substrate. (b, c) The corresponding polar plots of $M_{R,||}/M_s$, and $M_{R,\perp}/M_s$ respectively.

5.2.1.3 Angular dependent critical fields @ 300 K

Figure 5.10 shows the angular dependence of the critical fields such as coercivity (H_C) and switching fields (H_S) calculated from $M_{||}(H)$ and $M_{\perp}(H)$ loops respectively at zero crossing magnetization. For instance, in a pure biaxial anisotropy system, both the critical fields (H_C and H_S) also shows a four-fold symmetry with 90° periodicities. The coercive field 'H_c' is higher at easy axes and reduces as it approaches towards hard axes as shown in Figure 5.10 (a). As discussed in the section 5.2.1.1, there exists only one irreversible transition at easy axes and two irreversible transitions at and around hard axes. Therefore, the critical fields (H_C and H_S) coincide at and around easy axes are corresponds to single irreversible transition leading to 180° domain walls shaded in the grey regions. However, as we apply the field near to hard axes (shaded with the white region), H_S exhibit higher values around hard axes and reaches the maximum at the hard axes. Here, the magnetization reversal takes place with two irreversible transitions and probably related to nucleation and propagation of two consecutive 90° domain walls. These higher values for H_S at hard axes are also observed from the $M_{\perp}(H)$ loops in Figure 5.8.

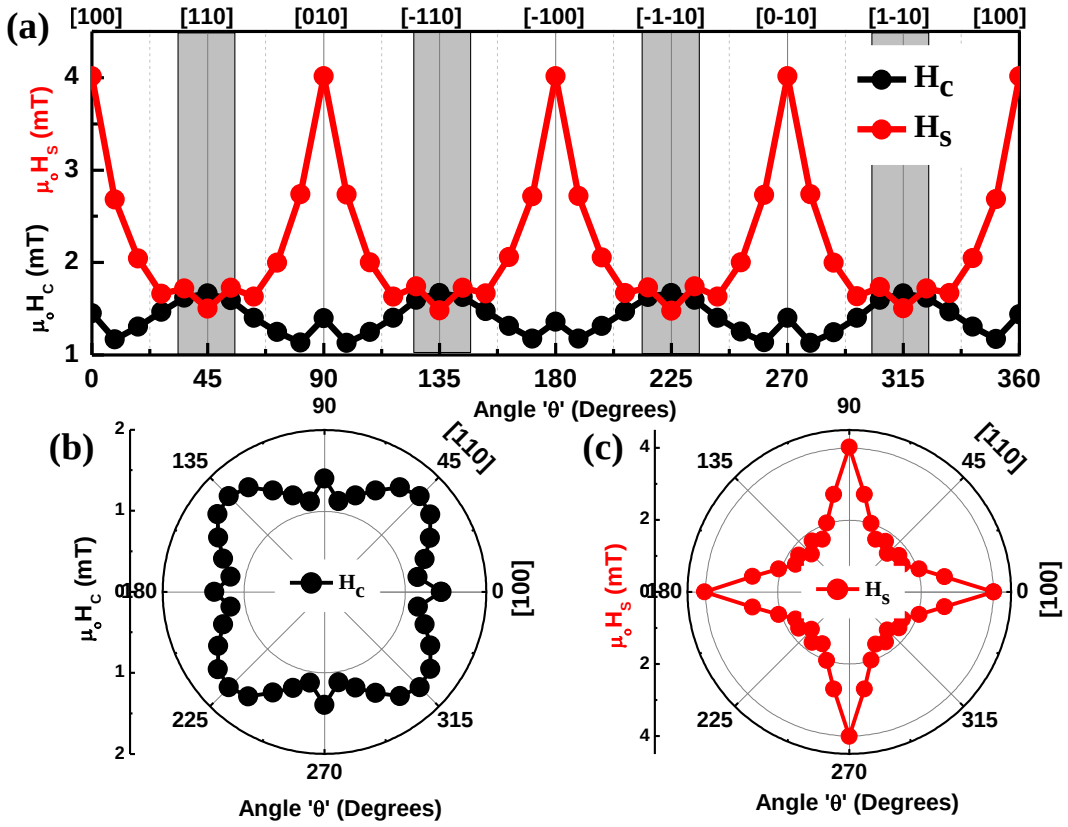

Figure 5.10: (a) RT angular evolution of the critical fields (coercivity 'H_C' and switching 'H_S') as a function of the applied field angle of the LSMO film of 50 nm thick grown on STO buffered MgO (001) substrate shows 90° periodicity, a pure bi-axial anisotropy. The grey shaded regions indicate the system exhibits only one irreversible transition, whereas, in the white regions, the system exhibits two consecutive irreversible transitions. (b, c) Polar plots representation of H_C and H_S that shows four symmetrical lobes and asteroid shape.

Discussion:

Structural properties are discussed briefly in the section 4.3.3 and here we will present them in detail. In order to determine the in-plane epitaxial relationship between the LSMO film and MgO (001) substrate, *Φ*-scans were performed along the (0-24) for MgO and (0-13) for LSMO as shown in Figure 5.11 (a). Four peaks in the *Φ*-scans with a separation of 90 degrees are observed for both MgO substrate and LSMO film which is expected to be cube-on-cube epitaxy i.e. [100] plane of the film is parallel to [100] plane of the substrate. Figure 5.11(c) shows the low-resolution asymmetrical reciprocal space mapping (RSM) scans of (0-13) plane of LSMO film and (0-24) plane of MgO substrate. RSM scans reveals that the film is fully relaxed. On the other hand, high-resolution RSM scan (Figure 5.11(d)) shows a double peak in the LSMO film, thus confirming the structure could be orthorhombic. And omega scans measured along the (002) peak of LSMO film (Figure 5.11(b)) shows double peak that can be qualitatively deduced by multi-peak fit. The distance between the two peaks i.e. 0.32° give us the misoreintation of the two adjacent planes as shown schematically in the inset of Figure 5.11(b). Hence, we ascribe the LSMO film structure to distorted orthorhombic (monoclinic). The insertion of STO buffer layer on MgO substrate reduced the distortion of

LSMO cell from 0.66° [138] to 0.32°. Hence, STO buffer layer improved the quality of LSMO film by accommodating all the structural defects in it.

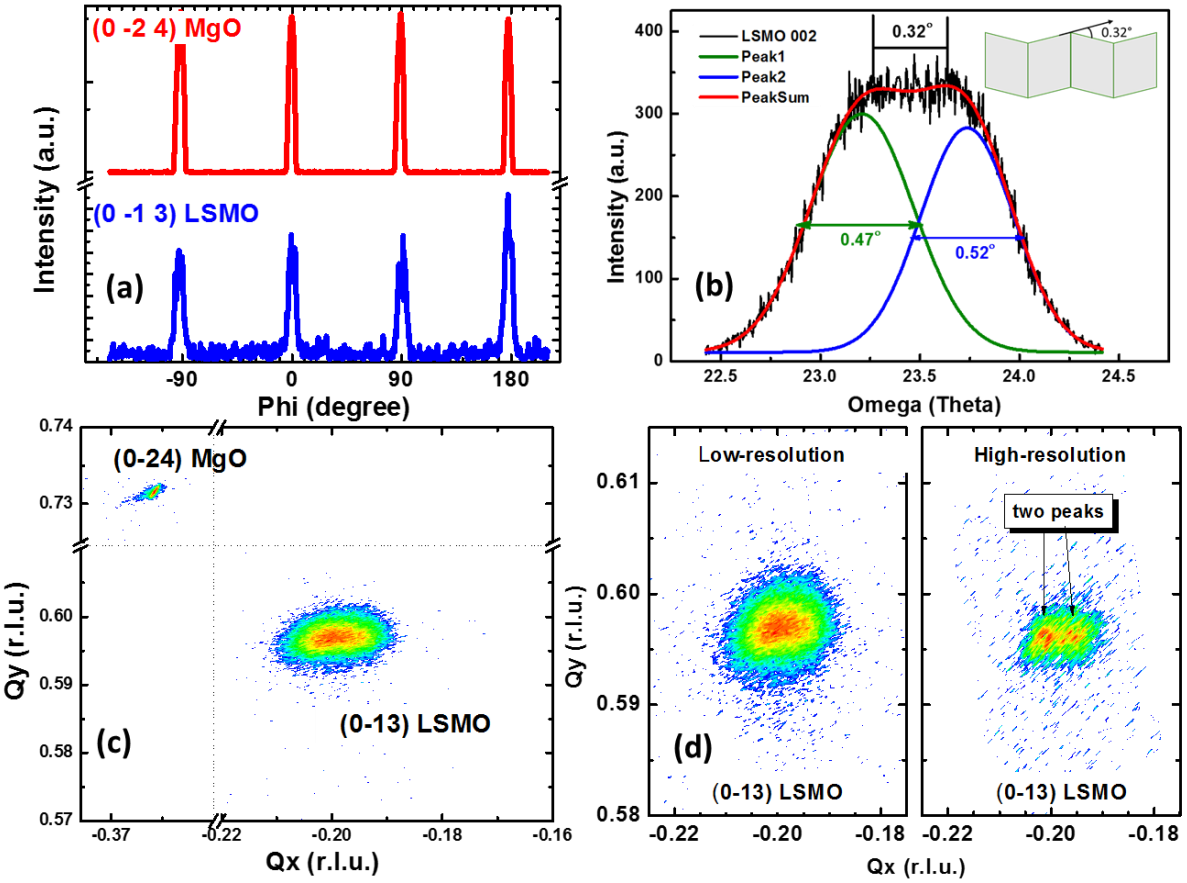

Figure 5.11: (a) Asymmetrical Phi scans of LSMO (001) film and MgO (001) substrate shows cube-on-cube epitaxy. (b)Omega scans around LSMO (002) shows the splitting of the LSMO peak is due to the misorientation of the planes. (c) RSM of (0-13) LSMO film on (0-24) MgO substrate shows that the film is fully relaxed, and (d) Comparison between low and high resolution (HR) (0-13) LSMO peaks that clearly shows a split in LSMO film peak in HR mode.

Since the LSMO film is fully relaxed, the magnetic properties of the film should also behave similarly to the bulk ones. Therefore, as described in the section 3.1.3, the easy axes magnetization direction in the LSMO film should also preferably align towards 45° <110> crystallographic axes ascribing it to magnetocrystalline nature of LSMO, leading to a pure biaxial anisotropy.

5.2.1.4 Angular dependent M (H) loops around characteristic axes @ 40 K

Figure 5.12 shows the normalized MOKE[x] hysteresis loops measured at different in-plane directions at 40 K, with the applied magnetic field at $\theta = 0°$ is aligned parallel to [100] crystallographic axis. As described in the previous section (5.2.1.1), here too we observed similar features with easy and hard axes present at 45° <110> and 90° <100> respectively.

[x] This low-temperature MOKE measurement was performed at CNR-IOM, Trieste, Italy. With this set-up, we don't have the possibility to acquire two *in-plane* components. Therefore, we measured only one *in-plane* component i.e., $M_{||}(H)$ (parallel to the applied magnetic field direction).

The coercive fields measured at easy and hard axes are 11.75 mT and 8.75 mT, respectively. Near to hard axes i.e., at $\theta = 70°$ and 80°, two irreversible transitions are observed owing to nucleation and propagation of two consecutive 90° domain walls. Therefore, as the temperature decreases from 300 K to 40 K, the strength of biaxial anisotropy increases. It is purely due to the magnetocrystalline anisotropy of LSMO, which is dominant at low temperatures, which was already seen in section 5.1.1.4.

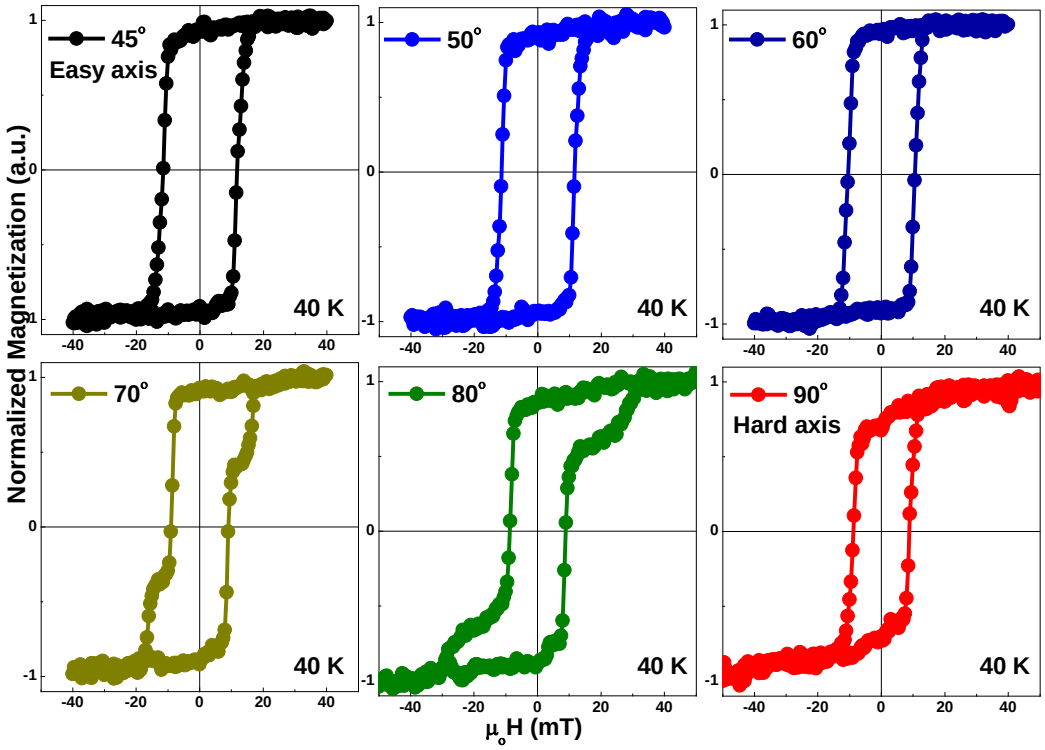

Figure 5.12: Normalized MOKE hysteresis loops of 50 nm LSMO film grown onto STO buffered MgO (001) substrate with the magnetic field applied along different *in-plane* directions around the first half quadrant measured at 40 K.

Temperature-dependent coercive fields measured at easy and hard axes at 300 and 40 K are shown in Figure 5.13. As temperature decreases, a tremendous increase in the coercive field is observed. There is an increase in coercive field of about 600% at both easy and hard axes respectively.

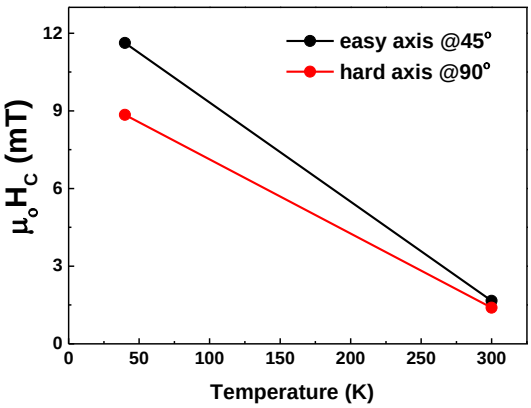

Figure 5.13: Temperature-dependent coercive fields of 50 nm LSMO film measured at the easy and hard axis, respectively.

5.2.1.5 Angular dependence remanence and critical fields @ 40 K

Figure 5.14 shows the angular dependency behavior of remanence and coercivity measured at 40 K. As expected, both remanence and coercivity show repeated features with 90° periodicity i.e., a pure biaxial anisotropy system. This is the similar behavior which we also observed in the angular dependent remanence polar plot at 20 K on LSMO films on STO (001) substrate as shown in Figure 5.6(d).

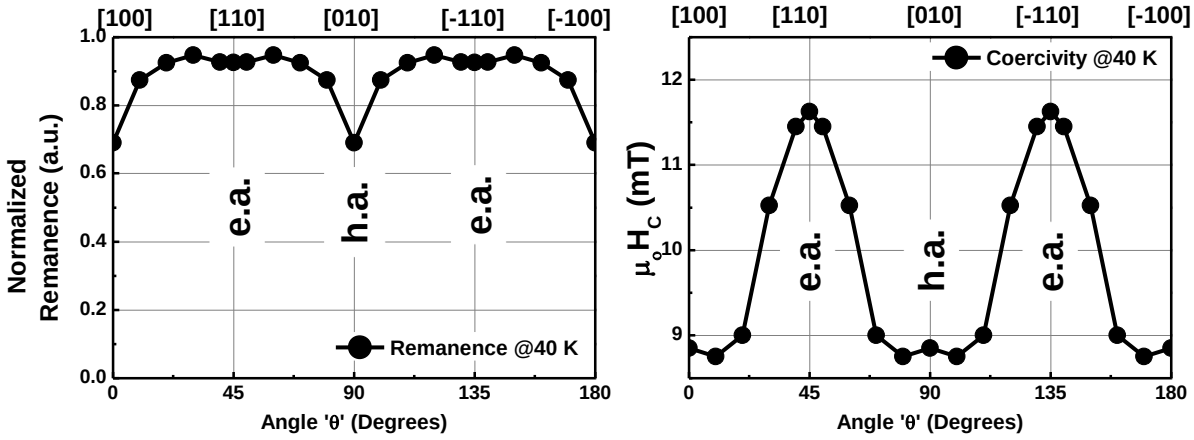

Figure 5.14: Angular dependence 2D plots of (top) remanence and (bottom) coercive fields for the 50 nm LSMO film measured at 40 K with 90° periodicity.

5.2.2 Summary

In conclusion, we have successfully fabricated LSMO thin films on STO buffered MgO (001) substrate by PLD and studied room temperature and low temperature *in-plane* magnetic anisotropy properties. The system exhibits pure bi-axial anisotropy at any given temperature. As temperature decreases, the strength of the bi-axial anisotropy increases. The easy and hard axes directions of the film are always aligned towards <110> and <100> crystallographic directions. The origin of magnetic anisotropy is purely due to magnetocrystalline anisotropy, which is an intrinsic property of LSMO. Unlike the LSMO thin films grown on STO (001) substrate that shows anomalies in magnetic anisotropy symmetry; films that are grown onto STO buffered MgO (001) substrate shows competitive electrical and magnetic properties and also displays well-defined biaxial anisotropy, that can be used in spintronics devices. However, it is worth to notice an important drawback of such structures is that there is a decrease in Curie temperature and magnetization signal measured at 300 K becomes very weak as the thickness of the film is lowered.

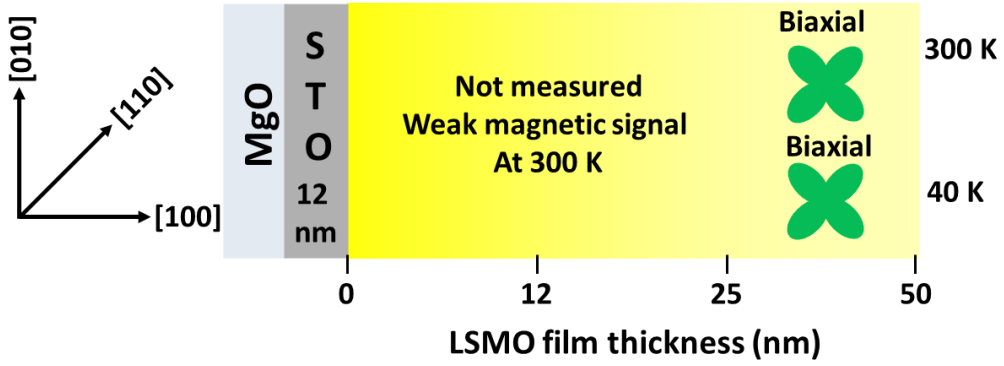

6 Magnetic anisotropy of LSMO films under compressive strain

As previously discussed in the sections 3.1.4.2 and 3.1.4.3, the magnetization in epitaxial LSMO thin films grown under compressive strain would tend to lie in the plane of the film. However, depending on the underlying substrate, structure, strain, thickness, temperature etc., the preferential magnetization aligns to its lowest possible energy i.e., easy axis (e.a.). In the following sections, you will get a glimpse of the magnetic anisotropies of LSMO thin films of different thicknesses grown onto orthorhombic NGO (110) and cubic LSAT (001) substrates measured at room temperature and low temperatures. The compressive strain in LSMO thin films increases with increase in the lattice mismatch. Therefore, LSMO films grown on LAO (001) substrates with -1.36 % lattice mismatch are not of very high quality. Hence, we didn't study magnetic anisotropy of LSMO films grown on LAO (001) substrates.

6.1 LSMO on NGO (110) by PLD and MBE

LSMO by PLD:

LSMO thin films of thicknesses (50, 25 and 12 nm) epitaxially grown onto orthorhombic NGO (110) substrate by PLD. Due to lattice mismatch, LSMO film undergoes anisotropic *in-plane* biaxial compressive strain. The detailed structural, electrical, morphological properties of LSMO thin films grown onto NGO (110) substrates has been discussed in the section 4.4.2. Here, I will present in-plane v-MOKE magnetometry measurements that have been performed in all the thickness of the film at room temperature

LSMO by MBE:

LSMO film of thickness 125 uc (50 nm) epitaxially grown onto NGO $(110)_o$ substrate by MBE technique[xi]. Figure 6.1 shows the RHEED patterns of NGO substrate and LSMO film. The streaks in the image are corresponding to (00) and (01) planes. The half order reflections indicated by white arrows are observed in the NGO substrate and are due to orthorhombic reflections. By comparing the RHEED patterns before and after deposition, we can observe that the half order reflections intensity present in the orthorhombic NGO substrate has been faded away with the cube-on-cube stacking of LSMO film. Hence, it is confirmed that the NGO $(110)_o$ substrate orientation results in a $(001)_{pc}$ oriented LSMO film due to the "cube-on-cube" stacking. The in-plane sides of the LSMO $(001)_{pc}$ are aligned along $[1\bar{1}0]_o$ and $[001]_o$ lattice directions of the NGO substrate.

[xi] MBE technique was used at CNR-IOM, Trieste, Italy. The detailed experimental process will be presented in the next chapter.

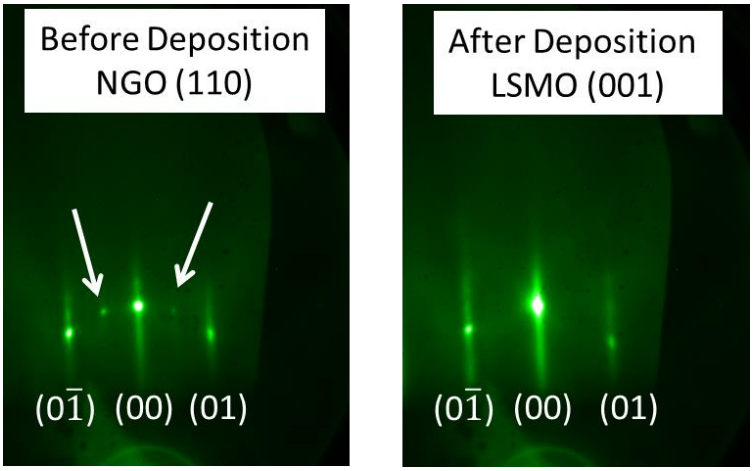

Figure 6.1: *In-situ* RHEED patterns of (left) $NdGaO_3$ (110) substrate and (right) 125 uc of LSMO film. The observed half orders indicated by the white arrows in the left image represent the orthorhombic reflections.

6.1.1 Magnetic characterization of PLD grown films

In order to probe the thickness and angular dependent magnetic properties of LSMO thin films epitaxially grown onto NGO (110), v-MOKE is used by operating in the longitudinal mode. All the measurements are performed by rotating the sample in the film plane for about 360 degrees. Hysteresis loops were taken at every 4.5° while keeping the applied external magnetic field (H) direction constant. Angle 'θ' is defined as the angle between the applied external magnetic field and crystallographic direction of the sample. Therefore, $\theta = 0°$ is defined as when the external field is aligned parallel to the $[1\bar{1}0]$ crystal direction of NGO (110) substrate.

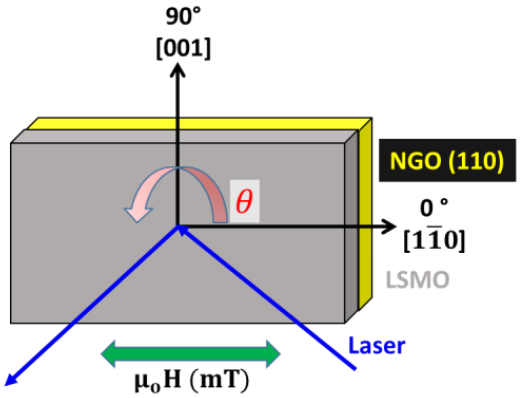

Figure 6.2: Schematic of the sample mounted on the goniometer in the v-MOKE set-up in the longitudinal mode. Here, the angle 'θ' indicates the direction of the rotation of the sample. The applied field direction is also presented. At θ=0°, the applied field is aligned parallel to [1$\bar{1}$0] crystallographic axis.

6.1.1.1 Angular dependent M (H) loops around characteristic axes for 12 nm

Figure 6.3 shows the normalized hysteresis loops of 12 nm LSMO film measured at and around characteristic axes, respectively. At $\theta = 45°$, the parallel $M_{||}$ hysteresis loops (black) present a perfect square loop while the transversal $M_{\perp}$ component shows negligible signal. As the applied field decreases from the positive to zero, there is no much change in

the remanent magnetization of $M_{||}$ component i.e., $M_{R,||} = M_S$ at $H = 0$. Further decrease in the field, a sharp irreversible transition has occurred from $+M_S$ to $-M_S$ at 0.23 mT. The backward hysteresis loop behaves in similar fashion with the increase in the applied external magnetic field. Therefore, the magnetization state is always aligned to the field direction. As a result, the transversal component $M_\perp$ is zero. This is expected to be easy axes where the magnetization reversal occurs by nucleation and propagation of domain walls that are parallel to anisotropy axis. It is also clear from the sign change in $M_\perp(H)$ hysteresis loops at 27° compared to 63°. Similarly, when the field is applied perpendicular to easy axes, i.e., at $\theta = 135°$, we observe the $M_{||}(H)$ exhibits typical uniaxial behavior. The $M_{||}(H)$ is linear with reversible transitions and the remanence and coercive fields at $H = 0$ are $M_{R,||} = H_C = 0$ and it reaches saturation magnetization with the anisotropy field range of about 3.2 mT.

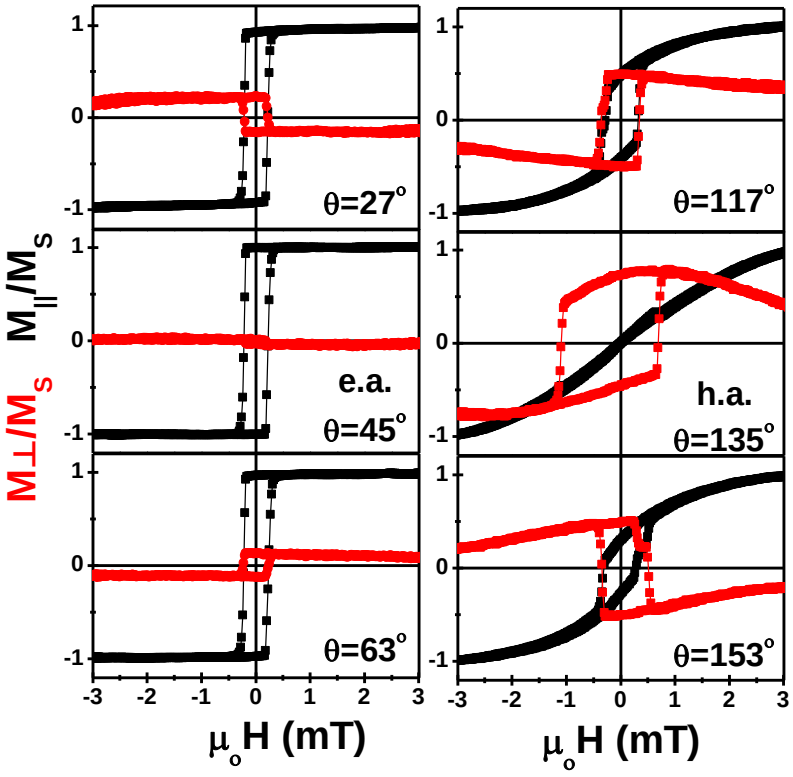

Figure 6.3: Magnetization reversal study of parallel ($M_{||}$) (black) and transverse ($M_\perp$) (red) component of 12 nm thick LSMO film grown onto NGO (110) substrate around easy (e.a.) and hard (h.a.) axes directions. The corresponding applied field angles '*θ*' are shown in the figure. Notice that the transverse component ($M_\perp$) changes it sign when the characteristic easy and hard axes are crossed.

As we decrease the field from positive to negative, the $M_{||}$ component shows linear behavior, on the contrary, the $M_\perp(H)$ component increases and reaches maximum i.e., $M_\perp \approx M_S$ at $H = 0$ indicating that at remanence, the magnetization is perpendicular to the field direction i.e., magnetization is aligned parallel to easy axes. Therefore, from the $M_\perp(H)$ component, we can observe that the spins continuously rotate away from the easy axis as a function of applied field. Furthermore, from the $M_\perp(H)$ component at $\theta = 117°$ and $\theta = 153°$ changes its sign confirming that the angle $\theta = 135°$ is a hard axis.

6.1.1.2 Angular dependent remanence and critical fields for 12 nm

As we have already discussed in the previous chapters, we can extract the remanence and critical fields from the $M(H)$ loops that are measured about 360° for every interval of 4.5° at RT. The angular dependence data has been extracted and plotted in Figure 6.4 for remanence and for the critical fields, respectively. The magnetic anisotropy symmetry can be easily recognized by the angular dependence remanence plots. The angular evolution of normalized remanence magnetization components i.e., $M_{R,||}/M_S$ and $M_{R,\perp}/M_S$ are shown in Figure 6.4(a) and Figure 6.4(b, c) in polar representation. There is a pronounced oscillation for every 180° in the remanence parallel component. The $M_{R,||}/M_S$ polar plot shows the characteristic two-lobe behavior, originated from the two-fold magnetic symmetry. Also, the sign of the remanence transversal component changes for every 90° i.e., when it crosses the characteristic easy and hard axes. All these confirm that the film exhibits pure uniaxial anisotropy.

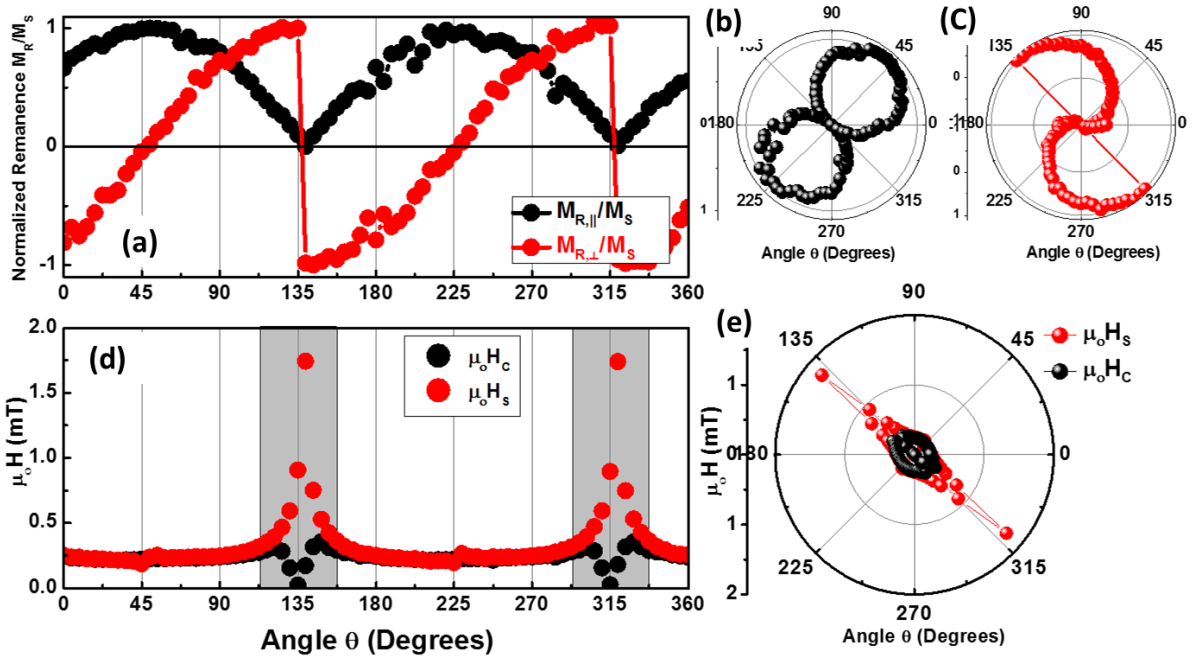

Figure 6.4: (a) RT angular dependence of normalized remanence magnetization ($M_{R,||}/M_S$ and $M_{R,\perp}/M_S$) of 12 nm thick LSMO film grown onto NGO (110) substrate. (b, c) The polar plot representation of $M_{R,||}/M_S$ and $M_{R,\perp}/M_S$. (d) Angular dependence of the coercive field μ_oH_C and switching field μ_oH_S of 12 nm thick LSMO film grown onto NGO (110) substrate. The grey shadowed regions indicate the angular range where the reversible rotation processes are the relevant mechanism during reversal. (e) The polar plots representation of μ_oH_C and μ_oH_S.

In addition, Figure 6.4 (d, e) shows the angular dependent 2D and polar plots for critical fields namely coercivity 'H_C' and switching fields 'H_S', which also shows the periodicity of 180°. Also, the coercive and switching fields have same value around the easy axes which are shaded with the white region. Whereas, near around hard axes, H_C tends towards zero and the H_S increases tremendously and reaches a maximum at hard axes, shaded in grey regions. The white areas are regions in which the magnetization reversals proceed by nucleation and propagation of magnetic domains, whereas the grey areas indicate rotative mechanisms [51].

6.1.1.3 Angular dependent magnetic properties for 25 nm

Figure 6.5 shows the summary of magnetic characterization for the 25 nm LSMO film grown onto NGO (110) substrate at RT. As discussed for the 12 nm in the previous section, the 25 nm film also shows similar uniaxial anisotropy. From the hysteresis loops, the hard and easy axes[xii] are aligned at θ = 45° and 135° that corresponds to zero and maximum remanence values. Also, the transversal component changes its sign every time it crosses each characteristic axes. The coercive fields at easy and hard axes are 0.55 mT and 0 T. Figure 6.5 (b-e) shows the polar plots of remanence and critical fields. Remanence $M_{R,||}$ and coercive field $\mu_o H_C$ displays 2-fold symmetry with 180° periodicities. Remanence $M_{R,\perp}$shows asymmetric in the shape and is due to the sign change after crossing every characteristic axes. The switching field $\mu_o H_S$ also behaves similarly to 12 nm film with the maximum value at hard axes and similar values at easy axes. Therefore, all the above-said features correspond to uniaxial anisotropy.

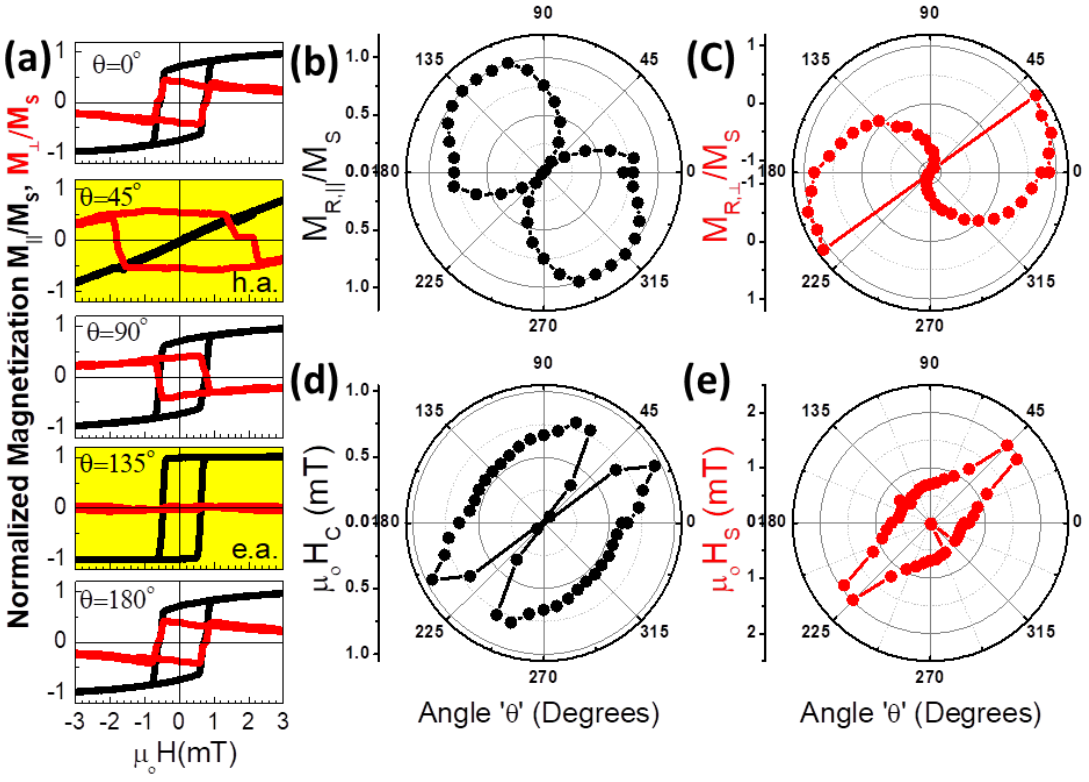

Figure 6.5: (a) RT magnetization reversal study of parallel ($M_{||}$) (black) and transverse ($M_{\perp}$) (red) component of 25 nm thick LSMO film grown onto NGO (110) substrate around easy (e.a.) and hard (h.a.) axes directions. The corresponding applied field angles '*θ*' are shown in the figure. Notice that the transverse component (M⊥) changes it sign when the characteristic easy and hard axes are crossed. (b, c) Angular dependent normalized remanence of parallel and transverse components. (d, e) Polar plot representation of angular dependent coercivity (H_C) and switching fields (H_S).

[xii] Please note that the easy and hard axes are shifted by 90° for 25 nm film compared with the 12 nm films. RSM maps are underway to confirm the in-plane directions. This can be purely due to the substrate cutting along different directions from the seller.

6.1.1.4 Discussion

As we know that NGO (110) is orthorhombic, LSMO film when grown onto NGO substrate experiences different in-plane compressive strain. Due to this anisotropic strain, the strain along the axes [1$\bar{1}$0] is higher compared to the strain along the [001] axis. As a result, the spins in the LSMO film tends to align towards the higher strain direction so as to have the minimum energy. Hence, the uniaxial anisotropy in LSMO films is dominant due to strain and is often called as "*magneto-elastic*" anisotropy, which was also observed by many authors [104]–[106]. Therefore, the origin of magnetic anisotropy at room temperature is dominated by magneto-elastic anisotropy irrespective of the film thickness (12, 25 and 50 nm[xiii]) while the magnetocrystalline contribution is negligible. Nevertheless, it is always interesting to compare the results with different growth technique and also at low temperatures which we will see in the next section.

6.1.2 Magnetic characterization of MBE grown films

Magnetic anisotropy of LSMO film is measured by longitudinal MOKE at 300 and 40 K respectively. Figure 6.6(top) shows the normalized magnetization hysteresis loops of 125 uc (50 nm) LSMO film on NGO (110) substrate. The easy and hard axes are present at 0° and 90° at 300 and 40 K respectively. Figure 6.6(bottom) shows the angular dependent coercive field at 300 K and 40 K respectively displays the lowest value at 90° corresponds to hard axes.

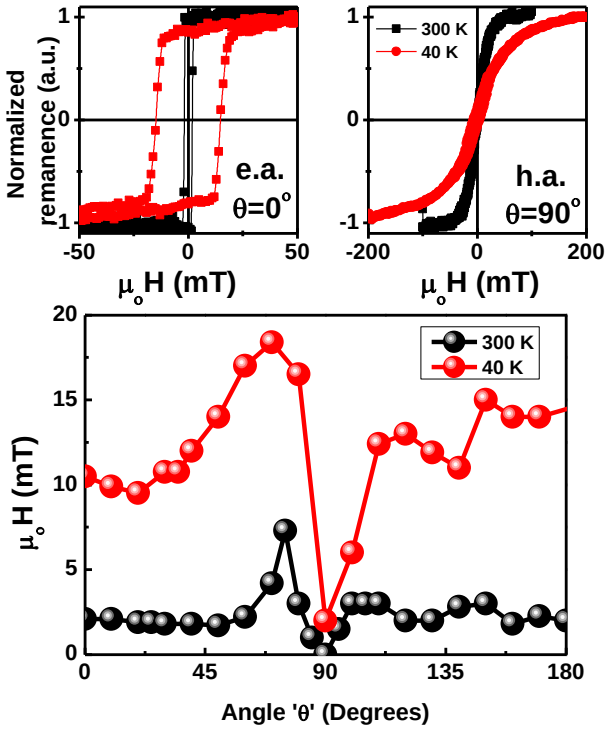

Figure 6.6: Temperature-dependent normalized hysteresis loops of 125 uc LSMO film on NGO (110) substrate at the characteristic easy and hard axes, respectively. (Bottom): Angular dependent coercive fields at 300 and 40 K respectively. Please note that the field scales are different for easy and hard axes for clarity.

[xiii] The results for 50 nm thick films are not shown here because it also exhibits uniaxial anisotropy that is similar to 12 and 25 nm.

Therefore, the film shows very strong uniaxial anisotropy at any temperature. The coercive fields at easy axes are 2 and 15 mT at 300 and 40 K respectively. As the temperature decreases, there is an increase in 650% of the coercive field at easy axes. At the hard axes, the values of remanence and coercivity are zero at 300 and 40 K. The saturating field or the anisotropy field at hard axes measured at 300 K is 60 mT and at 40 K is 220 mT. Therefore, as the temperature decreases, the strength of the uniaxial anisotropy increases. The biaxial or magnetocrystalline anisotropy of LSMO which is usually dominant at low temperatures is negligible in this case and it is dominant by magneto-elastic anisotropy.

6.1.3 Summary

In summary, we have successfully grown epitaxial LSMO thin films on NGO (110) substrate of different thickness (12, 25 and 50 nm) by PLD and 125 uc (50 nm) film by MBE technique. Angular dependent magnetic properties have been studied at room temperature on all the films and at 40 K on the film grown by MBE. All the films show strong in-plane uniaxial anisotropy with the easy axis directions aligned towards higher strain directions of the film. The easy axis directions are explained by *magneto-elastic* induced by the anisotropic in-plane strain. Therefore, LSMO films on NGO substrate may have advantages in magnetic tunnel junctions over STO substrate, as it displays strong uniaxial anisotropy at any given thickness and temperature with preferential easy axis direction.

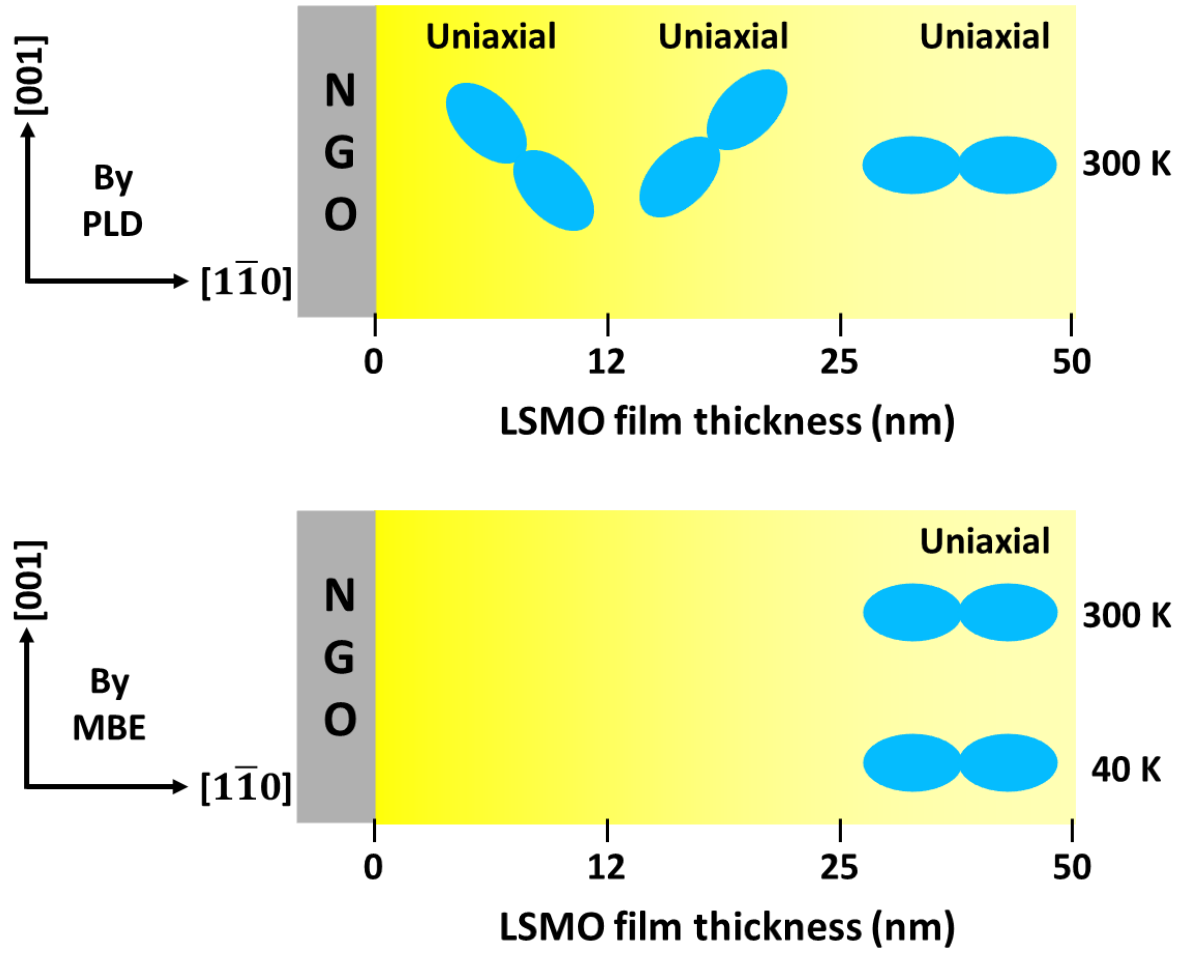

6.2 LSMO on LSAT (001) by PLD

In this section, I will present an accurate study of the magnetic anisotropy of LSMO films, with different thicknesses, deposited on an almost unexplored substrate, namely LSAT (001). The advantage of using this crystal as a substrate for the LSMO growth is its stability at high temperatures as well as its versatility for optoelectronics. While many works report on LSMO grew onto more conventional crystals such as STO, MgO, NGO or even Si-templates, a little is done on LSAT. Therefore, special interest has been taken to explore the properties from different directions.

LSMO thin films of thicknesses (50, 25 and 12 nm) were epitaxially grown onto cubic LSAT (001) substrate by PLD. Due to lattice mismatch, LSMO film undergoes an *in-plane* biaxial compressive strain ($a = b < c$, $\alpha = \beta = 90°$, $\gamma \neq 90°$). The detailed structural, electrical and magnetic properties are described in section 4.4.1. Here, I will present *in-plane* v-MOKE magnetometry measurements that have been performed in all the thickness of the film, from room temperature down to 20 K and also in-plane XRD characterization. We will also finally provide the evidence of a non-negligible perpendicular magnetic anisotropy that becomes relevant for larger thickness.

6.2.1 Magnetic characterization

In order to probe the temperature and angular dependent magnetic properties of LSMO thin films on LSAT (001), v-MOKE is used by operating in the longitudinal mode. The sample is mounted on eucentric goniometer that allows us to keep the reflection plane constant during the angular measurements as shown in Figure 6.7. All the measurements are performed by rotating the sample in the film plane for 360 degrees. Hysteresis loops were taken for every 4.5° while keeping the applied external magnetic field (H) direction constant. Angle 'θ' is defined as the angle between external magnetic field and crystallographic direction of the sample. Therefore, $\theta = 0°$ is taken when the external field is aligned parallel to the [100] in-plane crystal direction. The angular dependent magnetic anisotropy measurements are performed at temperatures 300, 170, 100 and 20 K respectively.

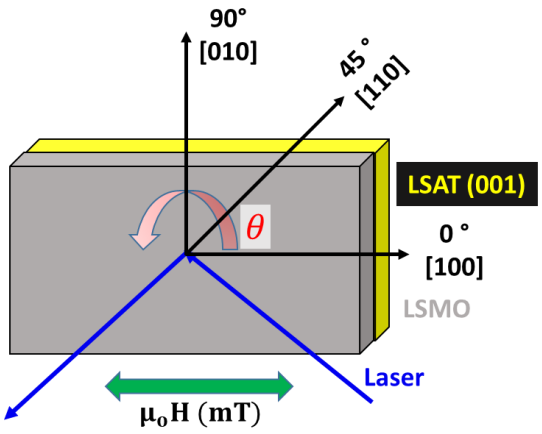

Figure 6.7: Schematic of the sample mounted on the goniometer in the v-MOKE set-up in the longitudinal mode. Here, the angle 'θ' indicates the direction of the rotation of the sample. The applied field direction is also presented. At θ=0°, the applied field is aligned parallel to [100] crystallographic axis.

6.2.2 Thickness and angular dependent magnetic properties @ 300 K

6.2.2.1 Results

The M (H) loops presented for the 50 nm thick LSMO film in Figure 6.8 (left) clearly indicates that the easy and hard axes are present at angles 0° [100] and 90° [010]. By careful inspection, we can observe that the remanence and coercive fields at hard axis are not equal to zero. Moreover, at h.a. an addition transition close to the coercive field appears. This is probably due to the complex structural distortion of the LSMO cell (this will be discussed later in the view of RSM analysis). The coercive fields at easy and hard axes are 2.88 mT and 1.7 mT respectively. Figure 6.8 (middle) panel shows the angular dependent normalized remanence ($M_{R,||}/M_S$) and coercivity ($\mu_o H_C$) of 50 nm (black) shows almost equal for all the angles except at 90° and 270°, terming it as very weak (dominant) uniaxial anisotropy. This particular anisotropy landscape of the sample reveals the existence of a complex interplay between anisotropies of different nature, as uniaxial and biaxial.

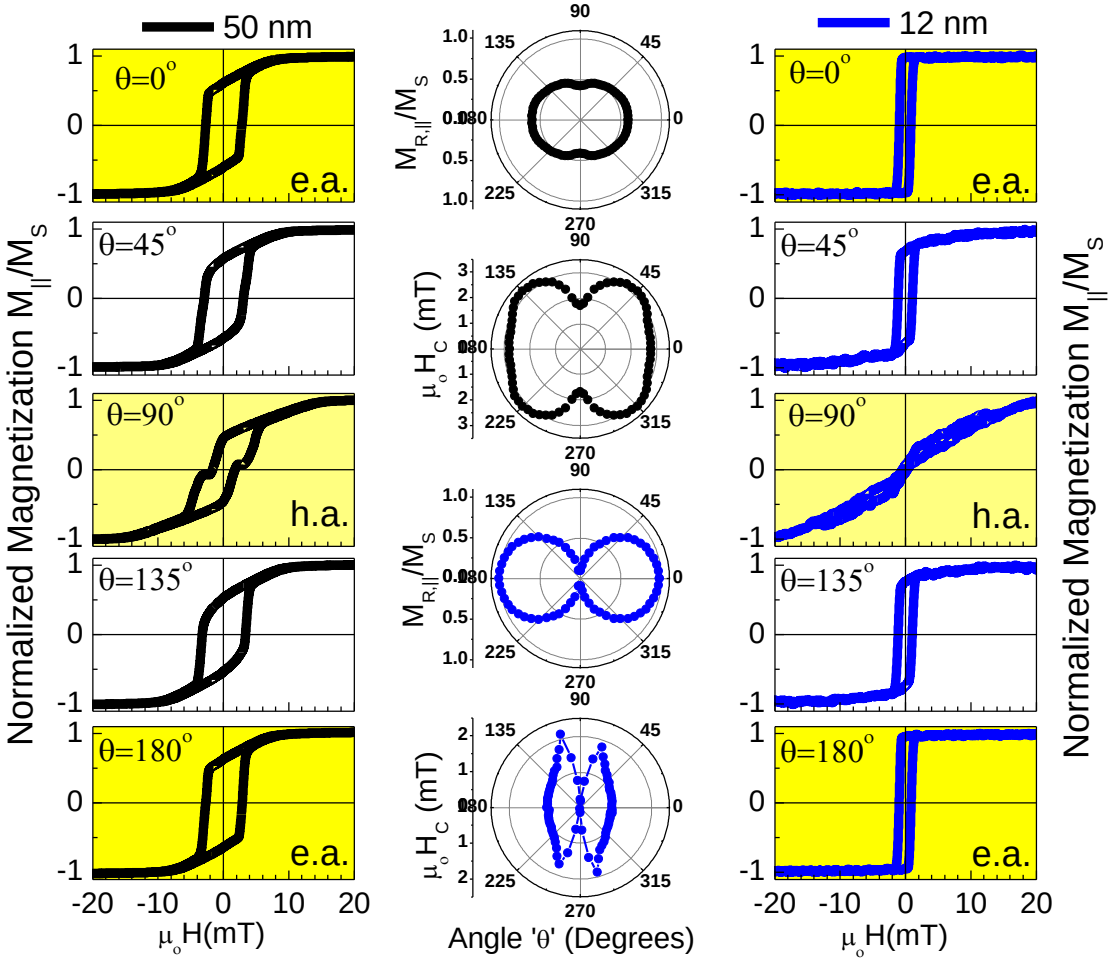

Figure 6.8: Magnetization reversal study of parallel ($M_{||}$)[xiv] component of 50 nm (Left, black) and 12 nm (Right, blue) thick LSMO films grown onto LSAT (001) substrate around easy (e.a.) and hard (h.a.) axes respectively. The corresponding applied field angles 'θ' are shown in the figure. Middle panel shows the polar plots representing angular dependent normalized remanence ($M_{R,||}/M_S$) and coercivity ($\mu_o H_C$) of 50 nm and 12 nm thick films respectively.

[xiv] For 12 nm and 50 nm films, I have shown only Parallel component and omitted transversal component for clarity to the reader.

Similarly, for the 12 nm LSMO film, the easy and hard axes are present at angles 0° [100] and 90° [010] as shown in Figure 6.8 (right). The coercive fields present at easy and hard axes are 0.88 mT and 0.1 mT respectively. Figure 6.8 (middle) panel shows the angular dependent normalized remanence ($M_{R,||}/M_S$) and coercivity ($\mu_o H_C$) of 12 nm (blue) shows two symmetrical lobes with 180° periodicity. In addition, remanence and coercivity at hard axis is almost equal to 'zero', indicating a stronger uniaxial anisotropy system.

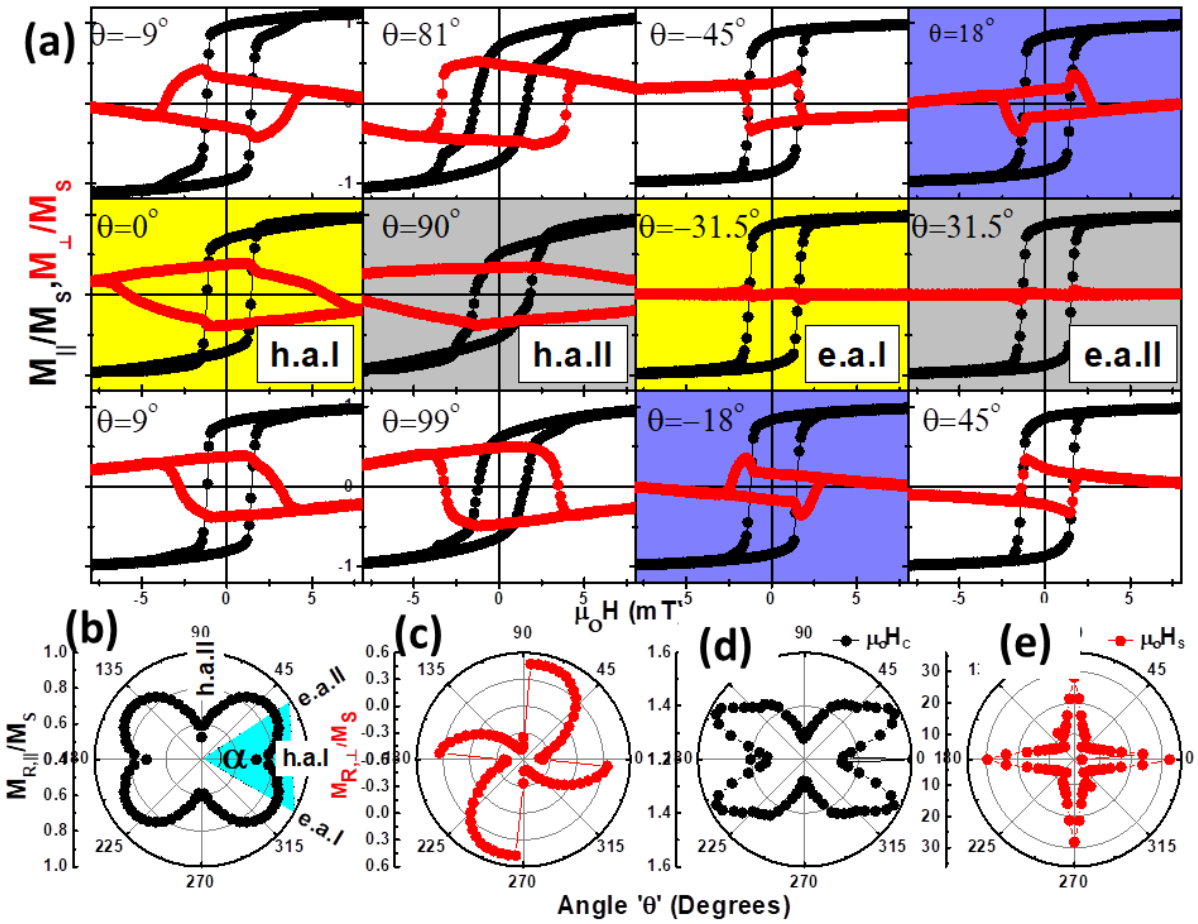

Figure 6.9: Magnetization reversal study of parallel ($M_{||}$) (black) and transverse ($M_{\perp}$) (red) component of 25 nm thick LSMO film grown onto LSAT (001) substrate around two easy (e.a.) and hard (h.a.) axes repectively. The corresponding applied field angles 'θ' are shown in the figure. Notice that the transverse component ($M_{\perp}$) changes it sign when the characteristic easy and hard axes are crossed. In addition, the two hard axes are orthogonal to each other, whereas, the angle between two easy axes are 63°. Bottom panel: Angular dependent normalized remanence of parallel (b) and transversal (c) component. Angular dependent critical fields i.e., coercivity (d) and switching (e) fields, respectively.

Let us now consider the 25 nm thick LSMO film, which is intermediate thickness and which displays complicated anisotropy. For that particular reason, we present the two in-plane orthogonal components i.e. $M_{||}$ and $M_{\perp}$ as shown in Figure 6.9. Therefore, both easy and hard axes can be located precisely just by looking at the change of sign of the $M_{\perp}(H)$ loops when the characteristic axes are crossed. The middle graphs in Figure 6.9(a) shows that the two hard axes are orthogonal to each other with h.a.I and h.a.II are aligned along 0° [100] and 90° [010] respectively. In contrary, the e.a.I and e.a.II are present at $-31.5°$ and $+31.5°$

respectively. Therefore, the easy axes are not orthogonal to each other that are also found in other epitaxial magnetic semiconductor compounds [120], [139]. The angle 'α' between two easy axes is 63°. The behaviors of the hysteresis loops at two easy axes are alike with the coercive field is about 1.62 mT. Whereas, the behavior of the reversal is non-symmetric for positive and negative angles around the easy axes which are highlighted by violet color. At $\theta = -18°$, which is the angle present below e.a.I, the transversal component $M_{\perp}(H)$ displays two transitions, while the above shows only one transition. In addition, it is exactly opposite in the case of e.a.II with two transitions above and one below. The hysteresis loops present at two hard axes are not alike and the coercive field and remanence are higher at h.a.I compared to h.a.II. The coercive field at h.a.I and h.a.II are 1.40 mT and 1.30 mT. Again, a different magnetization reversal is observed around two hard axes. Therefore, by considering the above magnetization reversals behavior, we argue that the magnetization reversal behavior is not consistent with pure cubic system. In a cubic anisotropy system, the magnetization reversal proceeds with one (two) irreversible transition, related to nucleation and propagation of 180° (90°) domain walls, when the field is applied close to one of the two easy (hard) axes directions which were already discussed in the section5.2 for LSMO thin films grown on STO buffered MgO substrate.

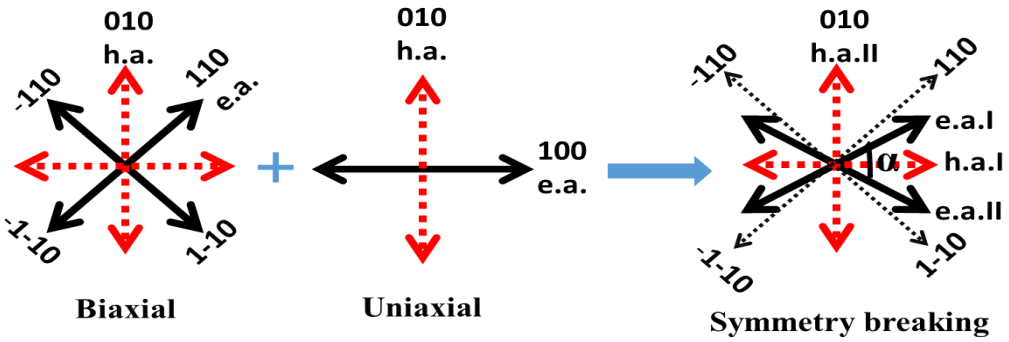

Figure 6.10: Schematic illustration showing the resultant symmetry broken system from the combination of biaxial and uniaxial anisotropy.

In order to have clear idea about the anisotropy type, angular dependent remanence ($M_{R,||}/M_S$ and $M_{R,\perp}/M_S$) and critical fields ($\mu_o H_C$ and $\mu_o H_S$) are plotted in the bottom panel of Figure 6.9. In general, for a pure cubic or biaxial anisotropy system, the periodicity between two successive easy and hard axes is 90°. The periodicity between two successive easy axes in remanence plots for 25 nm as shown in Figure 6.9(b) is not equal to 90° (shaded region) and the shape looks like butterfly structure. Similarly, remanence ($M_{R,\perp}/M_S$) polar plot in Figure 6.9(c) resembles the shape of wind-mill with unequal wings. It also confirms that there exists a mixed anisotropy system and it is due to the combination of "*bi-axial*" anisotropy with the easy axis present along 45° or [110] *plus* an additional "*uniaxial*" anisotropy with the easy axis present along 0°or [100] axes. This combination gives us the butterfly shape with two successive easy axes gets closer to [100] or 0°. Figure 6.9 (d, e) shows the angular dependence coercivity ($\mu_o H_C$) switching fields ($\mu_o H_S$). The coercive field 'H_C' presents the maximum value at the e.a. directions i.e., at ±31.5° and starts to decrease

slowly until it reaches its minimum value at the h.a direction i.e., at 0° and 90°. In contrast, switching field 'H_S' presents larger values as approaching to the h.a. direction. As reported in ref. [120], depending on the strength of the "uniaxial" anisotropy, the angle 'α' can be varied. The angle 'α' measured between e.a.I and e.a.II is 63°. Therefore, the anisotropy ratio can be calculated between uniaxial 'K_u' and biaxial 'K_b' term as in eq (4.5)

$$\alpha = cos^{-1}(K_u/K_b) \tag{4.5}$$

$$K_u/K_b = cos\,63^o = 0.454 \tag{4.6}$$

Where, α is the angle between easy axes I and II and K_u and K_b represents uniaxial and biaxial anisotropy contributions. These types of systems are often termed as symmetry broken systems where $\alpha \neq 90°$ as shown in Figure 6.10.

Depending on the relative anisotropy strengths, it can be divided into 3 cases.

i. For $K_u = K_b$, α = 0° or ±180° i.e., a pure uniaxial anisotropy with 180° periodicity
ii. For $K_u = 0$, α = 90° i.e., a pure bi-axial system with 90° periodicity
iii. For $|K_b| > |K_u| > 0$ i.e., a symmetry broken system (hard axes are orthogonal, easy axes 0° < θ < 90°)

6.2.2.2 Discussion

Structural properties are discussed briefly in the section 4.4.1 and here we will present them in detail. In order to understand the *in-plane* strain relaxation mechanism in the LSMO thin films, symmetric and asymmetric RSM scans were performed on the samples as shown in Figure 6.11.

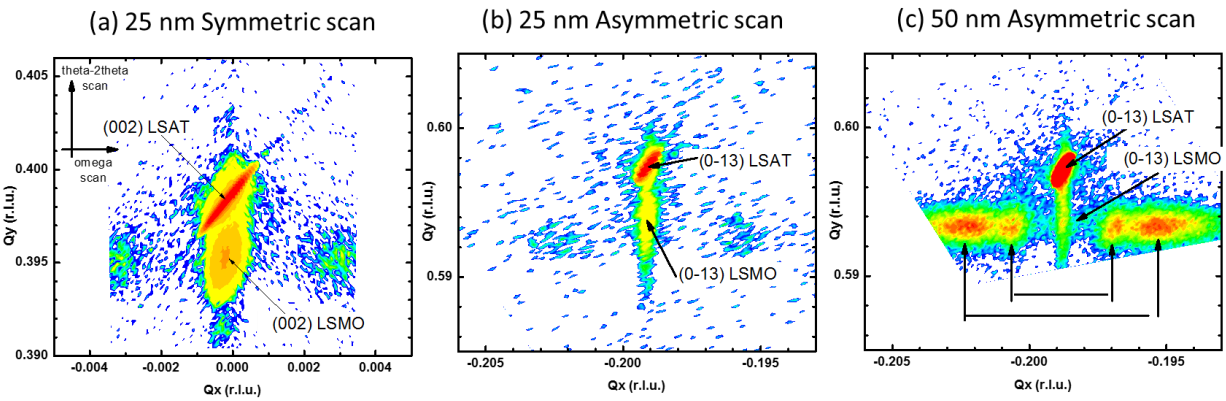

Figure 6.11: (a) Symmetric reciprocal space mapping of (002) reflection for 25 nm film. Asymmetric reciprocal space mapping of (0-13) reflection for (b) 25 nm and (c) 50 nm LSMO film grown on LSAT (001) substrate, respectively.

Symmetric RSM scans taken around the (002) reflection for 25 nm film (Figure 6.11 (a)) shows that the LSAT (002) and LSMO (002) peaks along the Q_X are vertically aligned.

Asymmetric scans around (0-13) reflection for 25 and 50 nm thick LSMO films[xv] are shown in Figure 6.11(b and c). The LSMO and LSAT reflections in both the thicknesses are aligned vertically that tells us that the LSMO films are pseudomorphically grown onto the LSAT (001) substrate. Along with the central peak, satellite peaks are observed in the reciprocal scans for all the films. These observed satellite peaks could be due to the formation of the in-plane superlattice; could originate from another type of strain relaxation mechanism called as "shear strain" and is denoted by 'γ'. Due to the very small lattice mismatch between LSMO film and LSAT substrate (- 0.2%), the strain relaxation mechanism through the formation of dislocations will be a very expensive route. Therefore, shear strain costs less energy and more favorable in less lattice mismatched (film/substrate) systems.

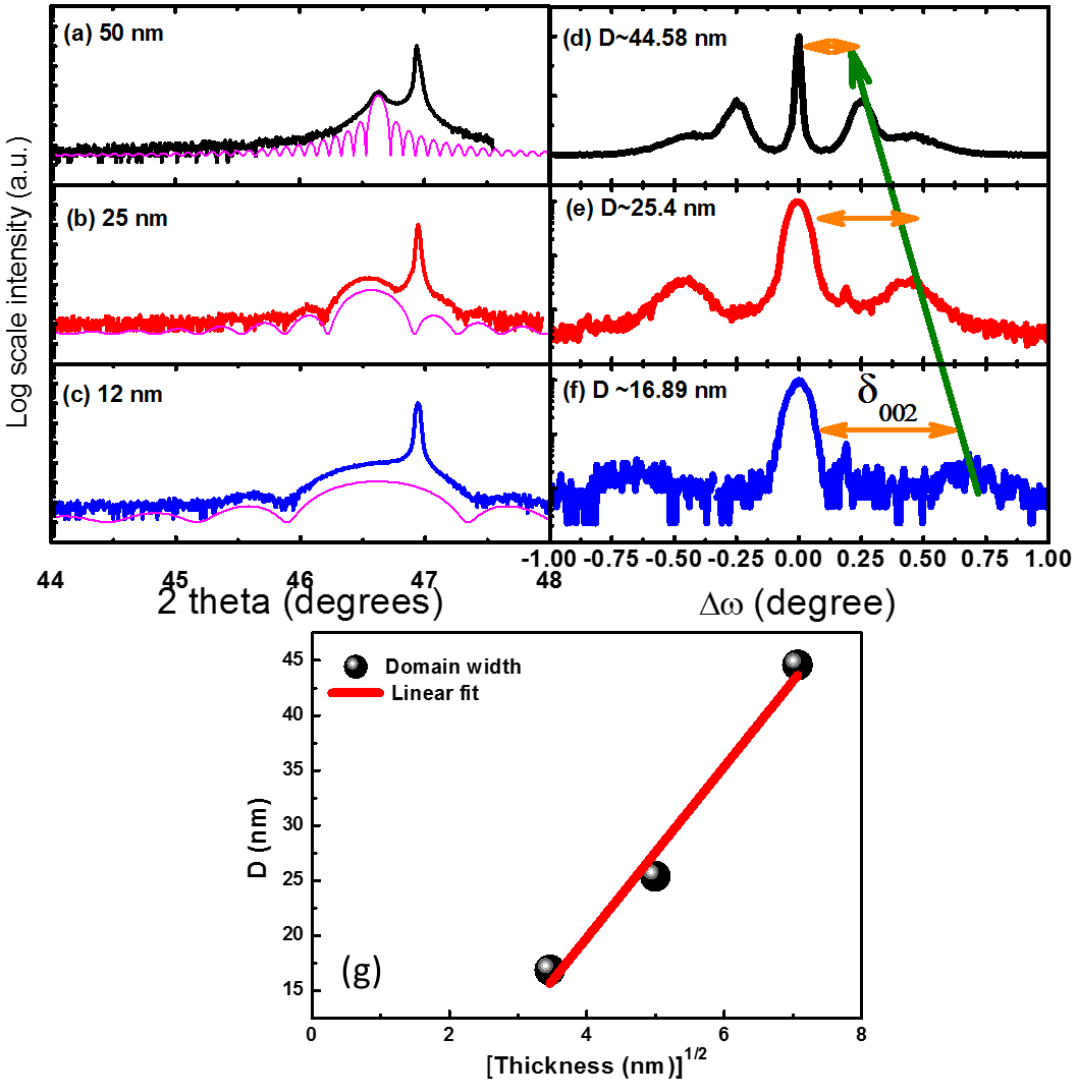

Figure 6.12: (a, b, and c) High-resolution θ-2θ XRD scans around (002) reflection, and (d, e, and f) rocking curves around LSMO (002) reflection for 50, 25 and 12 nm, respectively. (g) Domain size dependence on square root of thickness calculated from the rocking curves around (002) reflection. The red solid line indicates the linear fit.

[xv] RSM scans for 12 nm thick LSMO film also done (not shown here) and the film is fully strained too.

Figure 6.12 (a, b, and c) shows the high-resolution out-of-plane θ-2θ scans taken around the (002) reflections and (d, e, and f) shows the rocking curves about LSMO (002) reflections for the films with thicknesses 50, 25 and 12 nm respectively. Films show Laue fringes with narrow rocking curves indicating that the films are of high quality and very smooth. In Figure 6.12 (d, e, and f), it is noticeable that two satellite peaks with similar intensity appear symmetrically on both sides of the central peak. In addition, as the thickness of the film increases, the distance 'δ_{002}' between LSMO (002) central peak at '0' and the satellite peaks are decreased which is consistent with the literature [136] and marked with the arrow. These observed satellite peaks are possibly due to the lattice modulations, the formation of tilts, twin domains etc. [140]–[147] which are usually observed in the artificial superlattices. Such satellites are also observed in other systems as in LSMO/STO [142], [144] and LSMO/NGO [22] thin films.

One could also estimate the volume fraction of the nearly homogeneously strained pseudomorphic part of the film, i.e., the area under the central peak at '0' and the rhombohedral distortion of the cell due to shear strain under the satellite peaks. We can clearly see that the area under the central (satellite) peak decreases (increases) as increase in thickness of the film. Therefore, as the thickness of the film increases, the rhombohedral distortion also increases monotonically. These rhombohedral distortions can be of 4 different types depending on its body diagonal orientation ($r_1, r_2, r_3,$ and r_4) as mentioned in the reference [148]. The lattice modulation periodicity 'D' can be calculated as

$$D = \frac{\lambda}{2Q tan\delta_{002}}$$

Whereas $Q = \sin\theta = \frac{n\lambda}{2d}$; 'λ' is the wavelength of the x-ray source (0.15405 nm), 'd' is the out-of-plane lattice parameter, 'n' is the diffraction order and 'δ_{002}' is the distance between the central peak at '0' and 1st order satellite peaks in rocking curves. The calculated periodicities 'D' for 50, 25 and 12 nm LSMO film are 44.58, 25.4 and 16.89 nm, respectively. The red line in the Figure 6.12(g) is the liner fit indicating that the lattice modulation periodicity increases as the square root of the film thickness 't' [129]. This behavior is consistent with predictions from thermodynamic modeling of ferroelastic domains in epitaxial systems i.e., $D = (kD_{\text{ך}}t)^{1/2}$ where k is the numerical constant and $D_{\text{ך}}$ is the elastic length scale parameter [142]. By considering the above-mentioned structural properties, the uniaxial anisotropy observed at 12 nm could be related to these lattice modulations.

6.2.2.3 Summary

To conclude, the magnetic anisotropy of LSMO films at room temperature can be defined as thickness dependent. As thickness increases from 12, 25 to 50 nm, the magnetic anisotropy symmetry landscape changes from almost pure uniaxial to symmetry breaking system to weak uniaxial anisotropy. At this moment, we can vaguely consider that the uniaxial contribution in 12 and 50 nm films are due to steps, lattice modulations, octahedral rotations and orthorhombicity of LSMO crystal structure. Whereas, in the case of 25 nm film, the

mixed anisotropy can be due to magnetocrystalline or cubic crystal symmetry along with additional uniaxial contributing either from steps or orthorhombic structure. The exact origin of magnetic anisotropy is still unclear at this moment. However, in the light of recent RSM measurements, we can at least speculate on it. The X-ray structural analysis in face provided evidence of relevant rhombohedral distortions that produce structural twined domains on all the sample thickness. These distortions arise from the shear strain in the film and ultimately give rise to a complex lattice modulation in the film. In particular, we can envisage in-plane rotation and distortion of the LSMO cell which makes the symmetry breaking more complex. In addition, as pointed before, because of the compressive strain, a non-negligible spin reorientation from in-plane to out-of-plane magnetic anisotropy also has to be taken into account. In such complex scenario, we considered, therefore, temperature dependent magnetic anisotropy studies crucial for understanding the origin of thickness dependent magnetic anisotropy, which is present in next section.

6.2.3 Temperature-dependent magnetic properties

The angular dependent magnetic measurements on all the films are performed at temperatures 300, 170, 100 and 20 K respectively. The temperatures were carefully chosen by considering the structural phase transitions of LSAT (001) substrate from cubic at room temperature to either tetragonal (14/mcm) or orthogonal (Imma) symmetry at below transition temperature 'T_s'=150K. Figure 6.13 shows the temperature-dependent hysteresis loops measured along [100] and [010] for 12, and 50 nm, whereas, for the 25 nm[xvi] film, hysteresis loops are measured along [110] and [100] that corresponds to easy and hard axes, respectively. As the temperature decreases, the coercive field increases monotonically for all the films. In all the films, the anisotropy strength increases as a decrease in temperature.

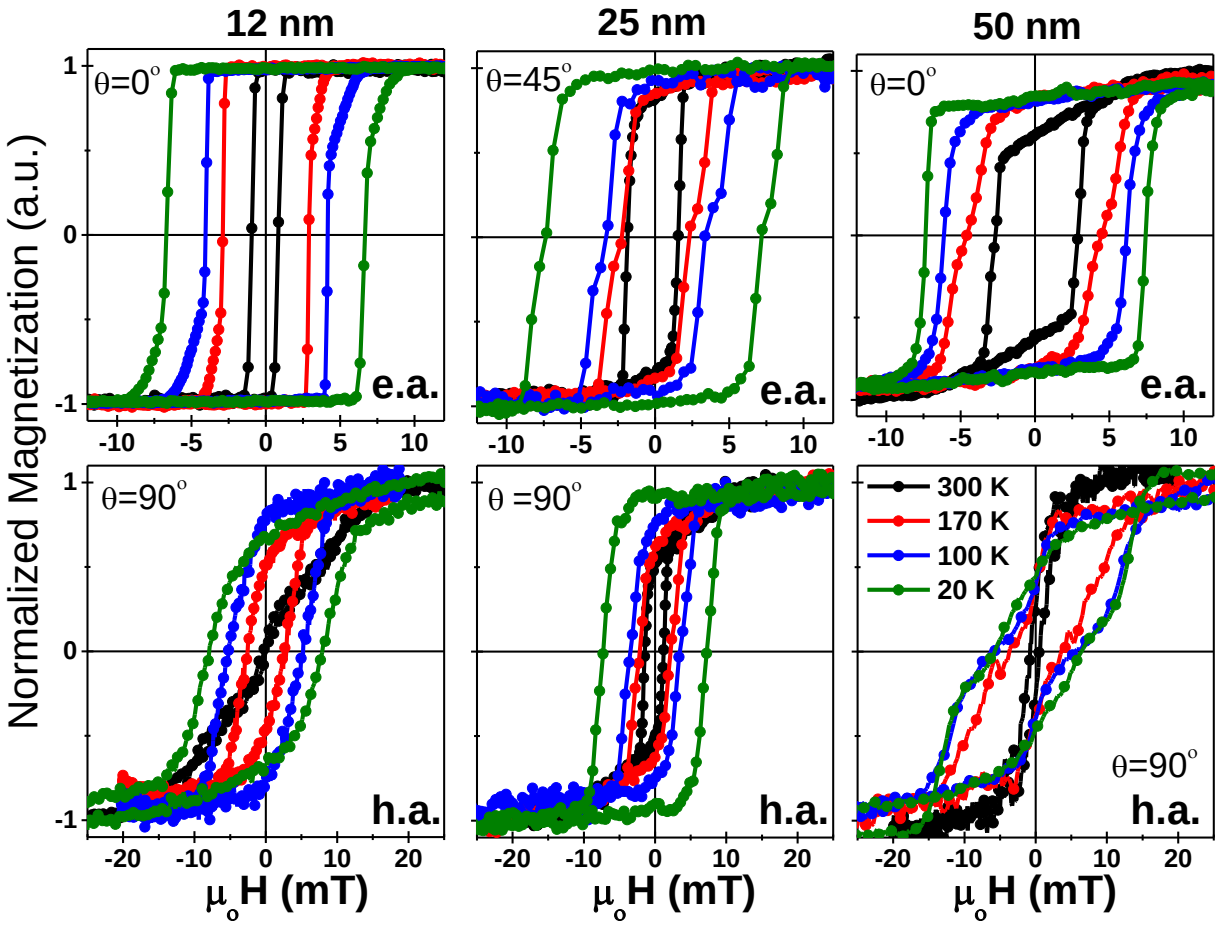

Figure 6.13: Temperature-dependent hysteresis loops at easy and hard axes for the 12 nm (left), 25 nm (middle) and 50 nm (right) respectively. Note that the field scales are different for easy and hard axes for clarity.

In order to understand the magnetic anisotropy behavior as the function of temperature, angular dependent remanence polar plots are depicted in Figure 6.14. For the 12 nm (Figure 6.14 left panel), as the temperature decreases from 300 to 20 K, uniaxial anisotropy is dominant with two symmetrical lobes. But, the remanence present at hard axes (90°) slightly

[xvi] For 25 nm thick film, please note that the angle θ=45° is not an easy axis at 300K due to symmetry broken system. However, for the other temperatures, θ=45° is an easy axes.

increases and it is also being observed with the opening of the loop as a decrease in temperature, revealing a weaker uniaxial anisotropy.

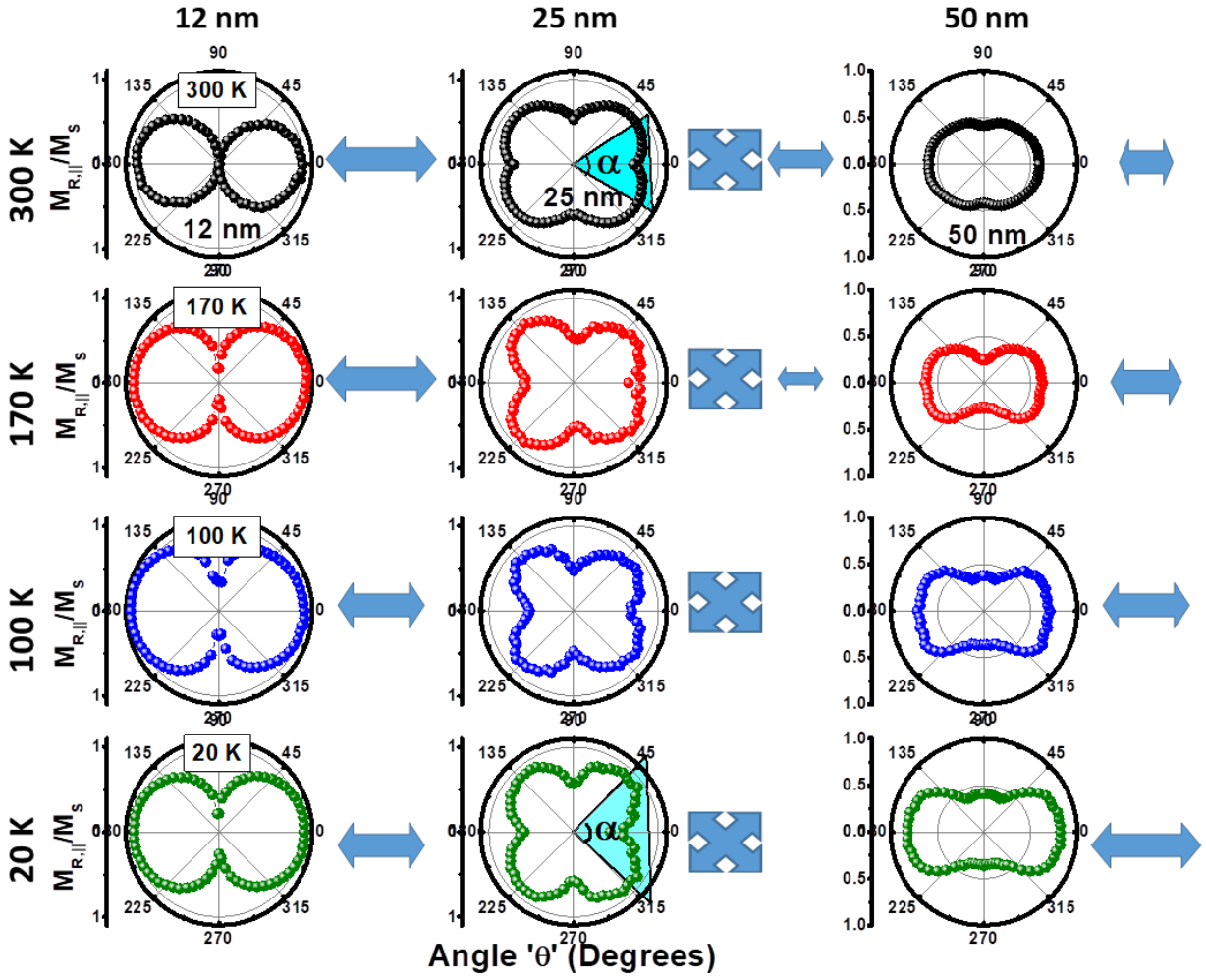

Figure 6.14: Symmetry of magnetic anisotropy as a function of temperature. The polar plots representation of normalized remanence for (left) 12 nm, (middle) 25 nm and (right) 50 nm films measured at 300, 170, 100 and 20 K respectively.

In the case of 25 nm (Figure 6.14 middle panel), as the temperature decreases from 300 to 20 K, the symmetry broken system has been changed into pure cubic or four-fold symmetry. It is also observed with the shift in highest remanence value from 31.5° to 45° which is being highlighted. Therefore, the angle 'α' between two easy axes has been increased from 63° to 90° with a decrease in temperature. For the 50 nm film (Figure 6.14 right panel), the uniaxial anisotropy remains and its strength increases as decreases in temperature. In the latter case, the additional biaxial anisotropies related to the lattice modulations may justify the complex symmetry landscape.

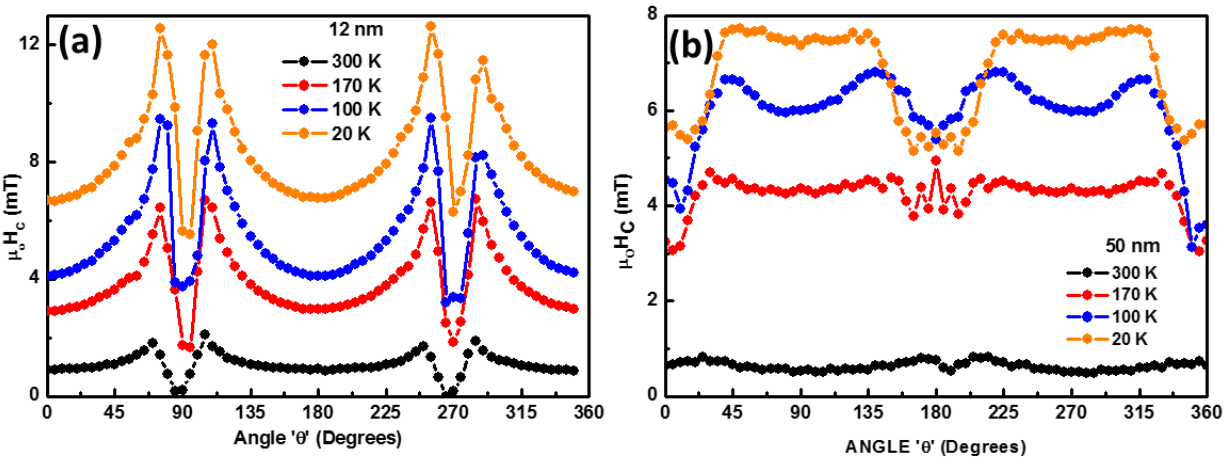

Figure 6.15: Angular evolution and temperature dependence of LSMO films of (a) 12 nm, and (b) 50 nm thick films respectively.

Figure 6.15 shows the temperature and angular dependent coercive fields for 12 nm and 50 nm LSMO film. The angular dependence coercive fields also show 180° periodicity that is similar to remanence.

Discussion

As LSAT (001) is cubic, LSMO films when grown onto LSAT (001) will experience an equal in-plane compressive strain imposed along with a, b crystal axis directions, results in structural changes accompanied by 'BO_6' octahedral network. Because of this cubic symmetry from the substrate, one would also expect that the magnetic anisotropy of the film would exhibit cubic (four-fold) symmetry. However, it is quite interesting to note that the magnetic anisotropy of LSMO films grown on LSAT shows abnormalities with cubic symmetry as a function of thickness that was similar to the films grown on STO substrate. In ABO_3 perovskites, the 'BO_6' oxygen octahedral plays a vital role in determining perovskite properties. According to Glazer notations [61], the bulk LSMO and LSAT (001) has #14 ($a^-a^-a^-$) and #23 ($a^0a^0a^0$) tilt pattern respectively. Here, the letters a, b, and c represents the magnitude of the tilt and the superscripts '+', '-', and '0' represents 'in-phase', 'anti-phase' and 'zero' tilting of 'BO_6' octahedra in adjacent layers respectively. Octahedral tilting and rotations [82] at interfaces plays a major role in determining properties in strained films. From the θ-2θ XRD scans, it is evident that the films are strained. Therefore, at low thickness regime (12 nm), the film is completely strained with LSAT (001) substrate. The epitaxial strain accommodated in the film is mediated through oxygen octahedral tilting and rotations and thus undergo structural phase transitions from bulk rhombohedral to either monoclinic or tetragonal symmetry in thin film form. Consequently, the 'BO_6' octahedral in the film accommodates to #9 ($a^+a^-c^-$) tilt pattern when grown onto LSAT (001) substrates. These octahedral rotations are dominant at the interface along three crystallographic axes, which further modifies its orbital overlapping; spin-orbit coupling that leads to different anisotropic properties. Hence, we termed our 12 nm LSMO film as interface dominant, and it is proposed that the origin of uniaxial magnetic anisotropy depends on octahedral rotations.

As the thickness increases, the strain in the film starts to relax progressively. By considering the 25 nm film (Figure 6.14 middle panel) in the intermediate thickness regime; film acts as an interface between the fully strained bottom layer and partially relaxed top layer. Therefore, the structure of the film is a composite of cubic (due to LSAT (001) substrate) and very weak orthorhombic (due to bulk LSMO) symmetry. Hence, depending on the strength of these two structures, the anisotropy differs from mixed to four-fold to any other symmetry. So, at 300 K, the origin of four-fold can be attributed to the cubic symmetry from the substrate and magnetocrystalline anisotropy of LSMO; two-fold can be attributed to the orthorhombicity of LSMO. Furthermore, as the temperature decreases, the strength of the uniaxial component present along [100] or 0° decreases monotonically. As a result, the biaxial anisotropy becomes dominant as a decrease in temperature. At 100 and 20 K, a pure biaxial (four-fold) anisotropy observed with easy axes aligned along 45° and the angle 'θ' between two successive easy axes are exactly 90°. Therefore, as the temperature decreases, the uniaxial anisotropy term $K_u \rightarrow 0$ and the ratio between $K_u / K_b \rightarrow 0$, enhancing the biaxial (four-fold) symmetry.

At higher thickness regime (50 nm), the film is partially or fully relaxed and often termed as bulk dominant with an orthorhombic crystal structure that could exhibit uniaxial anisotropy [107]. As the temperature decreases from 300 K to 20 K, the strength of the uniaxial anisotropy increases. Thus, in the case of 12 and 50 nm, uniaxial anisotropy is dominant but of different strengths and origins over magnetocrystalline anisotropy. The latter is usually dominant at low temperatures as we have already seen in STO and STO buffered MgO substrates but not fully on LSAT in the case of 12 and 50 nm thick films. However, it is to be noted that by precisely looking at M (H) loops, a weak biaxial anisotropy component is present.

6.2.4 Canted magnetization in LSMO/LSAT

As commented above, due to the compressive strain imposed by the LSAT substrate, the LSMO structures may experience a tilting of the magnetization from in-plane to out-of-plane. This would result in an additional magnetic anisotropy term (oriented along the [001] axis) that may be comparable to the in-plane magnetic anisotropies. Therefore, we investigated the hysteretic behavior of the out-of-plane magnetization component (i.e., M_z) in polar Kerr geometry at RT. The scheme of the set-up used is presented in Figure 3.10(c).

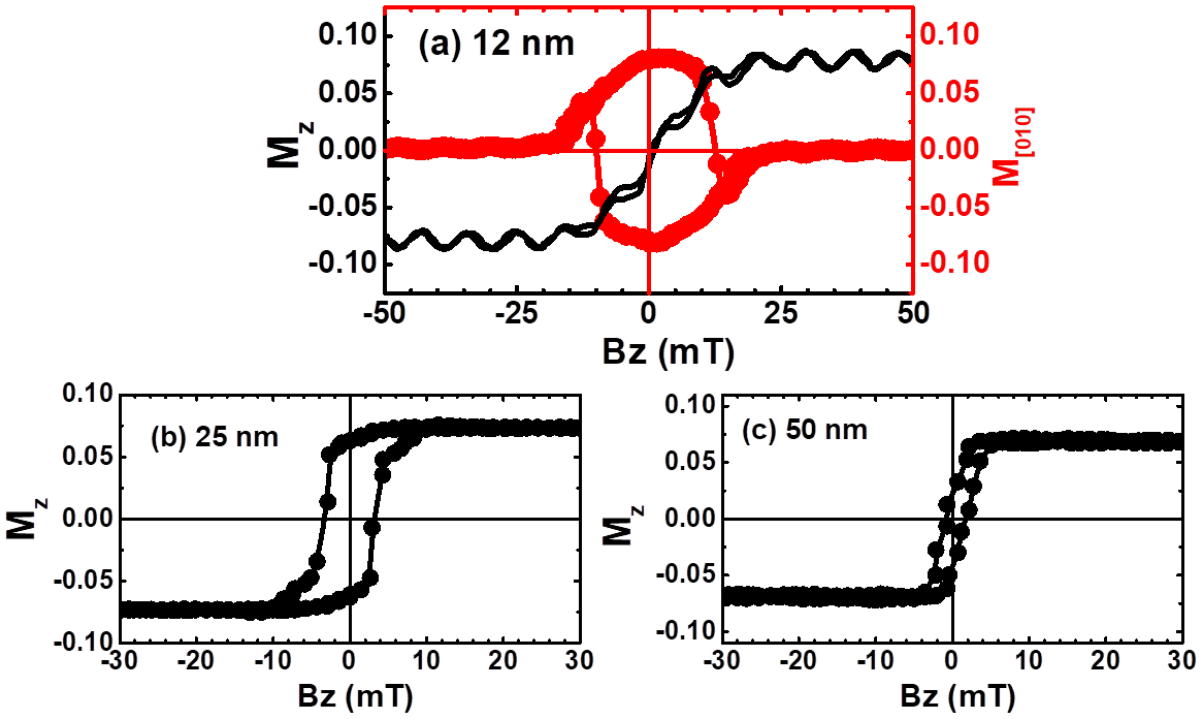

Figure 6.16: Out-of-plane Kerr hysteresis loops for the LSMO films grown onto LSAT (001) substrate of thicknesses 12, 25 and 50 nm respectively.

The results are shown in Figure 6.16. All samples present non-negligible Mz component measured by applying the external field along the [001] direction. This confirms the existence of a perpendicular magnetic anisotropy that scales with film thickness, i.e. thicker the film larger the perpendicular anisotropy. By looking at Table 4.2, we also see that as the thickness is reduced; the c-axis lattice parameter is also reduced, hence inducing a spin reorientation. In fact, in panel (a) the Mz displays a hard axis fully reversible loop and the in-plane magnetization component is almost circular meaning that the magnetization rotates in the plane during the OOP reversal. This suggests a small OOP canting of the magnetization. By increasing the film thickness, we observe squared Mz-Hz hysteretic loops with abrupt transitions indicating a clear reorientation of the magnetization along the field direction. However, in view of the in-plane magnetic anisotropy results in the intermediate thickness (25 nm), such a perpendicular magnetic anisotropy is not relevant; while it is significant in the 50 nm case (more pronounced spin reorientation). This increase in OOP magnetization component is also due to the increase in rhombohedral distortions in the LSMO film.

6.2.5 Summary

To conclude, LSMO thin films of 50, 25 and 12 nm thick were epitaxially grown onto LSAT (001) substrate. Temperature-dependent magnetic anisotropy measurements showed very interesting results. At 300 K, we found an intriguing competition between two in-plane magnetic anisotropies: steps, lattice modulations and orthorhombic induced uniaxial (two-fold) and biaxial (four-fold) magnetocrystalline anisotropy. The relevance of each over the other strictly depends on the film thickness. In particular, at low (12 nm) thickness, the film exhibits a dominant uniaxial anisotropy owing to octahedral tilting, lattice modulations, and terrace steps. At larger thickness, namely 25 nm, a biaxial anisotropy contributes the most due to the cubic substrate. At higher (50 nm) thickness, the magnetic anisotropy symmetry of LSMO shows again a dominant uniaxial anisotropy although very weak. As temperature decreases, there are not many relevant changes observed in 12 and 50 nm, whereas, in 25 nm, mixed anisotropy system changed into pure biaxial system owing to the magnetocrystalline anisotropy of LSMO. Along with *in-plane* magnetic anisotropy, there exists a non-negligible OOP magnetization component too and that becomes more evident with an increase in thickness of the film which is due to compressive strain and increases in rhombohedral distortions.

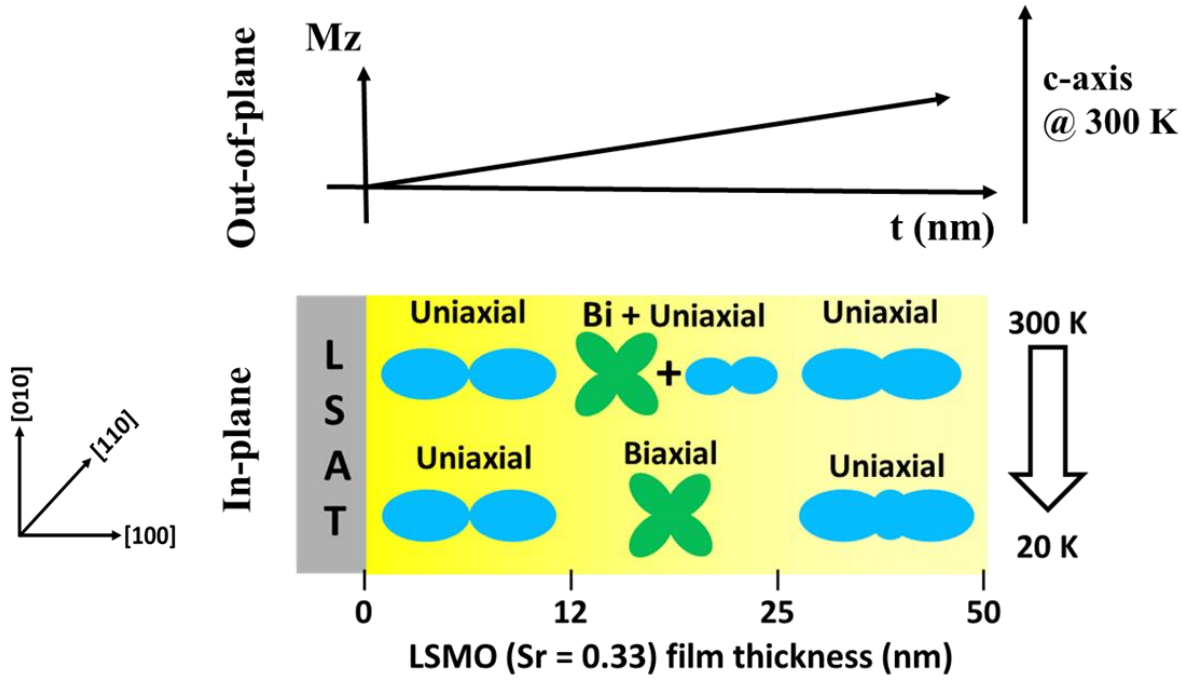

7 Magnetic anisotropy of $La_{1-x}Sr_xMnO_3$ films on LSAT (001) by MBE

In the previous chapter, we have discussed thickness and temperature dependent magnetic anisotropy symmetry landscape transitions in LSMO (x = 0.33) thin films grown on different substrates by PLD technique. Out of them, the lattice mismatch between LSMO film and LSAT substrate is quite small i.e., only -0.2%. As discussed in the section 4.4.1, the electrical and magnetic transport properties are exceptional. Also in section 6.2, we have observed very interesting magnetic anisotropy symmetry behavior as a function of thickness and temperature. Therefore, by considering the above-mentioned reasons, firstly, we narrowed down our choices to focus on LSMO films particularly grown onto LSAT (001) substrates. Secondly, we questioned ourselves, how the magnetic anisotropy properties of LSMO thin films will differ just by fine-tuning the 'Sr' doping concentration. Tuning of 'Sr' doping concentration is another route to alter strain in epitaxial thin films by keeping the same substrate. Sr doping concentration in thin films can be easily controlled by using MBE technique. Thanks to NFFA-EU an H2020 program, we got an opportunity to access Oxide MBE with *in-situ* RHEED and MOKE technique installed at CNR-IOM, Trieste, Italy. As a result, we have chosen two different doping concentrations of 'Sr'[xvii] such as 0.3 and 0.38 and to explore their magnetic anisotropy properties.

7.1 Experimental details

As said before, epitaxial $La_{1-x}Sr_xMnO_3$ thin films with different 'Sr' doping concentrations ($x = 0.3$ and 0.38) are deposited by Oxide MBE technique. In this technique, the metallic elements (La, Sr, and Mn) are individually evaporated in an oxidizing environment (here, pure ozone was used as the oxidizing element). The evaporation temperatures for La, Sr and Mn are ~1400, 400 and 800°C respectively. As discussed in the section 2.2.3.2, we used alternating shutter method to deposit our films. In this method, layers of AO and BO were supplied alternatingly. During deposition, the substrate temperature was maintained ~750°C and the background pressure P_{O3} ~10^{-6} mbar. The stoichiometry and thickness of the thin films were controlled by monitoring real-time RHEED oscillations and intensity variations. After deposition, films were quenched quickly to room temperature at a rate > 50°C min^{-1} in the same deposition pressure. Thin film thicknesses ranging from 15 uc (6 nm) to 250 uc (100 nm) for $x = 0.3$ and from 15 uc to 185 uc (75 nm) for $x = 0.38$ were grown onto LSAT (001) substrate. The LSMO films for all doping levels are fully strained with the LSAT substrates. Atomic Force Microscopy (AFM) was used to study the topography of the as-deposited films. AFM operated in tapping mode by using Nanoscope Veeco III at GREYC, Caen. In order to understand the thickness, temperature, and angular dependent magnetic properties, longitudinal MOKE connected *in-situ* to the MBE chamber was used for magnetic anisotropy measurements at CNR-IOM, Trieste.

[xvii] The doping concentration of 'Sr' for the films grown by PLD was Sr = 0.33.

7.2 Results and discussion

7.2.1 Structural characterization

Epitaxial LSMO thin films with x = 0.3 (x = 0.38) would experience *in-plane* biaxial compressive (tensile) strain when grown onto cubic LSAT (001) substrate. Figure 7.1 shows the scale bar with LSAT (001) substrate and LSMO thin films with different doping concentrations used in this study[xviii].

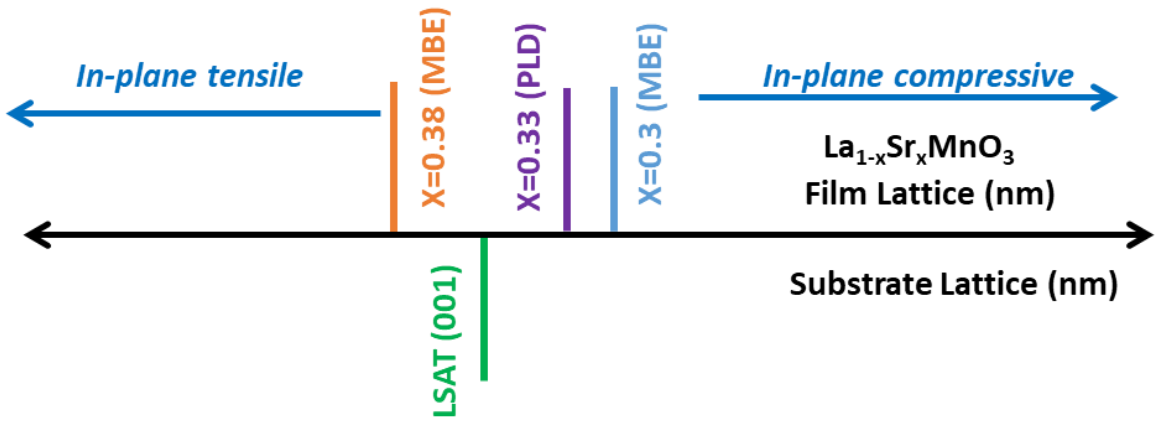

Figure 7.1: Scale bar representing the lattice mismatch between LSAT (001) substrate and the $La_{1-x}Sr_xMnO_3$ thin films with doping concentrations x = 0.3, 0.33 and 0.38.

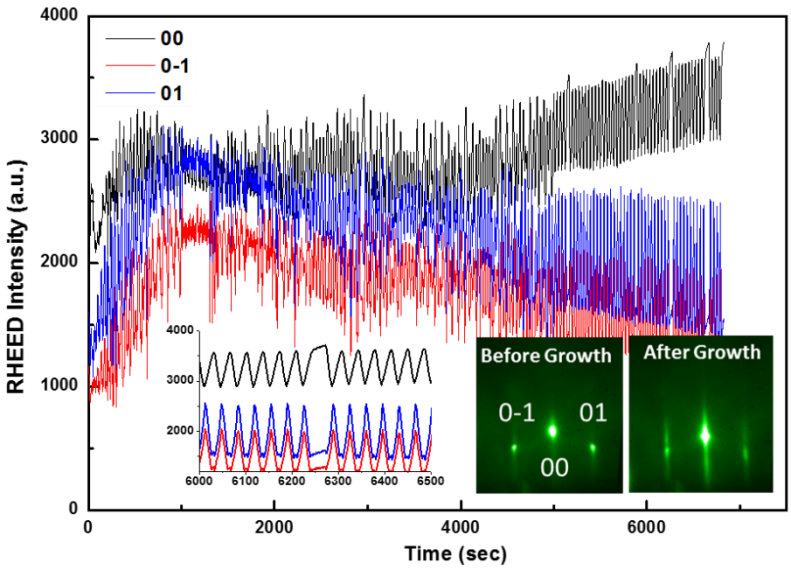

Figure 7.2: RHEED oscillations during the growth of 185 uc LSMO film onto LSAT (001) substrate. The inset shows the portion of RHEED oscillations and also RHEED patterns before and after the LSMO film growth.

Figure 7.2 shows the RHEED oscillations of the (00) (0-1) and (01) diffraction peaks of LSMO thin film grown onto LSAT (001) substrate by MBE. During the film deposition, the

[xviii] XRD measurements are underway so that we can deduce the exact misfit strain between film/substrate interfaces.

(La, Sr) and Mn shutters are opened alternately. During the growth of (La, Sr) O layer, the RHEED intensity increases, whereas during the growth of MnO_2 plane, the intensity decreases. The intensity variations are maintained constant and also no double peaks are observed that confirms the achievement of the desired stoichiometry as seen in Figure 7.2. If there were any double peaks observed around maxima (minima) intensity, the film stoichiometry would deviate from nominal values to La, Sr (Mn) rich conditions [38]. Inset of Figure 7.2 shows the RHEED diffraction patterns with well-defined streaks indicating the 2D growth mode of the film with high crystalline quality.

7.2.2 Surface characterization

The surface morphology of LSMO (Sr = 0.3) thin films characterized by AFM in tapping mode in the scan area of 2µm x 2µm is shown in Figure 7.3. As the thickness increases from 15 uc to 250 uc, the nucleation density also increased. Coming to the roughness of the films, no particular trend has been observed in roughness as an increase in thickness of the film. The RMS roughness values as measured for 62, 150 and 250 uc are ~ 0.4 nm, whereas, for the other thicknesses, the RMS roughness is ~ 1 nm. Table 7.1 below illustrates the detailed RMS surface roughness values for all the thicknesses.

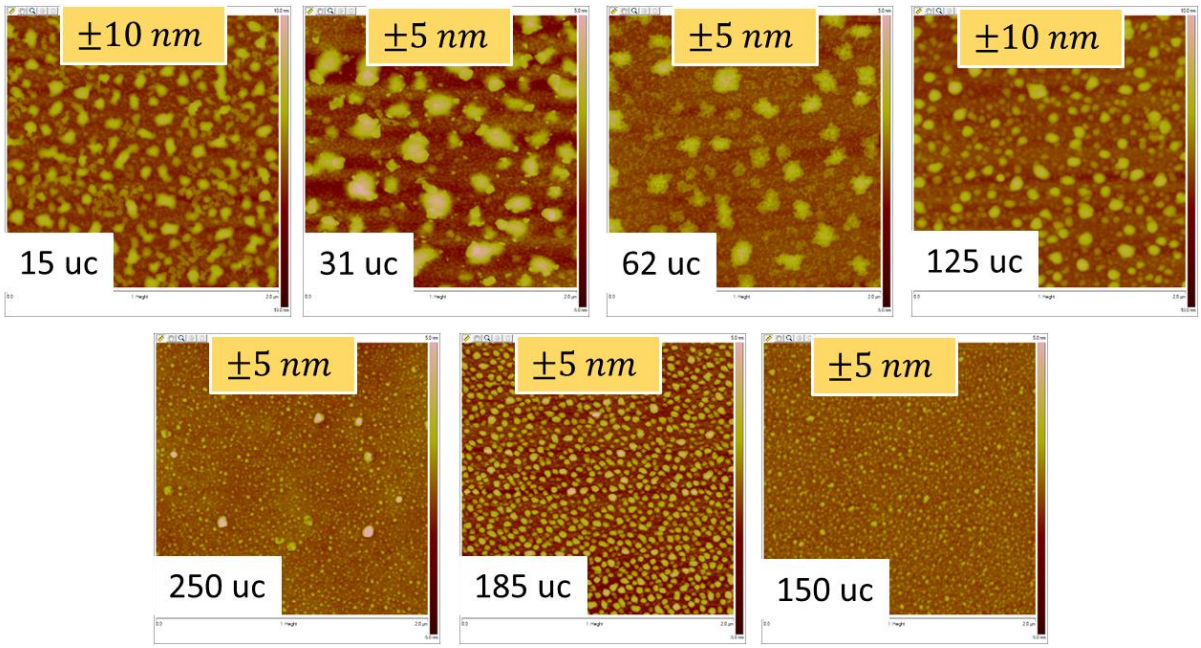

Figure 7.3: 2D AFM topography scans of LSMO (Sr = 0.3) thin films on LSAT (001) substrate in the scan area of 2 µm x 2 µm. The corresponding thicknesses of the film and height scale are also presented in their respective images. The height scale is not maintained and it is to enhance the features for clarity.

The surface morphology of LSMO (Sr = 0.38) thin films characterized by AFM in tapping mode in the scan area of 2µm x 2µm is shown in Figure 7.4. The RMS roughness of the 15 uc film is ~ 0.15 nm, which is quite smooth compared to the 15 uc LSMO film with Sr = 0.3 concentration. But, as the thickness increases from 31, 62 to 185 uc, the roughness of the film gradually decreased from 0.69, 0.52 to 0.19 nm. This shows that the LSMO films under tensile strain (Sr = 0.38) are smoother compared to the films under compressive strain (Sr = 0.3). Stripes or elongated type domains are observed for the 31 uc film. Pinholes are observed

in the 185 uc thick film and it can be attributed to dislocations developed in the film at higher thicknesses. Above all, LSMO films that were grown on LSAT (001) by PLD technique (section 4.4.1) are smoother compared to the films grown by MBE technique.

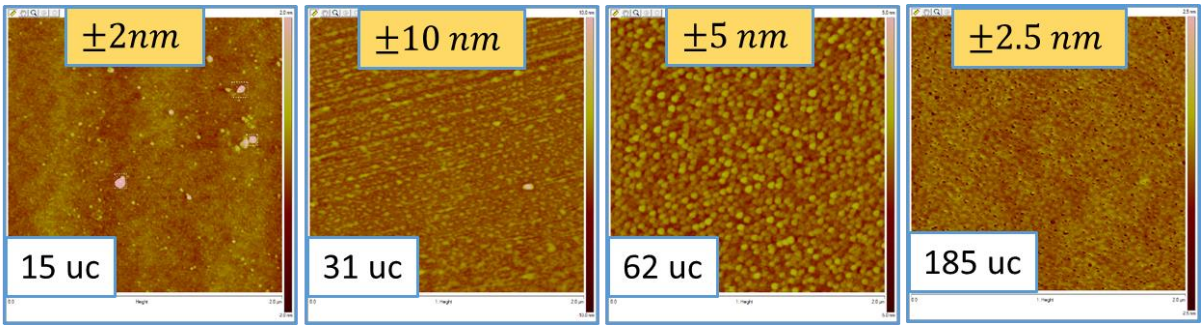

Figure 7.4: 2D AFM topography scans of LSMO (Sr = 0.38) thin films on LSAT (001) substrate in the scan area of 2 µm x 2 µm. The corresponding thicknesses of the film and height scale are also presented in their respective images. The height scale is not maintained and it is to enhance the features for clarity.

Table 7.1: RMS roughness values of the LSMO (Sr = 0.3 & 0.38) thin films of different thicknesses grown on LSAT (001) substrates.

LSMO (Sr = 0.3) Thickness	RMS roughness (nm)	LSMO (Sr = 0.38) Thickness	RMS roughness (nm)
15 uc (6 nm)	1.43	15 uc (6 nm)	0.15
31 uc (12 nm)	1.01	31 uc (12 nm)	0.69
62 uc (25 nm)	0.55	62 uc (25 nm)	0.52
125 uc (50 nm)	1.2	185 uc (75 nm)	0.19
150 uc (60 nm)	0.32		
185 uc (75 nm)	1.07		
250 uc (100 nm)	0.416		

7.2.3 Magnetic characterization

In order to probe the thickness, temperature and angular dependent magnetic properties of LSMO thin films on LSAT (001) substrates, MOKE technique is used by operating in the longitudinal mode. All the measurements are performed by rotating the sample in the film plane and by keeping the externally applied field direction constant as shown in Figure 7.5. Angle 'θ' is defined as the angle between external magnetic field and crystallographic direction of the sample. Therefore, $\theta = 0°$ is taken when the external field is aligned parallel to the [100] in-plane crystal direction. The angular dependent magnetic measurements are performed at 40 K for all the films. All measurements are done with applying both positive and negative fields and then averaged the signals in order to avoid any rotation contribution signal from the non-magnetic origin, for example, stress-induced birefringence [149].

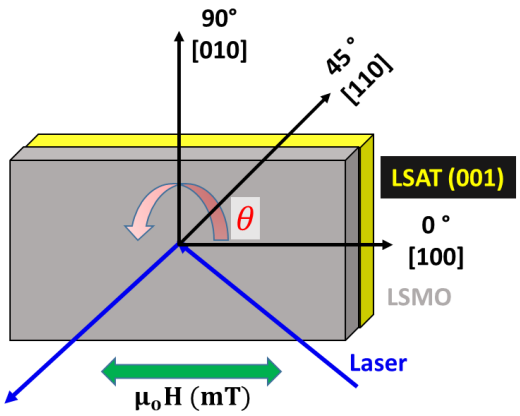

Figure 7.5: Schematic of the sample mounted on the Longitudinal MOKE set-up. Here, the angle 'θ' indicates the direction of the rotation of the sample. The applied field direction is also presented. At θ=0°, the applied field is aligned parallel to [100] crystallographic axis.

7.2.3.1 Thickness-dependent magnetic properties (Sr = 0.3)

LSMO thin films with Sr = 0.3 would experience in-plane biaxial compressive strain when grown onto LSAT (001) substrates. Figure 7.6 shows the normalized Kerr hysteresis loops of 15 uc LSMO film measured at and around characteristic axes shows that the easy and hard axes are present along 45° [110] and 90° [010] respectively. The coercive fields measured at easy and hard axis are 17 and 12 mT. By careful inspection, we have observed double transitions near hard axis i.e. θ = 70° and 80°. These hysteresis loops are similar to the one presented in the section 5.2.1.4. These two irreversible transitions take place by nucleation and propagation of two consecutive 90° domain walls, which is commonly observed in the cubic systems. Also, the angle between easy and hard axis is exactly 45°. Therefore, from the above arguments, it is clear that the film exhibits pure biaxial anisotropy.

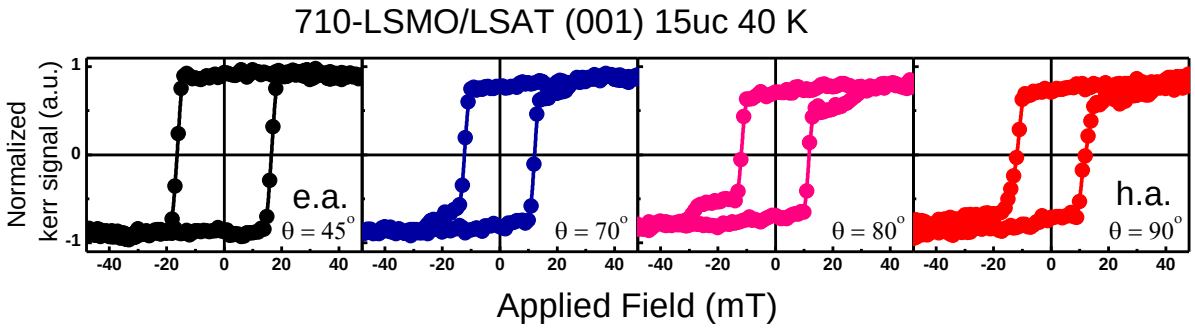

Figure 7.6: Magnetization reversal study of 15 uc (6 nm) thick LSMO (Sr = 0.3) film grown onto LSAT (001) substrate shows biaxial anisotropy with easy (e.a.) and hard (h.a.) axes directions along 45° and 90°, respectively. The corresponding applied field angles '*θ*' are shown in the figure.

As the thickness of the LSMO (Sr = 0.3) film increases from 15 uc to 31 uc, we have observed an entirely different magnetic anisotropy behavior, as shown in Figure 7.7. The easy and hard axes are present along 40° and 90° respectively. Therefore, the angle between easy and hard axis is 50°. The coercive fields measured at easy and hard axis are 11 and 6.6 mT. By comparing the hysteresis loops between 6 and 12 nm (Figure 7.6 and Figure 7.7), for 12

nm film, you could notice that the two irreversible transitions prolong to the larger angles away from the hard axis. This suggests that there exist an additional anisotropy along with biaxial anisotropy, leading to symmetry broken system; similar to the one we have observed in 25 nm LSMO film on LSAT by PLD (section 6.2.2). Therefore, the biaxial anisotropy is present along 45° <110> and the uniaxial anisotropy is present along 0° [100]. By recalling the equation (4.5), we can deduce the ratio between uniaxial and biaxial anisotropy for this 31 uc LSMO film i.e. $K_u/K_b = 0.25$. So, the angle 'α' calculated between two consecutive easy axes is ~75.5°.

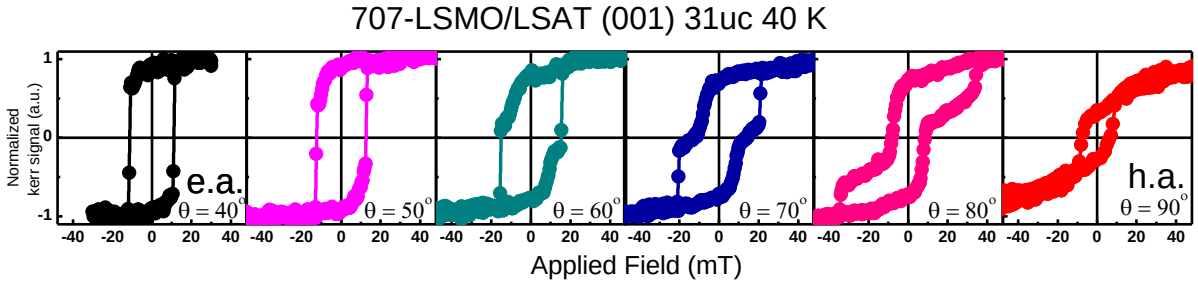

Figure 7.7: Magnetization reversal study of 31 uc (12 nm) thick LSMO (Sr = 0.3) film grown onto LSAT (001) substrate shows mixed anisotropy (biaxial + uniaxial) with easy (e.a.) and hard (h.a.) axes directions along 40° and 90°, respectively. The corresponding applied field angles 'θ' are shown in the figure.

Further increasing the thickness of the film from 31 uc to 62, 125 and 150 uc, we have observed pure uniaxial anisotropy in all the films with easy and hard axis aligned along 0° [100] and 90° [010] respectively, as shown in Figure 7.8. The coercive fields measured at easy axis for 62, 125 and 150 uc are 5.6, 3.4 and 3.8 mT, whereas the coercive field at hard axis is always 0 mT, which shows it is very strong uniaxial anisotropy.

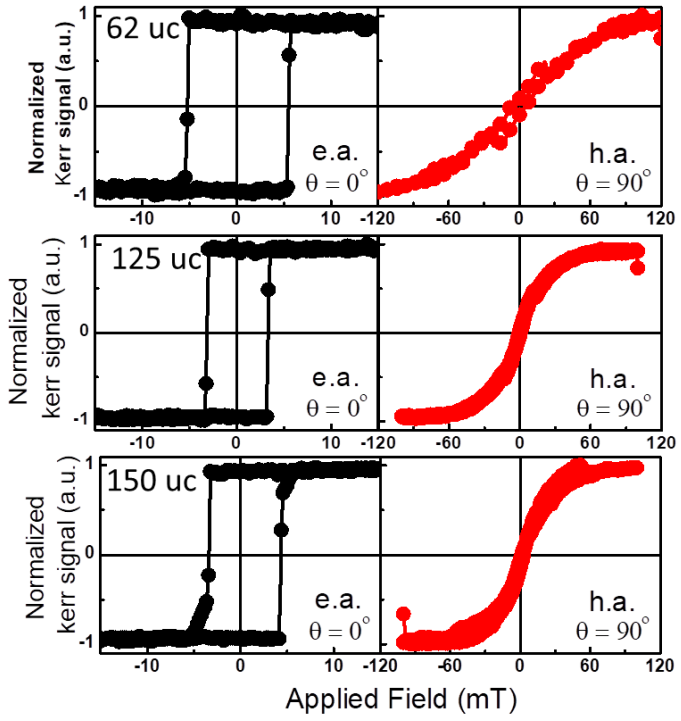

Figure 7.8: Magnetization reversal study of 62, 125 and 150 uc (25, 50 and 60 nm) thick LSMO (Sr = 0.3) film grown onto LSAT (001) substrate shows uniaxial anisotropy with easy (e.a.) and hard (h.a.) axes directions along 0° and 90°, respectively. The corresponding applied field angles 'θ' are shown in the figure. It is to be noted that the field scales are different for easy and hard axes.

Further increase in the thickness from 150 uc to 185 uc, the uniaxial anisotropy is still present, as seen in Figure 7.9 with easy and hard axes are aligned along 0° [100] and 90° [010] respectively. The coercive fields measured at easy and hard axis are 0.9 and 0 mT. Along with uniaxial, a very weak biaxial component is also present. This biaxial component can be seen in the M (H) loop at $\theta = 80°$, in the form of double transitions.

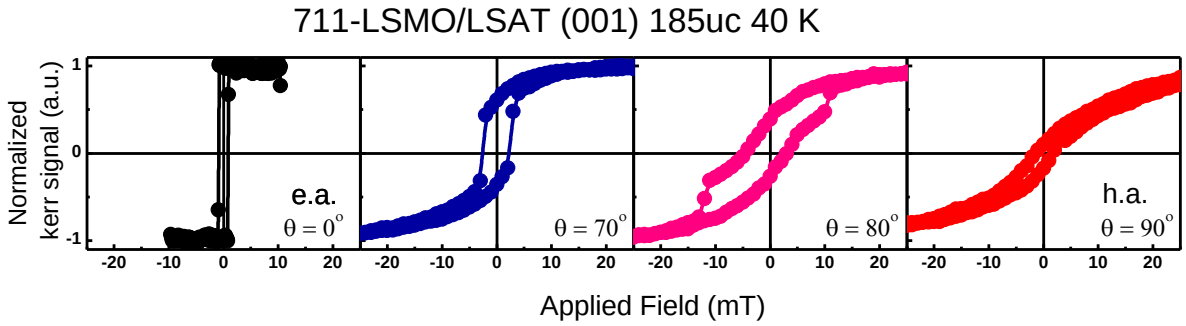

Figure 7.9: Magnetization reversal study of 185 uc (75 nm) thick LSMO (Sr = 0.3) film grown onto LSAT (001) substrate shows mixed anisotropy (uniaxial + very weak biaxial) with easy (e.a.) and hard (h.a.) axes directions along 0° and 90°, respectively. The corresponding applied field angles '*θ*' are shown in the figure.

As we increase the thickness from 185 uc to 250 uc, we have observed a kind of isotropic system with similar hysteresis loops present at different angles as shown in Figure 7.10. Although we can observe changes in the M (H) loops, they are not very significant. The coercive field measured at 0° and 90° is ~ 8 mT and ~ 11 mT respectively. Therefore, we believe that the magnetization for the 250 uc film is shifted from easy plane to easy cone (OOP) anisotropy.

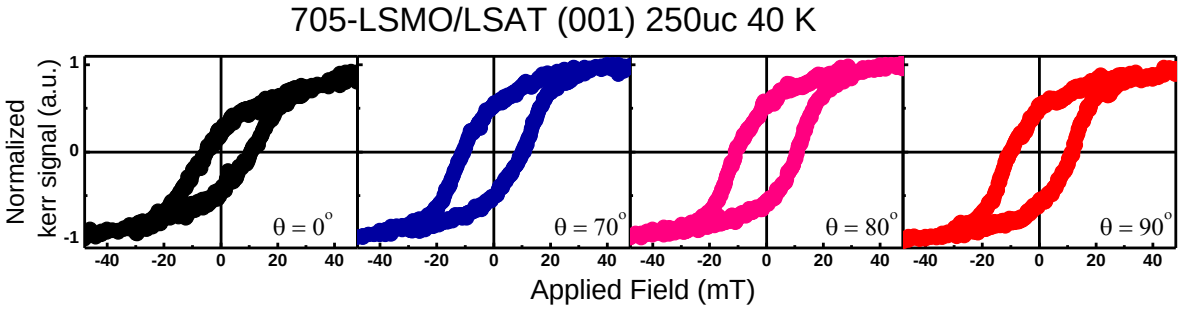

Figure 7.10: Magnetization reversal study of 185 uc (75 nm) thick LSMO (Sr = 0.3) film grown onto LSAT (001) substrate shows almost isotropic behavior. The corresponding applied field angles '*θ*' are shown in the figure.

Figure 7.11 shows the thickness dependent coercive field measured at easy axes of the films. A gradual decrease in the coercive field (17 mT to 0.9 mT) is observed as an increase in thickness from 15 uc to 185 uc and then increases suddenly to 11 mT at 250 uc thick film. It is well-known that the coercivity of a magnetic film is closely related to the microstructure of the film and magnetization reversal mechanism [150]. In addition, H_C also, depends on the grain size.

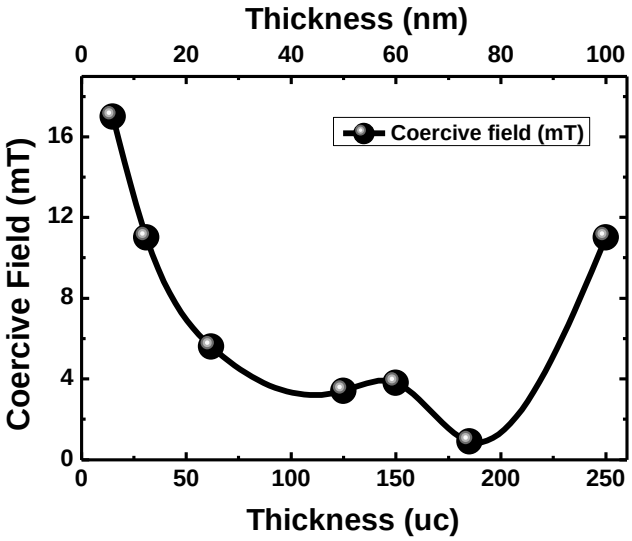

Figure 7.11: Thickness dependent coercive field of LSMO (Sr = 0.3) thin films measured at easy axes.

7.2.3.2 Thickness-dependent magnetic properties (Sr = 0.38)

LSMO thin films with Sr = 0.38 would experience in-plane biaxial tensile strain when grown onto LSAT (001) substrates. We have deposited 4 different thicknesses ranging from very thin i.e., 15 uc to very thick i.e. 185 uc LSMO films. Here, we will present the angular dependent magnetic properties of all the films measured at 40 K by MOKE magnetometry. Figure 7.12 shows the normalized Kerr hysteresis loops of 15 uc (6 nm) LSMO film measured at and around characteristic axes. The 15 uc LSMO film exhibit pure biaxial anisotropy with the easy and hard axes aligned along 45° <110> and 90° [010] respectively. The coercive fields measured at easy and hard axis for 15 uc are 4.3 and 4 mT.

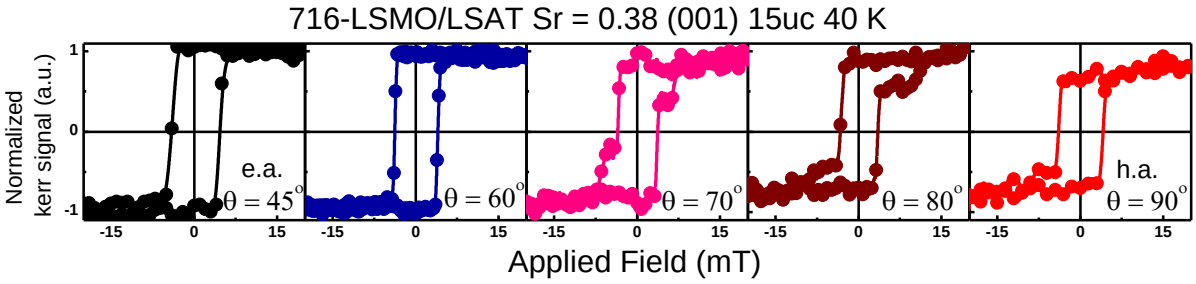

Figure 7.12: Magnetization reversal study of 15 uc (6 nm) thick LSMO (Sr = 0.38) film grown onto LSAT (001) substrate shows biaxial anisotropy with easy (e.a.) and hard (h.a.) axes directions along 45° and 90°, respectively. The corresponding applied field angles '*θ*' are shown in the figure.

Now, let us consider an intermediate thickness 30 uc (12 nm) which shows very complex *in-plane* magnetic anisotropy behavior i.e. biaxial plus an additional uniaxial component. As usual, the biaxial component with easy axis is aligned along <110> or 45°, whereas the uniaxial is not aligned parallel to [100] plane (which was previously observed in our LSMO films). But the uniaxial component aligns 40°±5° away from [100] crystallographic axis. This off-axis alignment of the uniaxial anisotropy could purely be the result of the elongated grain growth or domains or stripes formation on the film surface, revealed from AFM scans (Figure

7.4). I have highlighted the M (H) loops with the similar background color to enhance the visibility that the features are repeating by every 190°. Therefore, there exists an additional uniaxial contribution arisen from the surface effects.

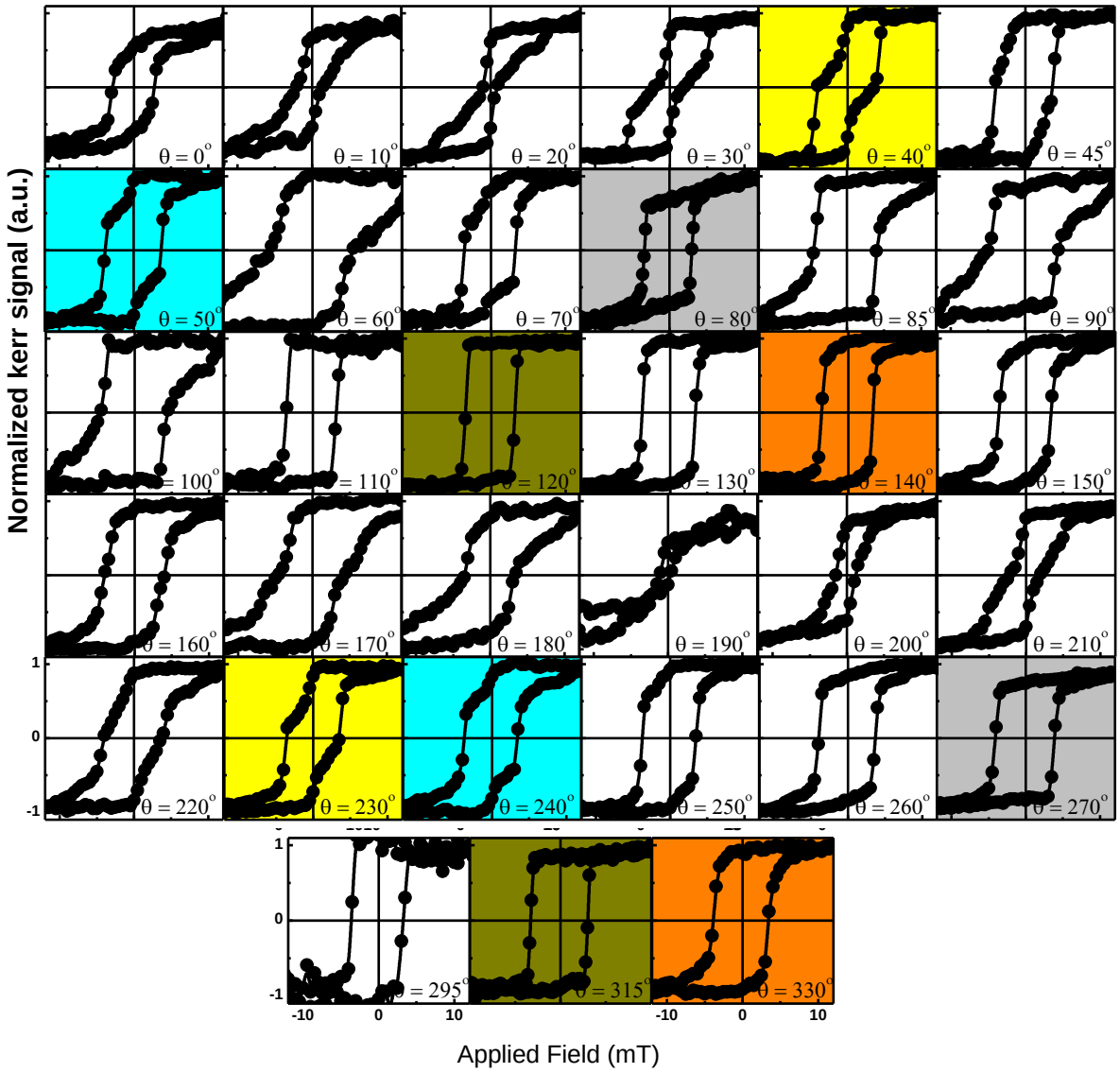

Figure 7.13: Magnetization reversal study of 30 uc (12 nm) thick LSMO (Sr = 0.38) film grown onto LSAT (001) substrate shows mixed anisotropy (biaxial + uniaxial). The corresponding applied field angles 'θ' are shown in the figure.

Let us move on to 62 uc thick (25 nm) LSMO film. By quick view, one could conclude that the film also exhibits pure biaxial anisotropy. But, we have observed tiny difference by comparing the M (H) loops at $\theta = 60°$ between 15 uc (Figure 7.12) and 62 uc (Figure 7.14) thick LSMO film. At $\theta = 60°$, an additional shoulder has been observed for 62 uc thick film, which hints us there exist an additional uniaxial component along with pure biaxial component. By recalling the equation (4.5), we can deduce the ratio between uniaxial and biaxial anisotropy for this 62 uc LSMO film i.e. $K_u/K_b \cong 0.2 - 0.22$. This suggests that there exist an additional anisotropy along with biaxial anisotropy, leading to symmetry broken system; similar to the one we have observed in 25 nm LSMO film on LSAT by PLD

(section 6.2.2). Therefore, the biaxial anisotropy is present along 45° <110> and the uniaxial anisotropy is present along 0° [100]. The coercive fields measured at 45° and 90° (h.a.) are 3.75 and 4.3 mT.

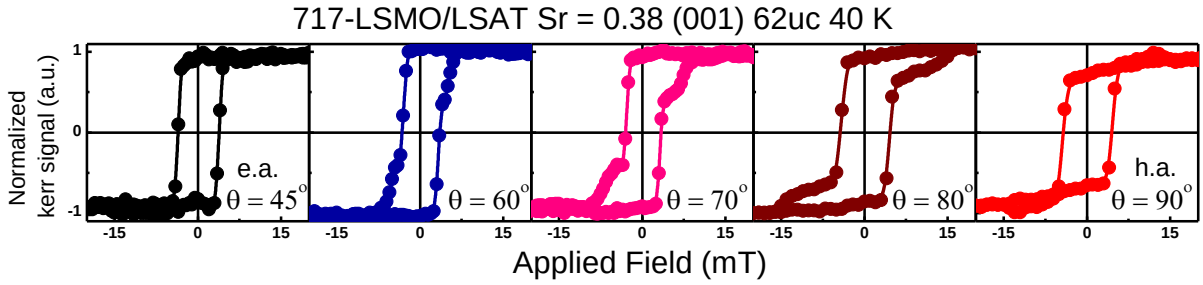

Figure 7.14: Magnetization reversal study of 62 uc (25 nm) thick LSMO (Sr = 0.38) film grown onto LSAT (001) substrate shows mixed anisotropy (biaxial + weak uniaxial). The corresponding applied field angles 'θ' are shown in the figure.

Further increase in thickness of LSMO film from 62 to 185 uc (75 nm), we have observed a sharp increase in coercive fields. The coercive fields measured at $\theta = 45°$ (e.a.) is 49 mT whereas at $\theta = 0°$ and 90° (h.a.) is 33.5 and 29 mT exhibiting very weak *in-plane* biaxial anisotropy (almost isotropic). This increase in coercive fields hints us that the magnetic anisotropy is tending towards OOP as increase in film thickness. This magnetic anisotropy behavior in LSMO thin films was also observed in our previous sections and chapter.

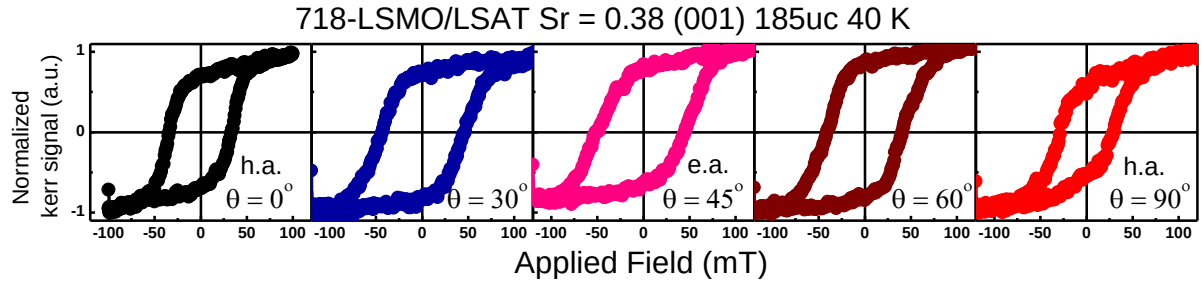

Figure 7.15: Magnetization reversal study of 185 uc (75 nm) thick LSMO (Sr = 0.38) film grown onto LSAT (001) substrate shows weak biaxial (almost isotropic) behavior. The corresponding applied field angles 'θ' are shown in the figure.

7.2.4 Summary

To conclude, LSMO thin films were grown on LSAT substrate with different Sr composition (0.3 and 0.38) and thickness ranging from 6-100 nm for Sr = 0.3 and 6-75 nm for Sr = 0.38 by Oxide MBE technique. All the films were monitored with real-time RHEED pattern to control the correct stoichiometric and thickness of the film. The *in-plane* magnetic anisotropy on all the films were measured at 40 K.

For instance, films with Sr = 0.3 composition showed biaxial and uniaxial contribution (both depends on the thickness of the film). As LSAT (001) is cubic, LSMO (Sr = 0.3) films when grown onto LSAT (001) substrates will experience an equal in-plane compressive strain imposed along with a, b crystal axis. Due to the epitaxial relationship, the in-plane lattice parameters of the film get locked with the substrates lattice. A possible explanation for this magnetic anisotropy symmetry transitions might be that as the thickness of the film increases, the film tends to relax. There can be structural changes in the film from tetragonal (at low thickness) to orthorhombic (at higher thickness), which causes the changes in anisotropy from cubic (four-fold) to uniaxial (two-fold). This kind of observation is not new and it was observed by Boschker *et al.*[107] but with different Sr composition i.e., Sr = 0.33. At higher thickness ~100 nm, the magnetization tends to OOP.

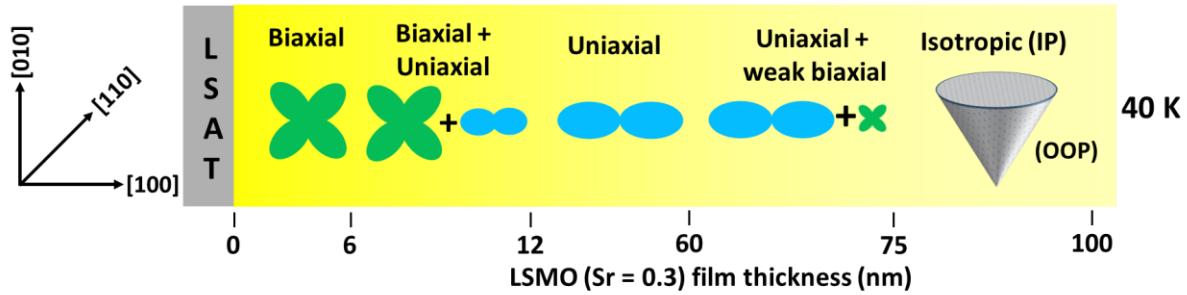

LSMO (Sr = 0.38) thin films on LSAT (001) would experience an equal *in-plane* biaxial tensile strain. Therefore, at the lower thickness (15 uc), the films lattice parameters are get matched with the substrate and exhibits biaxial (four-fold) anisotropy. As thickness increases to 30 and 62 uc, an additional uniaxial component is present, and its origin is not yet clearly understood. At higher thickness, the magnetization tends to OOP.

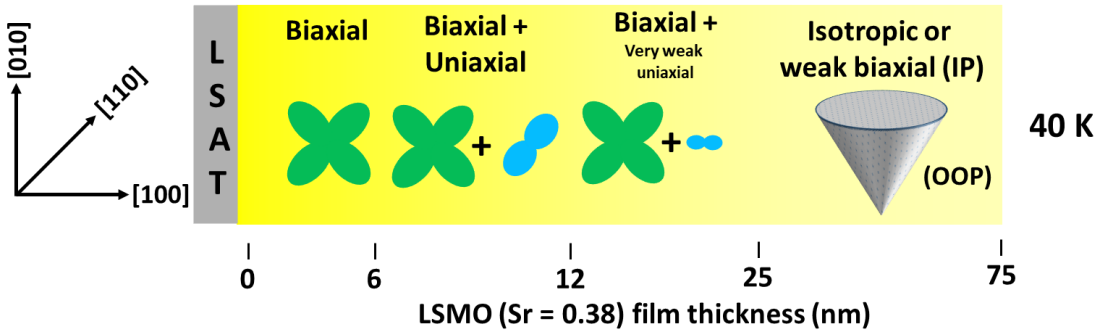

8 Conclusion and Future perspective

8.1 Conclusion

The first aim of this study was to determine the effects of strain in epitaxial LSMO (Sr = 0.33) thin films that were grown by PLD on STO, STO buffered MgO, MgO, NGO, LSAT and LAO substrates. From the XRD and electrical transport properties, we observed that the properties of the film are degraded when grown on large lattice mismatched substrates (LAO and MgO). Therefore, we narrowed down to the films that were grown on nearly matched substrates (STO, STO buffered MgO, NGO, and LSAT) and studied their magnetic anisotropy properties. In particular, we discussed the interplay between magnetic anisotropy symmetry landscapes as a function of thickness, temperature, and epitaxial strain.

For instance, magnetic anisotropy of LSMO films grown on STO substrate showed discrepancies as a function of thickness. At low thickness (12 and 25 nm), films exhibited uniaxial anisotropy although the directions are orthogonal to each other. At higher thickness (50 nm), film exhibited isotropic (weak biaxial) behavior. To overcome these above-mentioned anomalies, LSMO films that were grown on STO buffered MgO of 50 nm with similar electrical and magnetic transport properties showed perfect cubic or biaxial anisotropy. At low temperatures, LSMO films on both STO and STO buffered MgO showed pure biaxial anisotropy owing to magneto-crystallinity nature. Similarly, LSMO films that were grown on anisotropic in-plane strained substrate (NGO (110)) always exhibited uniaxial anisotropy at room temperature and at low temperatures too. Magnetic anisotropy of LSMO films grown on LSAT showed quite complex behavior. At 300 K, as thickness increases from 12, 25 and 50 nm, we observed symmetry transitions from pure uniaxial to symmetry broken system to weak but dominant uniaxial anisotropy. At low temperatures, uniaxial anisotropy is dominant in 12 and 50 nm whereas, for the 25 nm film, there was a change in anisotropy transition from symmetry broken to pure cubic or biaxial anisotropy. Also, non-negligible OOP magnetization is also observed which was dominant as increase in thickness.

The second aims of this study was to investigate the effects of magnetic anisotropy by tuning the ‘Sr’ dopant concentration (Sr = 0.3 and 0.38) in LSMO thin films and were grown onto LSAT substrates by MBE. This tuning of concentration is alternate way to tune the strain and the magnetic anisotropy observed results at 40 K is complex too. As thickness of the films with Sr = 0.3 increases, the magnetic anisotropy symmetry landscape changed from pure biaxial to uniaxial to OOP magnetization. The weight of each contribution is purely dependent on the thickness of the film. For Sr = 0.38 concentration, always the biaxial component is dominant along with weak uniaxial present in 12 and 25 nm thick. At higher thickness, the magnetization tends to OOP.

As discussed in the introduction, there are lots of applications based on magnetic anisotropy. This study helped us to understand and control the magnetic anisotropy as function of thickness and substrate. By precisely knowing the magnetic anisotropy beforehand, we could

directly proceed to fabricate the magneto-resistance devices that could ultimately pave a way towards commercialization of LSMO based devices.

Table 8.1: Thickness and epitaxial strain dependent magnetic anisotropy of LSMO thin films measured at 300 K

Substrates	LSMO thickness	Magnetic anisotropy	Possible origin	Anisotropy field H_a (mT)	Possible applications
STO (001)	50 nm	Isotropic (weak biaxial)	Unknown	3.3	User choice by inducing shape effects
	25 nm	Uniaxial	Steps, mis-cut angle of STO etc.	1.78	AMR sensors
	12 nm	Uniaxial		2	
STO (12 nm) /MgO (001)	50 nm	Pure biaxial	Magneto-crystalline	5.47	Four-state memory devices
NGO (110)	50 nm	Uniaxial	Magneto-elastic, lattice modulations	8.34	AMR sensors
	25 nm			4.23	
	12 nm			3.35	
LSAT (001)	50 nm	Uniaxial	Compressive strain, lattice modulations	17	
	25 nm	Biaxial + Uniaxial		12, 11	Magnetic memory
	12 nm	Uniaxial		20	

8.2 Ongoing work: To design magneto resistive sensor

One example of a possible use of LSMO thin films is to design Anisotropic Magnetoresistance as targeted in the FET OPEN project named as by Axon (H2020 2017 - 2020). In this application a clear uniaxial anisotropy with a small anisotropy field is required.

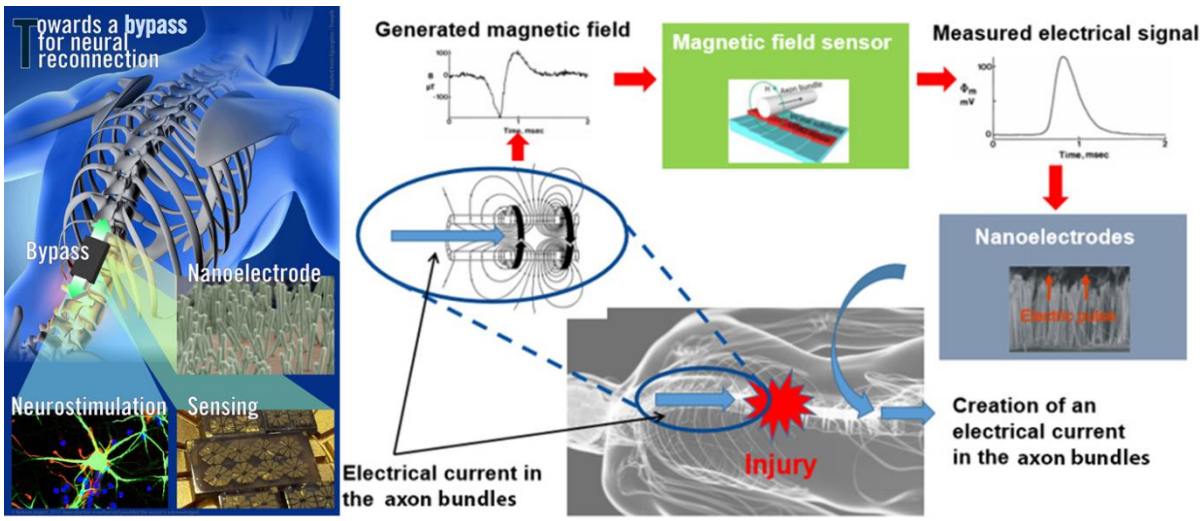

Figure 8.1: Schematic of the AMR sensor that connects the neural network (http://www.byaxon-project.eu/).

8.3 Future Perspective: Towards Flexible Electronics

Although most of the electronic circuitry comes in the form of rigid chips, devices like thin and flexible enough that can be rolled up like a newspaper are fast approaching [151], [152]. Silicon substrates are often thinned in the IC fabrication industries by Chemical Mechanical Polishing (CMP) process that helps to reduce the total device thickness and has the possibility to pack more devices into the same volume. By seeing the above-mentioned importance, we considered that studying the properties LSMO films is also essential by thinning the silicon substrate.

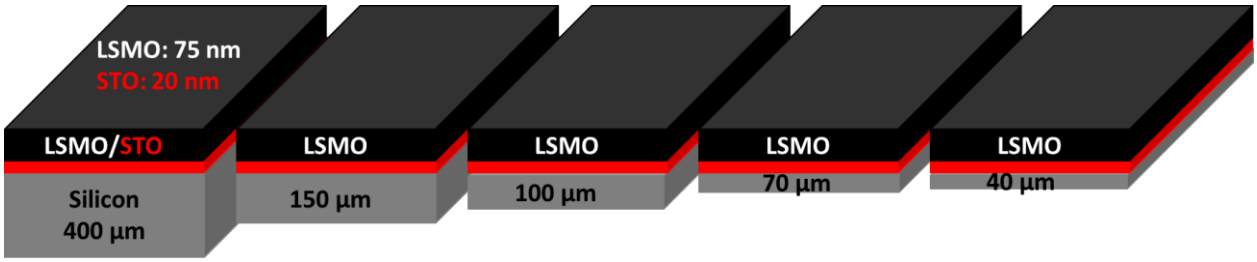

Figure 8.2: Schematic of the LSMO/STO/Si (75 nm / 20 nm / Si) structures in which the silicon substrate is progressively thinned (from 400 µm to 40 µm) by using CMP process.

Therefore, we polished the backside silicon on our LSMO/STO/Si samples by CMP process (Annex V) at CIMAP, Caen. Figure 8.2 shows the schematic of several samples with different silicon substrate thicknesses after polishing. Silicon substrate with a thickness of 400 µm is our reference sample for comparing the LSMO film properties before and after polishing. The LSMO films were deposited by MBE at Cornell University with the film growth conditions as described in the reference [153]. Figure 8.3 shows the M (H) loops measured at RT by MOKE at IMDEA Nanoscience, Madrid on the reference sample[xix] at different *in*-plane crystallographic directions. As seen, there is no significant change observed in either remanence or coercive fields at different angles. The inset of Figure 8.3 shows the remanence measured about 360° and the value is similar at all the angles concluding that the system is isotropic. Whereas LSMO films with 20 and 50 nm thick grown on STO/Si showed biaxial anisotropy [154].

[xix] Reference sample thickness LSMO/STO/Si (75 nm / 20 nm / 400 µm)

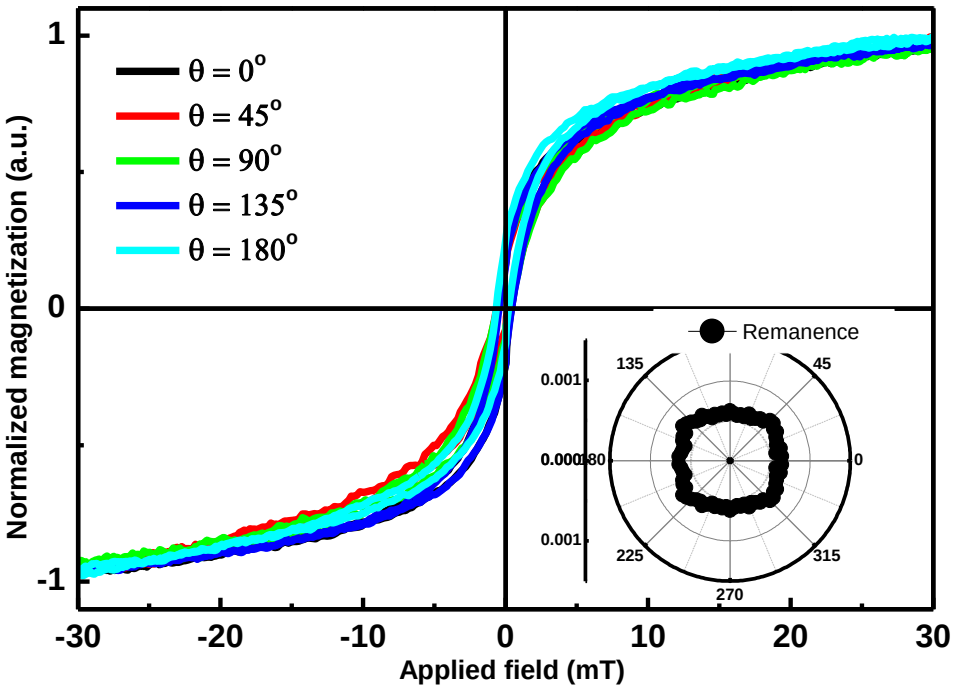

Figure 8.3: RT Normalized *in-plane* M (H) loops of LSMO/STO/Si (75 nm / 20 nm / 400 µm) film measured in different directions and the inset shows the polar plot of remanence measured about 360°.

Figure 8.4 shows the M (T) measured along [100] or 0° and [110] or 45° on various thinned samples measured at CRISMAT, Caen. The samples with thickness 70 and 40 µm show spin reorientation transition (SRT) as indicated by arrows, whereas for the thicker (150 and 100 µm) substrates, SRT is absent.

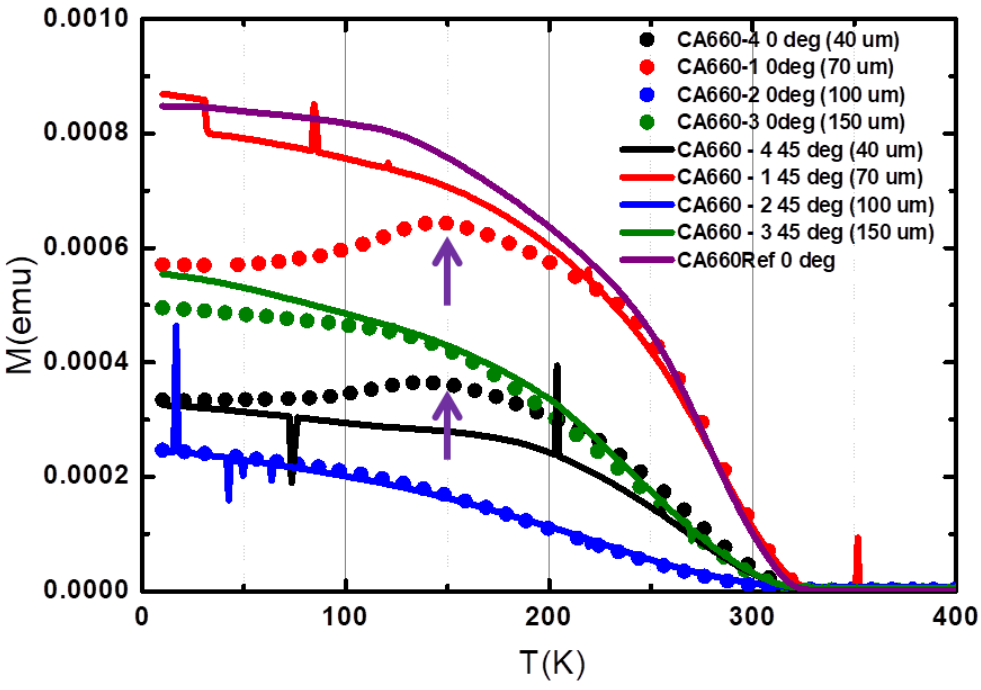

Figure 8.4: M (T) measured along two different *in-plane* crystallographic axes i.e. [100] and [110] of LSMO/STO/Si film respectively. The arrows at ~150 K indicate the spin reorientation transition observed only on very thin silicon substrates (70 and 40 µm).

These preliminary results with observed SRT on very thin samples are already interesting. This motivates us to take another step to study magnetic anisotropy on these thinned samples by using Ferromagnetic Resonance (FMR) in collaboration with University of Villetaneuse and also by applying stress at the same time by gluing the sample on a piezoelectric sample stage [45], [46].

8.4 Future Perspective: Towards MEMS

As silicon technology continues to dominate the microelectronics market, researchers around the world are looking from different views to integrate novel materials with the current silicon technology. One of the key goals is to integrate the functional materials, such as ferroelectric and ferromagnetic oxides, with silicon technology to produce commercially viable high-density, nonvolatile memories, magnetic sensors and other technologies [155]. Transition Metal Oxide (TMO) perovskites with different technological applications were discussed in previous chapters by tuning the epitaxial strain (static strain). In order to realize the dynamic strain effects, we have to design and fabricate Micro-Electro-Mechanical Systems (MEMS) devices. Figure 8.5 shows few examples that are taken from the literature. A lot of work has been done by fabricating MEMS based on piezoelectric materials (PMN-PT, PZT) [156]–[163] by integrating them onto silicon substrates. Only a few reports [47]–[49], [164] are available on LSMO and STO based MEMS either by integrating them on silicon substrates (Figure 8.5 (c)) or by using fully oxide materials. The residual strain developed in the structures due to epitaxial relation could destroy the devices during the fabrication process.

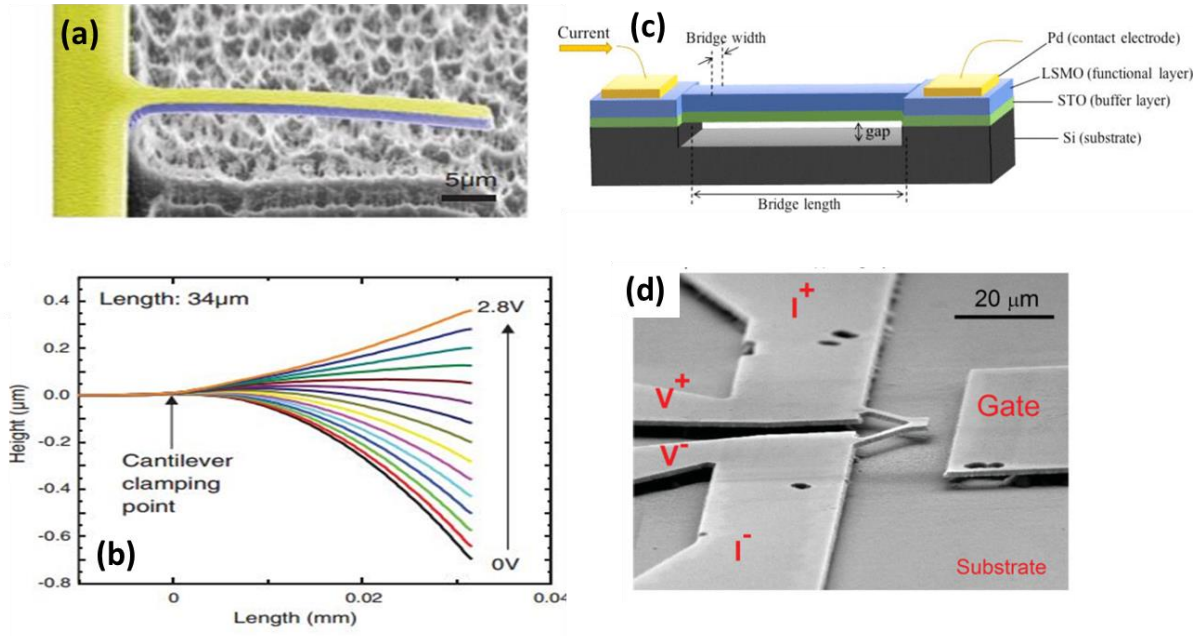

Figure 8.5: (a) SEM image of the PMN-PT cantilever, (b) PMN-PT cantilever profile as a function of applied voltage [165] **(c) Schematic of the LSMO/STO based Pirani device** [48] **(d) SEM micrograph of the LSMO/STO triangular cantilever along with a gate electrode for cantilever actuation** [164]**.**

To overcome this issue, we decided to integrate LSMO on silicon-on-insulator (SOI) substrates and to fabricate MEMS by taking the advantage of buried oxide layer (BOX) as a sacrificial layer. Figure 8.6 shows the schematic of different cantilever mask patterns that we designed by varying widths and lengths of the cantilever.

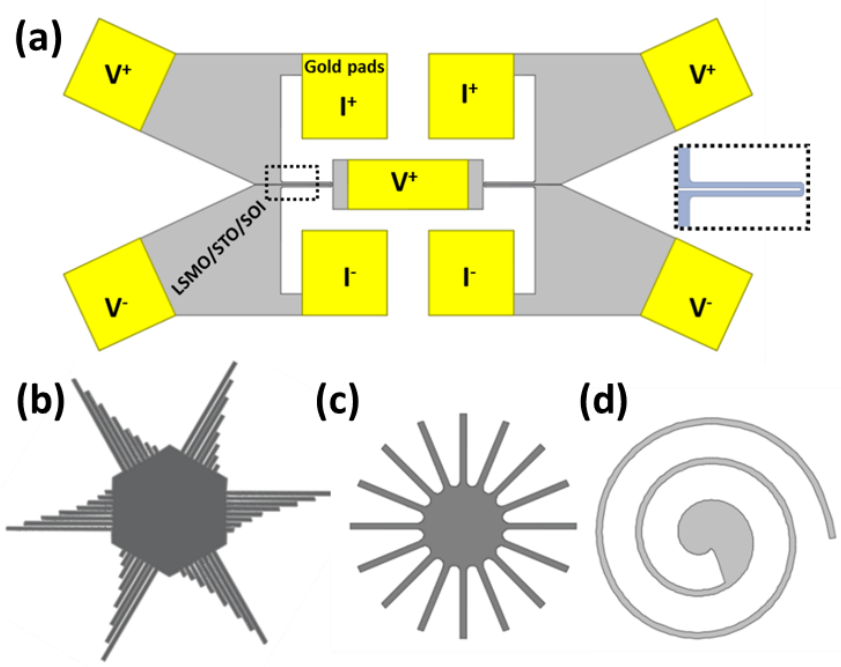

Figure 8.6: Cantilever mask design patterns: (a) cantilever mask with four contact pads (for four-probe measurements) along with the common gate electrode (for actuation) and the inset shows the zoomed version of the cantilever. (b, and c) cantilevers of different lengths to evaluate the strain along different directions, (d) spiral cantilever with a similar width which helps us to estimate the etching rate.

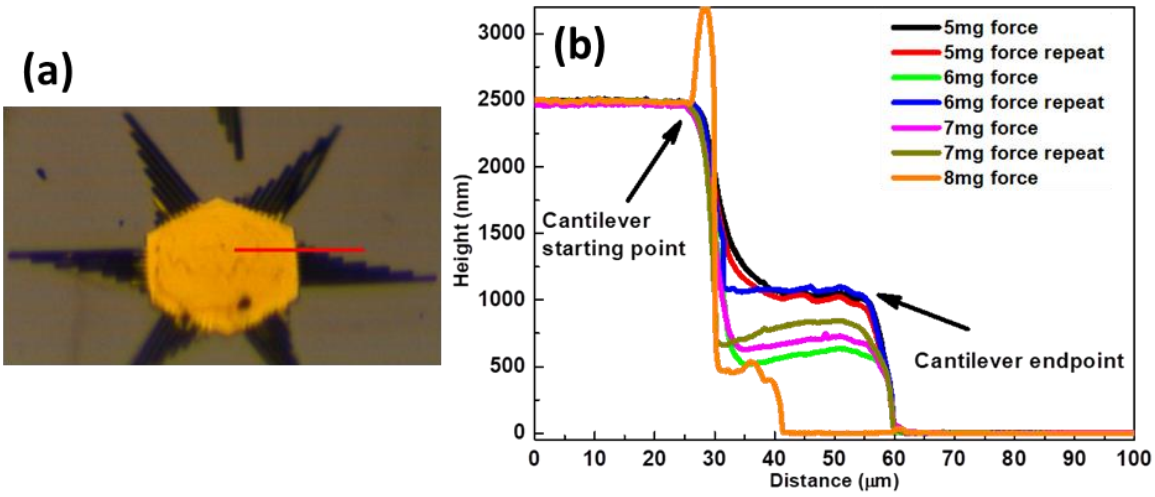

Figure 8.7: (a) Optical photograph of the suspended Au/Cr/Si cantilever after removing the SiO_2 sacrificial layer. (b) The deflection of the cantilever beam measured by mechanical profilometer with different applied tip loading force. The tip scans along the axis of the beam as indicated by the red line in the (a).

The detailed fabrication process is presented in Annex IV. However, we did not succeed in fabricating LSMO cantilevers (under progress); we succeeded in fabricating Au/Cr/Si

cantilevers as shown in Figure 8.7 (a). In order to understand the deflection of a cantilever beam by applying weight or pressure on the cantilever, stylus profilometer was used. With the help of profilometer tip, we scanned the cantilever along its length (as marked in the red line in Figure 8.7 (a)). We could see the bending of the beam (as it is suspended) as we scan along its axis. The higher the tip force, the maximum the bending as shown in Figure 8.7 (b).

Annex-I: Fabrication of thin films

Epitaxial LSMO thin films that were used in this thesis were grown by two PVD techniques namely Pulsed Laser Deposition (PLD) and Molecular Beam Epitaxy (MBE) techniques. Here, I will provide brief details of the same.

Pulsed Laser Deposition:

PLD is a well-known technique for its stoichiometric transfer of complex materials from target to the substrate in an oxygen environment. The basic principle involved in this technique is as follows: A high energetic pulsed laser beam is focused onto the target with the help of various lenses. The KrF excimer Laser hits the target at an angle of 45° or 60° and particles are ejected from the target in form of atoms, molecules. These ejected particles from the target are ionized/oxidized in the O_2 environment and form a plasma with the characteristic shape known as "Plume". The plume travel towards the heated substrate that is directly facing the target and then deposits on the substrate. Depending on the oxygen partial pressure in the vacuum chamber, the shape of the plume differs. If the oxygen partial pressure is high during the film growth (generally 0.35 mbar O_2 pressure for LSMO films), the mean free path of the ejected particles from target reduced and scattering increases thus forming a bright, wide shaped plasma plume. For a material, such as gold (Au) that is usually deposited at lower pressure ($\leq 2x10^{-5}$ mbar), the mean free paths of ejected particles will be higher and the interactions with the surroundings gases are reduced. Thus, the shape of the plume is confined to the narrow area. The quality of the film depends on various parameters such as laser energy (mJ), repetition rate (Hz), background partial pressure, the temperature of the substrate, substrate-to-target distance etc.

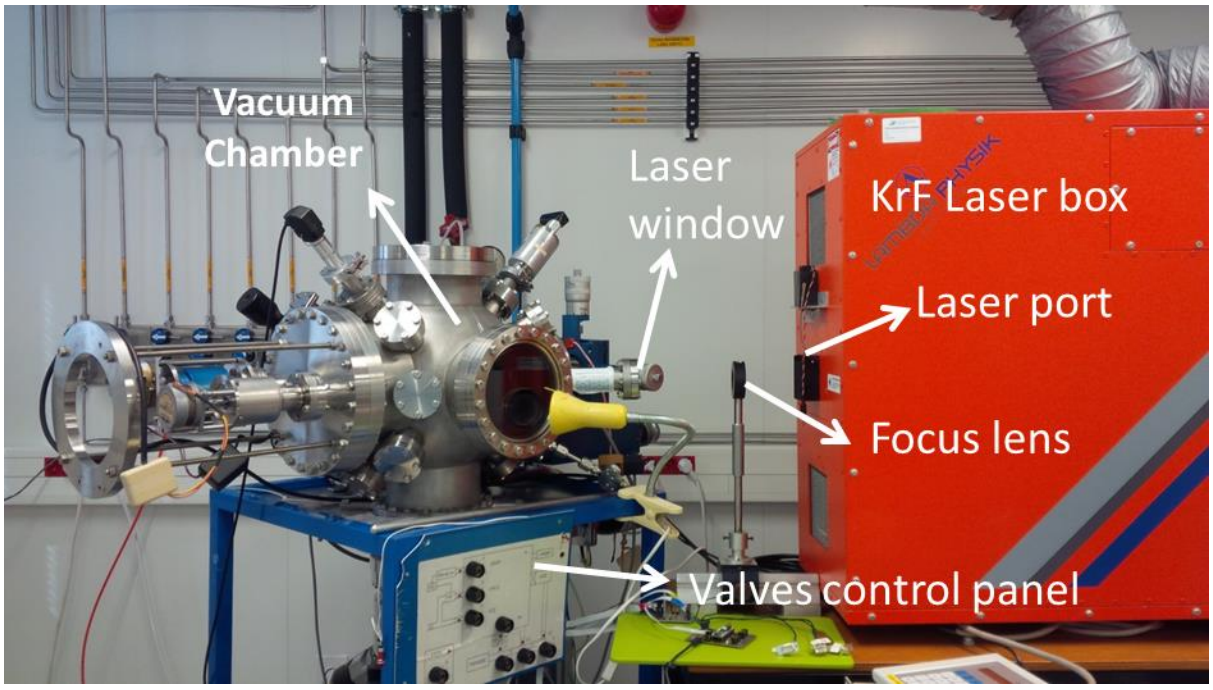

Figure 0.1: Photograph of PLD deposition chamber installed in the cleanroom at GREYC, Caen, France.

Here, at GREYC laboratory, we are using krypton fluoride (KrF) excimer laser with a wavelength of 248 nm and time period of 10-40 ns. The deposition parameters of various materials grown on different substrates in this thesis are tabulated below.

Table 0.1: Parameters that were used during the fabrication of different thin films by PLD technique.

Target	Laser Energy (mJ)	Repetition rate (Hz)	Substrate to target distance (cm)	Substrate temperature (°C)	Partial pressure (mbar)
LSMO	220	03	5	720	0.35
STO	220	03	5	720	0.35
Au	200	05	5	Room temperature	$\leq 2x10^{-5}$

Molecular Beam Epitaxy:

MBE is a well-known technique for its atomically controlled growth of thin films, artificial superlattices that may not be possible with other deposition techniques. Therefore, MBE enjoys its own status in the family of thin film growth techniques. The principle involved in this technique is as follows: The individual materials are heated separately in their cells. The evaporation temperatures for La, Sr and Mn are ~1400, 400 and 800°C respectively. Once the material exceeds its evaporation temperature, the molecules start ejecting from the cells. Since all this process was done under UHV, the ejected atoms/molecules have a large mean free path. The opening and closing of the shutters placed before each cell control the availability of atoms in the vacuum chamber. RHEED is used during the film growth to control the stoichiometry and growth rate of the film. The disadvantage of this technique is the growth rate is quite low so that if you want to grow thicker films (> 100 nm) it will take several hours long.

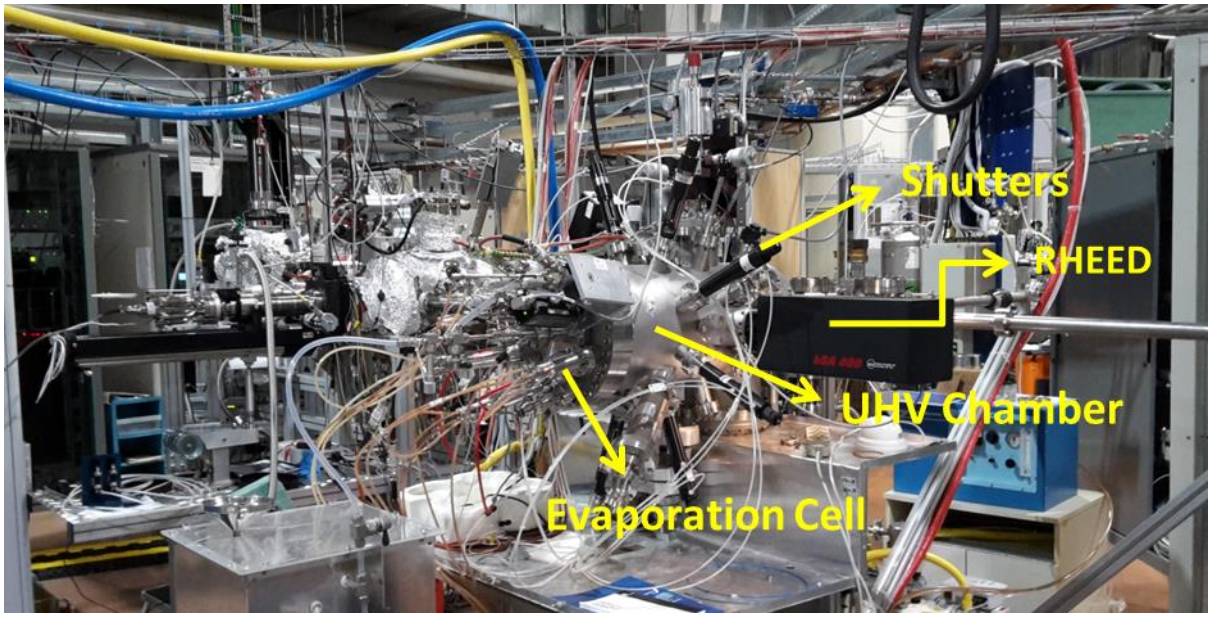

Figure 0.2: Photograph of the UHV- Oxide MBE at CNR-IOM, Trieste, Italy.

Table 0.2: Parameters that were used during the fabrication of LSMO thin films by MBE technique.

Material	Evaporation temperature (°C)	Substrate temperature (°C)	Partial pressure (P_{O3})
La	1400	750	10^{-6} mbar
Sr	400		
Mn	800		

GATAN:

GATAN PECS (*precision etching and coating system*) is often used to prepare samples for SEM, TEM characterization techniques. As the name suggests, this technique is used for uniform coating of films, etching or cleaning the contaminated surfaces of the samples. Here, in this thesis, we used PECS to deposit materials such as Au, Al, Cr, Ti, and Pt etc. These metals are used for fabricating contacts pads on the devices for electrical measurements. Sometimes, multilayers are used to increase the adhesion strength between layers on the surface of the film. The deposition rate by GATAN is quite high and the uniformity can be achieved by rotating the samples during deposition. The deposition rate and the thickness of the film can be easily controlled by adjusting the current passing into canon guns that are focused onto the target.

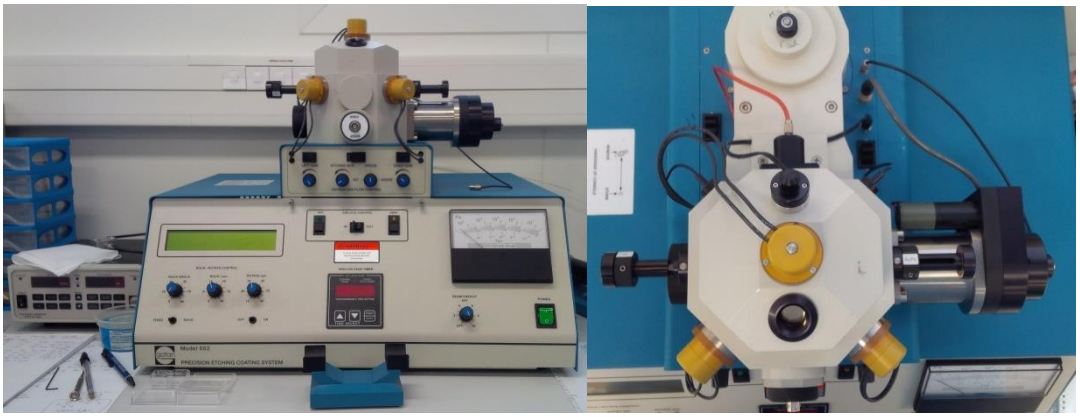

Figure 0.3: Side view and Top view of the precision etching and coating system installed in the cleanroom at GREYC, Caen.

The principle of operation: High voltage (10 keV) and currents (600 μA) are supplied to the two canons that are pointed towards the target at 45°. Once the current is stabilized in both the canons, Argon (Ar) is introduced into the vacuum chamber. Due to the high currents, the Ar gas is ionized into Ar^{+}, which is directed towards the target for bombardment. This physical action removes the material and is deposited onto the substrates placed below exactly at 45°. The strength of the physical action between the target and the Ar^{+} ions determines the deposition rate, which in turn depends on the supplied current. The thickness of the film is monitored real time by using quartz crystal.

Annex-II: Characterization Techniques

X-Ray Diffraction (XRD):

In order to determine the epitaxial quality of LSMO thin films, and to optimize the thin film deposition conditions, XRD technique is often used. XRD is a versatile and non-destructive technique that is used to determine the crystal structure, orientation of the films, phase purity, and to measure strain, lattice parameters etc. In this study, we mostly employed θ- 2θ XRD scans to study the epitaxial quality, strain and to calculate out-of-plane lattice parameters (d) of the film. Rocking curves (omega scans) are performed around the (002) peak of the LSMO film and substrates to study about the orientation of planes, distortions at the interface between film/substrate. Defects like mosaicity, dislocations, and lattice modulations can be studied with the help of rocking curve measurements.

- θ- 2θ symmetric XRD scans and rocking curves were performed using Panalytical X'Pert PRO located at LCS, Caen, France.
- Reciprocal Space Mappings (RSM) and asymmetrical scans were performed using Panalytical X'Pert four-circle XRD at CNR-IOM, Trieste, Italy.

The principle of operation: The characteristic X-rays that are generated from the target (Cu, Fe, Mo, Cr) material are focused onto the sample. Various filters and beam slits of different diameters are used in the X-ray path to remove the unwanted wavelengths and to narrow the beam size. The sample and detector are rotated; the intensities of the reflected X-rays from the sample is recorded. When the geometry of the incident X-rays impinging the sample satisfies the Bragg Equation, constructive interference occurs and a peak in intensity occurs. The Bragg's law is defined as:

$$n\lambda = 2dsin\theta$$

Where 'n' and 'd' are the diffraction order and the distance between two lattice planes, λ is the wavelength of X-rays and 'θ' is the angle between incident X-rays and the sample.

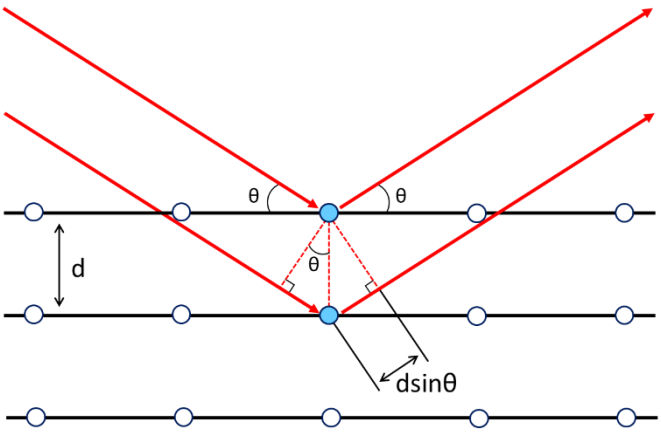

Figure 0.1: Schematic illustration of Bragg diffraction pattern

Four probe resistivity technique:

The four-probe method is a straightforward technique for measuring the resistivity of the sample. The measurement set-up consists of 4-probes that are placed equidistant and collinear. All probes have finite tip radius, supported by a spring to minimize the damage on the sample surface when the probes are pressed onto the surface. A current source is used to supply current in outer two probes and a voltmeter measures the voltage across the inner two probes to determine the sample resistivity. The inner probes do not draw any current because of the high input impedance voltmeter. Hence, this technique has an added advantage over two-probe technique because the inner probes draw no current and it eliminates the contact resistance between film/probes and increases the accuracy in the measurement. Units of resistance are *ohm* and resistivity is *ohm-m*. The resistivity can be obtained as:

$$\rho = \frac{V}{I} \times \frac{\pi}{\ln 2} \times s$$

Where ρ and s are the resistivity and distance between the probes, I and V are the applied current in the outer and measured potential difference between inner probes.

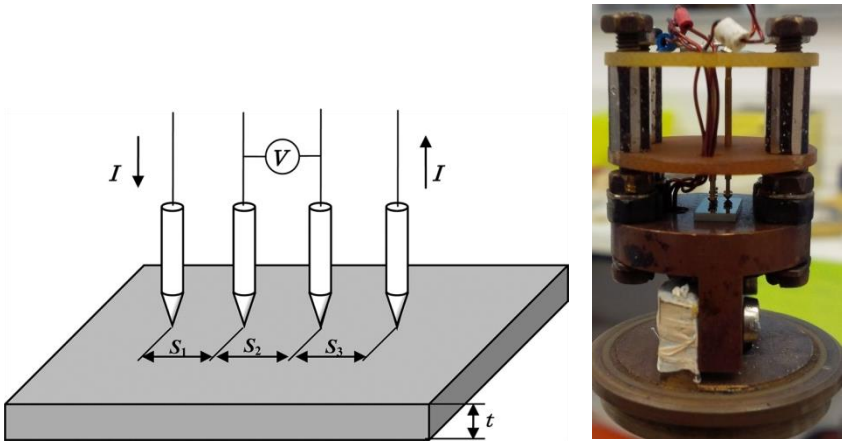

Figure 0.2: Schematic representation of the four-probe resistivity technique and the photograph of the sample holder with four probes installed at GREYC, Caen, France.

Atomic Force Microscopy (AFM):

The principle of operation: AFM consists of a cantilever with a sharp tip attached to the flexible end that is used to scan the sample surface. The cantilever is usually made up of silicon or silicon nitride with the tip radius of curvature is about nanometers. Therefore, the resolution of sample topography is directly dependent on the tip radius. When the tip is brought into proximity of a sample surface, forces between the tip and the sample lead to a deflection of the cantilever according to Hooke's law. In the nanometer scale, there could be multiple forces that act together such as attractive and repulsive forces, capillary forces, Vanderwall forces, chemical bonding etc. These forces between the tip and the sample cause deflection in the cantilever and these changes are captured by the photodiode with the help of a laser that is focused on the tip of the cantilever. Depending on the application operating

mode, the acquisition of the sample surface is different. The most basic imaging modes are static (contact) and dynamic (non-contact or tapping) mode.

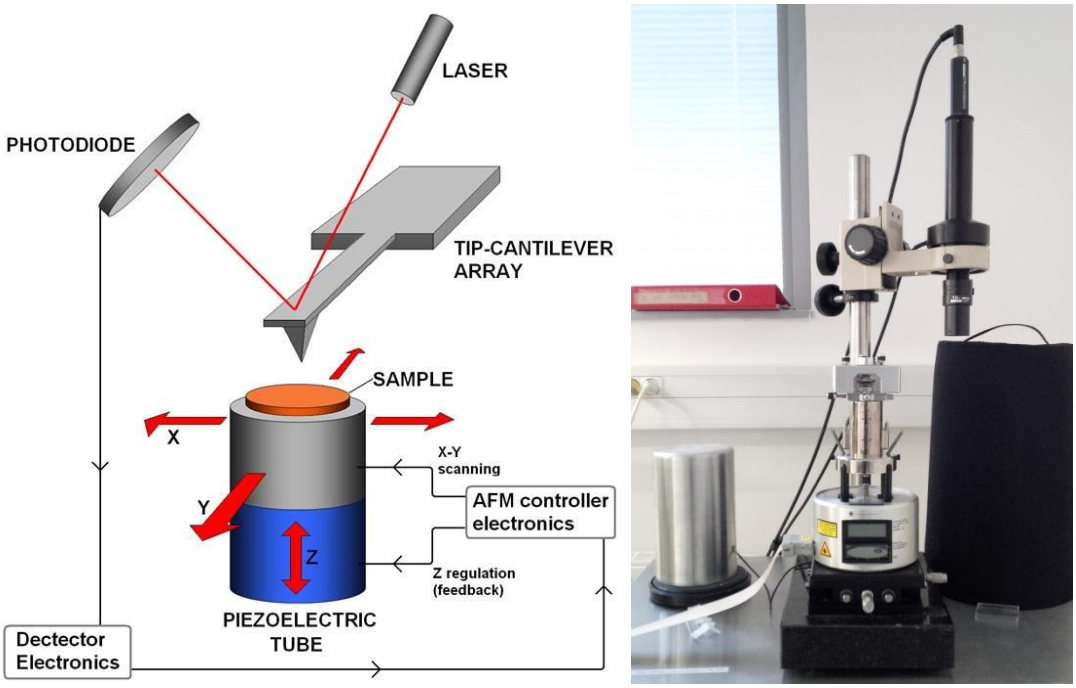

Figure 0.3: Schematic of the AFM set-up and the photograph of NanoScope AFM installed in GREYC/CIMAP, Caen, France.

Static Mode (contact mode):

In *static mode*, the tip touches the sample surface and scans the surface and the contours of the surface are measured by using the deflection of the cantilever directly.

Dynamic mode:

In *tapping mode*, the cantilever is driven to oscillate up and down at or near its resonance frequency. Hence, the tip directly hits the sample surface. This could damage the sample of the sample is very soft and also the lifetime of the tip is small compared to the contact mode. The frequency and drive amplitude of the cantilever is kept constant while scanning the sample.

Here, in my thesis, I always used *tapping mode* to study the surface morphology of the films.

Annex-III: Device Fabrication Techniques

In this thesis, we attempted to fabricate MEMS type devices by using SOI substrates and to integrate functional oxides on the SOI substrates. Therefore, here I will briefly introduce the techniques that are used for fabrication of devices in sequential order.

Spin coater:

Spin coating is considered as the first step in any fabrication process. It is used to evenly coat photoresist (PR) material (Shipley S 1813), a light-sensitive polymer that can be further used in microfabrication process.

The principle of operation: The flat substrate is held under vacuum and the small amount of coating material is applied at the center of the substrate which is either spinning at low/zero speed. Then the substrate is rotated at a very high speed in order to evenly spread the PR on the substrate by centrifugal force. The PR coated substrate is baked immediately on a hot plate at 90°C for 5 minutes, which is often termed this step as *soft-bake*. Once this step has finished, the sample is ready for the further lithography process.

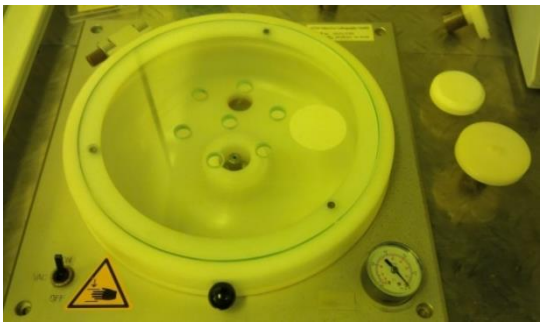

Figure 0.1: Photograph of spin coater used to apply photoresist on the surface of different materials such as LSMO, SOI, etc. in the cleanroom of class 1000 (ISO 6) at GREYC Laboratory.

MJB3 Mask Aligner:

The mask aligner is used in a photolithography process to transfer patterns from the mask onto the underlying substrates by using ultraviolet rays. Since we are using light rays, this type of lithography is also called as “optical lithography”. This system has the possibility to handle the wafer sizes up to 3 inches.

The principle of operation: Place the mask on the mask holder and substrate onto the chunk. Then, with the help of alignment screws, align the substrate under the desired mask pattern as parallel as possible. This parallel alignment step helps to minimize the errors that occur during the pattern transfer process. Once the alignment is finished, choose the desired exposure mode, exposure time and press the exposure button. Once the exposure finished successfully, the pattern from the mask will be transferred onto the substrate. One of the limitations using optical lithography is that the pattern on the mask is not 100% reproduced onto the substrate. It happens due to the proximity effects, UV lamp intensity distribution and most importantly scattering and diffraction of light. The Rayleigh equation is given as

$$W = \frac{K\lambda}{N.A}$$

Where 'K' 'λ' 'N.A' are the resolution, wavelength and the numerical aperture. Therefore, the resolution is mainly depends on the wavelength and the numerical aperture.

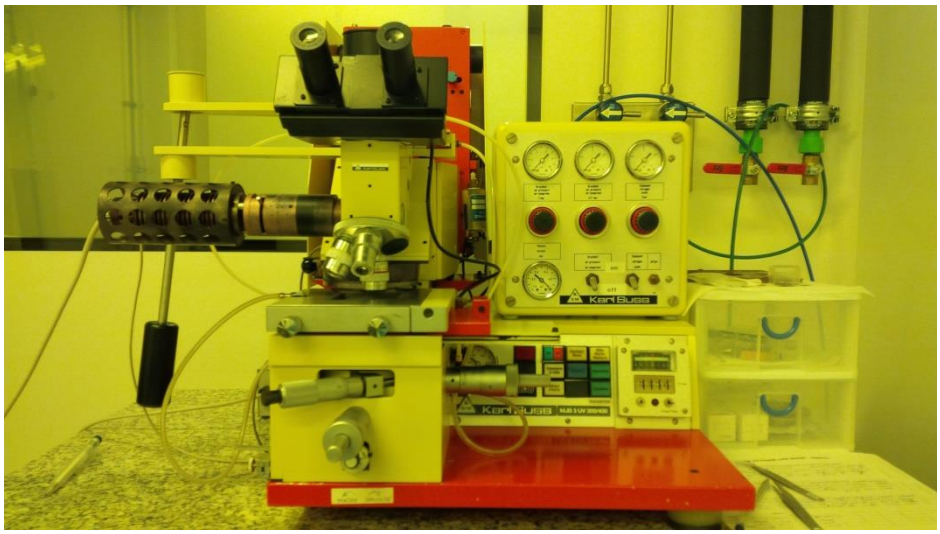

Figure 0.2: Photograph of the MJB3 Mask aligner for UV photolithography in cleanroom of class 1000 (ISO 6) at GREYC laboratory

Exposure Modes:

In MJB3 mask aligner, we have the possibility to choose between three different types of exposure modes just by selecting HP/ST button.

ST (standard) mode:

The ST mode is classified into two different modes i.e. *soft contact* and *hard contact* mode.

In *soft contact* mode, the substrate is held by vacuum and it is also pressed against the mask by means of mechanical pressure.

In *hard contact* mode, the substrate is pressed against the mask by N_2 gas and also mechanical pressure. Therefore, the resolution in hard contact mode is better than the soft contact mode.

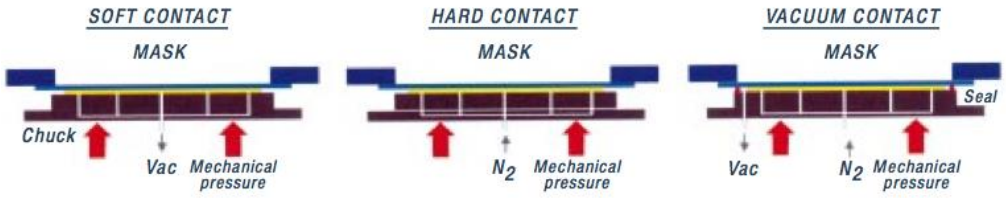

Figure 0.3: Three different types of contact modes available in the MJB3 mask aligner such as soft, hard and vacuum contact mode.

HP or Vacuum contact mode:

HP or *vacuum contact* mode is the combination of soft and hard contact modes. In this mode, a vacuum is applied between the substrate and the mask. Therefore, the vacuum helps to reduce the gap between substrate and mask. The gap is only limited to the roughness/flatness of the substrate/mask and/or due to dust particles, if present any. Additional to vacuum, the substrate is pressed against the mask by means of N_2 gas and mechanical pressure. Hence, HP mode is quite interesting as one could achieve the highest possible resolution. All the configurations are schematically depicted in Figure 0.3.

Developing:

After the lithography step, the substrates are immersed into developer solution (often the developer is a strong base). If it is positive PR, then the material exposed under UV is removed. If it is negative PR, then the unexposed part is removed. After developing, the substrates are baked again and are called as "*hard baking*". This step helps in having well-defined PR structure. Hence, the substrate is ready for etching.

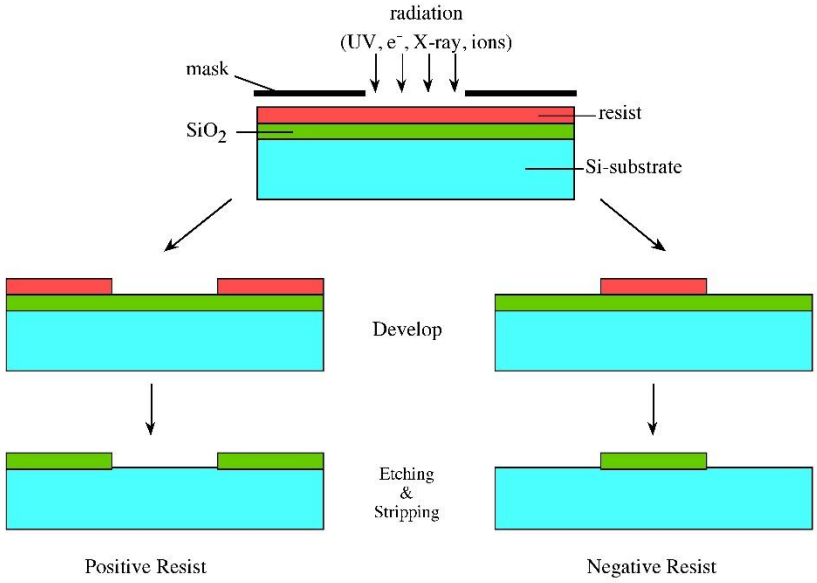

Figure 0.4: Schematic representation of the developing process step by using positive and negative photoresist.

Etching:

In order to fabricate any kind of microstructures or micro-devices, etching is an essential step. In layman terms, etching can be defined as "a process to remove unwanted material from the substrates". Etching can be classified into two types.

- Dry etching
- Wet etching

Dry etching:

Dry etching as the name suggests the etching is done in a dry environment. Depending on the process, one can use reactive gaseous species, physical bombardment, Plasma etching etc. In this thesis, we used two dry etching techniques such as Ion milling and reactive ion etching (RIE)

Ion Beam Etching:

Ion Beam Etching (IBE) is a widely used technique to etch wide range of materials during the fabrication process.

The principle of operation: Argon ions are extracted from an ion source are accelerated and directed to form a mono-energetic beam. It is used to etch any materials by pure physical sputtering (no chemistry dependence) such as piezo and ferroelectrics, magnetic materials etc. IBE produces anisotropic etching with well-defined sidewalls. Allows profile/sidewalls control thanks to a variable etch beam angle relative to sample surface features. In this thesis, we used IBE to etch LSMO, STO materials.

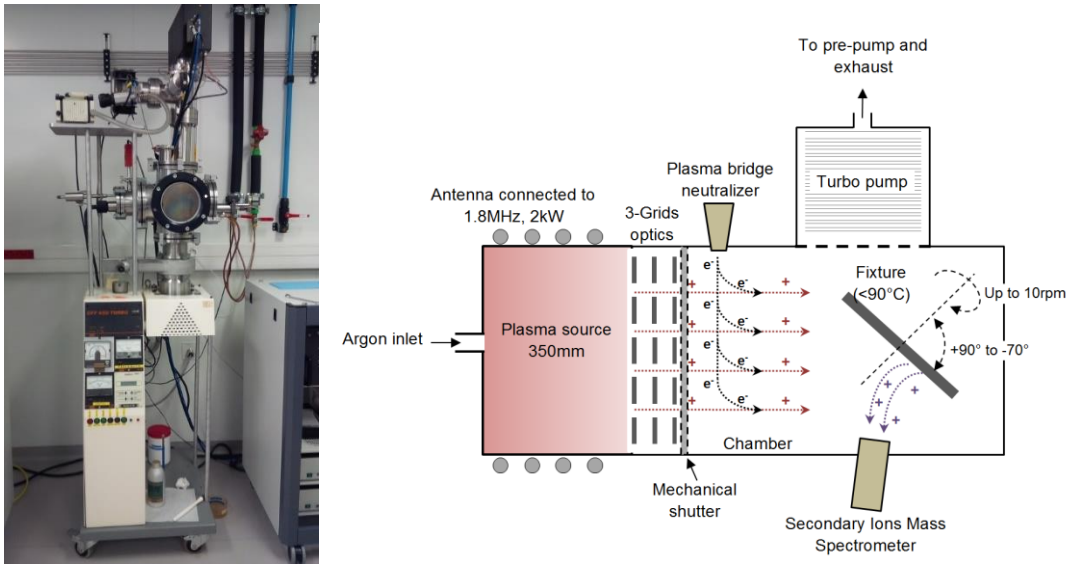

Figure 0.5: (left) Photograph of Ion Beam Etching (IBE) installed in the cleanroom at GREYC, Caen. (right) Schematic of the etching process.

Reactive Ion Etching (RIE):

RIE technique is a commonly used technique in the fabrication process. It is often used for anisotropic etching i.e. a directional etching process in which chemically reactive gases and ion bombardment are used to remove the material. RIE is directional etching technique that uses both physical action and chemical reaction to remove the etchant material. However, RIE does not have better selectivity compared to wet chemical etching. RIE is a well-known technique for anisotropic etching and to fabricate very high aspect ratios structures. And the advantage with dry technique is there is no additional step to rinse in liquid, avoiding stiction problems. Hence, it is a widely used technique

The principle of operation: The wafers are placed on a plate with electrical connections in the etching chamber and feed gases are introduced into the chamber. Depending on the etching material, the feed gases are wisely chosen. Once the desired vacuum is attained, the feed gases are introduced and RF power is switched ON. Plasma is initiated by applying RF power at 13.56 MHz to the powered electrode (cathode), whereas the other electrode (anode, or vacuum vessel, for example) is grounded. The electric field ionizes the gas molecules, creating the plasma. Generation of reactive gaseous species in the bulk plasma (excited molecules, radicals, etc.) and the density of the charged species (ions and electrons) totally depend on the applied RF power. An additional DC bias voltage is applied to extract the ions from the "bulk" plasma and energizes them towards the sample. Thus, DC bias contributes to the directionality of etching and desorption of reaction byproducts from a wafer surface.

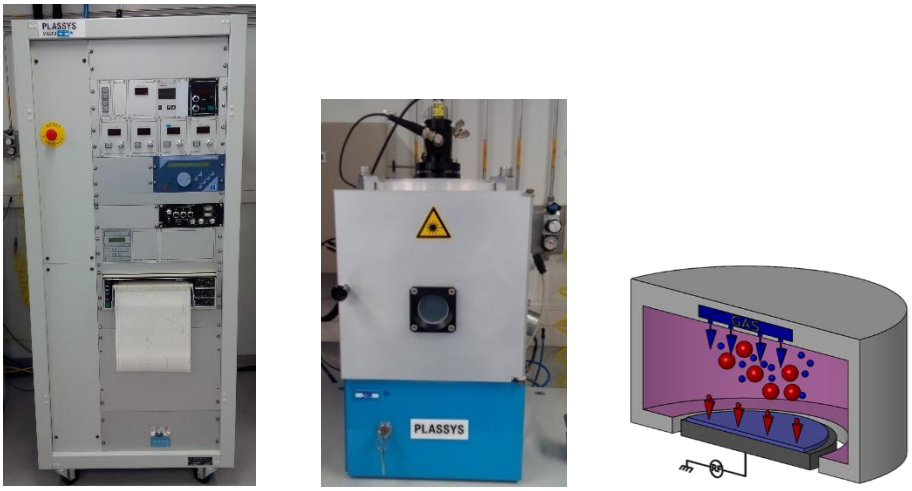

Figure 0.6: (left to right) Reactive Ion Etching controller, vacuum chamber (model: PLASSYS MG 200) installed in the cleanroom at GREYC, Caen and (right) schematic of the process during the plasma ignition.

Our RIE system is equipped with four gases such as Ar, O_2, CHF_3, and SF_6. The Table 0.1 illustrated below gives the details about the etching material and etchants along with the etching rate. In this thesis, we used RIE for etching Si and SiO_2.

Table 0.1: Parameters that were used in this study to etch Si and SiO_2 along with their etching rate is tabulated

Etching material	Etchant	Gas flux (sccm)	Power (W), pressure (Torr)	Etching rate
Silicon	SF_6	30	40, 0.03	~ 0.85 µm/min
SiO_2	CHF_3 + 2% O_2	30 + 0.6	75 , 0.04	~ 45 nm/min
Photoresist (Ashing)	O_2	20	15 , 0.03	~ 70 nm/min
Cleaning	Ar + O_2	20 + 20	30, 0.03	----------

Wet chemical etching:

Wet etching is the process of etching done at liquid phase. The chemicals used for etching process are called etchants. Wet etching uses a bath of etchants for etching. However, this method is not very precise; it is easy to handle compared to the dry etching process. The basic principle in wet etching is that the material that is to be removed is dissolved by immersing it in an appropriate chemical bath. In my thesis, I used wet etching technique to etch SiO_2 material in SOI substrate.

SiO_2 etching:

SiO_2 is always used as a sacrificial layer in all the microelectronic devices. It is etched by HF acid. Although the etching rate is quite fast in the wet etching, we also need to take care of the structures since they are prone to collapse due to strong Vander wall forces. This is called as *stiction* and it is the major problem one has to overcome in the wet etching process.

$$SiO_2 + 4\,HF \rightarrow SiF_4 + 2H_2O$$

$$SiO_2 + 6\,HF \rightarrow H_2SiF_6 + 2H_2O$$

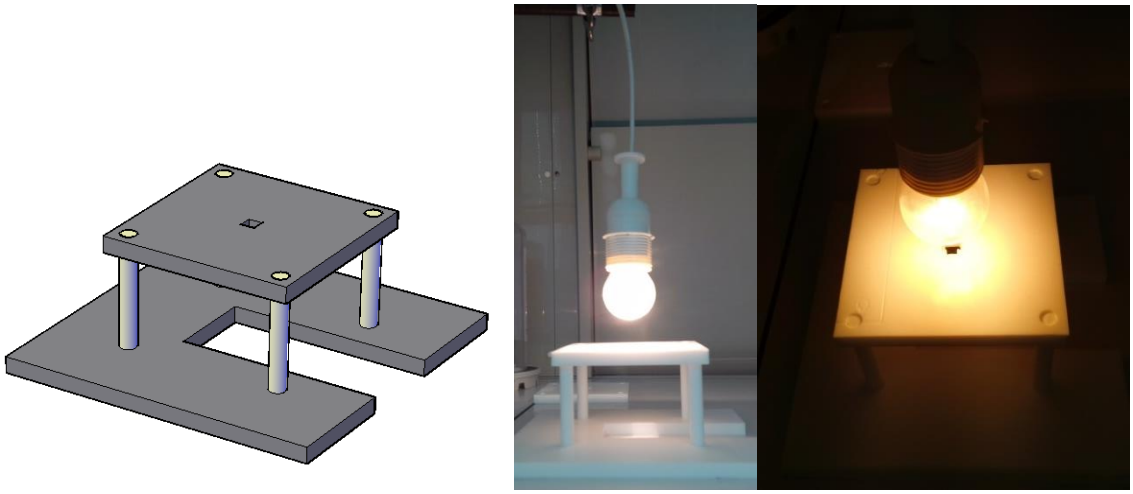

Figure 0.7: (Left) Design of the HF table by using AutoCAD, (right) side-view and top-view of the HF set-up table that was fabricated using Teflon sheets. The 60 watt light bulb in the picture helps us to heat the samples in non-contact mode.

In this thesis, we have used wet etching by immersing the SOI substrate into HF solution and to remove the unwanted portion of SiO_2. However, due to stiction problems, we have also employed another technique by using HF vapors. It helps to isotropic SiO_2 etching but there are a lot of limitations and challenges. The etching rate is quite low. The temperature window is too narrow to have best results during etching. HF is too dangerous to handle and additional safety precautions have to be taken. Along with SiO_2, HF also etches most of the metals such as Ti, Cr, Cu etc. that are generally used for interconnects, contact

pads in the devices. We have tried different ways to etch by playing with the temperature of the substrate, etching concentration. However, we are still at the beginning and further experiments are needed to be done to optimize the etching conditions.

Table 0.2: SiO_2 etching rate under different HF concentrations and configurations.

HF	Etching rate	Temperature	Without heating
HF Liq (4%)	28 nm/min	20°C	In the HF liquid cases, all the structures are stick to the bottom due to stiction and strong capillary forces acting between the microstructures.
HF Liq (10%)	60 nm/min	20°C	
HF Vapor (10%)	8 nm/min	20°C	
HF vapor (40%)	200 nm/min	20°C	
With bulb heating			
HF vapor (48%)		20°C	Condensation
HF vapor (48%)		80°C	No etching

Table 0.3: Difference between dry and wet etching techniques

	Dry etching	Wet etching
Definition	Etching is done in plasma phase	Etching is done in liquid phase
Etching profile	Anisotropic (mostly)	Isotropic
Selectivity	Less selective	More selective
Etching rate	Quite slow	Very fast
Precision	More precise	Less precise
Chemical usage	Few chemicals	Many chemicals
Cost	Expensive because of specialized equipment	Less expensive (only the cost of chemicals)
Safety	Much safer	Risky since one has to deal with many dangerous chemicals

Mechanical Profilometer:

Mechanical or stylus Profilometer is one of the metrology tools often used to measure the thickness, step heights, and widths on a sample surface. With add-ons, one could even construct 3D images of the surface.

The principle of operation: The operating principle is quite simple. The diamond coated tip with a radius of curvature varying between tens of microns to hundreds of micros. The sample is mounted on an XY-stage which can be rotated to adjust the position that you would like to scan. As soon as the tip approaches the sample surface, the tip starts to scan the

surface with predefined tip force, scan rate and scan speed etc. The advantage of this technique is the possibility to measure larger scan area with higher scan speed.

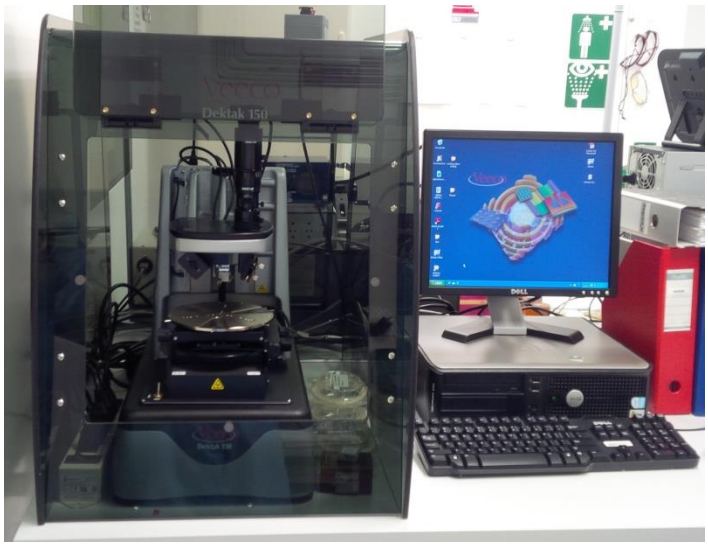

Figure 0.8: Pictograph of Mechanical Profilometer installed in the cleanroom at GREYC, Caen.

Here, in my thesis, I often used this technique to measure the thickness of the metallic layers (Au, Cr, Ti, and Pt) that are coated on the substrates. I also used this technique to measure the vertical height profiles during etching and fabrication of devices to evaluate the approximate etching rate.

Annex-IV: Device Fabrication Process

As said before, we made an attempt to fabricate MEMS-based devices such as cantilevers. Therefore, here I will provide the details of the fabrication process

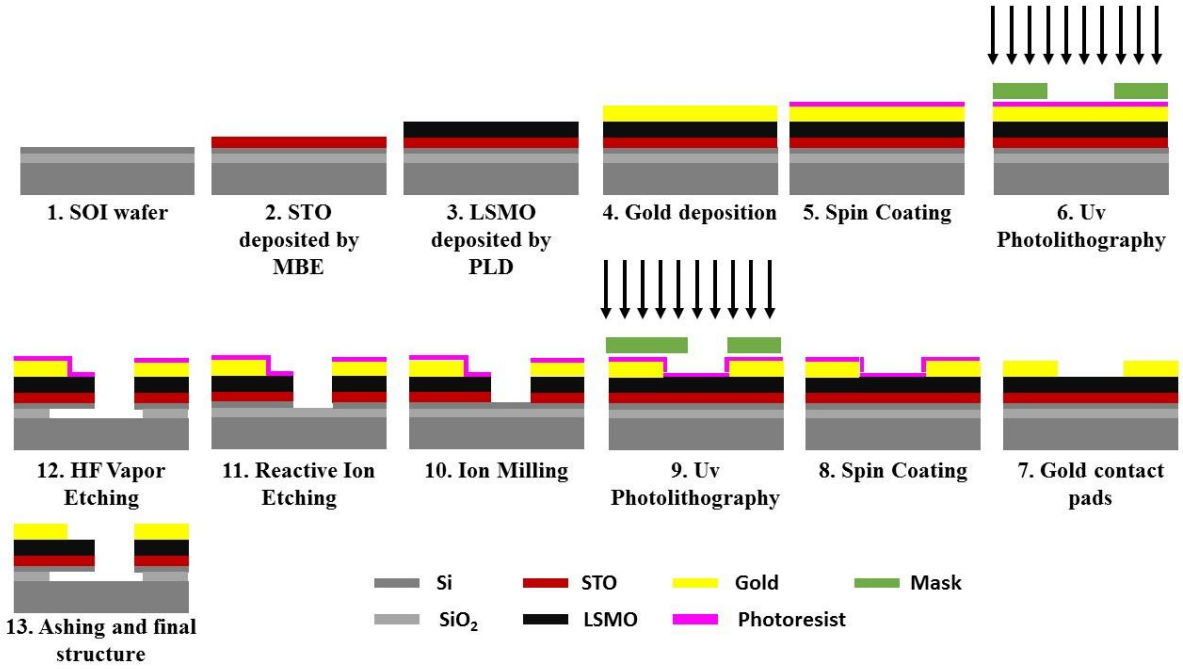

Figure 0.1: Schematic of the step-by-step process that are involved in the fabrication of LSMO/STO/Si cantilevers.

Steps involved in fabrication:

1. Here, we are using two different SOI substrates with different device layer thicknesses as 220 nm and 440 nm. Although, most of the Let us consider SOI with 440 nm thick device layer as SOI-1 and SOI 220 nm as SOI-2.
2. STO (001) thin films of 20 nm thick are deposited on SOI – 1 and 2 by MBE technique at Cornell University, USA on 3-inch wafers. These 3-inch wafers are then cut into 10x10 mm^2 and 5x10 mm^2 substrates by using a diamond wire cutter. The substrates were then subsequently rinsed with toluene, acetone, ethanol and DI water to remove all the residues from the surface of the film.
3. LSMO (001) thin films were deposited on top of STO (001) layer by PLD at GREYC, Caen[20].
4. Gold (Au) is deposited by GATAN with Cr as an adhesive layer.
    a. Au/Si is not strongly adhesive (the gold layer is getting peeled off from the silicon surface during the sonication process)
    b. An adhesive layer such as Cr, Pt, Ti can be deposited on Silicon as these layers improve the adhesiveness of Au.
5. Photoresist (PR) was deposited on 10x10 mm^2 and 5x10 mm^2 SOI substrates by using a spin coating.

[20] This step is still under progress to optimize the growth conditions by PLD technique

6. The PR coated substrates were patterned using UV photolithography. This step helps in fabricating contact pads
7. The substrates were then developed in KI solution to make Au contact pads.
8. Step 5 is repeated
9. Step 6 is repeated to pattern the device structures. After UV exposure, the samples are developed, baked to produce well-defined PR structures. This step is crucial in any device fabrication process because the final structures are almost replicate of the PR structures.
10. By using Ion Milling or IBE, LSMO and STO layers are anisotropically etched to create vertical wall profiles. We purposefully etch the samples a bit longer than the required time to ensure that the material is fully removed.
11. RIE is being used
    a. To etch Si anisotropically by using SF_6 plasma. (quite efficient)
    b. For etching SiO_2 isotropically, I used CHF_3 + 2% O_2 plasma. With different trails (different power, pressures and O_2%), I only succeeded in perfect anisotropic etching. As our goal is to etch SiO_2 isotropically, but there is no under etching which can also be seen in Figure 0.2.

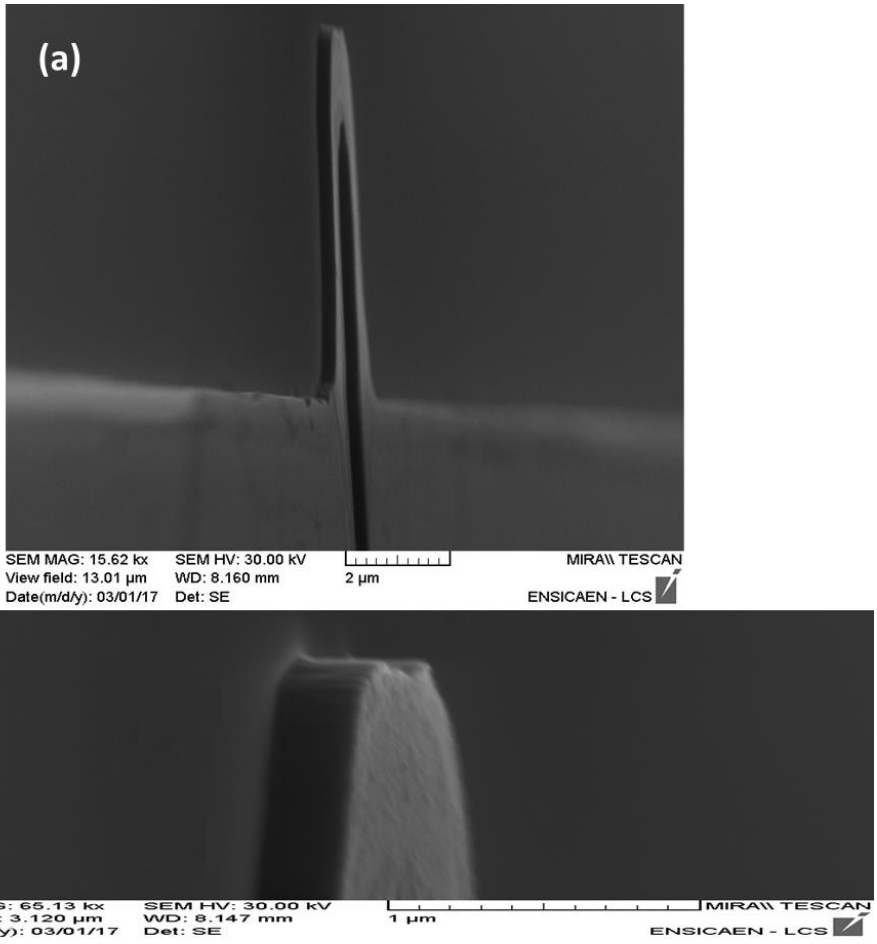

c.

Figure 0.2: SEM micrographs of the Si cantilevers after etching for about 1 hour in RIE. From the pictures, it is clear that there is no lateral etching of the SiO_2 surface.

This is because the by-product released during the reaction between CHF_3 and SiO_2 mixture of polymer chains with C-H bonds. Because of this polymerization on the surface, the directed ions couldn't remove the polymers on the sidewalls hence diminishing the etching and only helping it for vertical etching. Therefore, there is no way to use RIE for etching SiO_2 and I turned towards classical wet chemical etching technique.

12. HF vapor etching

Before discussing why we moved to HF vapor, I will briefly discuss the details and challenges that we faced by using WET HF chemical etching. Wet chemical etching is an efficient route to get better selectivity and etching rate for bulk material etching. Mostly, wet etching is isotropic (this is our goal) and the etching rates are different along different crystallographic orientations. In addition, while fabricating microstructures, chemical etching is not always recommended because of the stiction problem, the structures always get collapsed and are not useful for any MEMS practical applications. The stiction is due to very high capillary forces at the micron scale arises between the etchant liquid structures as can be seen in Figure 0.3. To overcome this stiction problem, critical point dryer is often used to release MEMS structures successfully, which is also a complicated process. As we don't have the possibility to use critical point dryer, we turned towards dry vapor etching techniques.

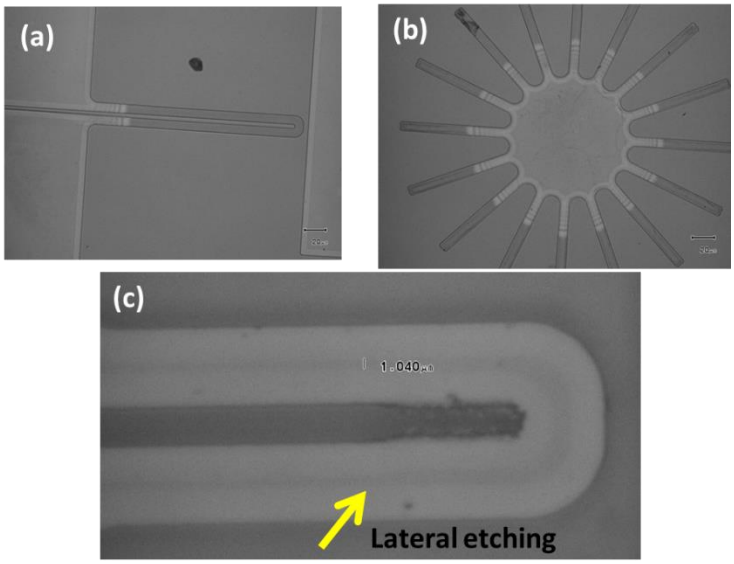

Figure 0.3: Optical microscopy photographs of the Si cantilevers after etching SiO_2 with wet HF technique. Thanks to wet chemical etching, we finally observed lateral etching of SiO_2 due to isotropic etching medium. But, because of strong capillary forces, the Si cantilevers are collapsed and get stuck to the bottom surface.

To avoid the above stiction problem, we have come with another idea to deposit Au/Cr on top of SOI substrates and to perform HF wet etching. To our surprise, this step was very successful as we could see the structures are suspended and not collapsed. This Au/Cr deposition would induce strain on the silicon cantilevers that is high enough to overcome the capillary forces at the interface between structures. The optical photographs of suspended Au/Cr/Si cantilevers can be seen in Figure 0.4. By considering the Figure 0.4(b) as a reference, by focusing in and out the optical lens, we could see the difference in structures in

Figure 0.4 (a and c). In addition, in Figure 0.4(e), there is a gradient change in the shining surface and this change is also due to the bending of cantilevers.

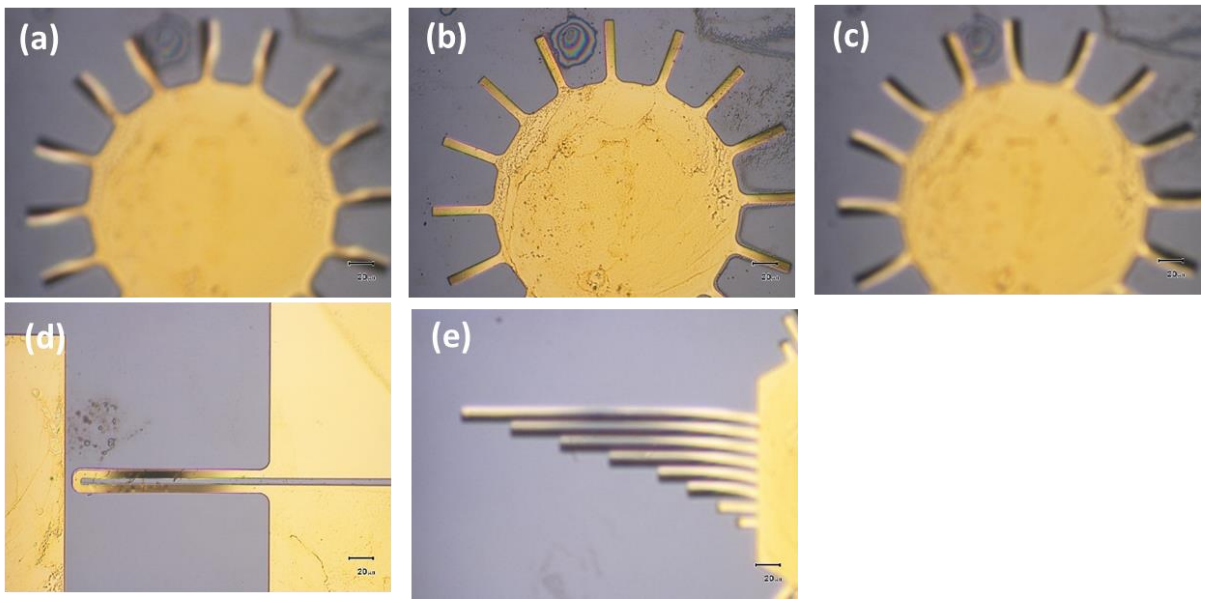

Figure 0.4: Optical microscopy photographs of Au/Cr/Si cantilevers that are suspended and can be easily visualized by observing the change in light diffraction, shadows etc.

HF Vapor etching:

HF vapor etching is another route to etch SiO_2 by considering this technique as pseudo-Dry etching. We made an attempt to check and overcome the stiction problems. HF at room temperature ~20-25°C will releases vapors and these vapors can be concentrated onto SiO_2 material that needed to be etched. The main challenge we faced here is to avoid condensation of by-products that are released during HF and SiO_2 interaction on the sample surface as shown in Figure 0.5. Therefore, in order to have an optimum SiO_2 etching rate and to avoid condensation on the sample surface, the temperature of the sample is a key factor. Fukuta Y *et al.* [166], had demonstrated very simple and reliable method to etch silicon oxide sacrificial layer by using HF vapor etching. One of the possible solutions is to heat the sample through non-contact mode, which helps in avoiding condensation on the sample surface. As the temperature on the sample surface increases, the etching rate monotonically decreases. On the other hand, if we decrease the temperature on the sample surface, condensation occurs that leads to stiction. Therefore, there exists a quite narrow temperature window as highlighted in Figure 0.5 as an area of interest. This process step is yet to be optimized.

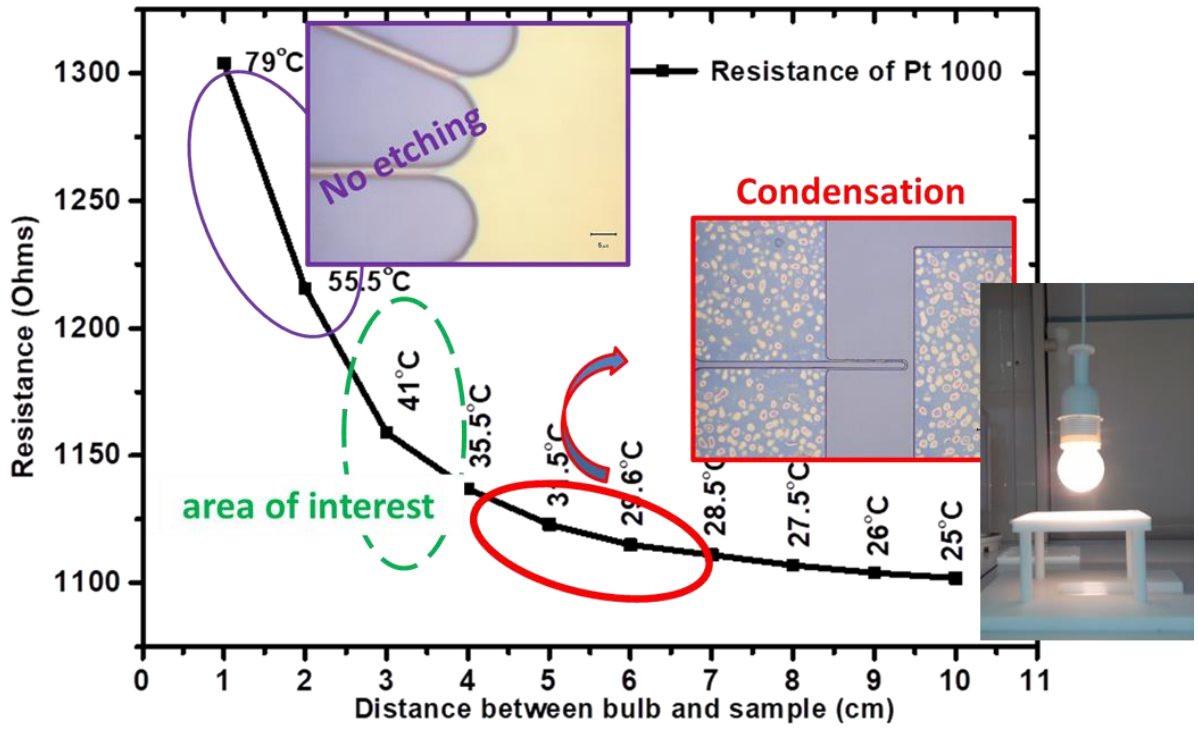

Figure 0.5: Temperature measured on the sample surface by varying the distance between the 60 W light bulb and sample.

Annex-V: Chemical Mechanical Planarization or Polishing (CMP) process

IBM invented CMP in the late 80's to allow for more metal layers in the integrated circuits (IC) that they produced. It is primarily used to remove the step heights of dielectrics at multiple stages in the IC fabrication. Recent years, CMP has been a very popular technique for polishing and for thinning the samples for TEM. However, the way we used CMP process is for completely different purpose. We used this method to thin the "silicon" substrate by removing the material from the backside of the substrate.

The principle of operation: This process is purely based on the frictional and rotational forces. In this, the sample surface that needs to be polished is faced towards the rotating plate. We apply the pressure on the sample head and is pushed onto the bottom rotating plate. CMP slurry is added during the process, which reduces the friction forces. It also helps to get rid of the waste material present under the substrate, which is removed during the process. This experimental set-up is located in the CIMAP laboratory, Caen.

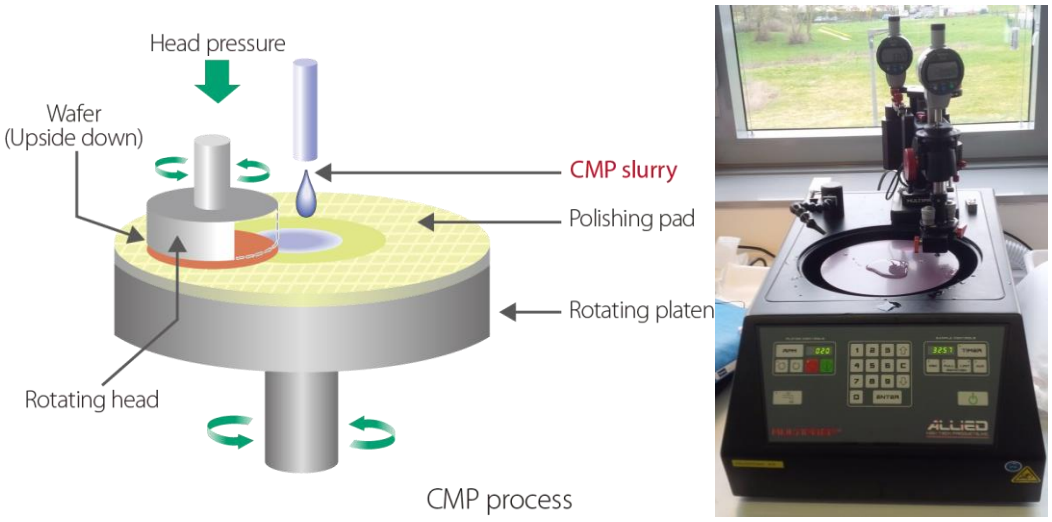

Figure 0.1: Schematic and the photograph of Chemical and Mechanical Polishing (CMP) process system that we used for thinning the silicon substrates.

Acknowledgements

First and foremost, I wish to thank my supervisor Dr. Laurence Mechin, responsible for the Electronic team at GREYC laboratory, for her expert guidance, support and encouragement since the days I began working on my thesis. She has been a great mentor and leader and provided me the right balance to complete my thesis.

I would like to offer my special thanks to Dr. Paolo Perna, researcher at IMDEA Nanoscience, Madrid who was very supportive during my stages in Madrid. He introduced to me MOKE magnetometry and always gives me constructive comments and warm encouragement.

Thanks to postdocs Dr. Olivier Rousseau (GREYC), Dr. Alice Galdi (Univ. of. Salerno) and PhD students at GREYC lab: May-Tia Yang, Elodie Portalier, Mario Eduardo, Vanuza Marques Do Nascimento and not to mention the master degree students Anass Taoussi, Aqel Ouefa, and Sergey Ivanchikhin with whom I had interesting discussions during my thesis.

I would like to especially thank Fernando Ajejas and Dr. Daniel Cano who helped me during my stages at IMDEA nanoscience, Madrid, Spain. Without their support, MOKE measurements wouldn't be possible.

Special thanks to

- Dr. Bruno Guillet, Prof. Stéphane Flament, and Dr. Olivier Mareschal at GREYC laboratory, Caen for assisting me with the mask design, COMSOL modeling and also at various stages during my thesis.
- Dr. Corentin Jorel and engineer Thomas Dietsch at GREYC for helping me in some of the fabrication techniques.
- Radu Constantin at GREYC for fabricating the Teflon table.
- Prof. Julio Camarero, IMDEA nanoscience, Madrid for fruitful discussions on MOKE during my stages in Madrid.
- Dr. Alain Pautrat, CRISMAT laboratory, Caen for SQUID measurements.
- Dr. Alexandre Petrov and Dr. Giovanni Vinai and Dr. Piero Torelli researchers at CNR-IOM, Trieste for helping us with MBE and MOKE techniques.
- Dr. Pasquale Orgiani, scientist at CNR-IOM, Trieste for HR-XRD measurements.
- Zhe Wang, Dr. Carolina Adamo and Prof. Darrell Schlom at Cornel University, USA for fabricating STO films on 3 inch SOI wafers by MBE technique.
- Dr. Damien Faurie, University of Villetaneuse, France for future FMR measurements under strain on our LSMO/STO/Si thinned samples.

I am also grateful to Marie-Pierre Chauvat and Cedric Frilay, technicians at CIMAP laboratory, Caen for helping me with CMP process and SiO_2 etching by using HF.

I would like to express my sincere gratitude to Nicole Delamotte and Gaelle Lenogue for taking care of the administrative works during my PhD journey.

I would like to thank everyone who helped me directly and indirectly during the course of a 3-year PhD journey in Caen, France.

I would like to acknowledge for the financial support received during my stages at IMDEA nanoscience, Madrid, Spain in June-July, 2015 and November-December, 2015 from Programme International de Coopération Scientifique (PICS) du CNRS and for September-October 2016 period from SIMEM Doctoral School.

I would also like to acknowledge TO – BE COST for financial support to attend International Summer school on Oxide Electronics (ISOE), held at Cargese, France in 2015. I also acknowledge NFFA – EU an H2020 program for accepting our project proposal ID: 334 and also providing financial support to perform experiments at CNR – IOM, Trieste, Italy.

Last but not least, I am very grateful to my parents Chaluvadi Hanmanth Rao and Chaluvadi Syamala Devi and my brother Chaluvadi Pradeep Kumar, who have provided me with moral and emotional support in my life. I am also grateful to my other family members and friends who have supported me along the way. Without their support and encouragement, this work would not be possible.

Sandeep Kumar Chaluvadi

List of Figures

List of Tables

References

[1] "50 Years of Moore's Law," *Intel*. [Online]. Available: https://www.intel.com/content/www/us/en/silicon-innovations/moores-law-technology.html.

[2] "Why EUV Is So Difficult," *Semiconductor Engineering*. [Online]. Available: https://semiengineering.com/why-euv-is-so-difficult/.

[3] "IBM100 - The Application of Spintronics." [Online]. Available: http://www-03.ibm.com/ibm/history/ibm100/us/en/icons/spintronics/.

[4] D. Sander, "The magnetic anisotropy and spin reorientation of nanostructures and nanoscale films," *J. Phys. Condens. Matter*, vol. 16, no. 20, pp. R603–R636, May 2004.

[5] C. Tannous and J. Gieraltowski, "The Stoner–Wohlfarth model of ferromagnetism," *Eur. J. Phys.*, vol. 29, no. 3, pp. 475–487, May 2008.

[6] S. S. P. Parkin, M. Hayashi, and L. Thomas, "Magnetic Domain-Wall Racetrack Memory," *Science (80-.).*, vol. 320, no. 5873, pp. 190–194, 2008.

[7] P. Perna, D. Maccariello, F. Ajejas, R. Guerrero, L. Méchin, S. Flament, J. Santamaria, R. Miranda, and J. Camarero, "Engineering Large Anisotropic Magnetoresistance in La 0.7 Sr 0.3 MnO 3 Films at Room Temperature," *Adv. Funct. Mater.*, vol. 27, no. 26, p. 1700664, Jul. 2017.

[8] M. Salehi-Fashami and N. D'Souza, "Exploring performance, coherence, and clocking of magnetization in multiferroic four-state nanomagnets," *J. Magn. Magn. Mater.*, vol. 438, pp. 76–84, Sep. 2017.

[9] M.V.PITKE, "Biaxial anisotropy for memory applications," *Czech J Phys B*, vol. 21, no. 2, pp. 467–469, 1971.

[10] S. Peng, M. Wang, H. Yang, L. Zeng, J. Nan, J. Zhou, Y. Zhang, A. Hallal, M. Chshiev, K. L. Wang, Q. Zhang, and W. Zhao, "Origin of interfacial perpendicular magnetic anisotropy in MgO/CoFe/metallic capping layer structures," *Sci. Rep.*, vol. 5, no. 1, p. 18173, Nov. 2015.

[11] D. Wu, Z. Zhang, L. Li, Z. Zhang, H. B. Zhao, J. Wang, B. Ma, and Q. Y. Jin, "Perpendicular magnetic anisotropy and magnetization dynamics in oxidized CoFeAl films," *Sci. Rep.*, vol. 5, p. 12352, Dec. 2015.

[12] T. Liu, Y. Zhang, J. W. Cai, and H. Y. Pan, "Thermally robust Mo/CoFeB/MgO trilayers with strong perpendicular magnetic anisotropy," *Sci. Rep.*, vol. 4, p. 5895, May 2014.

[13] J. M. Shaw, H. T. Nembach, M. Weiler, T. J. Silva, M. Schoen, J. Z. Sun, and D. C. Worledge, "Perpendicular Magnetic Anisotropy and Easy Cone State in Ta/Co 60 Fe 20 B 20 /MgO," *IEEE Magn. Lett.*, vol. 6, no. January, p. 3500404 (1-4), 2015.

[14] K.-W. Park, J.-Y. Park, S. C. Baek, D.-H. Kim, S.-M. Seo, S.-W. Chung, and B.-G. Park, "Electric field control of magnetic anisotropy in the easy cone state of Ta/Pt/CoFeB/MgO structures," *Appl. Phys. Lett.*, vol. 109, no. 1, p. 12405, Jul. 2016.

[15] W. S. Choi, J. H. Kwon, H. Jeen, J. E. Hamann-Borrero, A. Radi, S. Macke, R. Sutarto, F. He, G. A. Sawatzky, V. Hinkov, M. Kim, and H. N. Lee, "Strain-induced spin states in atomically ordered cobaltites," *Nano Lett.*, vol. 12, no. 9, pp. 4966–4970, 2012.

[16] J. M. Rondinelli and N. A. Spaldin, "Structure and properties of functional oxide thin films: Insights from electronic-structure calculations," *Adv. Mater.*, vol. 23, no. 30, pp. 3363–3381, 2011.

[17] S. Jin, T. H. Tiefel, M. McCormack, R. A. Fastnacht, R. Ramesh, and L. H. Chen, "Thousandfold Change in Resistivity in Magnetoresistive La-Ca-Mn-O Films," *Science*, vol. 264, no. 5157, pp. 413–415, Apr. 1994.

[18] A. M. Haghiri-Gosnet and J. P. J. Renard, "CMR manganites: physics, thin films and devices," *J. Phys. D. Appl. Phys.*, vol. 36, no. 8, pp. R127–R150, Apr. 2003.

[19] J. Hemberger, A. Krimmel, T. Kurz, H.-A. K. von Nidda, V. Y. Ivanov, A. A. Mukhin, A. M. Balbashov, and A. Loidl, "Structural, magnetic and electrical properties of single crystalline La_(1-x)Sr_xMnO_3 for 0.4 < x < 0.85," *Phys. Rev. B*, vol. 66, no. 9, pp. 22–24, 2002.

[20] A. Urushibara, Y. Moritomo, T. Arima, A. Asamitsu, G. Kido, and Y. Tokura, "Insulator-metal transition and giant magnetoresistance in La1-xSrxMnO3," *Phys. Rev. B*, vol. 51, no. 20, pp. 14103–14109, 1995.

[21] K. I. Doig, F. Aguesse, A. K. Axelsson, N. M. Alford, S. Nawaz, V. R. Palkar, S. P. P. Jones, R. D. Johnson, R. A. Synowicki, and J. Lloyd-Hughes, "Coherent magnon and acoustic phonon dynamics in tetragonal and rare-earth-doped BiFeO3 multiferroic thin films," *Phys. Rev. B*, vol. 88, no. 9, p. 94425, Sep. 2013.

[22] A. Vailionis, H. Boschker, W. Siemons, E. P. Houwman, D. H. A. Blank, G. Rijnders, and G. Koster, "Misfit strain accommodation in epitaxial ABO3 perovskites: Lattice rotations and lattice modulations," *Phys. Rev. B - Condens. Matter Mater. Phys.*, vol. 83, no. 6, pp. 1–10, 2011.

[23] J. M. D. Coey, M. Viret, and L. Ranno, "Electron Localization in Mixed-Valence Manganites," *Phys. Rev. Lett.*, vol. 75, no. 21, pp. 3910–3913, Nov. 1995.

[24] J. M. D. Coey, M. Viret, and S. von Molnár, "Mixed-valence manganites," *Adv. Phys.*, vol. 48, no. 2, pp. 167–293, Nov. 1999.

[25] Y. Tokura and Y. Tomioka, "Colossal magnetoresistive manganites," *J. Magn. Magn. Mater.*, vol. 200, no. 1–3, pp. 1–23, Oct. 1999.

[26] L. W. Martin, Y. H. Chu, and R. Ramesh, "Advances in the growth and characterization of magnetic, ferroelectric, and multiferroic oxide thin films," *Mater. Sci. Eng. R Reports*, vol. 68, no. 4–6, pp. 89–133, 2010.

[27] H. Lüth, *Solid Surfaces, Interfaces and Thin Films*, Fifth edit. Springer, 2010.

[28] Y. Wang, W. Chen, B. Wang, and Y. Zheng, "Ultrathin ferroelectric films: Growth, characterization, physics and applications," *Materials (Basel).*, vol. 6, no. 9, pp. 6377–6485, 2014.

[29] J. G. Bednorz and K. a. Muller, “Possible High Tc Superconductivity in the Ba - La - Cu - O System,” *Zeitschrift für Phys. B Condens. Matter*, vol. 64, pp. 189–193, 1986.

[30] J. Shen, Z. Gai, and J. Kirschner, *Growth and magnetism of metallic thin films and multilayers by pulsed-laser deposition*, vol. 52, no. 5–6. 2004.

[31] D. H. A. Blank, M. Dekkers, and G. Rijnders, “Pulsed laser deposition in Twente: from research tool towards industrial deposition,” *J. Phys. D. Appl. Phys.*, vol. 47, no. 3, p. 34006, Jan. 2014.

[32] H. M. Christen and G. Eres, “Recent advances in pulsed-laser deposition of complex-oxides H. M. Christen and G. Eres Materials Science and Technology Division, Oak Ridge National Laboratory, Oak Ridge, TN 37831, USA.”

[33] G. Rijnders, “The initial growth of complex oxides : study and manipulation (Doctoral dissertation),” 2001.

[34] N. Popovici, “Pulsed Laser Deposition of Oxides,” 2009.

[35] B. Shin, J. P. Leonard, J. W. McCamy, and M. J. Aziz, “Comparison of morphology evolution of Ge(001) homoepitaxial films grown by pulsed laser deposition and molecular-beam epitaxy,” *Appl. Phys. Lett.*, vol. 87, no. 18, pp. 1–3, 2005.

[36] Marc Madou, *Fundamentals of microfabrication*, Second edi. CRC press LLC, 1997.

[37] J. H. Haeni, C. D. Theis, and D. G. Schlom, “RHEED Intensity Oscillations for the Stoichiometric Growth of $SrTiO_3$ Thin Films by Reactive Molecular Beam Epitaxy,” *J. Electroceramics*, vol. 4, no. 2, pp. 385–391, 2000.

[38] T. W. Zhang, Z. W. Mao, Z. B. Gu, Y. F. Nie, and X. Q. Pan, “An efficient and reliable growth method for epitaxial complex oxide films by molecular beam epitaxy,” vol. 11601, no. 1 1, pp. 1–4, 2017.

[39] “UHV Molecular Beam Epitaxy,” *AdNaNotek - UHV system*, 2017. [Online]. Available: http://www.dualsignal.com.tw/molecular-beam-epitaxy-mbe.html.

[40] F. Tang, T. Parker, G.-C. Wang, and T.-M. Lu, “Surface texture evolution of polycrystalline and nanostructured films: RHEED surface pole figure analysis,” *J. Phys. D. Appl. Phys.*, vol. 40, pp. R427–R439, 2007.

[41] “Solutions | PASCAL CO., LTD.,” 2017. [Online]. Available: http://www.pascal-co-ltd.co.jp/solutions/index.html.

[42] B. Wang, L. You, P. Ren, X. Yin, Y. Peng, B. Xia, L. Wang, X. Yu, S. Mui Poh, P. Yang, G. Yuan, L. Chen, A. Rusydi, and J. Wang, “Oxygen-driven anisotropic transport in ultra-thin manganite films,” *Nat. Commun.*, vol. 4, no. May 2012, pp. 1–7, 2013.

[43] B. Cui, C. Song, G. Y. Wang, H. J. Mao, F. Zeng, and F. Pan, “Strain engineering induced interfacial self-assembly and intrinsic exchange bias in a manganite perovskite film.,” *Sci. Rep.*, vol. 3, p. 2542, 2013.

[44] C. Adamo, X. Ke, H. Q. Wang, H. L. Xin, T. Heeg, M. E. Hawley, W. Zander, J. Schubert, P. Schiffer, D. A. Muller, L. Maritato, and D. G. Schlom, “Effect of biaxial

strain on the electrical and magnetic properties of (001) La0.7Sr0.3MnO3 thin films," *Appl. Phys. Lett.*, vol. 95, no. 11, p. 112504, Sep. 2009.

[45] F. Zighem, D. Faurie, S. Mercone, M. Belmeguenai, and H. Haddadi, "Voltage-induced strain control of the magnetic anisotropy in a Ni thin film on flexible substrate," *J. Appl. Phys.*, vol. 114, no. 7, p. 73902, Aug. 2013.

[46] M. Gueye, B. M. Wague, F. Zighem, M. Belmeguenai, M. S. Gabor, T. Petrisor, C. Tiusan, S. Mercone, and D. Faurie, "Bending strain-tunable magnetic anisotropy in Co 2 FeAl Heusler thin film on Kapton ®," *Appl. Phys. Lett.*, vol. 105, no. 6, p. 62409, Aug. 2014.

[47] M. Biasotti, L. Pellegrino, E. Bellingeri, C. Bernini, A. S. Siri, and D. Marre, "All-Oxide Crystalline Microelectromechanical systems," *Procedia Chem.*, vol. 1, no. 1, pp. 839–842, 2009.

[48] D. Le Bourdais, G. Agnus, T. Maroutian, V. Pillard, P. Aubert, R. Bachelet, G. Saint-Girons, B. Vilquin, E. Lefeuvre, and P. Lecoeur, "Epitaxial manganite freestanding bridges for low power pressure sensors," *J. Appl. Phys.*, vol. 118, no. 12, p. 124509, Sep. 2015.

[49] M. Biasotti, L. Pellegrino, R. Buzio, E. Bellingeri, C. Bernini, A. S. Siri, and D. Marré, "Fabrication and electromechanical actuation of epitaxial SrTiO3 (001) microcantilevers," *J. Micromechanics Microengineering*, vol. 23, no. 3, p. 35031, 2013.

[50] M. Mathews, F. M. Postma, J. C. Lodder, R. Jansen, G. Rijnders, and D. H. A. Blank, "Step-induced uniaxial magnetic anisotropy of La0:67Sr0:33MnO3 thin films," *Appl. Phys. Lett.*, vol. 87, no. 24, p. 242507, Dec. 2005.

[51] P. Perna, C. Rodrigo, E. Jiménez, F. J. Teran, N. Mikuszeit, L. Méchin, J. Camarero, and R. Miranda, "Tailoring magnetic anisotropy in epitaxial half metallic La0.7Sr0.3MnO3 thin films," *J. Appl. Phys.*, vol. 110, no. 1, p. 13919, Jul. 2011.

[52] O. Rousseau, R. Weil, S. Rohart, and A. Mougin, "Strain-induced magnetic domain wall control by voltage in hybrid piezoelectric BaTiO3 ferrimagnetic TbFe structures.," *Sci. Rep.*, vol. 6, p. 23038, 2016.

[53] K. Dörr, O. Bilani-Zeneli, a. Herklotz, a. D. Rata, K. Boldyreva, J.-W. Kim, M. C. Dekker, K. Nenkov, L. Schultz, and M. Reibold, "A model system for strain effects: epitaxial magnetic films on a piezoelectric substrate," *Eur. Phys. J. B*, vol. 71, no. 3, pp. 361–366, Sep. 2009.

[54] A. Chen, J.-M. Hu, P. Lu, T. Yang, W. Zhang, L. Li, T. Ahmed, E. Enriquez, M. Weigand, Q. Su, H. Wang, J.-X. Zhu, J. L. MacManus-Driscoll, L.-Q. Chen, D. Yarotski, and Q. Jia, "Role of scaffold network in controlling strain and functionalities of nanocomposite films," *Sci. Adv.*, vol. 2, no. 6, pp. e1600245–e1600245, 2016.

[55] J. M. Rondinelli, S. J. May, and J. W. Freeland, "Control of octahedral connectivity in perovskite oxide heterostructures: An emerging route to multifunctional materials discovery," *MRS Bull.*, vol. 37, no. 3, pp. 261–270, 2012.

[56] A. Bhattacharya and S. J. May, "Magnetic Oxide Heterostructures," *Annu. Rev. Mater.*

Res., vol. 44, no. 1, pp. 65–90, 2014.

[57] J. H. Ngai, F. J. Walker, and C. H. Ahn, "Correlated Oxide Physics and Electronics," *Annu. Rev. Mater. Res.*, vol. 44, no. 1, pp. 1–17, 2014.

[58] C. a F. Vaz, "Electric field control of magnetism in multiferroic heterostructures," *J. Phys. Condens. Matter*, vol. 24, no. 33, p. 333201, 2012.

[59] P. Zubko, S. Gariglio, M. Gabay, P. Ghosez, and J.-M. Triscone, "Interface Physics in Complex Oxide Heterostructures," *Annu. Rev. Condens. Matter Phys.*, vol. 2, no. 1, pp. 141–165, 2011.

[60] V. K. Joshi, "Spintronics: A contemporary review of emerging electronics devices," *Eng. Sci. Technol. an Int. J.*, vol. 19, no. 3, pp. 1503–1513, 2016.

[61] A. M. Glazer, "The classification of tilted octahedra in perovskites," *Acta Crystallogr. Sect. B Struct. Crystallogr. Cryst. Chem.*, vol. 28, no. 11, pp. 3384–3392, Nov. 1972.

[62] D. G. Schlom, L.-Q. Chen, C.-B. Eom, K. M. Rabe, S. K. Streiffer, and J.-M. Triscone, "Strain Tuning of Ferroelectric Thin Films," *Annu. Rev. Mater. Res.*, vol. 37, no. 1, pp. 589–626, Aug. 2007.

[63] Z. Fang, I. V. Solovyev, and K. Terakura, "Phase Diagram of Tetragonal Manganites," *Phys. Rev. Lett.*, vol. 84, no. 14, pp. 3169–3172, Mar. 2000.

[64] Y. Tokura, "Orbital Physics in Transition-Metal Oxides," *Science (80-.).*, vol. 288, no. 5465, pp. 462–468, Apr. 2000.

[65] A. Tebano, C. Aruta, S. Sanna, P. G. Medaglia, G. Balestrino, A. A. Sidorenko, R. De Renzi, G. Ghiringhelli, L. Braicovich, V. Bisogni, and N. B. Brookes, "Evidence of orbital reconstruction at interfaces in ultrathin La0.67Sr0.33MnO3 Films," *Phys. Rev. Lett.*, vol. 100, no. 13, pp. 2–5, 2008.

[66] M. Huijben, L. W. Martin, Y.-H. Chu, M. B. Holcomb, P. Yu, G. Rijnders, D. H. A. Blank, and R. Ramesh, "Critical thickness and orbital ordering in ultrathin La0.7Sr0.3MnO3," *Phys. Rev. B*, vol. 78, no. 9, p. 94413, Sep. 2008.

[67] D. Pesquera, G. Herranz, A. Barla, E. Pellegrin, F. Bondino, E. Magnano, F. Sánchez, and J. Fontcuberta, "Surface symmetry-breaking and strain effects on orbital occupancy in transition metal perovskite epitaxial films," *Nat. Commun.*, vol. 3, p. 1189, Nov. 2012.

[68] M. B. Lepetit, B. Mercey, and C. Simon, "Interface effects in perovskite thin films," *Phys. Rev. Lett.*, vol. 108, no. 8, pp. 1–5, 2012.

[69] S. J. May, J. W. Kim, J. M. Rondinelli, E. Karapetrova, N. A. Spaldin, A. Bhattacharya, and P. J. Ryan, "Quantifying octahedral rotations in strained perovskite oxide films," *Phys. Rev. B - Condens. Matter Mater. Phys.*, vol. 82, no. 1, pp. 1–7, 2010.

[70] M. D. Biegalski, Y. Takamura, A. Mehta, Z. Gai, S. V Kalinin, H. Ambaye, V. Lauter, D. Fong, S. T. Pantelides, Y. M. Kim, J. He, A. Borisevich, W. Siemons, and H. M. Christen, "Interrelation between Structure - Magnetic Properties in La 0.5 Sr 0.5 CoO 3," *Adv. Mater. Interfaces*, vol. 1, no. 8, p. 1400203, Nov. 2014.

[71] J. M. Rondinelli and N. A. Spaldin, “Structural effects on the spin-state transition in epitaxially strained LaCoO3 films,” *Phys. Rev. B - Condens. Matter Mater. Phys.*, vol. 79, no. 5, pp. 1–7, 2009.

[72] Z. X. Cheng, X. L. Wang, S. X. Dou, M. Osada, and H. Kimura, “Strain modulated magnetization and colossal resistivity of epitaxial La2/3Ca1/3MnO3 film on BaTiO3 substrate,” *Appl. Phys. Lett.*, vol. 99, no. 9, p. 92103, 2011.

[73] R. K. Zheng, Y. Wang, H. L. W. Chan, C. L. Choy, and H. S. Luo, “Determination of the strain dependence of resistance in La0.7 Sr0.3 Mn O3 PMN-PT using the converse piezoelectric effect,” *Phys. Rev. B - Condens. Matter Mater. Phys.*, vol. 75, no. 21, pp. 1–4, 2007.

[74] C. Thiele, K. Dörr, S. Fähler, L. Schultz, D. C. Meyer, a. a. Levin, and P. Paufler, “Voltage-controlled epitaxial strain in La0.7Sr0.3MnO3/Pb(Mg1/3Nb2/3)O3-PbTiO3(001) films,” *Appl. Phys. Lett.*, vol. 87, no. 26, p. 262502, 2005.

[75] G. a. Ovsyannikov, a. M. Petrzhik, I. V. Borisenko, a. a. Klimov, Y. a. Ignatov, V. V. Demidov, and S. a. Nikitov, “Magnetotransport characteristics of strained La0.7Sr0.3MnO3 epitaxial manganite films,” *J. Exp. Theor. Phys.*, vol. 108, no. 1, pp. 48–55, Jan. 2009.

[76] M. K. Kinyanjui, Y. Lu, N. Gauquelin, M. Wu, A. Frano, P. Wochner, M. Reehuis, G. Christiani, G. Logvenov, H. U. Habermeier, G. A. Botton, U. Kaiser, B. Keimer, and E. Benckiser, “Lattice distortions and octahedral rotations in epitaxially strained LaNiO3/LaAlO3 superlattices,” *Appl. Phys. Lett.*, vol. 104, no. 22, pp. 4–8, 2014.

[77] E. J. Moon, P. V. Balachandran, B. J. Kirby, D. J. Keavney, R. J. Sichel-Tissot, C. M. Schlepütz, E. Karapetrova, X. M. Cheng, J. M. Rondinelli, and S. J. May, “Effect of interfacial octahedral behavior in ultrathin manganite films.,” *Nano Lett.*, vol. 14, no. 5, pp. 2509–14, May 2014.

[78] A. J. Millis, T. Darling, and A. Migliori, “Quantifying strain dependence in ‘colossal’ magnetoresistance manganites,” *J. Appl. Phys.*, vol. 83, no. 3, pp. 1588–1591, Feb. 1998.

[79] F. Tsui, M. C. Smoak, T. K. Nath, and C. B. Eom, “Strain-dependent magnetic phase diagram of epitaxial La0.67Sr0.33MnO3 thin films,” *Appl. Phys. Lett.*, vol. 76, no. 17, pp. 2421–2423, Apr. 2000.

[80] S. Jin, G. Gao, W. Wu, and X. Zhou, “Effect of angular-distortion-induced strain on structural and transport properties of epitaxial La 0.7 Sr 0.3 MnO 3 thin films,” *J. Phys. D. Appl. Phys.*, vol. 40, no. 2, pp. 305–309, Jan. 2007.

[81] E. Jiménez, “Experimental study of angular-dependent magnetic properties of nanostructures : Influence of Magnetic Anisotropy (Doctoral dissertation),” Universidad Autónoma de Madrid, 2011.

[82] Z. Liao, M. Huijben, Z. Zhong, N. Gauquelin, S. Macke, R. J. Green, S. Van Aert, J. Verbeeck, G. Van Tendeloo, K. Held, G. A. Sawatzky, G. Koster, G. Rijnders, Z. Zhong, N. Gauquelin, S. Macke, R. J. Green, S. van Aert, J. Verbeeck, G. Van Tendeloo, K. Held, G. A. Sawatzky, G. Koster, and G. Rijnders, “Controlled lateral anisotropy in correlated manganite heterostructures by interface-engineered oxygen

octahedral coupling.," *Nat. Mater.*, vol. 15, no. 4, pp. 425–31, Apr. 2016.

[83] D. Kan, R. Aso, R. Sato, M. Haruta, H. Kurata, and Y. Shimakawa, "Tuning magnetic anisotropy by interfacially engineering the oxygen coordination environment in a transition metal oxide.," *Nat. Mater.*, vol. 15, no. 4, pp. 432–7, Apr. 2016.

[84] "Nanotechnologists can now make orientation of magnetism adjustable in new materials," 2016. [Online]. Available: http://www.nanowerk.com/nanotechnology-news/newsid=42806.php#ixzz4iqrYOPoK.

[85] M. T. Johnson, P. J. H. Bloemen, F. J. a Den Broeder, and J. J. De Vries, "Magnetic anisotropy in metallic multilayers," *Reports Prog. Phys.*, vol. 59, no. 11, pp. 1409–1458, Nov. 1996.

[86] J. H. Van Vleck, "On the anisotropy of cubic ferromagnetic crystals," *Phys. Rev.*, vol. 52, no. 11, pp. 1178–1198, 1937.

[87] A. Aharoni, *Introduction to the theory of Ferromagnetism*, Second edi. Oxford, 2000.

[88] B.D. Cullity, *Introduction to Magnetic Materials*. Massachusetts: Addison-Wesley, 1972.

[89] N. Louis, "Anisotropie magnetique superficielle et surstructures d'orientation," *J. Phys. Radium*, vol. 15 (4), pp. 225–239, 1954.

[90] M. Konoto, T. Kohashi, K. Koike, T. Arima, Y. Kaneko, Y. Tomioka, and Y. Tokura, "Magnetic domain structure of a La0.7Sr0.3MnO3 (001) surface observed by a spin-polarized scanning electron microscope," *Appl. Phys. Lett.*, vol. 84, no. 13, pp. 2361–2363, 2004.

[91] A. Khapikov, L. Uspenskaya, I. Bdikin, Y. Mukovskii, S. Karabashev, D. Shulyaev, and A. Arsenov, "Magnetic domains and twin structure of the La0.7Sr0.3MnO3 single crystal," *Appl. Phys. Lett.*, vol. 77, no. 15, p. 2376, 2000.

[92] L. M. Berndt, V. Balbarin, Y. Suzuki, L. M. Berndt, V. Balbarin, and Y. Suzuki, "Magnetic anisotropy and strain states of (001) and (110) colossal magnetoresistance thin films," *Appl. Phys. Lett.*, vol. 77, no. 18, pp. 2903–2905, Oct. 2000.

[93] P. Lecoeur, P. L. Trouilloud, G. Xiao, A. Gupta, G. Q. Gong, and X. W. Li, "Magnetic domain structures of La0.67Sr0.33MnO3 thin films with different morphologies," *J. Appl. Phys.*, vol. 82, no. 8, pp. 3934–3939, Oct. 1997.

[94] Y. Suzuki, H. Y. Hwang, S.-W. Cheong, and R. B. van Dover, "The role of strain in magnetic anisotropy of manganite thin films," *Appl. Phys. Lett.*, vol. 71, no. 1, pp. 140–142, Jul. 1997.

[95] K. Steenbeck and R. Hiergeist, "Magnetic anisotropy of ferromagnetic La0.7(Sr, Ca)0.3MnO3 epitaxial films," *Appl. Phys. Lett.*, vol. 75, no. 12, pp. 1778–1780, Sep. 1999.

[96] Y. Suzuki, H. Y. Hwang, S.-W. Cheong, T. Siegrist, R. B. van Dover, A. Asamitsu, and Y. Tokura, "Magnetic anisotropy of doped manganite thin films and crystals," *J. Appl. Phys.*, vol. 83, no. 11, p. 7064, Jun. 1998.

[97] D. S. Chuang, C. A. Ballentine, and R. C. O'Handley, "Surface and step magnetic anisotropy.," *Phys. Rev. B. Condens. Matter*, vol. 49, no. 21, pp. 15084–15095, Jun. 1994.

[98] H. K. Lee, I. Barsukov, A. G. Swartz, B. Kim, L. Yang, H. Y. Hwang, and I. N. Krivorotov, "Magnetic anisotropy, damping, and interfacial spin transport in Pt/LSMO bilayers," *AIP Adv.*, vol. 6, no. 5, p. 55212, 2016.

[99] R. M. Reeve, C. Mix, M. König, M. Foerster, G. Jakob, and M. Kläui, "Magnetic domain structure of La0.7Sr0.3MnO3 thin-films probed at variable temperature with scanning electron microscopy with polarization analysis," *Appl. Phys. Lett.*, vol. 102, no. 12, p. 122407, Mar. 2013.

[100] H. Boschker, J. Kautz, E. P. Houwman, G. Koster, D. H. a. Blank, and G. Rijnders, "Magnetic anisotropy and magnetization reversal of La0.67Sr0.33MnO3 thin films on SrTiO3(110)," *J. Appl. Phys.*, vol. 108, no. 10, p. 103906, Nov. 2010.

[101] P. Perna, L. Méchin, M. Saïb, J. Camarero, and S. Flament, "Imaging the magnetization reversal of step-induced uniaxial magnetic anisotropy in vicinal epitaxial La0.7Sr0.3MnO 3 films," *New J. Phys.*, vol. 12, no. 10, p. 103033, Oct. 2010.

[102] K. Steenbeck and R. Hiergeist, "K. Steenbeck," *Appl. Phys. Lett.*, vol. 75, no. 12, pp. 1778–1780, Sep. 1999.

[103] V. V Demidov, G. A. Ovsyannikov, A. M. Petrzhik, I. V Borisenko, A. V Shadrin, and R. Gunnarsson, "Magnetic anisotropy in strained manganite films and bicrystal junctions," *J. Appl. Phys.*, vol. 113, no. 16, p. 163909, Apr. 2013.

[104] Z. Liao, M. Huijben, G. Koster, and G. Rijnders, "Uniaxial magnetic anisotropy induced low field anomalous anisotropic magnetoresistance in manganite thin films," *APL Mater.*, vol. 2, no. 9, p. 96112, Sep. 2014.

[105] H. Boschker, M. Mathews, E. P. Houwman, H. Nishikawa, A. Vailionis, G. Koster, G. Rijnders, and D. H. A. Blank, "Strong uniaxial in-plane magnetic anisotropy of (001)- and (011)-oriented La0.67Sr0.33MnO3 thin films on NdGaO3 substrates," *Phys. Rev. B*, vol. 79, no. 21, p. 214425, Jun. 2009.

[106] M. Mathews, R. Jansen, G. Rijnders, J. C. Lodder, and D. H. A. Blank, "Magnetic oxide nanowires with strain-controlled uniaxial magnetic anisotropy direction," *Phys. Rev. B*, vol. 80, no. 6, p. 64408, Aug. 2009.

[107] H. Boschker, M. Mathews, P. Brinks, E. Houwman, A. Vailionis, G. Koster, D. H. A. Blank, and G. Rijnders, "Uniaxial contribution to the magnetic anisotropy of La0.67Sr0.33MnO3 thin films induced by orthorhombic crystal structure," *J. Magn. Magn. Mater.*, vol. 323, no. 21, pp. 2632–2638, 2011.

[108] L. Méchin, C. Simon, and R. A. Chakalov, "Variable temperature magnetic force microscopy," *Int. J. Nanotechnol.*, vol. 5, pp. 818–826, 2008.

[109] A. Vailionis, H. Boschker, E. Houwman, G. Koster, G. Rijnders, and D. H. A. Blank, "Anisotropic stress relief mechanism in epitaxial La0.67Sr0.33MnO3 films," *Appl. Phys. Lett.*, vol. 95, no. 15, p. 152508, 2009.

[110] H. Boschker, "Perovskite oxide heteroepitaxy," University of Twente, Enschede, The

Netherlands, 2011.

[111] Y. Jiang, G. Y. Gao, Y. Wang, and H. L. W. Chan, “Temperature evolution of anisotropic stress induced highly ordered stripe magnetic domains in thin film on (110) substrate,” *Solid State Commun.*, vol. 150, no. 41–42, pp. 2028–2031, Nov. 2010.

[112] J. Kerr, “XLIII. On Rotation of the Plane of Polarization by Reflection from the Pole of a Magnet.,” *Philos. Mag.*, vol. 3, no. 19, pp. 321–343, Mar. 1877.

[113] J. Kerr, “XXIV. On reflection of polarized light from the equatorial surface of a magnet,” *Philos. Mag. Ser. 5*, vol. 5, no. 30, pp. 161–177, 1878.

[114] J. Leland and M. Tomatz, “The Magneto-Optical Kerr Effect,” 2002. [Online]. Available: http://mxp.physics.umn.edu/s02/Projects/MOKE/.

[115] P. Weinberger, “John Kerr and his effects found in 1877 and 1878,” *Philos. Mag. Lett.*, vol. 88, no. 12, pp. 897–907, 2008.

[116] A. Üstündağ, T. J. Gung, and M. Zahn, “Kerr electro-optic theory and measurements of electric fields with magnitude and direction varying along the light path,” *IEEE Trans. Dielectr. Electr. Insul.*, vol. 5, no. 3, pp. 421–442, 1998.

[117] V. Kalappattil, R. Geng, S. H. Liang, D. Mukherjee, J. Devkota, A. Roy, M. H. Luong, N. D. Lai, L. A. Hornak, T. D. Nguyen, W. B. Zhao, X. G. Li, N. H. Duc, R. Das, S. Chandra, H. Srikanth, and M. H. Phan, “Role of the magnetic anisotropy in organic spin valves,” *J. Sci. Adv. Mater. Devices*, Aug. 2017.

[118] D. Fadil, S. Wu, P. Perna, B. Renault, M. Saib, S. Lebargy, J. Gasnier, B. Guillet, J.-M. Routoure, S. Flament, and L. Mechin, “Direct observation of magnetization reversal and low field magnetoresistance of epitaxial La0.7Sr0.3MnO3/SrTiO3 (001) thin films at room temperature,” *J. Appl. Phys.*, vol. 112, no. 1, p. 13906, Jul. 2012.

[119] P. Perna, D. Maccariello, C. Rodrigo, J. L. F. Cuñado, M. Muñoz, J. L. Prieto, M. A. Niño, A. Bollero, J. Camarero, and R. Miranda, “Direct experimental determination of the anisotropic magnetoresistive effects,” *Appl. Phys. Lett.*, vol. 104, no. 20, p. 202407, May 2014.

[120] D. Ecija, E. Jiménez, N. Mikuszeit, N. Sacristán, J. Camarero, J. M. Gallego, J. Vogel, and R. Miranda, “Symmetry breaking effects in epitaxial magnetic thin films: Nonsymmetric reversal and butterfly remanence behavior,” *Phys. Rev. B*, vol. 77, no. 2, p. 24426, Jan. 2008.

[121] J. Camarero, J. Sort, A. Hoffmann, J. M. García-Martín, B. Dieny, R. Miranda, and J. Nogués, “Origin of the asymmetric magnetization reversal behavior in exchange-biased systems: Competing anisotropies,” *Phys. Rev. Lett.*, vol. 95, no. 5, pp. 1–4, 2005.

[122] Z. Q. Qiu and S. D. Bader, “Surface magneto-optic Kerr effect,” *Rev. Sci. Instrum.*, vol. 71, no. 3, p. 1243, 2000.

[123] P. Perna, C. Rodrigo, M. Muñoz, J. L. Prieto, A. Bollero, D. Maccariello, J. L. F. Cuñado, M. Romera, J. Akerman, E. Jiménez, N. Mikuszeit, V. Cros, J. Camarero, and R. Miranda, “Magnetization reversal signatures in the magnetoresistance of magnetic multilayers,” *Phys. Rev. B*, vol. 86, no. 2, p. 24421, 2012.

[124] E. R. Moog and S. D. Bader, “Smoke signals from ferromagnetic monolayers: p(1×1) Fe/Au(100),” *Superlattices Microstruct.*, vol. 1, no. 6, pp. 543–552, 1985.

[125] S. T. Purcell, M. T. Johnson, N. W. E. McGee, J. J. De Vries, W. B. Zeper, and W. Hoving, “Local structural and polar Kerr effect measurements on an ultrathin epitaxial Co wedge grown on Pd(111),” *J. Appl. Phys.*, vol. 73, no. 3, pp. 1360–1367, 1993.

[126] J. L. Costa-Krämer, D. M. Borsa, J. M. García-Martín, M. S. Martín-González, D. O. Boerma, and F. Briones, “Structure and magnetism of single-phase epitaxial ’-Fe4N,” *Phys. Rev. B*, vol. 69, no. 14, p. 144402, Apr. 2004.

[127] E. Jiménez, N. Mikuszeit, J. L. F. Cuñado, P. Perna, J. Pedrosa, D. Maccariello, C. Rodrigo, M. A. Niño, A. Bollero, J. Camarero, and R. Miranda, “Vectorial Kerr magnetometer for simultaneous and quantitative measurements of the in-plane magnetization components,” *Rev. Sci. Instrum.*, vol. 85, no. 5, p. 53904, May 2014.

[128] J. L. F. Cuñado, J. Pedrosa, F. Ajejas, A. Bollero, P. Perna, F. J. Teran, R. Miranda, and J. Camarero, “Note: Vectorial-magneto optical Kerr effect technique combined with variable temperature and full angular range all in a single setup,” *Rev. Sci. Instrum.*, vol. 86, no. 4, p. 46109, Apr. 2015.

[129] S. W. Jin, G. Y. Gao, Z. Huang, Z. Z. Yin, X. Zheng, and W. Wu, “Shear-strain-induced low symmetry phase and domain ordering in epitaxial La0.7Sr0.3MnO3 thin films,” *Appl. Phys. Lett.*, vol. 92, no. 26, pp. 1–4, 2008.

[130] A. K. Pradhan, D. Hunter, T. Williams, B. Lasley-Hunter, R. Bah, H. Mustafa, R. Rakhimov, J. Zhang, D. J. Sellmyer, E. E. Carpenter, D. R. Sahu, and J.-L. Huang, “Magnetic properties of La0.6Sr0.4MnO3 thin films on SrTiO3 and buffered Si substrates with varying thickness,” *J. Appl. Phys.*, vol. 103, no. 2, p. 23914, Jan. 2008.

[131] M. Spankova, Š. Chromik, I. Vavra, K. Sedlackova, P. Lobotka, S. Lucas, and S. Stancek, “Epitaxial LSMO films grown on MgO single crystalline substrates,” *Appl. Surf. Sci.*, vol. 253, no. 18, pp. 7599–7603, Jul. 2007.

[132] M. Sirena, L. Steren, and J. Guimpel, “Thickness dependence of the properties of La0.6Sr0.4MnO3 thin films,” *Thin Solid Films*, vol. 373, no. 1–2, pp. 102–106, Sep. 2000.

[133] R. P. Borges, W. Guichard, J. G. Lunney, J. M. D. Coey, and F. Ott, “Magnetic and electric ‘dead’ layers in (La0.7Sr0.3)MnO 3 thin films,” *J. Appl. Phys.*, vol. 89, no. 7, pp. 3868–3873, Apr. 2001.

[134] E. Gommert, H. Cerva, J. Wecker, and K. Samwer, “Influence of misfit stress on the magnetoresistive properties of La0.7Ca0.3MnO3−δ thin films,” *J. Appl. Phys.*, vol. 85, no. 8, pp. 5417–5419, 1999.

[135] M. J. Casanove, C. Roucau, P. Baulès, J. Majimel, J. C. Ousset, D. Magnoux, and J. F. Bobo, “Growth and relaxation mechanisms in La0.66Sr0.33MnO3 manganites deposited on SrTiO3(0 0 1) and MgO(0 0 1),” *Appl. Surf. Sci.*, vol. 188, no. 1–2, pp. 19–23, 2002.

[136] T. F. Zhou, G. Li, X. G. Li, S. W. Jin, and W. B. Wu, “Self-generated in-plane superlattice in relaxed epitaxial La 0.67Sr0.33MnO3 films,” *Appl. Phys. Lett.*, vol. 90,

no. 4, pp. 0–3, 2007.

[137] A. Tebano, A. Orsini, D. Di Castro, P. G. Medaglia, and G. Balestrino, “Interplay between crystallographic orientation and electric transport properties in La2/3Sr1/3MnO3 films,” *Appl. Phys. Lett.*, vol. 96, no. 9, p. 92505, Mar. 2010.

[138] V. Štrbík, M. Reiffers, E. Dobročka, J. Šoltýs, M. Španková, and Š. Chromik, “Epitaxial LSMO thin films with correlation of electrical and magnetic properties above 400 K,” *Appl. Surf. Sci.*, vol. 312, pp. 212–215, 2014.

[139] U.Welp, V.K.Vlasko-Vlasov, X. Liu, J. K. Furdyna, and T. Wojtowicz, “Magnetic Domain Structure and Magnetic Anisotropy in Ga1-xMnxAs,” *Phys. Rev. Lett.*, vol. 90, no. 16, p. 167206, Apr. 2003.

[140] E. Wahlström, F. Maci, J. E. Boschker, Å. Monsen, P. Nordblad, R. Mathieu, A. D. Kent, and T. Tybell, “Twinned-domain-induced magnonic modes in epitaxial LSMO/STO films,” *New J. Phys.*, vol. 19, no. 6, pp. 0–8, 2017.

[141] A. R. Damodaran, J. C. Agar, S. Pandya, Z. Chen, L. Dedon, R. Xu, B. Apgar, S. Saremi, and L. W. Martin, “New modalities of strain-control of ferroelectric thin films,” *J. Phys. Condens. Matter*, vol. 28, no. 26, p. 263001, 2016.

[142] J. Santiso, L. Balcells, Z. Konstantinovic, J. Roqueta, P. Ferrer, A. Pomar, B. Martínez, and F. Sandiumenge, “Thickness evolution of the twin structure and shear strain in LSMO films,” *CrystEngComm*, vol. 15, no. 19, p. 3908, 2013.

[143] A. Vailionis, H. Boschker, Z. Liao, J. R. A. Smit, G. Rijnders, M. Huijben, and G. Koster, “Symmetry and lattice mismatch induced strain accommodation near and away from correlated perovskite interfaces,” *Appl. Phys. Lett.*, vol. 105, no. 13, p. 131906, Sep. 2014.

[144] U. Gebhardt, N. V. Kasper, A. Vigliante, P. Wochner, H. Dosch, F. S. Razavi, and H. U. Habermeier, “Formation and thickness evolution of periodic twin domains in manganite films grown on SrTiO3(001) substrates,” *Phys. Rev. Lett.*, vol. 98, no. 9, pp. 1–4, 2007.

[145] J. L. Maurice, F. Pailloux, A. Barthélémy, O. Durand, D. Imhoff, R. Lyonnet, A. Rocher, and J. P. Contour, “Strain relaxation in the epitaxy of La2/3Sr1/3MnO3 grown by pulsed-laser deposition on SrTiO3(001),” *Philos. Mag.*, vol. 83, no. 28, pp. 3201–3224, 2003.

[146] F. Pailloux, R. Lyonnet, J. L. Maurice, and J. P. Contour, “Twinning and lattice distortions in the epitaxy of La0.67Sr0.33MnO3 thin films on (0 0 1) SrTiO3,” *Appl. Surf. Sci.*, vol. 177, no. 4, pp. 263–267, 2001.

[147] O. I. Lebedevy, S. Amelinckx, and F. Razavi, “Periodic microtwinning as a possible mechanism for the accommodation of the epitaxial film-substrate mismatch in the La1-xSrxMnO3/SrTiO 3 system,” *Philos. Mag. A*, vol. 81, no. 4, pp. 797–824, 2001.

[148] S. K. Streiffer, C. B. Parker, A. E. Romanov, M. J. Lefevre, L. Zhao, J. S. Speck, W. Pompe, C. M. Foster, and G. R. Bai, “Domain patterns in epitaxial rhombohedral ferroelectric films. I. Geometry and experiments,” *J. Appl. Phys.*, vol. 83, no. 5, pp. 2742–2753, 1998.

[149] P. Fumagalli, C. Spaeth, G. Guntherodt, R. von Helmolt, and J. Wecker, “Magneto-optic Spectroscopy of Perovskite-Type La1-x(Ba, Sr)xMn03,” *IEEE Trans. Magn.*, vol. 31, no. 6, pp. 3277–3279, 1995.

[150] Y. F. Ding, J. S. Chen, and E. Liu, “Controlling the crystallographic orientation and easy axis of magnetic anisotropy in L10 FePt films with Cu additive,” *Surf. Coatings Technol.*, vol. 198, no. 1–3, pp. 262–265, 2005.

[151] “Make Way for Flexible Silicon Chips.” [Online]. Available: https://spectrum.ieee.org/semiconductors/materials/make-way-for-flexible-silicon-chips.

[152] K. Greene, “Stretchable Silicon - MIT Technology Review.” [Online]. Available: http://www2.technologyreview.com/news/405528/stretchable-silicon/.

[153] L. Méchin, C. Adamo, S. Wu, B. Guillet, S. Lebargy, C. Fur, J.-M. Routoure, S. Mercone, M. Belmeguenai, and D. G. Schlom, “Epitaxial La0.7Sr0.3MnO3 thin films grown on SrTiO3 buffered silicon substrates by reactive molecular-beam epitaxy,” *Phys. Status Solidi*, vol. 209, no. 6, pp. 1090–1095, 2012.

[154] M. Belmeguenai, S. Mercone, C. Adamo, L. Méchin, C. Fur, P. Monod, P. Moch, and D. G. Schlom, “Temperature dependence of magnetic properties of La0.7Sr0.3MnO3/SrTiO3 thin films on silicon substrates,” *Phys. Rev. B*, vol. 81, no. 5, p. 54410, 2010.

[155] R. Ramesh and D. G. Schlom, “Orienting ferroelectric films,” *Science (80-.).*, vol. 296, no. June, pp. 1975–1976, 2002.

[156] J. Baborowski, “Microfabrication of piezoelectric MEMS,” *J. Electroceramics*, vol. 12, no. 1–2, pp. 33–51, 2004.

[157] R. Maeda, J. J. Tsaur, S. H. Lee, and M. Ichiki, “Piezoelectric microactuator devices,” *J. Electroceramics*, vol. 12, no. 1–2, pp. 89–100, 2004.

[158] S. Kim, G. Barbastathis, and H. L. Tuller, “MEMS for optical functionality,” *J. Electroceramics*, vol. 12, no. 1–2, pp. 133–144, 2004.

[159] P. Muralt, “<Thin film piezoelectrics for MEMS.pdf>,” pp. 7–17, 2004.

[160] D. Shen, J.-H. Park, J. Ajitsaria, S.-Y. Choe, H. C. Wikle, and D.-J. Kim, “The design, fabrication and evaluation of a MEMS PZT cantilever with an integrated Si proof mass for vibration energy harvesting,” *J. Micromechanics Microengineering*, vol. 18, no. 5, p. 55017, 2008.

[161] M. D. Nguyen, H. N. Vu, D. H. A. Blank, and G. J. H. M. Rijnders, “Epitaxial Pb(Zr,Ti)O3 thin films for a MEMS application,” *Adv. Nat. Sci. Nanosci. Nanotechnol.*, vol. 2, no. 1, p. 15005, 2011.

[162] H. Funakubo, M. Dekkers, A. Sambri, S. Gariglio, I. Shklyarevskiy, and G. Rijnders, “Epitaxial PZT films for MEMS printing applications,” *MRS Bull.*, vol. 37, no. 11, pp. 1030–1038, 2012.

[163] A. Sambri and N. Federico, “Microactuation and microsensing devices based on epitaxial Pb(Zr,Ti)O3 thin films,” 2014, no. September, pp. 22–23.

[164] L. Pellegrino, M. Biasotti, E. Bellingeri, C. Bernini, A. S. Siri, and D. Marré, "All-oxide crystalline microelectromechanical systems: Bending the functionalities of transition-metal oxide thin films," *Adv. Mater.*, vol. 21, no. 23, pp. 2377–2381, 2009.

[165] S. H. Baek, J. Park, D. M. Kim, V. a. Aksyuk, R. R. Das, S. D. Bu, D. a. Felker, J. Lettieri, V. Vaithyanathan, S. S. N. Bharadwaja, N. Bassiri-Gharb, Y. B. Chen, H. P. Sun, C. M. Folkman, H. W. Jang, D. J. Kreft, S. K. Streiffer, R. Ramesh, X. Q. Pan, S. Trolier-McKinstry, D. G. Schlom, M. S. Rzchowski, R. H. Blick, and C. B. Eom, "Giant Piezoelectricity on Si for Hyperactive MEMS," *Science (80-.).*, vol. 334, no. 6058, pp. 958–961, 2011.

[166] Y. Fukuta, H. Fujita, and H. Toshiyoshi, "Vapor Hydrofluoric Acid Sacrificial Release Technique for Micro Electro Mechanical Systems Using Labware," *Jpn. J. Appl. Phys.*, vol. 42, no. Part 1, No. 6A, pp. 3690–3694, Jun. 2003.

Influence of the epitaxial strain on magnetic anisotropy in LSMO thin films for spintronics applications

Sandeep Kumar CHALUVADI

I Introduction

Half-metallic perovskite oxides promise great advantages over conventional spintronics metallic materials for applications such as magnetic sensors, magnetic random access memory (MRAM), magnetic tunnel junctions (MTJs), domain wall race-track memories[1] etc. Oxides, in general, appear to be a new contender for many novel applications that were considered traditionally beyond its range. This was due to the fact that the complex interplay between orbital and spin properties in determining their overall conduction mechanisms have been not fully understood so far.[2,3] Irrespective of the applications, one of the key properties that need to be considered for a ferromagnetic sample is its magnetic anisotropy that dictates the magnetization reversals pathways.[4] For example, a defined *uniaxial anisotropy* is essential for magnetic field sensors based on anisotropic magneto-resistance (AMR).[3] A defined *biaxial anisotropy*, which has four stable magnetization states and a capability to encode more information (four binary bits: "00", "01", "10", "11"), can be used in memory and logic devices, in voltage controlled resistive switching in giant magnetoresistance (GMR) and MTJs.[5,6]

Half-metallic $La_{0.67}Sr_{0.33}MnO_3$ (LSMO) compound is considered as a potential spintronic candidate for its peculiar properties such as nearly 100% spin polarization. It is a room temperature Ferromagnetic Metal (FM) with Curie temperature T_c~370 K. The structural, electrical and magnetic properties of LSMO thin films are very sensitive to external perturbations, epitaxial strain being one of them.[7] In general, in a tensile (compressive) strained film, the electron occupancy in 'e_g' doublet favors in-plane (out-of-plane) x^2-y^2 ($3z^2$-r^2) orbitals.[8]

II Experimental details

Epitaxial LSMO thin films of different thicknesses were grown on various substrates such as STO (001), LSAT (001), NGO (110), LAO (001), MgO (001) and STO buffered MgO (001) by pulsed laser deposition (PLD) using KrF excimer laser of wavelength 248 nm. The choice of choosing different substrates is to induce different epitaxial strain in LSMO thin films as shown in Figure 1. The deposition was made at 0.35 mbar oxygen pressure while maintaining the substrate temperature at 720°C. After deposition, the substrates were cooled down to room temperature at 10°C per minute in $7x10^2$ mbar oxygen background pressure. Here, the thickness of LSMO films are 50, 25 and 12 nm and STO buffer layer is 12 nm, respectively. Structural, morphology, magnetic and electrical transport measurements were done by PANalytical X'Pert X-Ray Diffraction (XRD), Atomic Force Microscopy (AFM), Superconducting Quantum Interference Device (SQUID), and four-probe technique, respectively. Angular dependent *in-plane* magnetization reversal process, coercivity, and magnetic anisotropy measurements were

performed at 300 K and 40 K by using vectorial Magneto-Optical Kerr (v-MOKE) magnetometry.

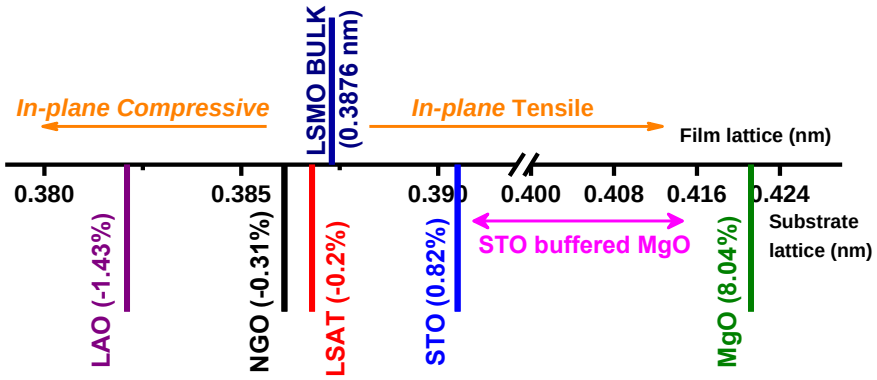

Figure 1: Lattice mismatch between LSMO and the substrates that are used in this study; -1.36% for LAO, -0.31% for NGO, -0.12% for LSAT, +0.82% for STO, +8.04% for MgO. '-' indicates compressive strain whereas '+' indicates tensile strain.

III Effect of substrates

Figure 2 (left) shows the XRD pattern of LSMO films of 50 nm thick grown onto different lattice mis-matched substrates. Films grown on nearly matched substrates experience fully strained in the whole thickness range. On contrary, films grown on large mis-matched substrate such as on MgO (001) is fully relaxed.

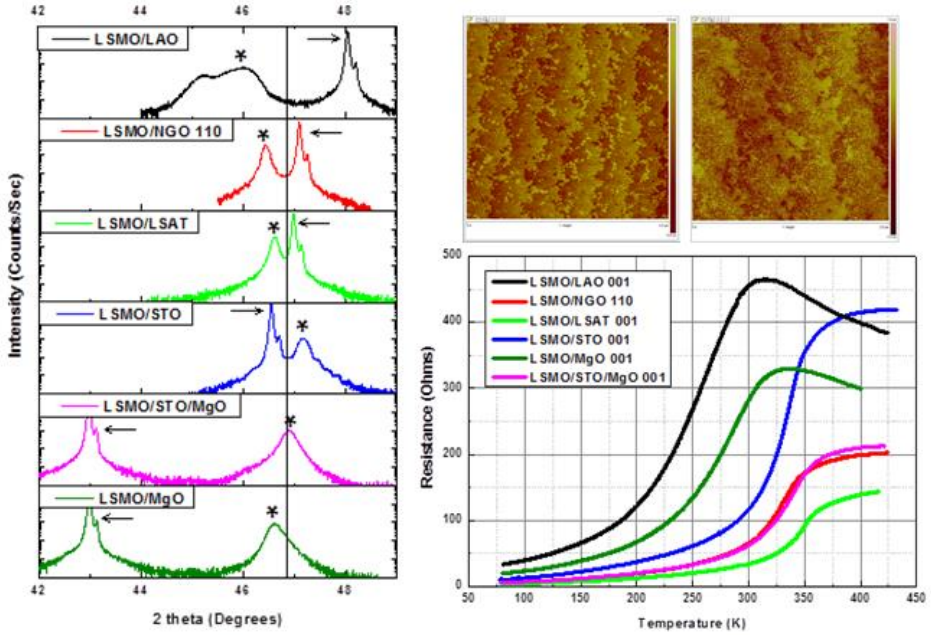

Figure 2: (Left panel) XRD plots of epitaxial LSMO (00l) thin films of 50 nm thickness grown on different single crystal substrates. The solid line indicates the LSMO Bulk value, * and arrow represents (002) peak of LSMO film and film respectively. (Right panel) Top shows the AFM topography images of LSMO film grown on STO (001) and NGO (110) substrates and bottom shows temperature dependent resistance of LSMO film.

Due to parallel twin boundaries and domains present on LAO (001) substrate, we observed two different peaks that are either fully strained or relaxed as per the domain. Surface topography of films were characterized by AFM (Figure 2 (right top)) shows the films are grown atomically flat with roughness as low as ~ 0.1 nm to ~ 0.4 nm. Substrate induced epitaxial strain in LSMO thin films showed significant effects on metal-insulator transition temperature (T_{MI}). The T_{MI} (Figure 2 (right bottom)) is found ~420K for the nearly lattice matched substrates (STO, LSAT, NGO) whereas for the film onto LAO and MgO, there is a reduction in T_p to nearly room temperature.

Figure 3 gives the detailed analyses of LSMO film properties as a function of thickness and substrate. The measured *out-of-plane* lattice parameter 'c' of the film as a function of thickness and substrate is shown in Figure 3 (a). Bulk LSMO value is also shown as a black solid line for reference. As we go from the compressive to tensile strain, the lattice parameter of the film 'c' decreases. However, for the film grown on STO buffered MgO shows higher values than that grown on bare STO because the film is partially relaxed, enhancing the 'c'. The films that were grown on MgO too show higher 'c' values because the film is completely relaxed due to large misfit strain (+8.04 %). The similar effect is observed in omega scans as showed in Figure 3 (b). Films that grown on the low mismatched substrate are of higher quality with FWHM values under ~ 0.15°; whereas on large mismatched substrates (STO buffered MgO and MgO); the values are as high as 2°. Figure 3 (c) indicates the average RMS roughness of the films. As the strain in the film increases, the roughness of the film also increases, which is consistent with the literature. The influence of biaxial strain on MIT 'T_p' of the thin films grown on various substrates are shown in Figure 3 (d) clearly indicates that the film under compressive strain exhibits higher 'T_p' compared to the films under tensile strain which is quite consistent with the Millis [9] prediction. However, as the strain increases, the T_p falls rapidly. Also, it should be noted that the 'T_p' values for the 50 nm film on all the substrates are the highest values reported so far. The maximum temperature coefficient of resistance is presented in Figure 3 (e) has the maximum value on LSAT substrate (nearly matched substrate) compared to all other substrates. Figure 3 (f) gives the information about the Curie temperature T_C. The T_C of LSMO film increases under compressive strain and it is due to the reduction in $Mn-O-Mn$ bond angle which enhances the electron hopping probability. On the other hand, LSMO films under tensile strain will experience the increase in $Mn-O-Mn$ bond angle which could diminish the electron hopping probability that reduces the T_p and T_C.

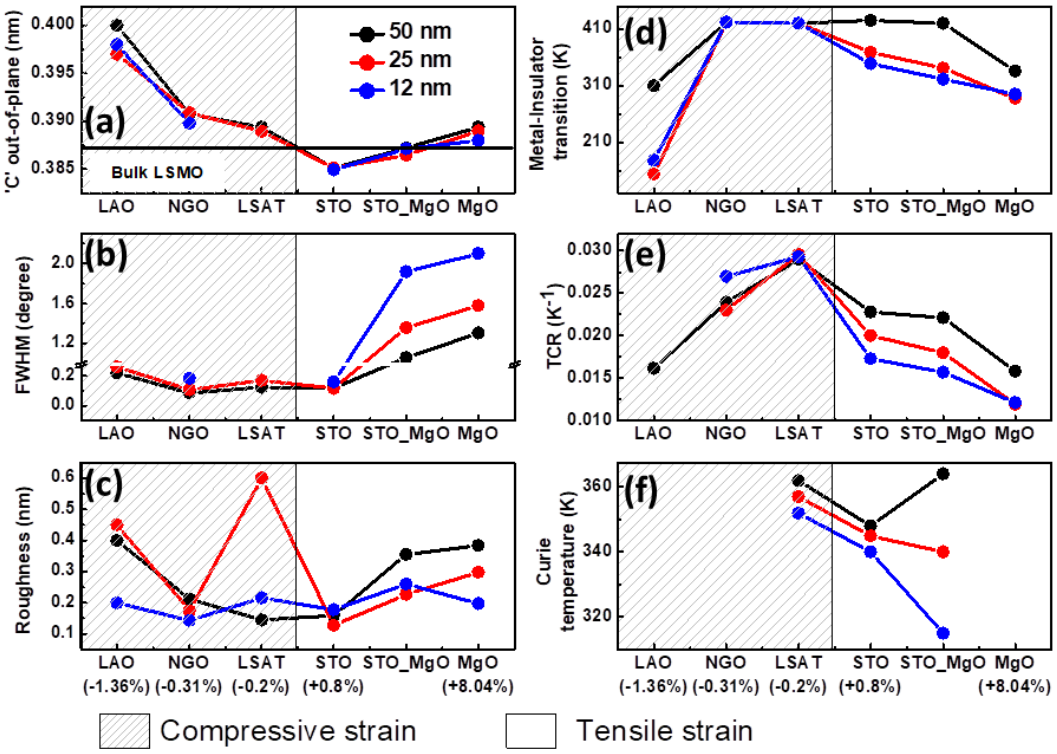

Figure 3: Epitaxial strain and thickness dependent properties of LSMO thin films as a function of strain. (a) 'c-axis' out-of-plane lattice parameter measured from XRD scans, (b) FWHM calculated from rocking curves from their corresponding LSMO (002) peak, (c) average RMS roughness values of the thin films measured by AFM on the scan area of 2µm x 2µm, (d, f) metal-insulator transition temperature and Curie temperature of the films, and (e) maximum temperature coefficient of resistance calculated from $\frac{1}{R}\frac{dR}{dT}$.

IV Magnetic anisotropy in LSMO thin films

In order to understand the inherent magnetic properties of LSMO thin film grown onto various substrates, angular dependent magnetic properties was probed by using v-MOKE @ IMDEA, Madrid. The measurements were performed in the longitudinal mode. The sample is mounted on eucentric goniometer that allows us to keep the reflection plane constant during the angular measurements as shown in Figure 4. At $\theta = 0°$, the applied external magnetic field is aligned parallel to the [100] crystallographic axis of the substrate. *In-plane* Kerr hysteresis loops are acquired between 0° and 360° with the step of every 9° by rotating the sample in the plane of the film and keeping fixed the external magnetic field direction. The remanence, coercive fields are calculated from each hysteresis loops in order to track the angular evolution of about 360°.

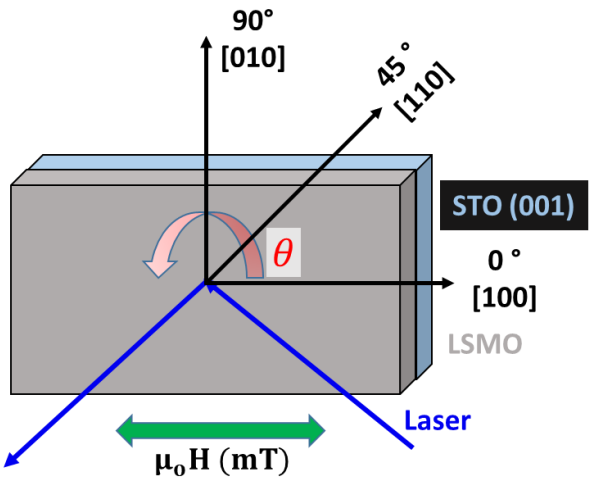

Figure 4: Schematic of the sample mounted on the goniometer in the v-MOKE set-up in the longitudinal mode. Here, the angle 'θ' indicates the direction of the rotation of the sample. The applied field direction is also presented. At θ=0°, the applied field is aligned parallel to [100] crystallographic axis.

a) LSMO/STO (001)

Figure 5 shows the angular dependence of normalized remanence magnetization of LSMO/STO (001) films of varying thickness with easy axis (e.a) and hard axis (h.a) indicated by arrows respectively. Figure 5 (a) shows the angular dependent remanence fields of LSMO film of 50 nm thick has biaxial anisotropy with easy axes aligned along <110> axis. Figure 5 (b) shows the polar plot of remanence magnetization that has butterfly structure with four lobes showing a biaxial anisotropy. One should observe that the strength of easy axes is not same in all the directions and also the periodicity between easy axis and immediate hard axis is not exactly 45°, suggesting that there is an additional anisotropy present in the film (unless very weak) that is induced by the surface symmetry breaking due to the step formation. Therefore, there exists a competition between a biaxial (strong) due to magnetocrystalline anisotropy and uniaxial (weak) due to steps formation with a small offset angle. Moreover, as the thickness of the thin film decreases from 50 to 12 nm, there is a change in anisotropy from biaxial to uniaxial. The results are clearly visualized in the angular dependent plots of the remanence magnetization Figure 5 (d)) of the LSMO film of 25 nm thick. There are periodic oscillations observed with 180° periodicity and the easy axis is aligned along [100], whereas the hard axis is aligned along [010] axis. Figure 5 (g) shows the remanence plot of 12 nm film shows uniaxial anisotropy and there is a change in easy axis direction as compared to 25 nm film and this can due to the different mis-cut angle and direction of STO (001) substrate. Figure 5 (e and h) shows the remanence polar plots of 25 and 12 nm respectively, with symmetrical lobes clearly indicating a well-defined uniaxial anisotropy. As STO (001) is cubic, the LSMO film undergoes an *in-plane* biaxial tensile strain. The magneto-elastic energy (due to strain) is constant in the film plane. Therefore, the cause for anisotropy is not due to magneto-elastic effects but it is owing to defects in crystal structure. Due to step formation, there are broken bonds along the step edges and direction (as

observed in AFM topography in Figure 5 (c, f and i). As the thickness of LSMO film decreases, magnetic anisotropy exhibits a strong uniaxial anisotropy. This suggests that the film at lower thickness has strong influence of steps and mis-cut angle from STO (001) substrates in determining the magnetic anisotropy.

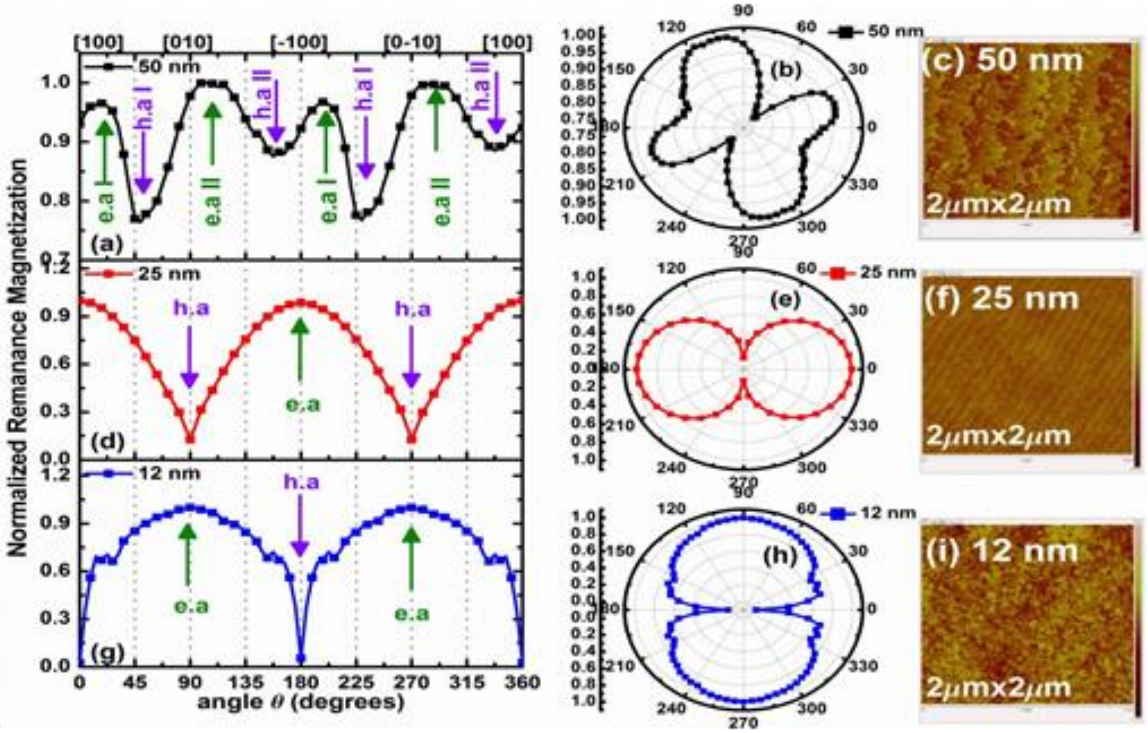

Figure 5: (a, d and g) v-MOKE angular dependent remanence magnetization of LSMO films of varying thickness grown on STO (001) substrate; (b, e, h and c, f, i) are the corresponding polar plots and AFM topography respectively.

LSMO/STO/MgO (001):

The normalized remanence plots ($M_{R,\parallel}/M_S$ and $M_{R,\perp}/M_S$) calculated from $M_\parallel(H)$ and $M_\perp(H)$ loops at the applied field $\mu_oH=0$ as a function of angle 'θ' is shown in Figure 6 (a). Both the magnetization components show repeating features with the periodicity of 90°. Also, $M_{R,\perp}$ changes its sign for every 45° i.e., whenever it crosses the characteristic axes. The polar plots of $M_{R,\parallel}/M_S$, and $M_{R,\perp}/M_S$ are presented in Figure 6 (b, c). The $M_{R,\parallel}/M_S$ polar plot resembles a butterfly structure with the highest and lowest values pointing towards e.a. and h.a. of film i.e., [110] and [100] and their equivalent crystallographic directions. The $M_{R,\perp}/M_S$ polar plot shows four lobe shape with positive and negative values depicted with solid with open circles and is due to the inversion of the sign after crossing every characteristic axes. Figure 6 (b) shows the angular dependence of the critical fields i.e., coercive (H_C) and switching (H_S) fields calculated from $M_\parallel(H)$ and $M_\perp(H)$ loops at zero crossing magnetization. The value of 'H_C' (H_S) is higher (lower) at e.a. i.e., [110] and decreases (increases) as it approaches towards h.a. i.e., [010]. The H_C and H_S coincide at and around easy axes are corresponds to one irreversible transition leading to 180° domain walls. The grey shaded area indicates the regions with one irreversible transition.

As we move away from the e.a. (white region), H_S exhibit higher values around h.a. and reaches the maximum at the h.a. In these regions, the magnetization reversal takes place with two irreversible transitions that relate to the nucleation and propagation of two consecutive 90° domain walls. The polar plots of the H_C and H_S are presented in Figure 6 (e, f) shows symmetrical four lobes and asteroid shape. Similar to remanence polar plots, the critical fields also displays symmetrical features with 90° periodicities. The angles between two adjacent e.a. and h.a. are orthogonal to each other confirming that the LSMO film exhibits a pure biaxial (four-fold) anisotropy.[10] Since the LSMO film is relaxed, we expect that the magnetic anisotropy of the film also behaves similarly to the bulk ones with easy axes aligned towards 45° [110] ascribing it to magnetocrystalline nature of LSMO, leading to a pure biaxial anisotropy.[11]

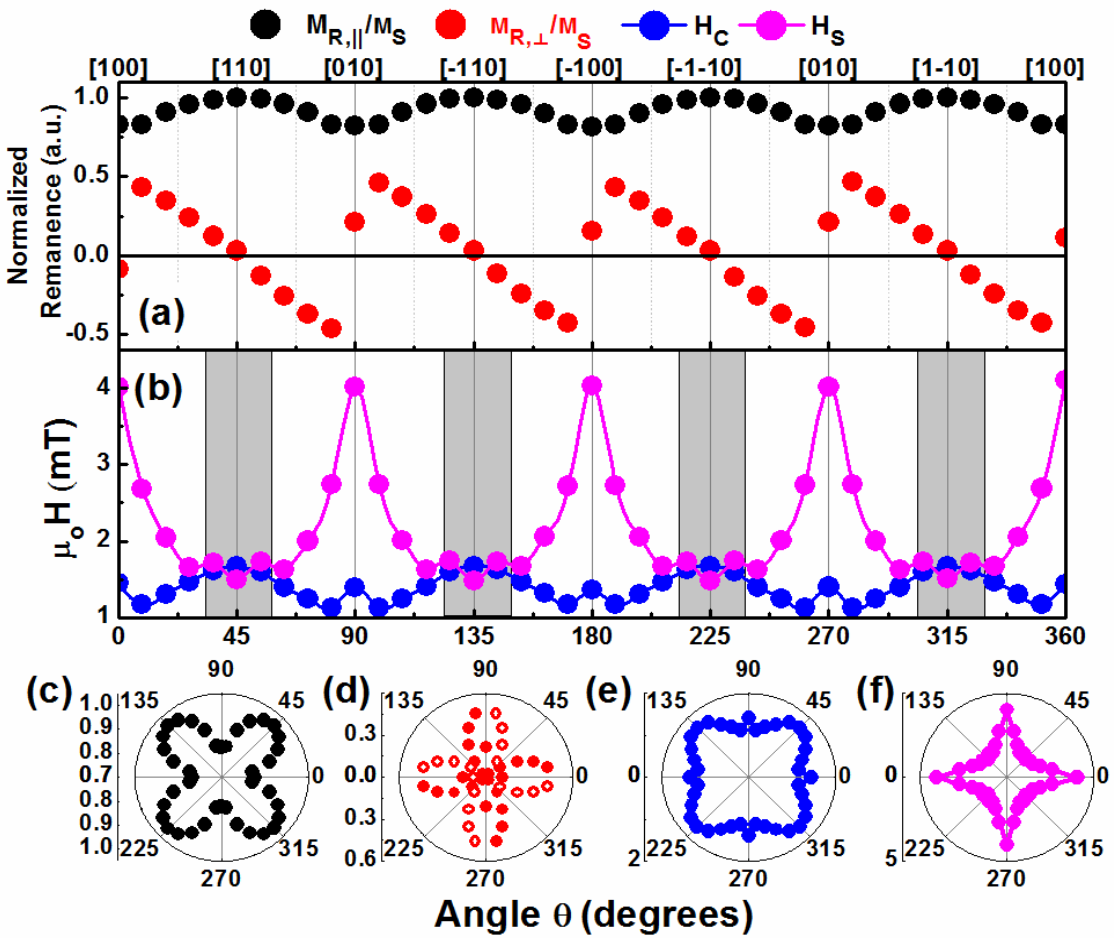

Figure 6: (Color online) Angular evolution at 300 K of the magnetic properties of 50 nm thick LSMO film grown on STO buffered MgO (001) substrate. (a) Normalized remanence magnetization $M_{R,\parallel}/M_s$ (black) and $M_{R,\perp}/M_s$ (red), (b) critical fields (coercivity 'H_C' (blue) and switching 'H_S' (magenta)) as a function of the applied field angle '*θ*' shows well-defined 90° periodicity i.e., a pure bi-axial anisotropy. The grey shaded regions in (b) indicate the system exhibits only one irreversible transition, whereas, in the white regions, the system exhibits two consecutive irreversible transitions. (c-f) Polar plots of $M_{R,\parallel}/M_s$, $M_{R,\perp}/M_s$, H_C and H_S respectively. Positive and negative values in (d) are represented with solid and open circles.

b) LSMO/LSAT (001)

Similar to the films grown on STO (001) substrates, we have grown 3 LSMO thicknesses (50, 25 and 12 nm) on LSAT (001) substrates. The films grown on LSAT are under compressive strain. At room temperature, 12 nm film exhibited pure uniaxial anisotropy. Whereas the 25 nm film exhibits a combination of biaxial and uniaxial anisotropy leading to symmetry broken system. The 50 nm film again showed a dominant but weak uniaxial anisotropy. In order to understand the magnetic anisotropy behavior as the function of temperature, angular dependent remanence polar plots are depicted in Figure 7. For the 12 nm (Figure 7 left panel), as the temperature decreases from 300 to 20 K, uniaxial anisotropy is dominant with two symmetrical lobes. But, the remanence present at hard axes (90°) slightly increases and it is also being observed with the opening of the loop as a decrease in temperature, revealing a weaker uniaxial anisotropy.

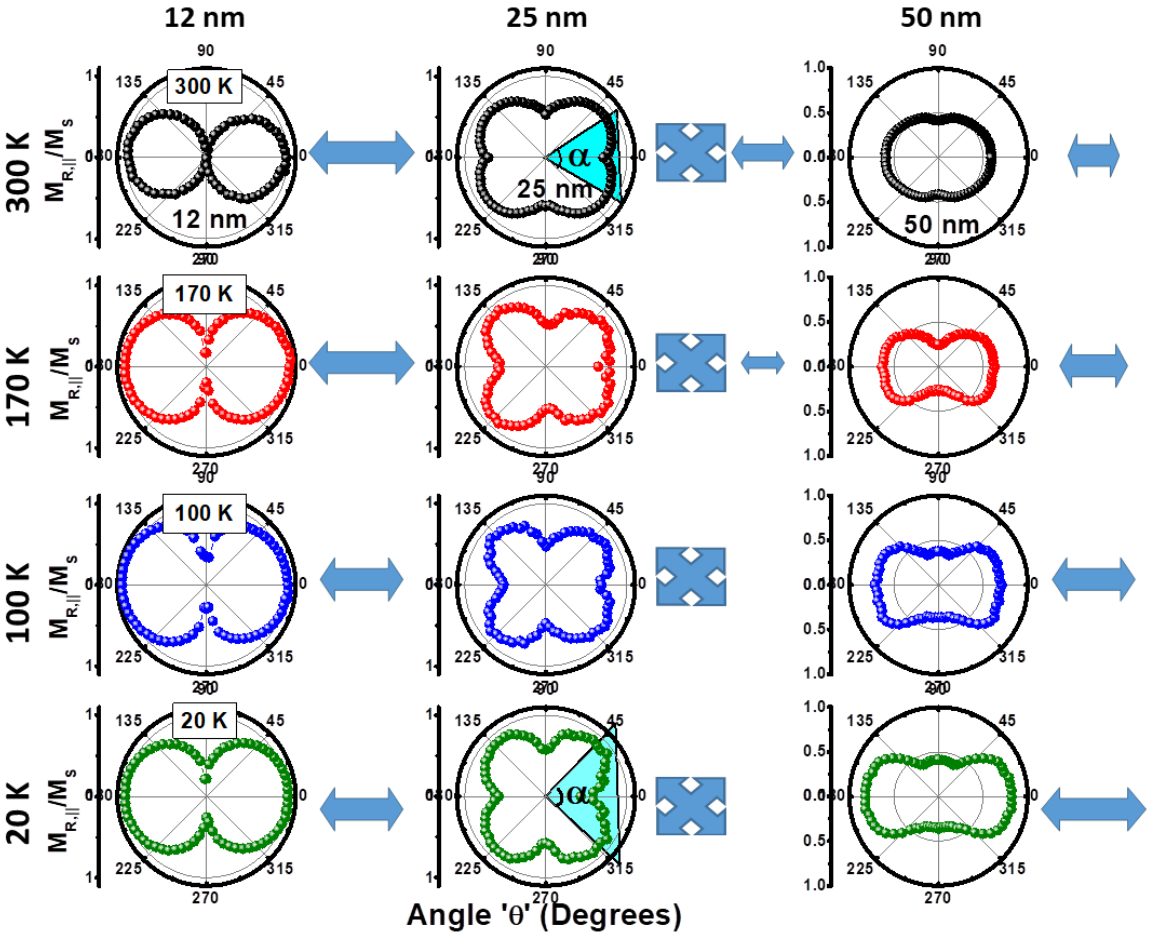

Figure 7: Symmetry of magnetic anisotropy as a function of temperature. The polar plots representation of normalized remanence for (left) 12 nm, (middle) 25 nm and (right) 50 nm films measured at 300, 170, 100 and 20 K respectively.

In the case of 25 nm (Figure 7 middle panel), as the temperature decreases from 300 to 20 K, the symmetry broken system has been changed into pure cubic or four-fold symmetry. It is also observed with the shift in highest remanence value from 31.5° to 45° which is being highlighted.

Therefore, the angle ‘α’ between two easy axes has been increased from 63° to 90° with a decrease in temperature. For the 50 nm film (Figure 7 right panel), the uniaxial anisotropy remains and its strength increases as decreases in temperature. In the latter case, the additional biaxial anisotropies related to the lattice modulations may justify the complex symmetry landscape. At low thickness, the uniaxial (two-fold) is ascribed to either step-surfaces or octahedral rotations of the LSMO, whereas the biaxial (four-fold) contribution comes from the strain induced by cubic substrate. At intermediate and higher thickness regime, the uniaxial contribution comes from orthorhombic symmetry of LSMO and biaxial from magneto-crystalline anisotropy. The weight of such contributions depends on the film thickness, strain and the growth technique.

Due to the compressive strain imposed by the LSAT substrate, the LSMO structures may experience a tilting of the magnetization from in-plane to out-of-plane. This would result in an additional magnetic anisotropy term (oriented along the [001] axis). In fact, in panel Figure 8 (a) the Mz displays a hard axis fully reversible loop and the in-plane magnetization component is almost circular meaning that the magnetization rotates in the plane during the OOP reversal. This suggests a small OOP canting of the magnetization. By increasing the film thickness, we observe squared Mz-Hz hysteretic loops with abrupt transitions indicating a clear reorientation of the magnetization along the field direction. However, in view of the in-plane magnetic anisotropy results in the intermediate thickness (25 nm), such a perpendicular magnetic anisotropy is not relevant; while it is significant in the 50 nm case (more pronounced spin reorientation). This increase in OOP magnetization component is also due to the increase in rhombohedral distortions in the LSMO film.

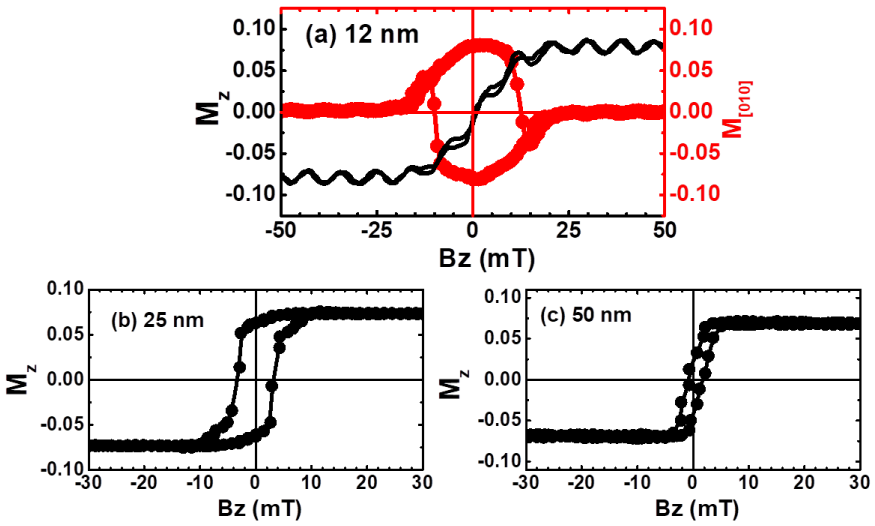

Figure 8: Out-of-plane Kerr hysteresis loops for the LSMO films grown onto LSAT (001) substrate of thicknesses 12, 25 and 50 nm respectively.

These findings will hint us the importance of thickness driven magnetic anisotropy transitions and its complex nature in functional oxides for spintronics applications.

References:

[1] S.S.P. Parkin, M. Hayashi, and L. Thomas, Science (80-.). **320**, 190 (2008).
[2] E. Dagotto, Science (80-.). **309**, 257 (2005).
[3] P. Perna, D. Maccariello, F. Ajejas, R. Guerrero, L. Méchin, S. Flament, J. Santamaria, R. Miranda, and J. Camarero, Adv. Funct. Mater. **27**, 1700664 (2017).
[4] P. Perna, C. Rodrigo, M. Muñoz, J.L. Prieto, A. Bollero, D. Maccariello, J.L.F. Cuñado, M. Romera, J. Akerman, E. Jiménez, N. Mikuszeit, V. Cros, J. Camarero, and R. Miranda, Phys. Rev. B **86**, 24421 (2012).
[5] M. Salehi-Fashami and N. D'Souza, J. Magn. Magn. Mater. **438**, 76 (2017).
[6] M.V.PITKE, Czech J Phys B **21**, 467 (1971).
[7] C. Adamo, X. Ke, H.Q. Wang, H.L. Xin, T. Heeg, M.E. Hawley, W. Zander, J. Schubert, P. Schiffer, D.A. Muller, L. Maritato, and D.G. Schlom, Appl. Phys. Lett. **95**, 112504 (2009).
[8] D. Pesquera, G. Herranz, A. Barla, E. Pellegrin, F. Bondino, E. Magnano, F. Sánchez, and J. Fontcuberta, Nat. Commun. **3**, 1189 (2012).
[9] A.J. Millis, T. Darling, and A. Migliori, J. Appl. Phys. **83**, 1588 (1998).
[10] D. Ecija, E. Jiménez, N. Mikuszeit, N. Sacristán, J. Camarero, J.M. Gallego, J. Vogel, and R. Miranda, Phys. Rev. B **77**, 24426 (2008).
[11] M. Konoto, T. Kohashi, K. Koike, T. Arima, Y. Kaneko, Y. Tomioka, and Y. Tokura, Appl. Phys. Lett. **84**, 2361 (2004).

Résumé long en français par Sandeep Kumar CHALUVADI

Effet de la contrainte liée à l'épitaxie sur l'anisotropie magnétique dans les couches minces de LSMO en vue d'applications spintroniques

I- Introduction:

Les oxydes demi-métaux de structure perovskite sont prometteurs si on les compare aux maériaux métalliques conventionnelles utilisées dans les applications tells que les capteurs magnétiques, les mémoires MRAM (magnetic random access memory), les jonctions tunnel magnétiques (MTJ), les mémoires à déplacement de parois de domaine[1] etc. Les oxydes, en général, apparaissent aujourd'hui être de nouveaux concurrents pour de nombreuses applications pour lesquelles ils n'étaient pas considérées. Cela était lié à la très grande complexité des interactions entre les propriétés des orbitales et du spin qui gouvernent les mécanismes de conduction et qui n'avaient pas été entièrement compris jusqu'à présent.[2,3] Quelle que soit l'application, une des propriétés essentielles qui doit être considérée dans un échantillon ferromagnétique est l'anisotropie magnétique qui gouverne le retournement d'aimantation.[4] Par exemple, une anisoptropie uniaxiale est necessaire pour les capteurs de champ magnétique basés sur la magnetoresistance anisotrope (AMR).[3] Une anisotropie biaxiale , qui a quatre états d'aimantation stables et donc la possibilité de coder plus d'information ("00", "01", "10", "11"), peut être utilisées dans les mémoires et les dispositifs logiques, dans les interrupteurs contrôlés par la tension dans les magnétorésistances géantes (GMR) et les MTJ.[5,6]

La composition semi-métallique $La_{0.67}Sr_{0.33}MnO_3$ (LSMO) est considérée comme un candidat potentiel pour les applications spintroniques grâce à une polarisation en spin proche de 100%. C'est un métal ferromagnétique (FM) à temperature ambiante qui présente une temperature de Curie T_c~370 K. Les propriétés structurales, électriques, et magnétiques des couches de LSMO sont très sensibles aux perturbations externes, parmi lesquelles la contrainte liée à l'épitaxie.[7] En général, dans le cas de films étirés (comprimés), l'occupation des électrons dans le doublet 'e_g' favorise des orbitales dans le plan (hors plan) x^2-y^2 ($3z^2$-r^2).[8]

II- Experimental details:

Des films LSMO de différentes épaisseurs ont été déposées sur différents substrates tells que STO (001), LSAT (001), NGO (110), LAO (001), MgO (001) et STO / MgO (001) par ablation laser pulsée (PLD) avec laser excimer KrF de longueur d'onde 248 nm. Le choix de ces substrats permet d'induire des contraintes épitaxiales variées dans les films LSMO comme indiqué en Figure 1. Les dépôts ont été réalisés à 0.35 mbar d'oxygène tandis que la temperature du substrat était 720°C. Après le dépôt, les substrats sont refroidis à température ambiante à une vitesse de 10°C par minute dans $7x10^2$ mbar de pression d'oxygène. Ici, l'épaisseur des films

LSMO sont 50, 25 et 12 nm, STO 12 nm. Les caractérisations structurales, de morphologie, magnétiques et électriques, ont été réalisées respectivement par diffraction de rayons X (XRD), micrscopie à force atomique (AFM), magnétomètre à SQUID (Superconducting Quantum Interference Device), et la technique quatre points. Le retournement d'aimantation dans le plan, le champ coercitif, l'anisotropie magnétique ont été réalisées en fonction de l'angle à 300K et 40K en fonction de l'angle par magnétométrie magnéto-optique vectorielle (v-MOKE).

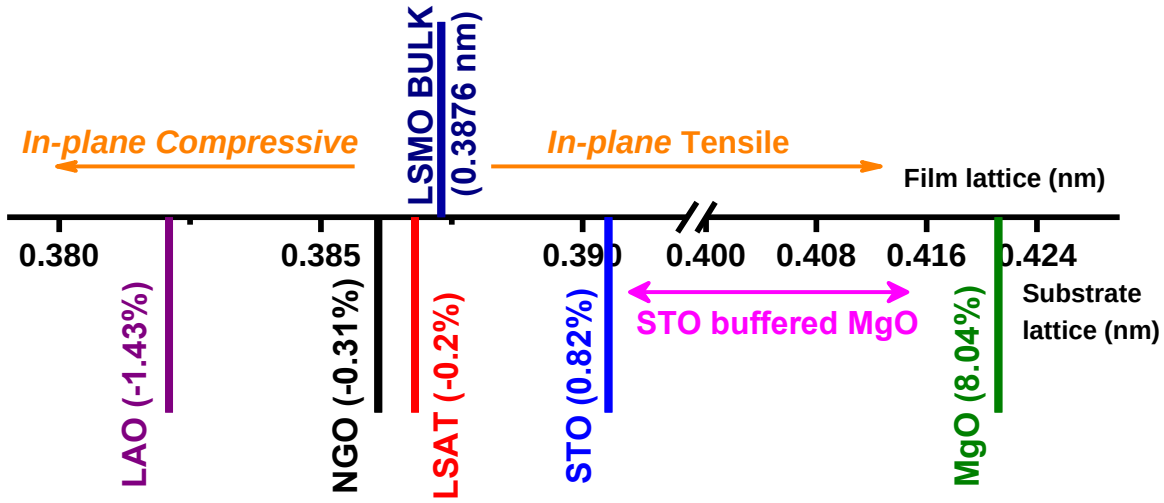

Figure 1: Lattice mismatch between LSMO and the substrates that are used in this study; -1.36% for LAO, -0.31% for NGO, -0.12% for LSAT, +0.82% for STO, +8.04% for MgO. '-' indicates compressive strain whereas '+' indicates tensile strain.

III- Effet du substrats

La Figure 2 (gauche) montre les diagrammes XRD de films LSMO d'épaisseur 50 nm déposés sur différents substrats. Des films déposés sur des substrats aux paramètres de maille proche du LSMO sont contraints pour toute la gamme d'épaisseur étudiée. Au contraire, les films déposés sur des substrats aux paramètres de maille très différents du LSMO tels que MgO (001) sont entièrement relaxés.

La topologie de surface des films par AFM (Figure 2 (en haut à droite)) montre que les films sont atomiquement plats avec une rugosité de ~ 0.1 nm à ~ 0.4 nm. La contrainte liée à l'épitaxie induit des effets importants sur la température de transition métal-isolant (T_{MI}). T_{MI} a été mesuré de l'ordre de 420 K (Figure 2 (en bas à droite)) dans le cas des substrats aux paramètres de maille proches de LSMO (STO, LSAT, NGO) tandis que pour les films déposés sur LAO et MgO, il y a une réduction de T_p.

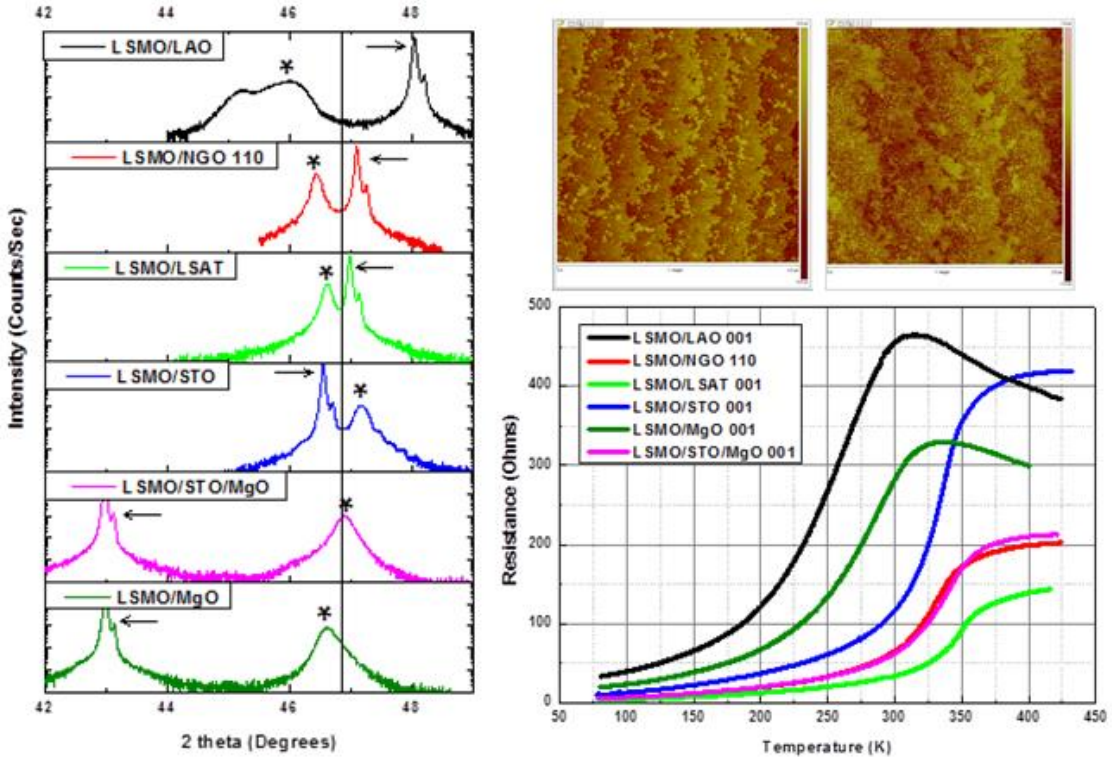

Figure 2: (Left panel) XRD plots of epitaxial LSMO (00l) thin films of 50 nm thickness grown on different single crystal substrates. The solid line indicates the LSMO Bulk value, * and arrow represents (002) peak of LSMO film and film respectively. (Right panel) Top shows the AFM topography images of LSMO film grown on STO (001) and NGO (110) substrates and bottom shows temperature dependent resistance of LSMO film.

La Figure 3 donne les analyses détaillées des propriétés de films LSMO en fonction de l'épaisseur et du substrat. Le paramètre hors plan 'c' des films en fonction de l'épaisseur et du substrat est présenté à la Figure 3 (a). La valeur pour le LSMO massif est aussi présentée par une ligne solide pour comparaison. Lorsque nous passons de la contrainte compressive à étirée, le paramètre de maille du film 'c' diminue. Cependant, les films LSMO déposés sur STO / MgO montrent des valeurs plus élevées que pour les films deposes sur STO car le film est partiellement relaxé. Les films déposés sur MgO présentent des valeurs de 'c'plus élevées car le film est complètement relaxé à cause du grand désaccord de (+8.04 %). Une effet similaire est observé dans les ω-scans (Figure 3 (b)). Les films déposés sur des substrats à faible désaccord de maille sont de meilleurs qualité avec des valeurs de FWHM inférieures à ~ 0.15°; cependant sur des substrats à fort désaccord de maille (STO buffered MgO et MgO) elles deviennent égales à 2°. La Figure 3 (c) représente la rugosité RMS des films. Quand la contrainte dans le film augmente, la rugosité du film augmente également. L'influence de contrainte biaxiale sur la transition métal-isolant et 'T_p' des films déposés sur différents substrats sont présentées à la Figure 3 (d). Elle indique que les films sous contrainte compressive présentent des 'T_p' plus élevées comparées aux films sous contrainte en tension, ce qui est cohérent avec la littérature.[9] Cependant, quand la contrainte augmente, T_p décroit rapidement.

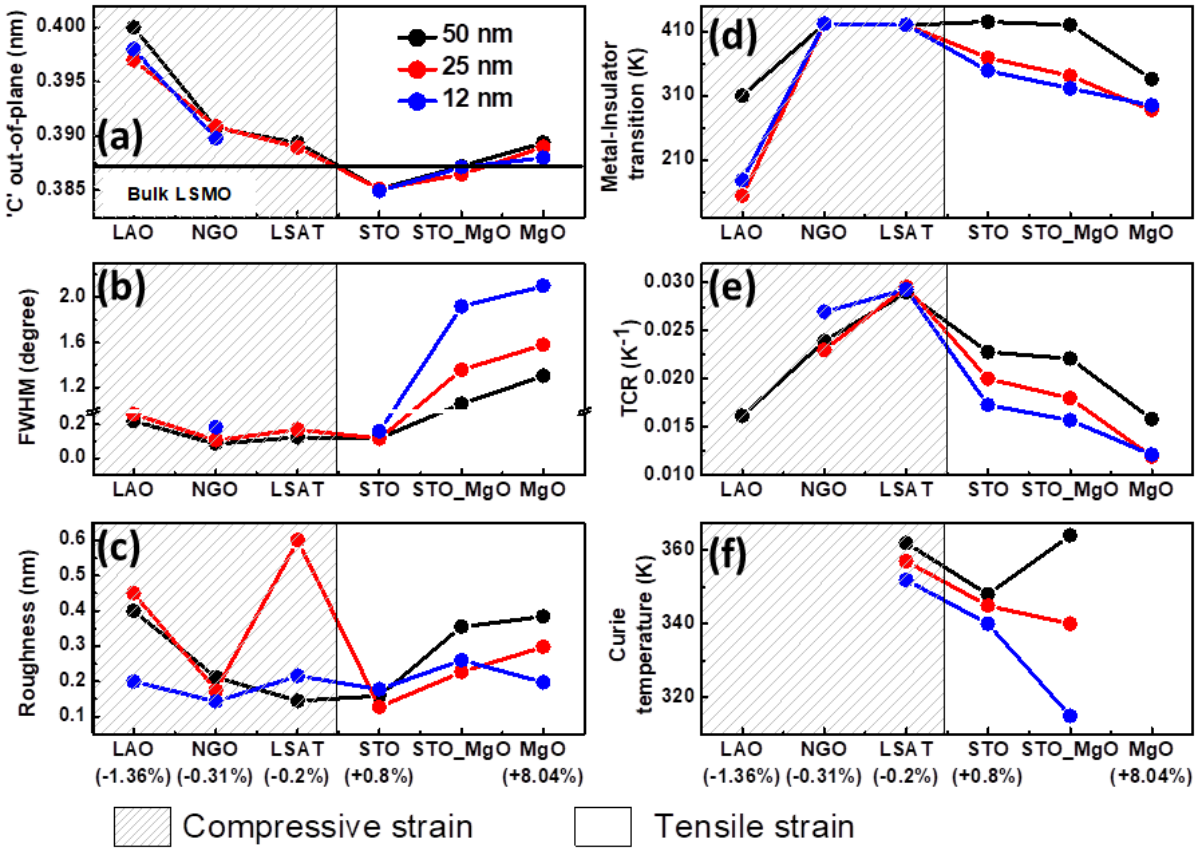

Figure 3: Epitaxial strain and thickness dependent properties of LSMO thin films as a function of strain. (a) 'c-axis' out-of-plane lattice parameter measured from XRD scans, (b) FWHM calculated from rocking curves from their corresponding LSMO (002) peak, (c) average RMS roughness values of the thin films measured by AFM on the scan area of 2µm x 2µm, (d, f) metal-insulator transition temperature and Curie temperature of the films, and (e) maximum temperature coefficient of resistance calculated from $\frac{1}{R}\frac{dR}{dT}$.

IV- Anisotropie magnétique dans les couches minces LSMO

Les mesures par v-MOKE ont été réalisés à IMDEA Madrid dans le mode longitudinal. Les échantillons ont été montées sur un goniomètre eucentrique qui permet de garder le plan de réflexion constant pendant les mesures angulaires comme le montre la Figure 4. A $\theta = 0°$, le champ magnétique appliqué est aligné parallèlement à l'axe cristallographique [100] du substrat. Les cycles d'hystéresis dans le plan ont été acquises entre 0° et and 360° avec un pas de 9° en tournant l'échantillon dans le plan du film et en gardant fixe la direction du champ magnétique externe. L'aimantation à remanence, et le champ coercitif sont calculés à partir de chaque cycle d'hystéresis afin de suivre l'évolution sur 360°.

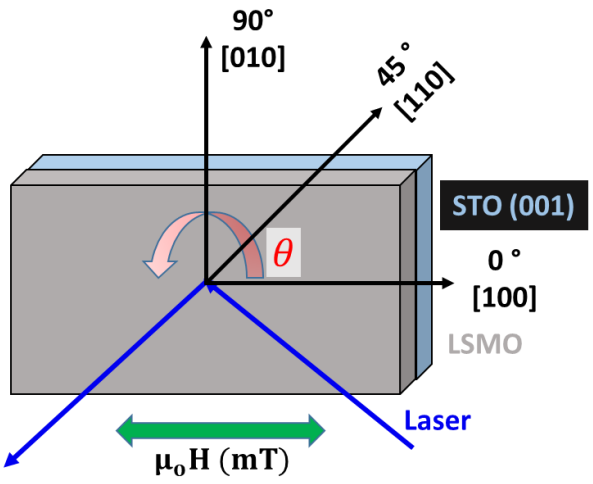

Figure 4: Schematic of the sample mounted on the goniometer in the v-MOKE set-up in the longitudinal mode. Here, the angle 'θ' indicates the direction of the rotation of the sample. The applied field direction is also presented. At θ=0°, the applied field is aligned parallel to [100] crystallographic axis.

a) LSMO/STO (001):

La Figure 5 présente la dépendence angulaire de l'aimantation de films LSMO/STO (001) de différentes épaisseurs avec l'axe facile (e.a) et axe difficile (h.a) indiqués par des flèches. La Figure 5 (a) montre la dependence angulaire de l'aimantation à remanence de films LSMO d'épaisseur 50 nm, avec une anisotropie biaxiale où les axes faciles sont alignés selon les axes <110> axis. La Figure 5 (b) montre le graphe polaire de l'aimantation à remanence avec une structure en papillon avec quatre lobes indiquant une anisotropie biaxiale. On peut observer que la valeur sur l'axe facile n'est pas la même dans toutes les directions. La périodicité entre axe facile et l'axe difficile n'est pas exactement 45°, suggérant que il existe une anisotropie supplémentaire dans le film (même si plus faible) qui est induit par la cassure de symétrie de surface à cause de la formation de marches. Il y a donc une compétition entre une anisotropie biaxiale (forte) due à l'anisotropie magnétocristalline et une anisotropie uniaxiale (faible) due à la formation de marches liée à un petit angle de miscut. Lorsque l'épaisseur diminue de 50 à 12 nm, il y a un changement d'anisotropie de biaxiale à uniaxiale. Les résultats ont clairement mis en évidence la dépendence angulaire de l'aimantation à rémanence d'une couche LSMO d'épaisseur 25 nm (Figure 5 (d)).

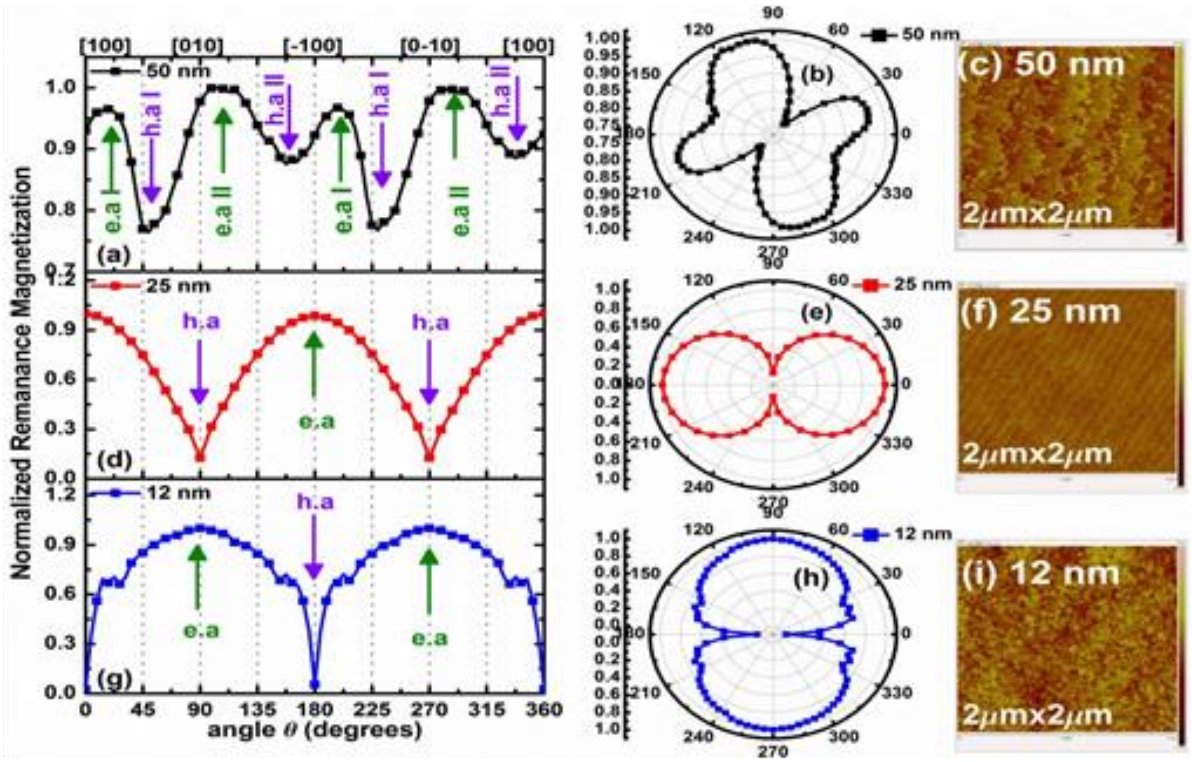

Figure 5: (a, d and g) v-MOKE angular dependent remanence magnetization of LSMO films of varying thickness grown on STO (001) substrate; (b, e, h and c, f, i) are the corresponding polar plots and AFM topography respectively.

b) LSMO/LSAT (001):

De façon similaire aux films déposés sur STO (001), nous avons déposés 3 films LSMO d'épaisseurs (50, 25 and 12 nm) sur LSAT (001). Les films déposés sur LSAT subissent une contrainte compressive. A température ambiante, le film d'épaisseur 12 nm montre une anisotropie uniaxiale. Tandis que le film d'épaisseur 25 nm montre une combinaison d'anisoptropie biaxiale et uniaxiale conduisant à un système à symétrie brisée. Le film d'épaisseur 50 nm montre à nouveau une anisotropie uniaxiale dominante mais faible. Des graphes polaires en fonction de la température sont présentés à la Figure 6. Pour le film d'épaisseur 12 nm (Figure 6 à gauche), l'anisotropie uniaxiale est dominante lorsque la température diminue. Mais la rémanence à l'axe difficile (90°) augmente légèrement et une ouverture du cycle est observée, indiquant une anisotrope plus faible.

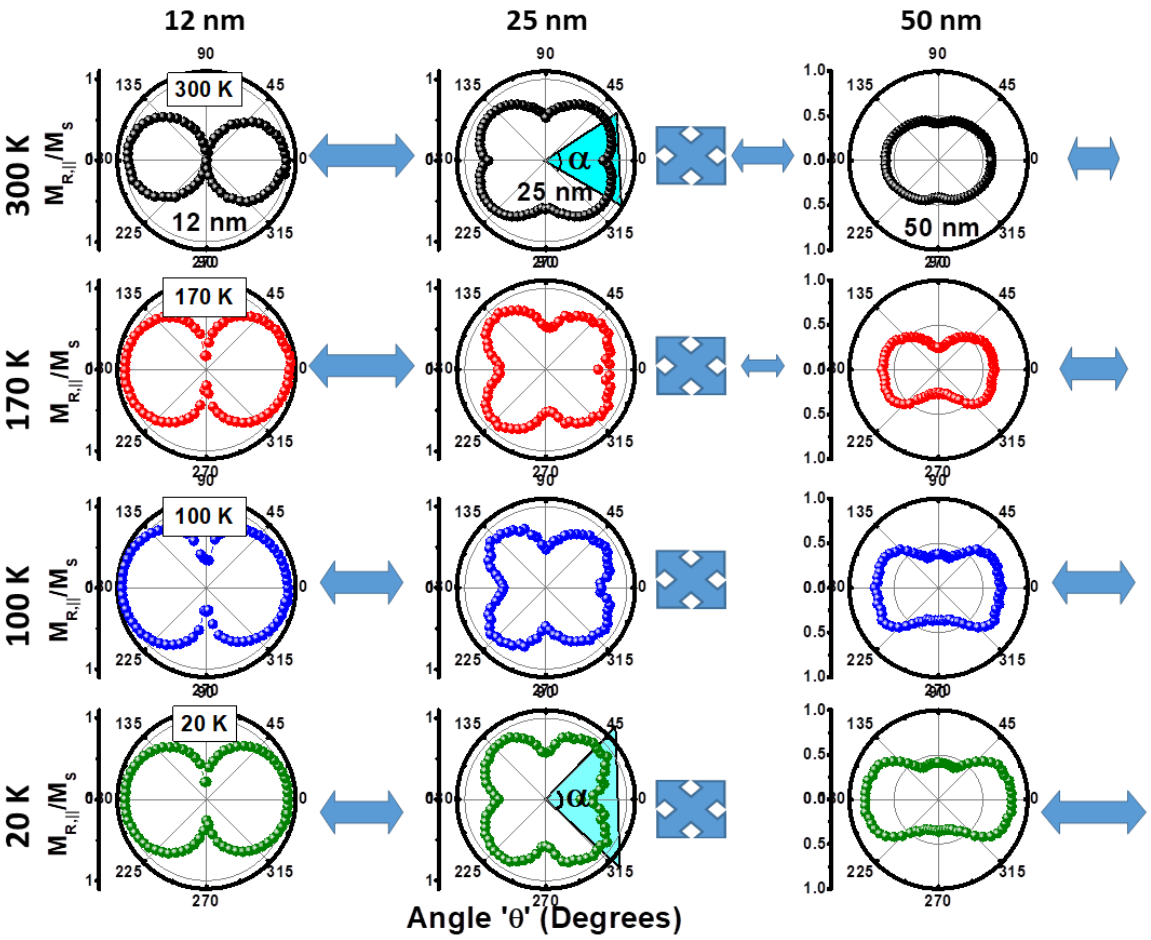

Figure 6: Symmetry of magnetic anisotropy as a function of temperature. The polar plots representation of normalized remanence for (left) 12 nm, (middle) 25 nm and (right) 50 nm films measured at 300, 170, 100 and 20 K respectively.

Dans le cas de film d'épaisseur 25 nm (Figure 6 milieu), lorsque la temperature diminue de 300 à 20K, on retrouve une pure symétrie cubique. Il a également été observé par le décalage de la valeur de rémanence de 31.5° à 45° qui est représenté. Pour le film d'épaisseur 50 nm (Figure 6 droite), l'anisotropie uniaxiale se maintient et sa force augmente lorsque la température diminue. Dans le dernier cas, les anisotropies additionnelles liées à des modulations de paramètres de maille peuvent expliquer les observations rapportées. A faible épaisseur, l'anisotropie uniaxiale peut être attribuée à des marches en surface ou à des rotations d'octahèdres, alors que la contribution biaxiale provient de contraintes induites par le substrat cubique. A des épaisseurs intermédiaires et plus élevées, la contribution uniaxiale provident de la symétrie orthorhombique et la biaxiale de l'anisotropie magneto-cristalline. Le poids de telles contributions dépend de l'épaisseur de film, de contrainte et de la technique de croissance.

A cause de la contrainte compressive imposée par le substrat LSAT, les structures LSMO peuvent présenter une rotation de l'aimantation du plan vers hors plan. Cela pourrait conduire à une anisotropie magnétique additionnelle (orientée selon [001]). EN fait, dans la Figure 7 (a) Mz

montre un axe difficile entièrement réversible et une composante dans le plan qui est pratiquement circulaire indiquant que l'aimantation tourne dans le plan pendant le retournement OOP. Cette anisotropie existe aussi dans les couches plus fines mais n'est pas significative. L'augmentation de l'anisotropie hors plan peut être lié à des distorsions rhombohédriques.

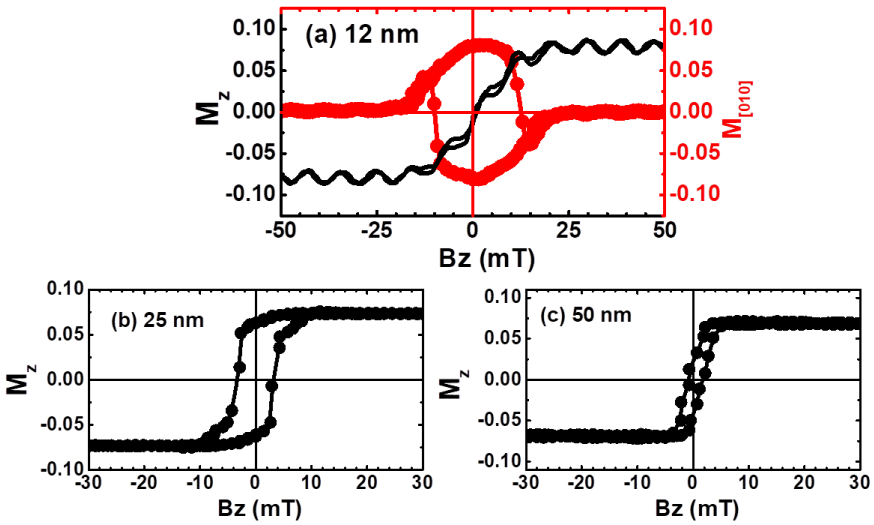

Figure 7: Out-of-plane Kerr hysteresis loops for the LSMO films grown onto LSAT (001) substrate of thicknesses 12, 25 and 50 nm respectively.

V- Conclusions/Résumé

Nous avons présenté une étude des effets de contrainte induits par l'épitaxie dans des couches minces $La_{1-x}Sr_xMnO_3$ (LSMO) (001) (x = 0.33) pour 3 épaisseurs de films (50, 25 et 12 nm) déposés par Ablation Laser Pulsée (PLD) sur différents substrats tels que $SrTiO_3$ (STO) (001), STO buffered MgO (001), $NdGaO_3$ (NGO) (110) et $(LaAlO_3)_{0.3}(Sr_2AlTaO_6)_{0.7}$ (LSAT) (001). L'étude a été complétée par l'effet de la composition sur les propriétés magnétiques de couches minces de $La_{1-x}Sr_xMnO_3$ avec x=0,33 et 0,38 déposées par Epitaxie à Jets Moléculaires (MBE). Des caractérisations par diffraction de rayons X (XRD), et microscopie à force atomique (AFM), des mesures de résistivité électrique en quatre points en fonction de la température, d'aimantation par magnetometrie à SQUID (Superconducting Quantum Interference Device) et d'anisotropie magnétique par magnétométrie magnéto-optique Kerr vectorielle (MOKE) sont présentées. Les évolutions angulaires de l'anisotropie magnétique, de l'aimantation à rémanence, du champ coercitif et du champ de renversement d'aimantation ont ainsi pu être analysées pour des films épitaxiés LSMO de différentes épaisseurs. Des études en fonction de la température complètent les données. L'origine de l'anisotropie (magnétique, magnétocristalline, magnétostrictive ou liée aux effets de marches et d'angle de désorientation du substrat) a finalement été discutée.

Références:

[1] S.S.P. Parkin, M. Hayashi, and L. Thomas, Science (80-.). **320**, 190 (2008).
[2] E. Dagotto, Science (80-.). **309**, 257 (2005).
[3] P. Perna, D. Maccariello, F. Ajejas, R. Guerrero, L. Méchin, S. Flament, J. Santamaria, R. Miranda, and J. Camarero, Adv. Funct. Mater. **27**, 1700664 (2017).
[4] P. Perna, C. Rodrigo, M. Muñoz, J.L. Prieto, A. Bollero, D. Maccariello, J.L.F. Cuñado, M. Romera, J. Akerman, E. Jiménez, N. Mikuszeit, V. Cros, J. Camarero, and R. Miranda, Phys. Rev. B **86**, 24421 (2012).
[5] M. Salehi-Fashami and N. D'Souza, J. Magn. Magn. Mater. **438**, 76 (2017).
[6] M.V.PITKE, Czech J Phys B **21**, 467 (1971).
[7] C. Adamo, X. Ke, H.Q. Wang, H.L. Xin, T. Heeg, M.E. Hawley, W. Zander, J. Schubert, P. Schiffer, D.A. Muller, L. Maritato, and D.G. Schlom, Appl. Phys. Lett. **95**, 112504 (2009).
[8] D. Pesquera, G. Herranz, A. Barla, E. Pellegrin, F. Bondino, E. Magnano, F. Sánchez, and J. Fontcuberta, Nat. Commun. **3**, 1189 (2012).
[9] A.J. Millis, T. Darling, and A. Migliori, J. Appl. Phys. **83**, 1588 (1998).
[10] D. Ecija, E. Jiménez, N. Mikuszeit, N. Sacristán, J. Camarero, J.M. Gallego, J. Vogel, and R. Miranda, Phys. Rev. B **77**, 24426 (2008).
[11] M. Konoto, T. Kohashi, K. Koike, T. Arima, Y. Kaneko, Y. Tomioka, and Y. Tokura, Appl. Phys. Lett. **84**, 2361 (2004).